



City Research Online

City, University of London Institutional Repository

Citation: Xu, Z.G. (1991). An investigation of two-phase flow of organic working fluids in the inlet port of a Lysholm screw expander. (Unpublished Doctoral thesis, City, University of London)

This is the accepted version of the paper.

This version of the publication may differ from the final published version.

Permanent repository link: <https://openaccess.city.ac.uk/id/eprint/28576/>

Link to published version:

Copyright: City Research Online aims to make research outputs of City, University of London available to a wider audience. Copyright and Moral Rights remain with the author(s) and/or copyright holders. URLs from City Research Online may be freely distributed and linked to.

Reuse: Copies of full items can be used for personal research or study, educational, or not-for-profit purposes without prior permission or charge. Provided that the authors, title and full bibliographic details are credited, a hyperlink and/or URL is given for the original metadata page and the content is not changed in any way.

City Research Online:

<http://openaccess.city.ac.uk/>

publications@city.ac.uk

CITY UNIVERSITY

DEPARTMENT OF MECHANICAL ENGINEERING & AERONAUTICS

AN INVESTIGATION OF
TWO-PHASE FLOW OF ORGANIC WORKING FLUIDS
IN THE INLET PORT OF A LYSHOLM SCREW EXPANDER

by

Zhi Guo Xu

A thesis submitted to
The City University
for the degree of
Doctor of Philosophy

August 1991

020167945

ABSTRACT

Lysholm twin screw expanders are being developed to recover work from the two phase flash expansion of organic fluids. The work described in this thesis was carried out to maximise the efficiency of such machines by improving the inlet port design. To this end the flow in the inlet port was investigated both analytically and experimentally.

The theoretical analysis was carried out on the assumption of one-dimensional steady flow allowing for thermal non-equilibrium and relative motion between the phases with corrections to allow for boundary layer growth. The equations thereby developed were solved by means of a numerical procedure together with the calculus of variations to design the port as a circular cross section nozzle of optimum adiabatic efficiency. The resulting design was then modified to progressively transform its cross section from circular at the inlet to the characteristic irregular shape of a screw expander inlet port at the exit.

The experimental work involved the construction of both the circular and modified cross section port designs and their testing in a closed loop containing Refrigerant 113 as the working fluid. The loop was well instrumented and the void fraction distribution in the port exit plane was measured with a fibre optic probe whose tip position was varied by a specially designed computer controlled traversing system.

Predicted and measured values of void fraction differed on average by only 2.1% in the circular cross section design and 4.5% in the transformed design. The corresponding differences in pressure along the port length were well within 1.0%. The procedure developed for improved design therefore appears to be substantially validated.

LIST OF CONTENTS

	<u>PAGE</u>
ABSTRACT	1
LIST OF CONTENTS	2
LIST OF FIGURES	6
NOMENCLATURE	9
ACKNOWLEDGEMENTS	12
<u>CHAPTER 1: INTRODUCTION</u>	14
1.1. SUMMARY	14
1.2. POWER FROM LOW GRADE HEAT	14
1.3. THE IDEAL THERMODYNAMIC SYSTEM	17
1.4. PRACTICAL SYSTEMS	22
1.4.1. Total Flow System	22
1.4.2. Flash Steam System	24
1.4.3. Binary System	26
1.4.3.1. Organic Rankine Cycle System	26
1.4.3.2. Trilateral Flash Cycle System	29
<u>CHAPTER 2 : LITERATURE SURVEY</u>	34
2.1. SUMMARY	34
2.2. TWO-PHASE EXPANDERS	34
2.2.1. The Lysholm Total Flow Expander	35
2.2.2. Two-Phase Turbines	39
2.2.3. Lysholm Screw Expander for TFC system	42
2.3. TWO-PHASE FLOW	47
2.3.1. Flow Regimes and Flow Regime Maps	47
2.3.2. Pressure Drop Calculation and Flow Modelling	52
2.3.2.1. Empirical Methods	54
2.3.2.2. Analytical Modelling	57
2.3.2.2.1. Homogeneous Equilibrium Flow Model	57
2.3.2.2.2. Separated Flow Model	58
2.3.3. Void Fraction Measurement Technique	61
2.3.3.1. Average Void Fraction Measurement	62
2.3.3.2. Local Void Fraction Measurement	64
<u>CHAPTER 3 : OBJECT OF RESEARCH</u>	69

	<u>PAGE</u>
<u>CHAPTER 4 : THEORETICAL ANALYSIS</u>	71
4.1. SUMMARY	71
4.2. PHYSICAL MODEL	72
4.2.1. Basic Assumptions	74
4.2.2. Equations Employed	75
4.3. DEVELOPMENT OF CONSERVATION EQUATIONS	76
4.3.1. The Continuity Equation for a Two-Phase Mixture	76
4.3.2. The Momentum Equation for a Two-Phase Mixture	78
4.3.3. The Energy Equation for a Two-Phase Mixture	80
4.3.4. The Drag Equation for Liquid Droplets	81
4.3.5. The Heat Transfer Equation for Liquid Droplets	83
4.4. CONSTITUTIVE AND STATE EQUATIONS	84
4.4.1. Droplet Size	85
4.4.2. Drag Coefficient	87
4.4.3. Heat Transfer Coefficient	88
4.5. BOUNDARY LAYER MOMENTUM EQUATION	89
<u>CHAPTER 5 : NUMERICAL SOLUTION</u>	96
5.1. SUMMARY	96
5.2. DERIVATION OF THE DISCRETISATION EQUATIONS	98
5.3. SOLUTION PROCEDURE	106
<u>CHAPTER 6 : INLET PORT DESIGN AND OPTIMISATION</u>	114
6.1. SUMMARY	114
6.2. THE THEORY OF THE CALCULUS OF VARIATIONS	115
6.2.1. Solution of the Simplest Problem	116
6.2.2. Solution of the Isoperimetric Problem	118
6.3. INLET PORT OPTIMISATION PROBLEM FORMULATION	121
6.4. INLET PORT DESIGN PROCEDURE	126
6.5. TRANSFORMATION PROCEDURE	131
6.5.1. Transformation between Two Parallel Cross Sections	132
6.5.2. Transformation between Two Nonparallel Cross Sections	134

	<u>PAGE</u>
<u>CHAPTER 7 : EXPERIMENTAL DETAILS</u>	140
7.1. SUMMARY	140
7.2. DESCRIPTION OF THE TEST RIG	140
7.2.1. Main Feed Pump	142
7.2.2. Fluid Heater	142
7.2.3. Fluid Control Valve	143
7.2.4. Condenser	143
7.3. DESCRIPTION OF THE INLET PORTS	144
7.4. INSTRUMENTATION	145
7.4.1. System Pressures	146
7.4.2. System Temperatures	147
7.4.3. Working Fluid Flow Rate	148
7.4.4. Cooling Water Flow Rate	148
7.4.5. Local Void Fraction	149
7.4.5.1. Fibre Optic Probe	149
7.4.5.2. Probe Traversing System	151
7.4.5.3. Programming	155
7.4.6. Data Logging System	157
7.5. EXPERIMENTAL PROCEDURES	158
7.5.1. Preparations for Start Up	158
7.5.2. Starting Procedure	160
7.5.3. Shut-down Procedure	162
<u>CHAPTER 8 : RESULTS AND DISCUSSION</u>	163
8.1. SUMMARY	163
8.2. TEST CONDITIONS	163
8.3. STEADY STATE CONDITION AND DATA COLLECTION PROCEDURE	164
8.4. COMPARISON OF EXPERIMENTAL AND COMPUTED PRESSURE DISTRIBUTIONS	167
8.5. LOCAL VOID FRACTION MEASUREMENT RESULTS	172
8.5.1. Results for No.1 Inlet Port	175
8.5.2. Results for No.2 Inlet Port	177
<u>CHAPTER 9 : CONCLUSIONS</u>	179
<u>REFERENCES AND BIBLIOGRAPHY</u>	181

PAGE

APPENDICES

A. Computer Program Documentation and Listing	187
B. The Secant Method for Simultaneous Nonlinear Equations	218
C. Pressure Force on a Spherical Droplet	220
D. Figures	

LIST OF FIGURES

- 1.1. Hot Dry Rock Technology
- 1.2. Temperature-Entropy Diagram of Carnot Cycle
- 1.3. Ideal Thermodynamic Cycle
- 1.4. Total Flow System
- 1.5. Flashed Steam System
- 1.6. Organic Rankine Cycle System
- 1.7. Trilateral Flash Cycle System
- 1.8. Comparison of TFC and ORC Ideal Efficiencies
- 1.9. Screw Expander and Turbine Combination
- 2.1. Layout of Lysholm Screw Expander
- 2.2. Organic Two-Phase Turbine System
- 2.3. Schematic Diagram of SPHERE Test Rig
- 2.4. A Side-view of the Old Inlet Port
- 2.5. Basic Flow Regimes
- 2.6. X-ray Absorption Method for Flow Regime Detection
- 2.7. Danel & Delhaye Fibre Optic Probe
- 2.8. Operational Principle of Optical Methods
- 4.1. Schematic Diagram of Two-Phase Flow Model
- 5.1. Discretisation of Flow Field
- 5.2. Block Diagram of Choking Flow Rate Search
- 6.1. Layout of the New Lysholm Screw Expander Inlet Port
- 6.2. Inlet Port Exit Cross-Section
- 6.3. Effect of Inlet Port Length on Efficiency
- 6.4. Relationship between Lagrange Multiplier and Port length
- 6.5. Optimum and Practical Inlet Port Contours
- 6.6. Axial Pressure Distribution

- 6.7. Liquid and gas Velocity Distributions
- 6.8. Averaged Void Fraction Distribution
- 6.9. Droplet Diameter Distribution
- 6.10. Transformation between Two Parallel Cross Sections
- 6.11. Transformation between Two Nonparallel Cross Sections
- 7.1. A Photographic View of the Test Rig
- 7.2. Schematic Diagram of the Test Rig
- 7.3. Schematic of the Feed Pump
- 7.4. Feed Pump Characteristic
- 7.5. Scale Drawing of No.1 Inlet Port
- 7.6. Schematic Drawing of No.2 Inlet Port
- 7.7. No.2 Inlet Port in Situ
- 7.8. Dimensions of the Fibre Optic Probe
- 7.9. Void Fraction Unit and Probe Traversing System
- 7.10. Front View of Mechanical Traversing Unit
- 7.11. Components of Mechanical Traversing Unit
- 7.12. Schematic of Stepper Motor Controller Unit
- 7.13. Stepper Motor Controller Connection Diagram
- 7.14. Block Diagram of Motor Control & Signal Processing Operation
- 7.15. Flow Chart of Probe Movement & Signal Processing Program
- 7.16. Schematic Diagram of Data Logging System
- 8.1.-8.12. Comparison of Experimental and Computed Pressure Distributions for No.1 Inlet Port
- 8.13.-8.24. Comparison of Experimental and Computed Pressure Distributions for No.2 Inlet Port
- 8.25. Void Fraction Measurement Points (No.1 Inlet Port Exit)
- 8.26.-8.37. Void Fraction Distribution at No.1 Inlet Port Exit
- 8.38.-8.40. Comparison of Experimental and Computed Average Void Fractions at No.1 Inlet Port Exit
- 8.41. Void Fraction Measurement Points (No.2 Inlet Port Exit)

8.42.-8.53. Void Fraction Distribution at No.2 Inlet Port Exit

8.53.-8.56. Comparison of Experimental and Computed Average
Void Fractions at No.2 Inlet Port Exit

A.1. Flow Chart of Numerical Solution Procedure

C.1. Differential Surface Area of A Spherical Droplet

LIST OF TABLES

1.1. Detailed Comparison between TFC and ORC systems

2.1. Helical Rotor Expander Size for Total Flow System

6.1. Computational Results for Practical Inlet Port

7.1. Instrumentation Schedule

8.1. Summary of Planned Refrigerant 113 Test Data

8.2. Summary of Test Conditions for No.1 Inlet Port

8.3. Summary of Test Conditions for No.2 Inlet Port

NOMENCLATURE

a	vapour velocity factor
A	cross-sectional area
A_d	droplet surface area
b	liquid velocity factor
C_G	gas specific heat
C_L	liquid specific heat
C_D	interfacial drag coefficient
C_f	two-phase friction factor
C_{f1}	liquid friction factor
D	droplet diameter
F_D	drag force on single droplet
F_P	pressure force on single droplet
H	total enthalpy
h	heat transfer coefficient
h_G	gas specific enthalpy
h_L	liquid specific enthalpy
h_{LG}	latent heat
I	thrust or intensity
i	computational mesh point
K	isoperimetric constant
K_G	gas thermal conductivity
L	flow channel length
\ln	natural logarithm
\dot{m}	mass flow rate
m_d	droplet mass
N	number of computational steps

\dot{N}_d	number flow rate of droplets at one cross section
Nu	Nusselt number in heat transfer correlation
P	static pressure
Q	heat
Re	Reynolds number
R_o	radius of the revolution of the body
S	perimeter
s	slip ratio
T	temperature
t	time
V	velocity
\bar{V}	mass-weighted mean velocity
W	work
We	Weber number
x	dryness fraction
X	independent variable
y_o	radius of channel from the centre axis
y	distance measured from channel wall
Z	axial distance measured from port entry

Greek symbols

α	void fraction, given by the ratio A_G/A
ρ	density
ρ'	mass-weighted mean density
μ	viscosity
λ	Lagrangian multiplier
δ	boundary layer thickness
δ^*	boundary layer displacement thickness

θ boundary layer momentum thickness or wall angle
 Δ designate a difference when used as a prefix
 τ_0 shear stress evaluated at wall surface
 σ surface tension

Subscripts

accel accelerational component of pressure drop
cri critical
e refer to port exit
fric frictional component of pressure drop
G gas phase
grav gravitational component of pressure drop
hom homogeneous
i refer to port inlet
L liquid phase
m mid-position of each computation step
max maximum
min minimum
o optimum
sat saturation
t total
TP two-phase

ACKNOWLEDGMENTS

This project was conducted with the joint sponsorship of the British Council and China State Education Commission, under Technical Cooperation Training Award. This support is gratefully acknowledged.

Special thanks go to my supervisor, Dr.I.K. Smith for all his help, guidance and enthusiasm throughout the work, and for obtaining the necessary financial support when my British Council scholarship expired. Without this the project could not possibly have been completed. In this respect I would also like to thank TFC Power Systems Ltd. and its chairman Mr.Peter Kalms.

I would like to acknowledge my indebtedness to many people in the Department of Mechanical Engineering & Aeronautics, City University who have assisted me during the course of the work, consciously or otherwise. In particular, Dr.C.A. Aldis lent his valuable support in the design and construction of the test rig and acquisition of necessary equipment. Mr.J. Lee, technician, did excellent work manufacturing and assembling the mechanical traversing unit under the leadership of departmental superintendent Mr.J. Spencer, then chief technician. The help of Mr.J. Dutton, chief technician, Mr.G. Rudland and Mr.G.G. Gatehouse, workshop technicians, is also gratefully acknowledged.

I appreciate very much the help of The City University Computer Unit's staff, especially that of Mr.J. Cooper, who expertly assembled the stepper motor controller circuit boards and provided necessary

equipment for our microcomputers. As regards the stepper motors and controller I would also like to thank Mr.C. Maxwell, chief technician of the Department of System Engineering, for his kind help and guidance.

I am also indebted to Dr.D.G. Elliott of Jet Propulsion Laboratory, California Institute of Technology, U.S.A. for his useful and unselfish suggestions in correspondence concerning the numerical methods and computer programming.

Finally, I wish to express my sincere thanks to my wife Xiao Yun who has helped and supported me in so many ways throughout the work, and to my parents and family for their understanding and support.

CHAPTER 1
INTRODUCTION

1.1. SUMMARY

In this chapter various power conversion systems for recovering low grade heat are reviewed. Among them the trilateral flash cycle, conceived and developed by Smith [1985], is shown to be the simplest in system configuration, while offering relatively high conversion efficiency. The components required by the cycle are the same as those in a conventional power plant utilising a simple Rankine cycle. The trilateral flash cycle is featured by heating the working fluid up to its boiling point and then expanding completely in a two-phase region. Because of the close match between the source and fluid temperatures, a very high recovery of heat is possible combined with a high cycle efficiency. However, as the expansion process for this cycle occurs entirely in the two-phase region, a mechanical expander which can accept two-phase mixtures and operate at a high efficiency is crucial and the success of the whole system concept depends upon this. A survey of the two-phase expanders proposed is to be conducted in the next chapter.

1.2. POWER FROM LOW GRADE HEAT

During the last two decades there has been a remarkable growth of industrial and public interest in the recovery and utilisation of low grade heat for electricity production from sources such as industrial

processes, geothermal aquifers and even warm oceans where maximum temperatures are less than 300K. There are a number of reasons for this. Firstly, there is uncertainty in the cost of primary fuels, the outstanding example being the rise in the price of oil in 1973. Then there has been a rise in the 'energy-content' cost of most goods and services. Also there is a general realisation that fossil fuels, wherever they may exist, are not in infinite supply and must be conserved for purposes which they alone can satisfy.

Geothermal energy is recognised today as the only one of the low grade heat sources that has proven itself technically and economically, and that is commercially viable for electric power production. Basically there are two varieties of geothermal systems: hydrothermal convection systems and geopressurised systems. The first electrical power generation in a geothermal area began at Larderello, Italy in 1904. Today, Seventeen countries operate geothermal plants. By 1990 the world total installed capacity of the electric power generated from such an energy source amounted to 5,500 MWe, with individual units ranging in size from a few hundred kilowatts to 135 MWe (Dipippo [1988]). It is projected that by the turn of the next century approximately 12,000 to 20,000 MWe of geothermal power plants will be installed worldwide, which involves approximately \$14 to \$30 billion worth of capital investment over the next ten years.

Another potentially large heat source is the so-called Hot Dry Rock (HDR). Geothermal energy in the broad sense refers to the thermal energy stored in the earth. Of this, more than 99% exists in the hot dry rock. HDR is the term that is used to refer to areas of

crust that exhibit high conductive heat flow (with temperature gradients usually greater than $25^{\circ}\text{C}/\text{km}$) and that are 'dry' (no significant amount of associated formation water) owing to limited permeability. Such rocks are known to occur over at least 25% of the global continental area and must therefore represent a vast potential resource base.

The current concept of hot dry rock energy extraction involves the drilling of two wells (a doublet), spaced at about 300 meters, to a depth at which rock temperatures exceed a prerequisite surface production temperature. For power generation this would be, say, 200°C . After these wells are drilled a reservoir is created by fracture of the rock between them. Cold water is circulated down the 'injection' well (generally deeper), pressure-forced through the rock reservoir and then recovered through the 'production' well, as shown in Fig.1.1. In the U.K. and Europe, current HDR investigations offer far more potential hot water resources of $150^{\circ} - 200^{\circ}\text{C}$ than those available from known natural hydrothermal supplies. The areas most favourable for generation of large amounts of electricity are those where the rate of increase of temperature with depth is relatively high. In the U.K. these are principally in the South West of England, and it is believed that the HDR geothermal energy, if fully tapped, could supply electricity for the whole South West of England for over 300 years.

Unfortunately, the development of geothermal energy resources for power generation has not progressed as rapidly as was originally predicted. One of the main problems facing the use of these energy

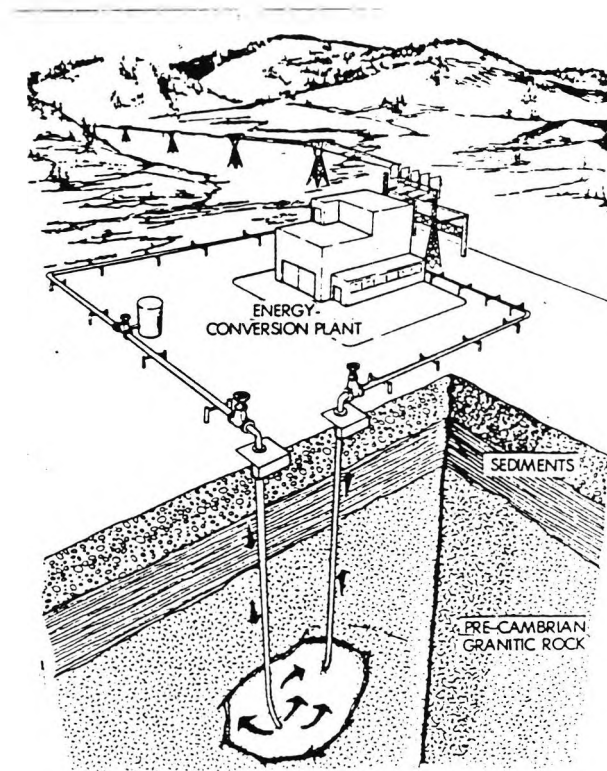


Fig.1.1. Hot Dry Rock Technology

resources is that of all known geothermal resources 80% are pressurised hot water, or in other words, low enthalpy fields. The recovery of power from these by conventional methods of energy conversion is both inefficient and expensive. A power conversion system which utilises liquid dominated geothermal resources more efficiently would greatly enhance their exploitation.

1.3. THE IDEAL THERMODYNAMIC SYSTEM

Before various power conversion systems for low grade heat source can be examined, it is necessary to know what the ideal thermodynamic system should be. In classical thermodynamics, the requirements for

ideal power conversion system are often expressed by reference to the well known Carnot cycle, originally demonstrated as the ideal heat engine to operate between an infinite heat source and sink. This can be depicted on a Temperature-Entropy diagram as a rectangle as shown in Fig.1.2. For this cycle the heat transfer from the heat source to the heat engine occurs at constant temperature and hence the process is reversible. However, when power is to be recovered from a single phase heat source in which the transfer of heat is dependent upon a fall in source temperature, as for instance from a pressurised hot water stream, the Carnot cycle, with its isothermal heat reception process, is not ideal. This is because heat transfer from the source to the heat engine must be irreversible and any residual heat in the source at temperatures below the cycle maximum cannot be recovered.

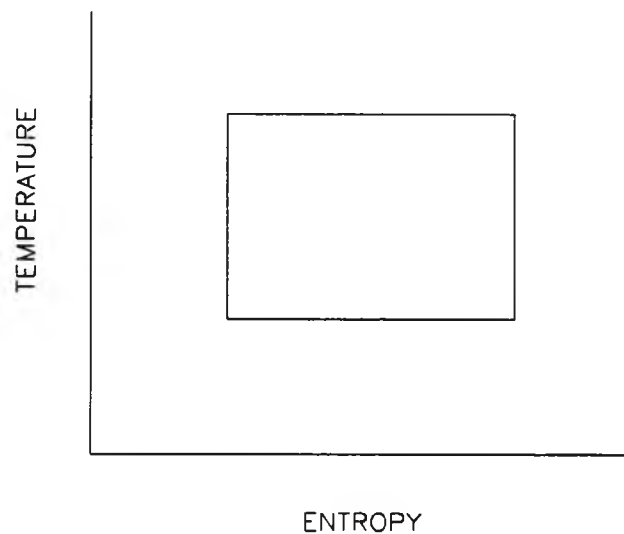


Fig.1.2. Temperature-Entropy diagram of Carnot Cycle

The maximum work which can be extracted from such a heat source can be derived by considering the exergy change of the brine as it cools at constant pressure from its initial state with temperature T_1 to its final state with temperature T_2 . According to definition, the maximum work for such a system is

$$W_{max} = (h_1 - T_0 s_1) - (h_2 - T_0 s_2) \quad (1.1)$$

where h , s are the two physical properties known as enthalpy and entropy, and T_0 is the ambient temperature. The enthalpy and entropy changes accompanying the process ($h_1 - h_2$) and ($s_1 - s_2$) can be evaluated from the specific heat C_p and the temperatures as follows

$$h_1 - h_2 = C_P \cdot (T_1 - T_2) \quad (1.2)$$

and

$$\begin{aligned} s_1 - s_2 &= \int_{T_1}^{T_2} \frac{C_P}{T} dT \\ &= C_P \ln \frac{T_1}{T_2} \end{aligned} \quad (1.3)$$

Substituting these expressions into Eqn.(1.1), the final form of the maximum work per unit mass is then

$$W_{max} = C_P \cdot (T_1 - T_2) - C_P T_0 \ln \frac{T_1}{T_2} \quad (1.4)$$

If the power is recovered by heat transfer from the brine to a working fluid contained in a heat engine operating in a closed cycle then the overall arrangement is described by geothermal engineers as a binary system. For a binary system associated with a single phase heat source the supply of heat can only be considered to be at

constant temperature for an infinitesimal amount of heat transferred to the heat engine. The ideal cycle for recovery of heat from such sources is then a succession of infinitesimal Carnot cycles each operating over a diminishing ideal temperature difference as shown in Fig.1.3A. In the limit this can be shown as a single cycle with a varying source temperature as depicted in Fig.1.3B. Such a cycle has been described by Wilson [1977] as an ideal trilateral cycle.

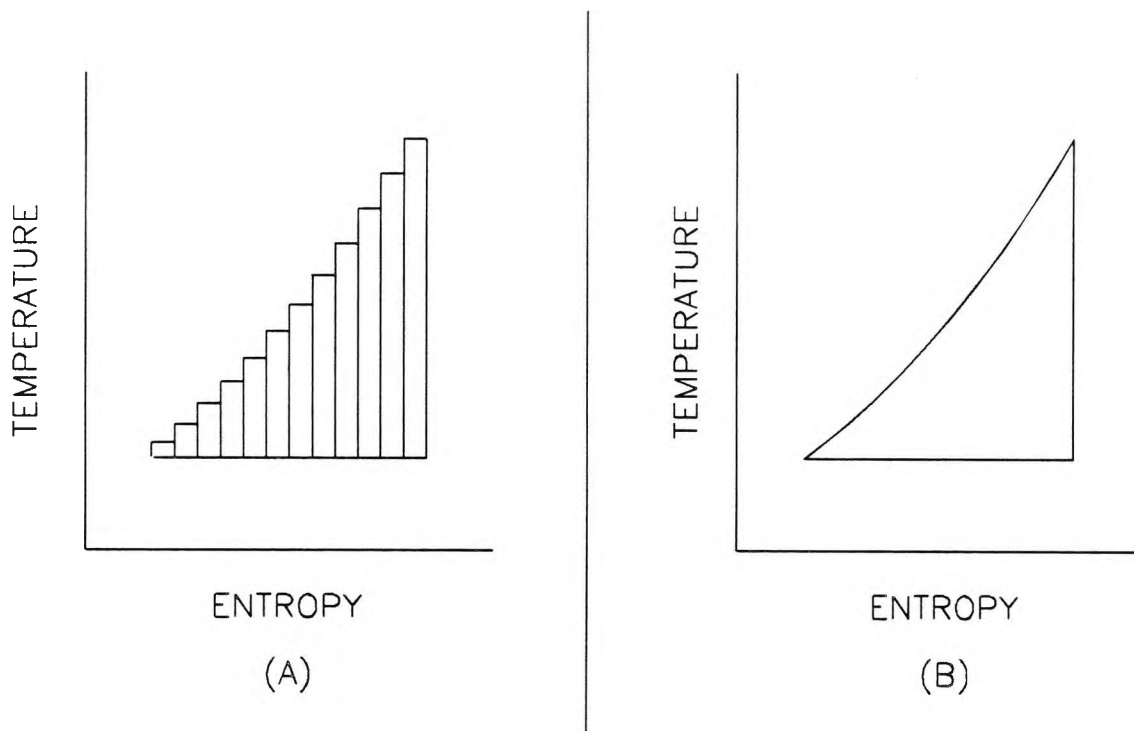


Fig.1.3. Ideal Thermodynamic Cycle

The cycle efficiency of such an ideal thermodynamic system is the ratio of the maximum work done to the amount of heat transferred from the heat source to the heat engine cycle. As the heat transferred is

Eqn.(1.2), the cycle efficiency can be expressed as

$$\eta_c = 1 - \frac{T_o \ln \frac{T_1}{T_2}}{T_1 - T_2} \quad (1.5)$$

It should be pointed out that the more appropriate efficiency for comparison of low grade heat cycles is the "utilisation efficiency" or "recovery efficiency" instead of cycle efficiency. It is defined by Smith [1985] as the ratio of power output to the heat available. The heat available is the heat that could be extracted by cooling the source fluid all the way to the ambient temperature T_o and can be calculated as

$$Q_A = C_P \cdot (T_1 - T_o) \quad (1.6)$$

Then the utilisation efficiency is

$$\eta_u = \frac{W_{max}}{Q_A} \quad (1.7)$$

It can be seen from the above relationship that utilisation efficiency is the cycle efficiency multiplied by the ratio of actual to available source fluid temperature drop

$$\eta_u = \eta_c \frac{T_1 - T_2}{T_1 - T_o} \quad (1.8)$$

The advantage of the trilateral cycle is that it simultaneously maximises both cycle and utilisation efficiencies, whereas the Carnot cycle can only raise the cycle efficiency at the expense of utilisation efficiency.

1.4. PRACTICAL SYSTEMS

For the recovery and conversion of energy from water-dominated geothermal resources, three main types of power conversion system have been proposed and tested over the past twenty years. These are:

- (1) total flow
- (2) flash steam
- (3) binary cycle.

Combinations of these, i.e., hybrid systems, are also used; but for brevity, are not considered.

1.4.1. Total Flow System

The total flow system is featured by the direct two-phase expansion of the entire flow of hot brine from the wellhead to sink conditions. Its system components and T-s diagram are illustrated in Fig.1.4. Based on fundamental thermodynamic principles, this process has the potential for conversion of the greatest fraction of the available energy and provides an upper bound on system efficiency. Furthermore, because of its simplicity, the potential capital costs are low. However, as the hot brine expands entirely in the two-phase region, it is essential to develop an expander which would accept the two-phase flow of steam and water at an acceptable efficiency and reliability. As a result conventional turbines have to be ruled out. The two serious contenders for use in the total flow system are the positive displacement Lysholm twin screw expander (McKay and Sprankle [1974]) and the two-phase turbine (Elliott [1982]), which will be described in greater detail in the next chapter.

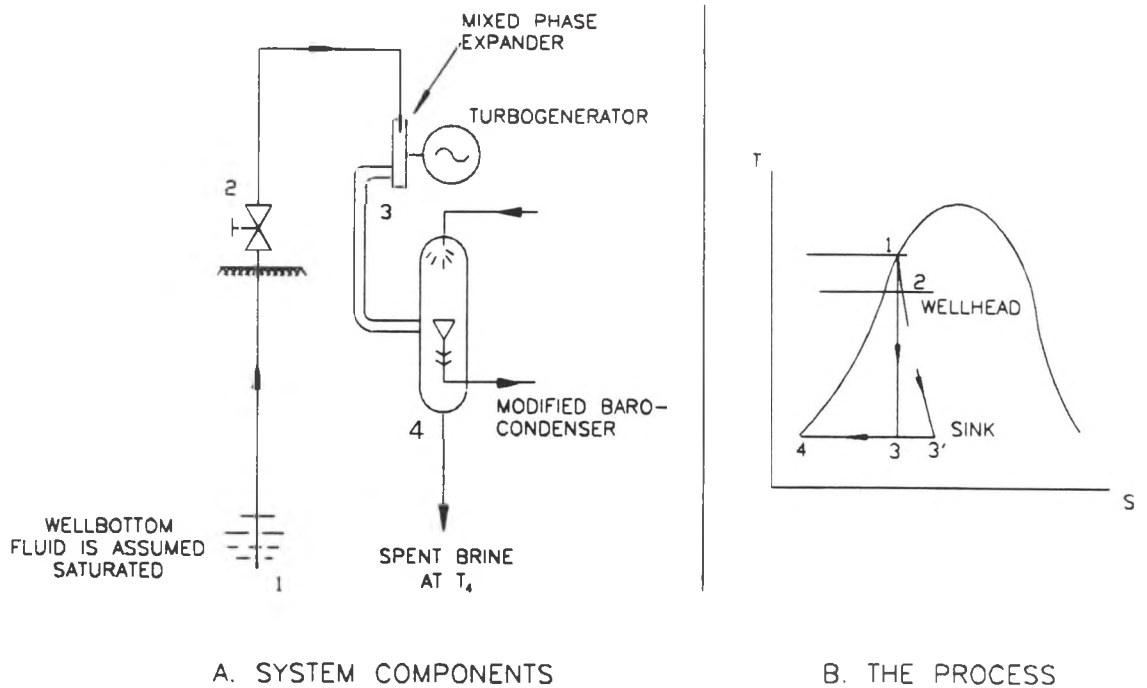


Fig.1.4. Total Flow System

In spite of the fact that the total flow system is simple and would provide the most direct means of geothermal energy conversion, various attempts to utilise it have not been successful for the following main reasons:

i) Due to the physical characteristics of water as working medium, the liquid content, even at the end of expansion, must be very large, which leads to poor adiabatic efficiencies of two-phase expanders.

ii) For expansion of the steam to condense at about 50°C , rotors of about 16 ft diameter are required for a unit output of as little as 10 MW, whereas the largest screw machine built up to date has a diameter of just over 3 ft.

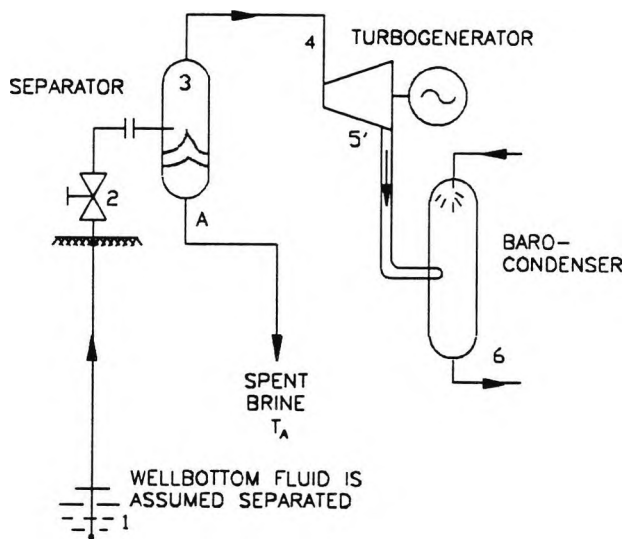
iii) For condensation at lower temperatures there are large power losses due to deaeration requirements as well as the need for even larger expanders.

iv) The adiabatic efficiencies of both screw expanders and turbines with flashing steam as the working medium were found to be very low.

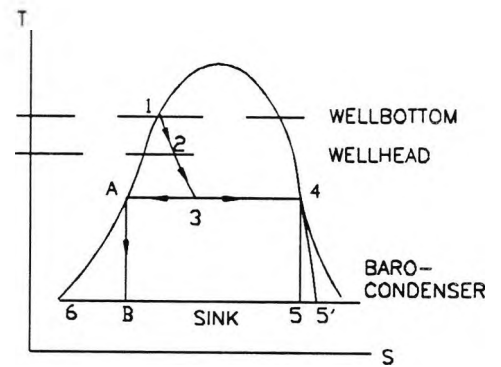
1.4.2. Flash Steam System

The usual method for large-scale recovery of conversion of energy from hot geothermal brine is the flash steam system. It was pioneered by New Zealand in the early 1960. Fig.1.5A illustrates schematically the elements of a single stage flash steam system. As in a total flow system, the brine itself is employed as working fluid. In a flash steam system, however, a two phase isenthalpic pressure reduction of the brine occurs prior to and at entry to a flash separator which separates the vapour and liquid fractions. As can be seen, the brine is flash expanded to a lower pressure through a valve and the hot liquid is separated from the vapour. Then the vapour is expanded as in normal steam plant through a turbine and the separated liquid is returned to the ground unused. The accompanying T-s diagram in Fig.1.5B illustrates the basic thermodynamic process involved.

The flash steam system is a well-established and proven system. Since only vapour is passed through the expansion system to produce power, conventional steam turbines can be used. The main disadvantage of this system is that a substantial fraction of the available energy or exergy is lost in the liquid separated, in the flashing process required to obtain steam from the hot water. The greater the liquid



A. SYSTEM COMPONENTS



B. THE PROCESS

Fig.1.5. Flashed Steam System

content of the brine, the smaller the percentage of it which can be converted to steam with sufficient energy to generate power. In the extreme case of a pure liquid brine, flashing produces only about 10% of useful vapour.

Overall plant thermal efficiencies are generally below 10% for a single flash system (Austin [1980]). Greater utilisation of the fluid energy, however, can be achieved by carrying out the flashing in more than one stage and separating the steam and water at each stage. Theoretically an infinite number of stages would produce an ideal system but in practice it is not economical to use more than two flash stages. Depending on the temperature of the geothermal brine improvements of the order of 20% to 30% can then be achieved over a single stage system with the same brine rate.

Apart from its relatively low efficiency due to the need to reject the hot separated water, the flash steam system has two other defects. The first of these is that at low temperatures the vapour pressure of steam becomes very low and hence its specific volume becomes large. This implies that the steam turbine to be used is large and expensive. The second is that expansion of saturated steam leads to the formation of liquid within the turbine. It is well known that each percent of moisture formed at the turbine exit reduces the turbine efficiency by roughly one percent below what is attainable with dry steam. Typically flash steam turbines have adiabatic efficiencies of the order of 73%. The third is that high condensing temperatures (50°C) are needed to avoid high vacuum and hence big deaeration power requirements.

1.4.3. Binary Systems

A number of binary systems of varying complexity have been proposed. However, for brevity only two are described here. These are the organic Rankine cycle and the trilateral flash cycle.

1.4.3.1. Organic Rankine Cycle System

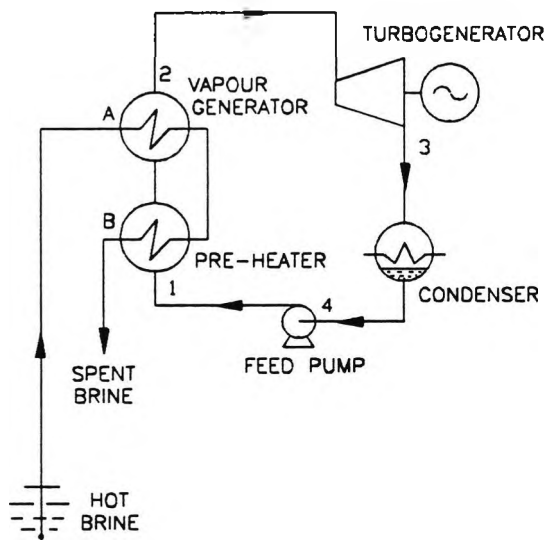
Due to the low efficiency and other problems associated with flash steam, the most widely used alternative for low grade heat applications today is the organic Rankine cycle (ORC) system. The hot brine heats a secondary more volatile organic working fluid, which in turn expands and produces power in a traditional Rankine cycle system. The components required for an organic Rankine cycle system

are the same as in a simple steam power plant. Fig.1.6A illustrates the system components of a subcritical organic Rankine cycle. As shown in the diagram, the organic working fluid is heated and vaporised in the heat exchanger. It then expands in a turbine from which work is extracted. The vapour from the turbine exhaust is condensed and the condensate is pumped back to the heat exchanger inlet by a feed pump. A T-s diagram of this cycle is given in Fig.1.6B.

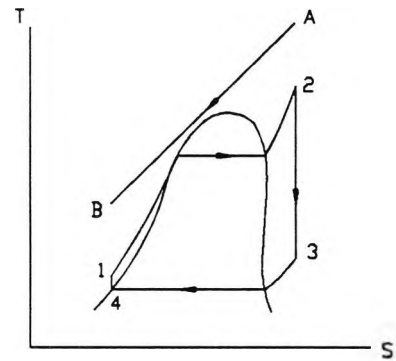
The use of organic working fluids in Rankine cycle power plant is now established and more than 4,000 units are in operation throughout the world with over 120 installed in geothermal applications. The main advantages of an ORC system can be summarised as follows: 1) Organic working fluids are much denser than steam at low temperatures, 2) they dry out during expansion and, 3) because their molecular weights are higher than that of water, they enable more of the available heat to be used in the power recovery cycle. Smaller and more efficient turbines are therefore possible leading to systems with higher conversion efficiencies than from flash steam. A well designed ORC system can achieve an overall energy conversion efficiency 5 - 10% better than a double flash steam system.

The main disadvantages associated with ORC systems are:

i) A subcritical ORC system requires a large amount of heat to vaporise the working fluid at constant temperature, which leads to a poor match between the heat source and working fluid in the heat exchanger and hence low utilisation efficiency. To increase heat recovery from the source a supercritical ORC system can be used to



A. SYSTEM COMPONENTS



B. THE PROCESS

Fig.1.6. Organic Rankine Cycle System

follow the cooling curve of the heat source better. For a supercritical cycle, the turbine power output will be high. However, heating the organic fluid far above the critical temperature can lead to wasteful desuperheat after the expansion process, and the power input to the feed pump is much greater than in subcritical cycles because of the higher turbine inlet pressure. The effect of the feed pump power input on the nett output is large due to the relatively low enthalpy drop in the expansion process.

ii) Due to the poor heat transfer properties of organic working fluids, the heat exchangers used are relatively large resulting in higher heat exchanger costs.

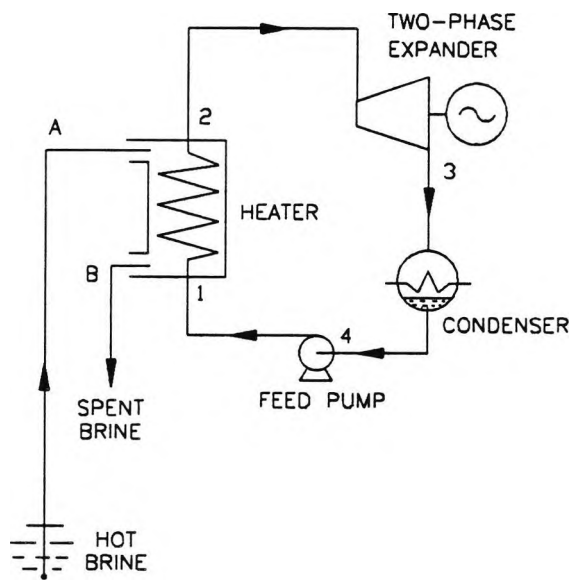
iii) There are flammability or toxicity problems which require the system to be totally sealed.

1.4.3.2. Trilateral Flash Cycle System

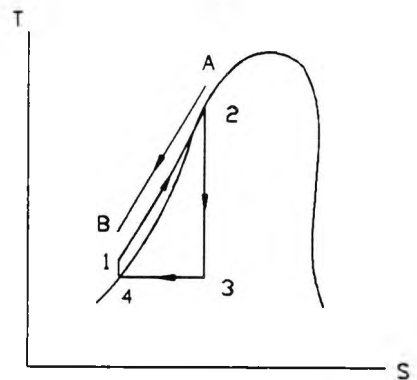
The problems inherent in Rankine cycles led to the development of a novel system known as the Trilateral Flash Cycle (TFC) system proposed by Smith [1985]. Mechanically the components required for this system are identical to those required for ORC system; namely a feed pump, heat exchanger, expander, and condenser, as shown in Fig.1.7A. However, unlike the latter, the liquid working fluid is heated only to its saturation point and does not require evaporation before the fluid enters an expander to produce work. Consequently expansion is in two-phase and therefore a Lysholm twin screw machine is more suitable than a turbine. As shown in Fig.1.7B, this leads to a much better matching of the heat source and working fluid and consequently a higher utilisation efficiency can be obtained. Also, since it operates at subcritical pressures, feed pump losses are much less significant than in supercritical ORC systems.

The TFC system has the ability to absorb approximately 80% of the available heat from a single phase fluid stream and is closest to the ideal trilateral cycle. To be more specific, the idealised utilisation efficiencies of TFC and ORC systems can be calculated and compared on the basis of reversible processes. The results are presented in Fig.1.8, which shows that the TFC system can produce more power than the subcritical ORC system over a wide range of source temperatures.

It is imperative to quantify the extent of the efficiency advantage of the TFC system over the ORC system. A detailed study was



A. SYSTEM COMPONENTS



B. THE PROCESS

Fig.1.7. Trilateral Flash Cycle System

conducted by Smith [1986] using a suite of powerful cycle analysis programs. These programs can model both systems and take full account of irreversibilities throughout the system and auxiliary power loss associated with the circulation of the heating and cooling medium. The cycle analysis programs are attached to an optimisation package to ensure the best matching of the cycle to the heat source. For illustration purposes, only the output obtained for n-pentane are given in Table 1.1, which shows that the advantage of the TFC over the ORC is present at all source temperatures. However the relative effect is greatest at lower temperatures, i.e. 70% improvement for a source temperature of 120°C compared to 40% for 200°C. It should be noted that the efficiencies assumed are 80% for the ORC turbine and 76% for the TFC two-phase expander.

The critical element in the trilateral flash cycle system is the two-phase expander and the efficiency which can be obtained in it. All the other components in the system are quite conventional. Smith [1985] pointed out that two-phase expanders with adiabatic efficiencies as low as 60% can produce nett outputs in excess of ORC systems with turbines of 82%. However due to the close match between the working fluid and its heat source and the larger amount of heat transferred, the heat exchanger required for the TFC is considerably larger and more expensive. The same also applies to the condenser unit. As a result, for a two-phase expander adiabatic efficiency of 70% the TFC system costs roughly the same per unit output as an ORC system, while real economic advantages can only be obtained from it if the expander efficiency can reach 75%.

One of the main features of organic working fluids as opposed to water is that for a large number of them the saturated vapour line has a positive gradient, when plotted on T-s coordinates (a 'drying fluid'). As a result, if the initial temperature of the working fluid is sufficiently high, in some cases the working fluid may be expanded all the way to dry vapour. A conventional turbine can then be used for the final stage of expansion. Hence the two-phase expansion process may start with a combination of screw expanders and end with a turbine. The T-s diagram of such a combination is shown in Fig.1.9.

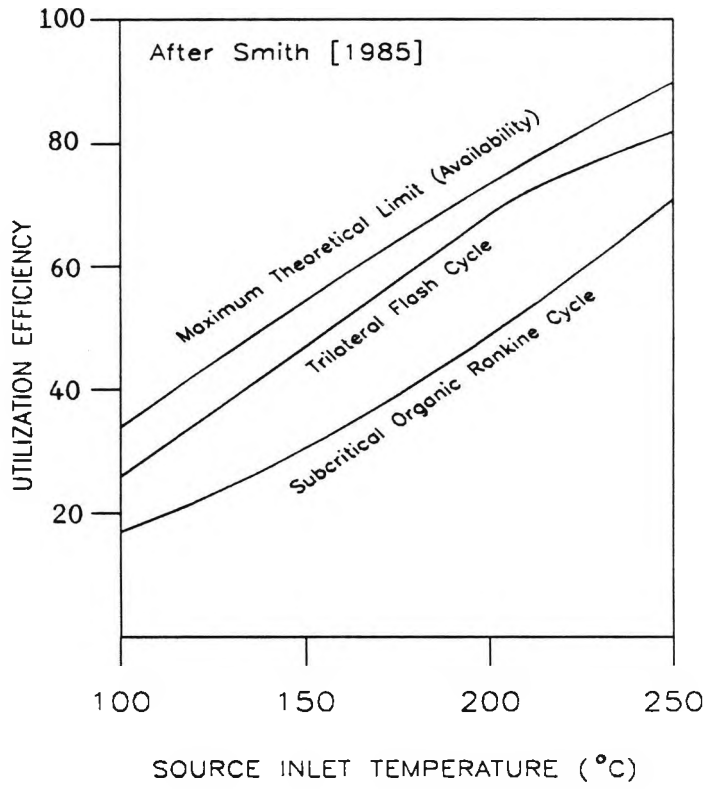


Fig.1.8. Comparison of TFC and ORC Ideal Efficiencies

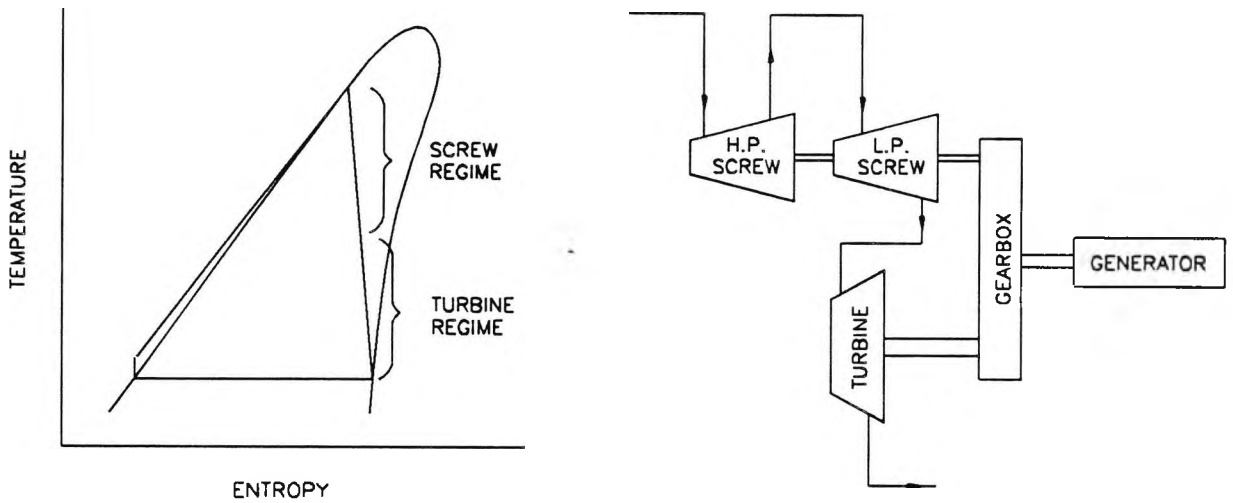


Fig.1.9. Screw Expander and Turbine Combination

Table 1.1. Calculated Optimum Conditions for Trilateral Wet Vapour Cycle Machine,
With a Geothermal Source Stream (50 kg s⁻¹) Working Fluid (n-pentane)

Source Stream		Working Fluid			Efficiency		Net Power kW(e)	Total Auxiliary Losses kW(e)	ORC Net Power kW(e)
T _P °C	T _I °C	Turbine Exit Pressure atm	Heat Exchanger		η _C %	η _T %			
			Inlet	Outlet					
120	32	8.3	113	25	6.8	5.6	1,173	443	689
140	33	12.0	131	20	8.4	7.2	1,798	571	1,131
160	34	15.9	149	20	10.0	8.6	2,524	713	1,696
180	34	21.1	166	25	11.4	10.0	3,338	866	2,397
200	34	26.5	181	25	12.7	11.2	4,228	1,030	3,021

Assumptions: Expander Lysholm twin screw rotor
 Expander efficiency 0.8
 Gearbox efficiency 0.97
 Electrical generator efficiency 0.95
 Feed pump efficiency 0.75
 Coolant pump efficiency 0.75
 Fan and pump motors efficiency 0.95
 Heat sink Cooling tower with water at 20°C

Source: Heppenstall and Smith (1985).

CHAPTER 2

LITERATURE SURVEY

2.1 SUMMARY

In this chapter previous efforts to develop efficient two-phase expanders are thoroughly surveyed. It is demonstrated that a Lysholm twin screw expander is most suited for use in the Trilateral Flash Cycle system. From this the reasons to initiate the current investigation are given and the main difficulties anticipated are described. Then a survey of the various techniques currently used for the analysis of liquid-gas two-phase flow is presented, with particular reference to the adiabatic flow system. The survey covers both theoretical and experimental work on two-phase flow, including flow regimes representation, flow modelling and void fraction measurement.

2.2. TWO-PHASE EXPANDERS

Apart from its use in low grade heat recovery, efficient two-phase expanders have been sought for many years for various applications. One of these is in throttle valve replacement in process flow and refrigeration. Instead of throttling a refrigerant to produce cold liquid, the refrigerant could be expanded in a two-phase expander. The work conventionally lost in the irreversible throttling process would be recovered as shaft power, which could in turn assist in driving the compressor. The electricity consumption

for refrigeration would be reduced by about 10% (Elliott [1982]).

It is a well established fact that conventional turbines and reciprocators are not suitable for the expansion of hot liquids in this manner since liquid droplets erode turbine blades and reduce the aerodynamic efficiency of the turbine while they wash the lubricating oil off the cylinder walls of reciprocating expanders and so promote wear and seizure of the mechanism. Alternative methods have been considered for this purpose. These are:

1) Positive displacement machines such as a Lysholm twin screw expander and rotary sliding vane machine. The presence of liquid in these should promote lubrication and reduce leakage.

2) Specially designed two-phase turbines.

2.2.1. The Lysholm Total Flow Expander

Serious attempts to produce efficient two-phase expanders were made in the U.S. during the 1970's for developing the total flow concept. The main inspiration for work in this field was the patents by Sprankle [1973][1976] to use a Lysholm twin screw machine as a direct two-phase expander of geothermal brines. The Lysholm design consists of a pair of parallel rotors with meshing helical lobes which, in the casing, form compression or expansion chambers. This configuration was patented in Sweden by Lysholm in 1934. The design has found its main use as a heavy duty air compressor, known for ruggedness and reliability. The use of the Lysholm design as an engine has been suggested at several times, including the suggestion for its use in geothermal energy conversion. Lysholm [1967] had much

earlier proposed his screw machines as dry gas expanders.

The Lysholm twin screw expander is a positive displacement machine which operates by the direct expansion of fluids. With the aid of Fig.2.1, the principle of operation of the expander can be described as follows. The pressurised fluid flows through the throttle valve T and enters the high pressure pocket formed by the meshed rotors, the rotor case bores and the case end face. This pocket, designated by A in the figure, is mostly hidden by the rotor lobes, but can be seen in the plan section view. As the rotors turn, the pocket elongates, splits into a V, and moves away from the inlet port to form the region designated by B. With continued rotation, the V lengthens, expanding successively to C, D, and E as the point of meshing of the rotors appears to retreat from the expanding fluid. The expanded fluid at low pressure is then discharged into the exhaust port. Energy is extracted from the fluid in the process. Engine geometry determines the theoretical volumetric expansion ratio, which is the ratio of the final to the initial chamber volumes.

Testing of the Lysholm engine has since been conducted by the Lawrence Livermore Laboratory(LLL), by the Jet Propulsion Laboratory (JPL), and by the Department of Mechanical Engineering at University of California, Berkeley. The unit tested was an air compressor unit with 152.4 mm rotors modified by Sprankle. A maximum efficiency of 55% was observed for a power output of 30 kW at 5,000 rpm. Latterly a smaller version of this (with 130 mm rotors) was built from which a maximum expander efficiencies of only 53% was obtained at 47 kWe

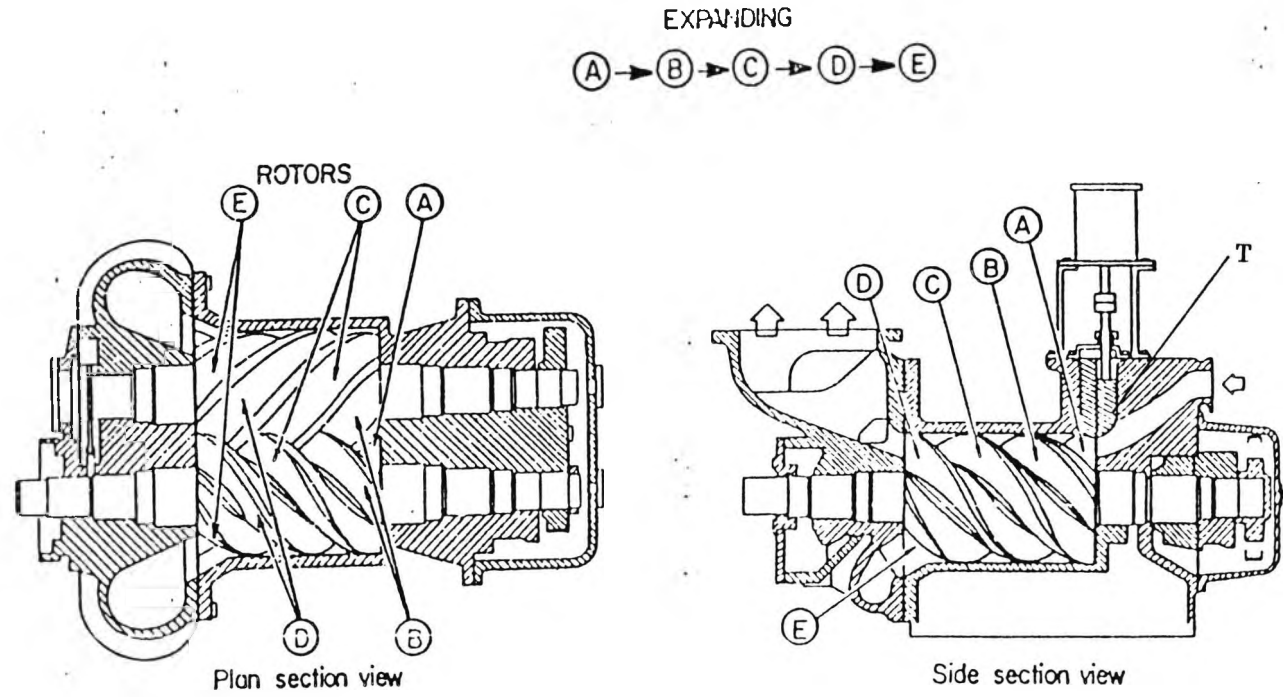


Fig.2.1. Layout of Lysholm Screw Expander

output (Steidel [1982]). Despite extensive experimental work, there had been a general lack of theoretical analysis on the Lysholm screw expander. Steidel proposed an empirical model using a curve fitting technique. However it is doubtful whether it could be applied to the other machines with different geometrical characteristics. More recently Taniguchi et al [1988] developed an analytical method for estimating the performance of a two-phase flow screw expander. The operation of a screw expander was simulated by the expansion of a fluid between two pistons with appropriate leakage paths. Good agreements were obtained against the experimental results from a prototype machine with a diameter of 81.6mm and a length of 135mm. However, the various frictional losses and two phase interaction were not accounted for in the procedure.

In addition to the low efficiencies observed with the Lysholm screw expander as used in the total flow system, the other main drawback is the huge size required of the machine if expansions continue to normal condensing temperatures. As a class, positive displacement expanders are limited in volume flow rate capacity relative to turbomachines. House [1976] of LLL conducted an analysis of potential applications for the helical rotor expander in the total flow system. He concluded that engine efficiencies will generally be below 70% because of an expansion ratio limitation of 15 and a maximum pressure differential of 758 kPa imposed by conditions of mechanical strength. With different reservoir conditions the expander sizes for single stage expansion to 49°C (120°F) were calculated and the results are summarised in Table 2.1.

Table 2.1 Helical Rotor Expander Size for Total Flow System

Shaft Power (MWe)	Rotor Diameter (m)	Rotor Length (m)
5	3.2 - 4.5	4.8 - 6.7
10	4.5 - 6.3	6.7 - 9.5
20	6.3 - 9.0	9.5 - 13.5
40	9.0 - 12.7	13.5 - 19.0

House pointed out that these large sizes can be reduced to more reasonable values by staging or by using the expander in combination with vapour turbines. It appears that, because of the large sizes required for single stage expansion to subatmospheric conditions, more suitable applications for the helical rotor expanders are for noncondensing, low-power output uses or in hybrid systems with helical rotor exhaust pressures above one atmosphere.

2.2.2. Two-Phase Turbines

During the same period, work was initiated at JPL and LLL to seek an alternative efficient two-phase expander system aimed at overcoming the restrictions imposed by the positive displacement type machine. The goal of their work was a turbine efficiency of above 70%. Austin [1973] and his geothermal group at the LLL proposed a two-phase impulse turbine for geothermal application in which the two-phase brine from geothermal wells would be passed through the turbine. It was hoped that the water drops would be small enough for the steam and water to behave as a homogeneous fluid and give these turbines efficiencies comparable to those of vapour turbines. However the detailed calculations on drop sizes and trajectory showed that

the liquid drops in two-phase turbines would be too large to follow the gas phase, and that the liquid would impinge on the blades and form a thin liquid film. The friction drag of this film would be so high that the efficiency of single-stage impulse turbines would be limited to little more than 50%.

As a result of low efficiencies achieved by the two-phase impulse turbines a rotary separator turbine was developed by Biphase Energy Systems [1982]. The basic idea is to replace the throttle valve with a separator system in the traditional flashed steam cycle system. In place of the throttle valve, the geothermal fluid is expanded in a two-phase nozzle with an adiabatic efficiency of around 90%. The high velocity liquid and vapour so formed are then separated in a rotary drum. The steam is then passed to the steam turbine as in the flashed steam system, while the liquid is either used in a liquid turbine to produce additional power or pressurised in a diffuser to reduce the reinjection power. This rotary separator turbine was investigated and tested experimentally in the laboratory and at three geothermal resources. The machines were reported to operate well and a power gain of some 20 - 25% more than from a simple single flash steam system was achieved. A maximum adiabatic efficiency of the separator system of 35% was measured although it was predicted that improved designs with up to 50% efficiency were attainable in the future. It was thought that the impact and other losses in the rotary separator would limit the turbine efficiency as severely as the liquid friction in bladed turbines.

Further work on a specially designed two-phase turbine was

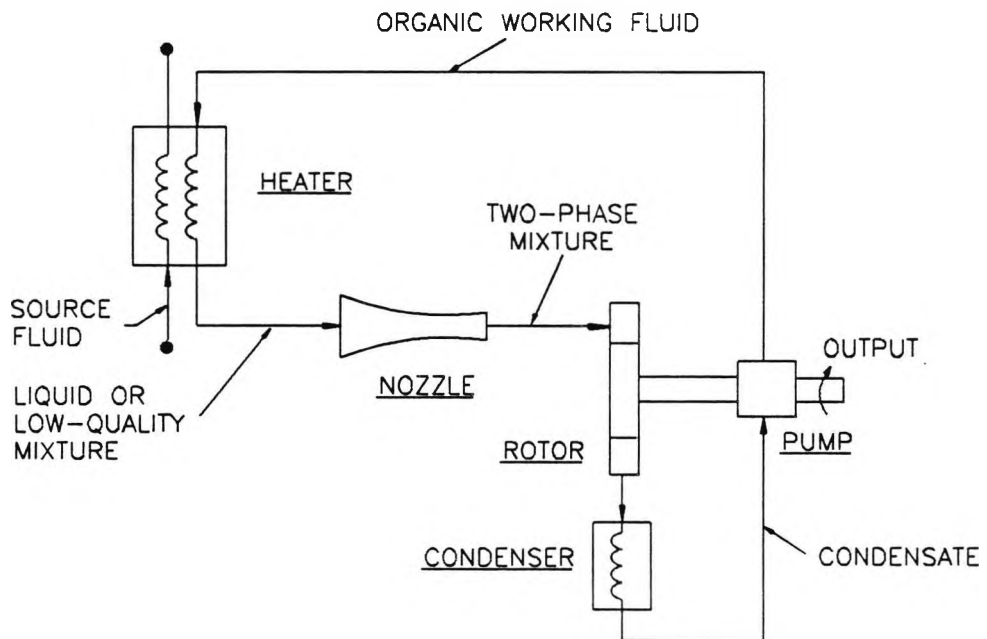


Fig.2.2. Organic Two-Phase Turbine System

attempted by Elliott [1982] at the JPL using either steam for total flow or organic fluids in what was effectively a TFC system. The organic two-phase turbine system is shown schematically in Fig.2.2.

The two-phase turbine utilised a uniform mixture of liquid and gas accelerated in a two-phase nozzle which is similar in design to that used in the rotary separator turbine. The mixture acts directly on an axial flow or tangential impulse turbine. Based on this concept he predicted an upper limit efficiency of about 65% for two-phase turbines, and probably only attainable with organic working fluids. This prediction could not be justified by the extensive experimental test programme carried out at both JPL and LLL, which showed that

this efficiency was not attainable and a maximum efficiency of only 55% was achieved using organic fluids. However it was found that the JPL two-phase nozzle study calculated velocities which are within 2-4 percent of measured values and nozzles showed good performance over a wide range of operating conditions in the experiment.

2.2.3. Lysholm Screw Expander for Trilateral Flash Cycle System

In filing his patent for the Trilateral Flash Cycle system, Smith [1981] proposed the Lysholm twin screw expander as a primary two-phase expander for such a system. His study revealed that by careful choice of organic working fluids in place of water the volume flow rate and hence the size of the machine would be one tenth or less than that for water, and the volume ratio of the expander would be reduced by a factor of the order of 20. Therefore an experimental programme was initiated with the construction of 600 kWth test loop at the Thermo-Fluids Eng. Research Centre of the City University to determine the performance of a small Lysholm expander using R113 as the working fluid. The Lysholm machine used was a reversed oil free Howden compressor with a built-in volume ratio of approximately 5:1. The rotors were 204 mm in diameter and 224.4 mm in length. A general layout of the test loop is given in Fig.2.3. An additional loop is shown in parallel with the screw expander. This was to test a small rotary sliding vane machine of 5-10 kWe. Expanders of this kind are suitable only for outputs of up to approximately 30 kWe and therefore are not of interest for large scale power generation.

The screw expander was tested at various expander speeds and heat

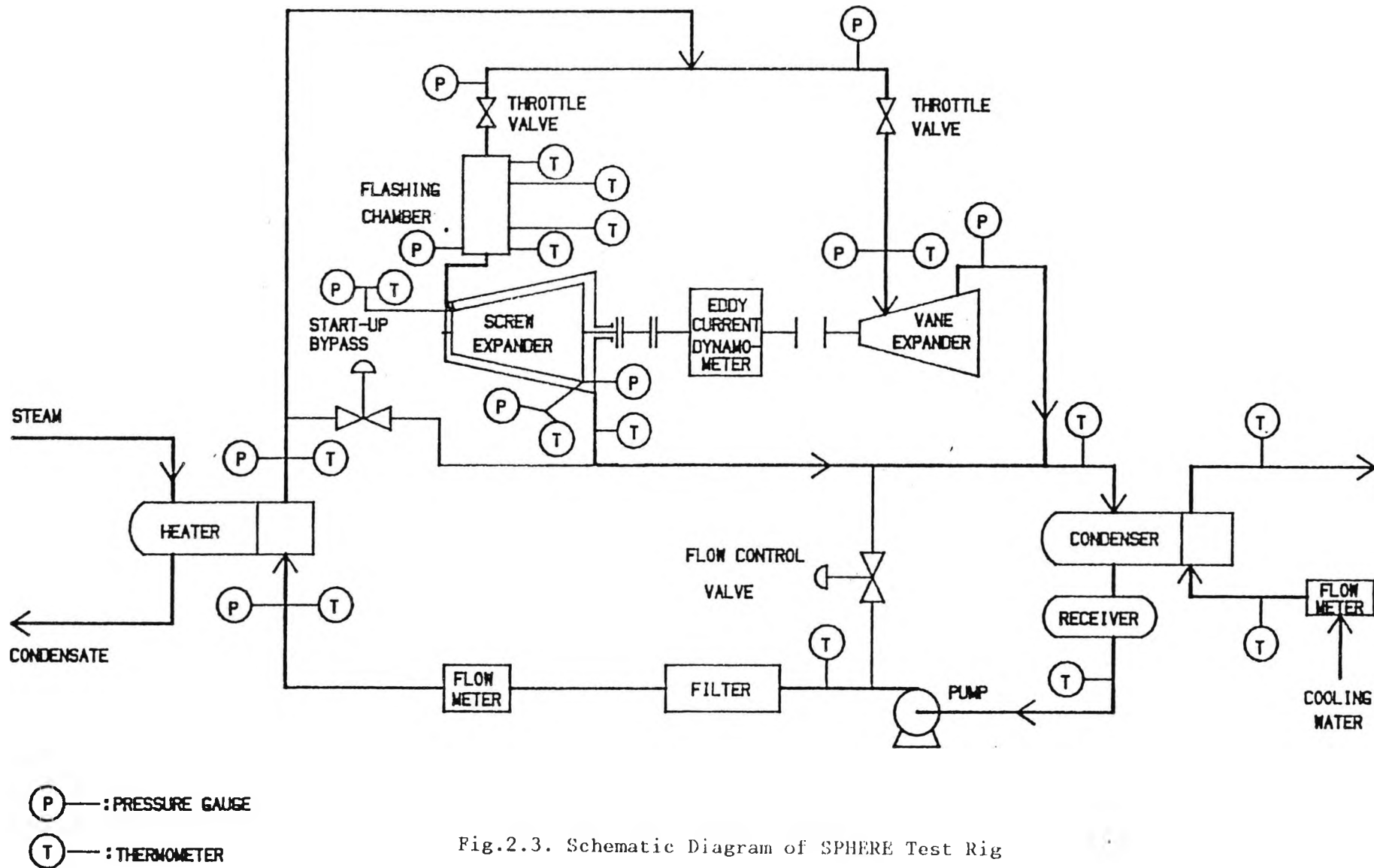


Fig.2.3. Schematic Diagram of SPHERE Test Rig

exchanger exit temperatures. Average expander efficiencies of 65% were obtained over a wide range of operating conditions and a peak efficiency of 72% measured at 120°C and 3,000 rpm. These were far better than those results obtained with similar machines using water as the working medium and led to the predictions of expander efficiencies of 75% or more on larger machines. Hence it proved experimentally that the concept of the TFC system is practically workable. However the main difficulties with this machine were that the high efficiencies could not be maintained at higher speeds and the operating range was restricted. Furthermore the predicted expander back pressures were in poor agreement with the experimental values. This was believed to have been caused by choking phenomena in the inlet port. Fig.2.4 is a side view of the inlet port used in the tested expander which shows a poorly designed three-dimensional bend with abrupt changes in cross section which could cause flow separation. By treating the flow across the rotor entry as similar to that through an orifice plate, Smith found the coefficients of discharge at high expander speeds to be of the order of only 0.2 - 0.3. It was thought that an improved inlet port design could raise this value and thus enhance the rotor entry filling. Higher speeds and outputs should then be attainable and by this means it was believed to be possible to raise the efficiency to over 75%. The inlet port used in Sprankle's total flow expander was envisaged as a variable throttle port which not surprisingly led to a low expander efficiency in his experiment.

The initial test results were so encouraging that it was then decided to design and build a new screw expander based on the

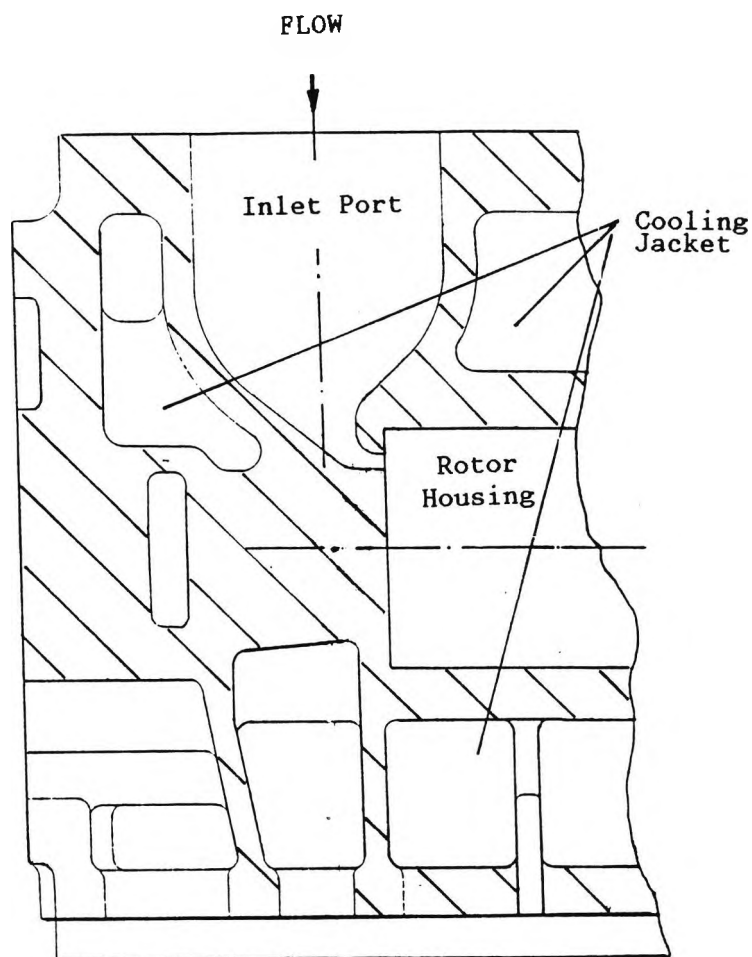


Fig.2.4. A Side View of the Old Inlet Port

knowledge and experience gained from the first test programme. The main aim was to improve the operating range and this could be achieved by employing an inlet port that could eliminate choking effect as well as reduce throttling. An independent study by SRY, the Swedish licensor of Lysholm screw technology, confirmed that the inlet port design was of the greatest importance and that any improvement in it should result in higher tip speeds and adiabatic

efficiencies. These formed the basis for the initialisation of the current investigation of two-phase flow in the inlet port of a Lysholm screw expander.

To the best of the author's knowledge, little theoretical work had been carried out in this field, largely because the flow inside the screw machine is a complex process. Steidel et al [1982] used some empirical formulae from their own expander tests. Others simply assume an adiabatic efficiency and then work out the end state from the isentropic process on a T-s diagram. Both of them are a crude approximation of real situation in the machine even in their best form. The difficulties with the detailed flow analysis through the inlet port are mainly in the following two aspects:

i). The flow of fluid in the TFC system is essentially steady through the pumps, heat exchangers and turbines but in the screw expander itself it is pulsating because the fluid is distributed into a series of passages in the rotor with separate expansion in each passage. It is possible to analyse screw machines by non-flow techniques but these are very complex. Moreover the working fluid is a two-phase mixture and the flow patterns are so complex that it was doubtful if non-flow predictions would lead to accurate estimates without many man years of analysis and experiment, if ever. The steady flow approach was therefore adopted from the outset.

ii). Due to the meshing requirement of the two rotors, the flow passage cross sectional shape at the inlet port exit is both complex and irregular.

2.3. TWO-PHASE FLOW

Two-phase flow of liquid-gas and liquid-vapour mixtures is a common phenomenon in many engineering applications other than a Lysholm screw expander such as heat exchangers, turbines and condensers of a conventional power plant. Understanding the behaviour of such flows is essential to the design of such equipment, requiring in general a detailed knowledge of two-phase pressure drop, heat transfer rate, and phase distribution etc.

Knowing the pressure drop in two-phase flow is of primary interest to the designer and researcher alike to establish the pumping load and prescribe the longitudinal pressure variation necessary to compute the fluid properties along a flow channel. The problem is vastly more complicated than in single phase flow. The difficulties stem from the multi-dimensional variation in the mass and velocity distribution of the two phases. Therefore much of the two-phase research so far has been centred on the determination of phase distribution. As a result two sections of the literature survey on two-phase flow are devoted to this, namely:

- 1) flow regimes and flow regime maps;
- 2) void fraction measurement technique.

2.3.1. FLOW REGIMES AND FLOW REGIME MAPS

It is well established in two-phase flow that liquid and gas phases may assume different geometrical configurations when flowing simultaneously. Depending on the flow conditions, there exist regions

of the channel where one phase is continuous and the other discontinuous, e.g., a flow of a mist of droplets in a continuum of gas or the flow of a dispersion of bubbles in a continuum of liquid. Such flow configurations are usually termed two-phase flow regimes or flow patterns. A change of flow pattern usually means a change in the modes of transport of mass, momentum and energy. The effects of flow regimes on pressure drops have been studied by Govier, Radford and Dunn [1957].

Many different regimes have been defined in the literature. The nature of the regimes varies with channel geometry and orientation. However there are four basic flow regimes which have been identified and are illustrated in Fig.2.5.

Diagram 1 shows a bubbly flow regime in which the gas phase flows as bubbles dispersed in the liquid. It occurs typically at low gas superficial velocities and high liquid velocities.

Diagram 2 shows a slug flow regime in which large, characteristically bullet-shaped bubbles are formed and may be separated by regions containing dispersions of smaller bubbles. It occurs when the bubbles coalesce at higher gas flows and eventually the bubble diameter approaches that of the tube.

Diagram 3 shows an annular flow regime in which the liquid flows on the wall of the tube as a film, and the gas phase flows in the centre. Usually, some of the liquid phase is entrained as small droplets in the gas core.

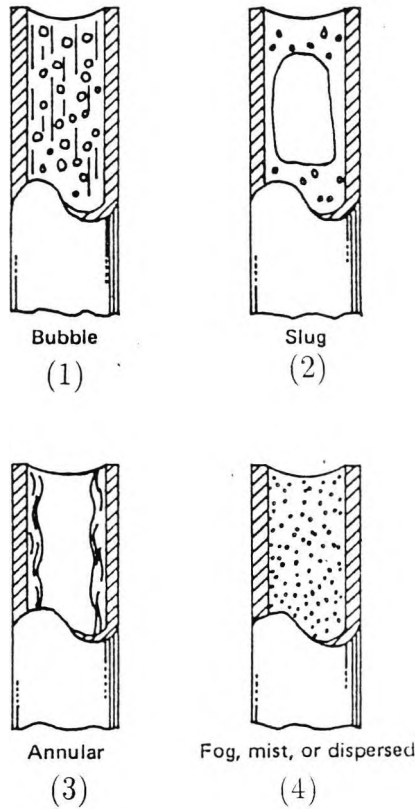


Fig.2.5. Basic flow regimes

Diagram 4 shows a mist flow regime in which discrete liquid droplets are dispersed in a continuous gas phase. It is topologically complementary to bubbly flow and occurs typically at higher gas flow rates.

Most of the earlier work on the determination of flow regimes was carried out using direct visual observation. Later this was supplemented by evidence obtained through high speed photography. Developments in the photography of two-phase flow are described by Cooper et al [1963] and Arnold & Hewitt [1967]. Unfortunately, even with high-speed photography, it is often not possible to observe the

structure of the flow clearly, due to the complex light-refraction paths within the medium. The general unreliability of photographic methods has led some investigators to seek other techniques for flow regime categorisation. The most popular of these are the method depending on the statistical analysis of fluctuating quantities such as local pressure and void fraction. In X-ray absorption measurements of void fraction, for instance, the output from the detector is converted into a signal representing the instantaneous void fraction; in turn, this signal is analysed to give a probability distribution $P(\alpha)$ for void fraction. A single peak at low void fraction indicates bubble flow; a single peak at high void fraction, annular flow; and double peaks, slug flow, as shown in Fig.2.6.

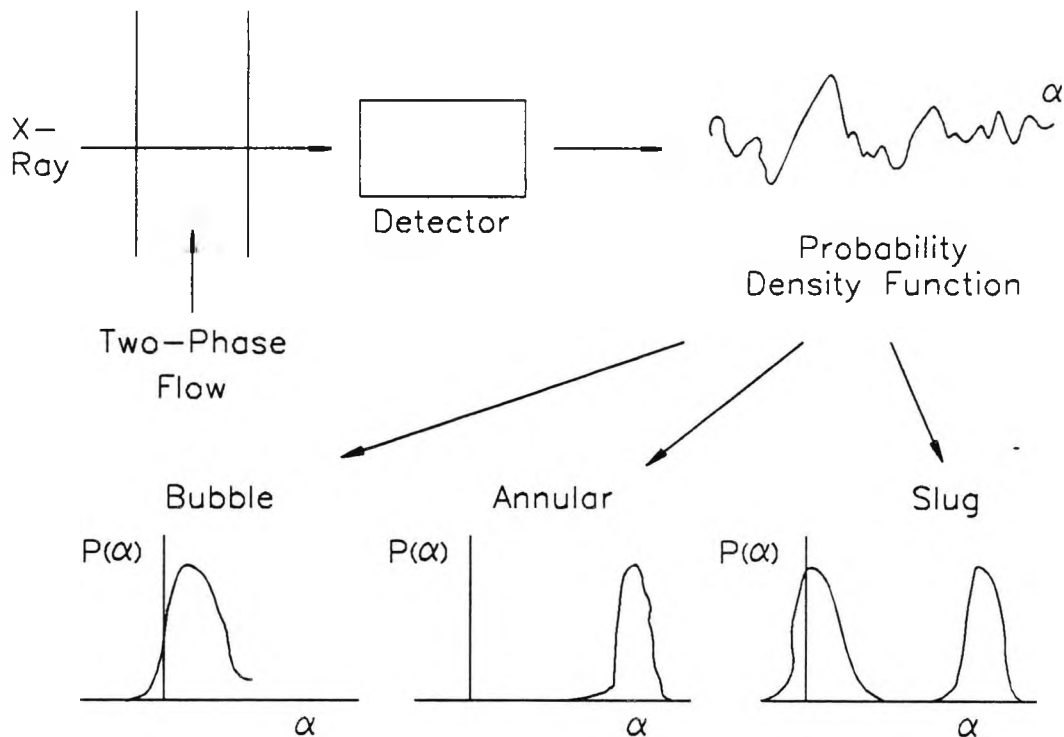


Fig.2.6. X-ray absorption method for flow-regime detection

The flow regime is a very important subject of study in two-phase flow and therefore a great deal of work has been done to determine characteristics of various flow regimes and the boundaries between them. The results are often represented by means of a flow regime map, where lines are drawn on the graph to represent the boundaries between the various regimes of flow. The most common coordinates for the flow regime map are liquid flow rate (either mass or volume flow rate) versus gas flow rate. The map proposed by Baker [1954] is probably the best known for horizontal flow. For vertical flow the map by Hewitt & Roberts [1969] and Griffith & Wallis [1961] are recommended. And more recently Weisman [1979] studied the effects of fluid properties and pipe diameters on two-phase flow regimes in horizontal lines. Research on flow regimes in vertical two-phase flow is due to McQuillan and Whalley [1985].

Taitel et al [1976] presented an alternative to the experimental methods of obtaining flow regime maps. They considered the conditions necessary for the existence of each of the flow regimes, and postulated mechanisms by which the transitions between the various flow regimes might occur. They then modelled these transitions and produced a series of equations which, given the phase physical properties and the tube diameter, enabled the flow regime boundaries to be calculated. The resulting flow regime maps were compared with existing experimental flow maps and with their own air-water data, and reasonable agreement was obtained. This theoretical approach to flow regime prediction has also been used by Mishima and Ishii [1984].

The conclusion that can be drawn from the above survey is that to the best of author's knowledge no one flow regime map available to date is successful in all situations. Most of the available information has been obtained for a narrow range of conditions; typically, air-water flows have been studied at near atmospheric pressure in a limited range of channel cross section. For this reason, extensions to other conditions of pipe size, or inclination, fluid properties, and flow rates are of uncertain reliability. There is an obvious need for a wide range of systematic investigations into the mechanism by which transitions could take place. On the credit side, however, the experimental and theoretical work carried out so far on flow regime transitions by those investigators give useful indications of the flow conditions when used with care. The statistical analysis of local parameter fluctuations is a powerful tool in identifying flow regimes and offers great potential.

2.3.2. PRESSURE DROP CALCULATION AND FLOW MODELLING

The pressure drop may be defined as the integral along the channel length L of the pressure gradient dP/dZ

$$\Delta P = \int_L \frac{dP}{dZ} \Big|_{TP} dZ \quad (2.1)$$

In analogy with single phase flow, the pressure gradient inside the integral can be broken down into three components: frictional pressure gradient $dP/dZ|_{\text{fric}}$, accelerational pressure gradient $dP/dZ|_{\text{accel}}$ and gravitational pressure gradients $dP/dZ|_{\text{grav}}$. According to Hsu [1976], we have

$$\left. \frac{dP}{dZ} \right|_{TP} = \left. \frac{dP}{dZ} \right|_{fric} + \left. \frac{dP}{dZ} \right|_{accel} + \left. \frac{dP}{dZ} \right|_{grav} \quad (2.2)$$

where

$$\left. \frac{dP}{dZ} \right|_{fric} = \frac{\tau_o S}{A} \quad (2.3)$$

$$\left. \frac{dP}{dZ} \right|_{accel} = \frac{d}{dZ} \left[\frac{1}{A} \int_A [\rho_L(1-\alpha)V_L^2 + \rho_G\alpha V_G^2] dA \right] \quad (2.4)$$

$$\left. \frac{dP}{dZ} \right|_{grav} = \frac{1}{A} \int_A g \sin \theta [\rho_L(1-\alpha) + \rho_G\alpha] dA \quad (2.5)$$

and S is the perimeter of the flow channel and θ is the inclination angle of the flow channel with respect to the horizontal.

It is obvious that an accurate determination of pressure gradient requires a complete description of the void fraction and velocity distribution since V_L , V_G and α can vary with both axial and transverse position. These parameters are strongly dependent on the flow regime which exists in the section of interest. Unfortunately the flow regime is not usually known a priori and one must use an empirical approach and a certain amount of approximation in order to arrive at a reasonable estimate.

The importance of pressure drop prediction is reflected in the numerous methods available in the literature. For the sake of convenience these methods may be divided up into two main categories: empirical and analytical modelling. The former method relies totally

on the data collected from laboratory testing. These data in relation to flow conditions are represented in a graph or made into some form of empirical correlations by using numerical procedures such as least squares curve fitting. The latter method, in contrast, is concerned with examining the flow mechanism, such as interaction between the two phases. It often results in a system of simultaneous differential equations, which may have to be solved numerically with the help of a computer. Both methods have their merits and each of them will be discussed in the following two sections.

2.3.2.1. Empirical Methods

Historically, the most widely used correlation for two-phase frictional pressure drop is that of Lockhart & Martinelli [1949], who used dimensionless parameters known as two-phase multipliers ϕ_G^2 and ϕ_L^2 defined as follows

$$\phi_G^2 = \frac{(dP/dZ)_{TP}}{dP/dZ)_G} \quad (2.6)$$

$$\phi_L^2 = \frac{(dP/dZ)_{TP}}{dP/dZ)_L} \quad (2.7)$$

and related ϕ_G^2 and ϕ_L^2 to the parameter X defined as follows

$$X^2 = \frac{(dP/dZ)_L}{dP/dZ)_G} \quad (2.8)$$

where $(dP/dZ)_L$ and $(dP/dZ)_G$ are the pressure gradients for the liquid and gas phase flowing alone in the channel. Lockhart & Martinelli

presented the relationship in graphical form. Different curves were suggested, depending on whether the phase-alone flows were laminar ("viscous") or turbulent, and the multipliers are subscripted accordingly.

All the curves by Lockhart & Martinelli were obtained from correlating data of two-component systems at low pressure. The deviations from this correlation are particularly large for steam-water mixtures at high pressure. This led to the extension by Martinelli and Nelson [1948] of the approach to the high-pressure water-steam system which is a one-component system. The main difference is that in the one-component system the void changes with distance, causing significant acceleration pressure drop and also causing variation in the frictional pressure drop. They produced a revised multiplier correlation which was fitted to data for steam-water mixtures over a range of pressures based on an arbitrary correction for the region between atmospheric and critical pressures.

The method of using the ratio of the pressure drop of the liquid (ΔP_L) to the pressure drop of the gas (ΔP_G) as the independent parameter to correlate ΔP_{TP} has been used extensively since 1949. Perhaps the most widely used advanced empirical correlation is the one proposed by Chisholm [1967], which is expressed as

$$(\Delta P_{TP}/\Delta P_G) = 1 + C[\Delta P_L/\Delta P_G]^{0.5} + (\Delta P_L/\Delta P_G) \quad (2.9)$$

where C is an empirical constant which depends on the density ratio of the flowing phases,

$$C = \frac{1}{E} \sqrt{\frac{\rho_L}{\rho_G}} + E \sqrt{\frac{\rho_G}{\rho_L}} \quad (2.10)$$

and

$$E = \sqrt{\frac{\rho_L}{\rho_{hom}}} \quad (2.11)$$

Chisholm developed this correlation by accounting for the shear forces between phases of a two-phase mixture flowing in a pipe. This theory is also shown to provide a satisfactory basis for the correlation of data for the flow of gas/liquid and steam/water mixtures through orifices and venturis. Chisholm & Sutherland [1969] further developed the correlation to predict the pressure drop during two-phase flow through fittings and a simple equation was presented by the same author [1971].

The main advantages of using Martinelli-type correlations are that the complexity normally associated with phase changes in two-phase mixture is avoided, and that there is reasonable agreement between predicted and experimental data when used carefully in a similar situation. There are however some severe difficulties with this method. The main one is that the empirical correlations are based on the assumption that the frictional pressure gradient is a function only of channel cross-sectional geometry, mass flux, and physical properties. However, in two-phase flow, the effects of flow development are very considerable, and any wide-ranging data bank on two-phase flow contains data with a variety of inlet configurations and channel lengths, which will give a range of pressure gradients for the same nominal conditions. It is generally accepted that further improvement in prediction methods for two-phase pressure drop

depends on having a better physical representation of the flow.

2.3.2.2. Analytical Modelling

Analytical models for two-phase flow range all the way from the homogeneous equilibrium model, which is essentially a single-phase flow technique, to methods that attempt to represent (at least approximately) all of the non-equilibrium phenomena. In between are many hybrid models that treat some of the non-equilibrium aspects by simplifying assumptions or empiricism.

For convenience the models to be surveyed are placed in the following two categories:

- (1) Homogeneous equilibrium flow model
- (2) Separated flow model (two-fluid model)

2.3.2.2.1. Homogeneous Equilibrium Flow Model

The feature of the homogeneous equilibrium flow model is that the gas and liquid phases are assumed to be intimately mixed so that the two phases are everywhere in equilibrium with equal temperature and velocity; properties such as thermodynamic quality can be obtained from steam tables or some general "equation of state". The critical problem with this model is how to determine the transport properties such as viscosity of the homogeneous mixture (or fictitious fluid).

This two-phase flow model has been known for many years. The early investigators who used this technique include Isbin [1957],

Henry [1968], Smith [1963], Steltz [1961], and Sozzi & Sutherland [1975]. Their results showed that the homogeneous equilibrium model is not a bad way of predicting the critical mass flux in long pipes where there is sufficient time for equilibrium to be achieved and when the flow pattern is conducive to interphase forces that are adequate to repress relative motion. Errors can be large (a factor of 5 or so on flow rate) for short pipes, in which there is insufficient time for the vapour formation to proceed to equilibrium, and significant in long pipes if the flow regime, such as annular flow, allows large differences in phase velocities.

In the homogeneous equilibrium flow model, the two-phase mixture can be described by the same equations as an equivalent single phase flow. It removes the need for specifying detailed relationships for momentum and energy transport rates. Therefore despite the fact that it fails to look into the microscopic structure of two-phase flow this model was still used more recently by Bilicki [1983] et al for its simplicity and reasonable accuracy in predicting choking flow.

2.3.2.2.2. Separated Flow Model

Because of the deficiencies of the homogeneous flow model in representing a wide range of experimental results, a number of models were suggested by various investigators. These models are capable of accounting for the non-equilibrium effects inherent in two-phase flow in one way or another. Of them the most effective and widely accepted is the separated flow model or two-fluid model.

Contrary to the homogeneous equilibrium flow model, the main emphasis of the separated flow model is on the behaviour of each of the individual phases and their interfacial interactions. To ensure the success of this flow model a knowledge of the flow regime under study, from which the transport process across the interphase might be possibly examined, is required.

The major advantage of the model is its flexibility and accuracy in the analysis of two-phase flow process. It may be developed with various degree of complexity, ranging from the simplest version where only velocity is allowed to differ, to the most sophisticated one where both velocity and temperature are allowed to differ for the phases. In using this model, separate conservation equations are written for each phase (or for one phase and the combined phases separately) and interaction terms are included to represent the interfacial heat, mass and momentum transfer. Upstream conditions are supplied as one boundary condition and the solution is developed numerically in the downstream direction.

A thorough description of the general mathematics of the solution technique is due to Boure [1975] and Ishii [1975]. They formulated the one-dimensional conservation equations of mass, momentum and energy for each phase together with rate equations in general terms. Critical flow is achieved as a local mathematical singularity and approached by solving the entire history of the flow. Hence the success of this analysis can be checked by pressure and void fraction measurements along the flow channel besides recording the critical flow rate.

The main cause of discrepancy between the analysis and experiment using a separated flow model is the selection of interfacial terms such as shear stress and heat transfer. Ardron [1976][1978] described the interfacial forces in the bubbly flow as the sum of drag and virtual mass force and suggested that heat transfer from the liquid to the bubble takes place mainly by diffusion. Thus no convection term is included. Yet in a later paper, Ardron & Ackerman [1978] examined their experimental result and concluded that convection is dominant. However in their model the changes in liquid temperature were not accounted for.

Richter [1983] used the separated flow model for steam-water critical two-phase flow through a long pipe, in which the flow regime transitions were expected to occur. He proposed that the void fraction could be used to indicate the transition of different flow regimes, e.g. if the void fraction exceeds about 0.3 a transition from bubbly to another flow regime called "churn-turbulent" would occur; and when the void fraction is 0.8 the flow regime would be annular. He further assumed that mass transfer was limited by heat transfer between the phases and heat transfer coefficients included conduction as well as convection. In bubbly and annular flow regimes, the interfacial shear stress and heat transfer coefficients were obtained from some empirical formulas. The churn-turbulent flow regime is not well defined and therefore the interfacial terms for this regime were interpolated from bubbly and annular flow regimes. This procedure is yet to be justified. However the comparison with experiment by Zaloudek [1964], Henry [1970] and Sozzi & Sutherland [1975] shows generally good agreement. The main problem is that the

initial bubble diameter and bubble density must be specified in order to start the computation.

Others who also used a separated flow model are Wallis [1968], Elliott & Weinberg [1968] and Martindale & Smith [1982]. An examination of their equations revealed that almost all of their formulations are compatible with each other. Differences occur when they are applied to a specific problem. These differences usually involve terms concerning transport rates such as shear stress and heat transfer, as discussed above. It is realised that the most appropriate way to handle them is to develop strong links between theory and experiment as the basis to judge the difference between various theories, when each theory is useful and what practical advantage there may be from different levels of sophistication in the formulation.

2.3.3. VOID FRACTION MEASUREMENT TECHNIQUE

It is clear throughout the previous sections that void fraction may be one of the most important parameters in the study of two-phase flow. Its distributions across a flow channel are essential for the calculation of pressure drop, heat transfer and for the validation of the theoretical flow model proposed. Moreover it is useful for identifying the flow regimes. As a result, much of the experimental work on two-phase flow has been centred on void fraction measurement.

Two-phase flow instrumentation for void fraction measurement can be classified as global or local. Global methods give average void

fraction over a full section of the channel, over a given channel cross section or across the diameter of a channel of circular cross section. A typical example of the technique is the quick-closing valve. By contrast, local instantaneous methods provide measurements at specific locations. Usually, this void fraction is obtained on a time average basis at the position of interest .

2.3.3.1. Average Void Fraction Measurement

Johnson & Abou-Sabe [1952] and Serizawa [1975] employed a quick-closing valve system to measure the average void fraction in a flow channel. In such a system the valves which can be quickly and simultaneously operated are positioned at the beginning and end of the channel section. At the appropriate moment, the valves are actuated and the liquid phase trapped in the channel is drained and its volume measured. Since the volume of the flow channel is known, the average void fraction can then be determined.

The main advantage of this method is its simple operation and remarkable degree of reproducibility of measurement. Nonetheless it should be noted here that of all the possible void fraction measurement techniques this one, the quick-closing valve technique, is the worst, due to the synchronisation difficulty between the two valves. The reason for this is that to close the valves a finite time is required. This must, in principle, lead to an inaccuracy in the method since, during the valve closure time, the flow pattern within the channel must be changing. In addition, harmful pressure transients might occur within the system.

A more accurate method of void fraction measurement is the attenuation-radiation technique. This involves measurement of the attenuation of a beam of gamma rays or X-rays in the flow. It is known that the attenuation of gamma beams in passing through materials occurs by three distinct processes, the relative importance of which varies with the gamma photon energy and with the attenuating material. These are:

- 1) Photoelectric effect
- 2) Pair production
- 3) Compton effect

The absorption of a collimated beam of initial intensity I_0 (photons per square meter per second) is described by an exponential absorption law as follows:

$$I = I_0 e^{-\mu z} \quad (2.12)$$

where μ is the linear absorption coefficient, and z the distance travelled through a homogeneous absorbing medium. In applying this technique to the measurement of void fraction, a collimated beam of gamma rays is passed through the channel wall, through the two-phase mixture, and through the opposite channel wall before it passes into a detector. The received intensities I_G and I_L with the channel full of gas and liquid, respectively, are first measured. The void fraction is then related to the intensity I measured during the two-phase flow in the channel and to I_G and I_L as follows:

$$\alpha = \frac{\ln I - \ln I_L}{\ln I_G - \ln I_L} \quad (2.13)$$

The gamma-ray absorption method for void fraction determination has been employed by Hooker & Popper [1958], Isbin [1959], Miropolski & Shneyerova [1960] and Thomas [1977]. Their works are mainly on isothermal and evaporating systems without particular reference to the flow regimes present although a number of these studies were predominantly in the annular flow regime. The most common sources of soft gamma-rays are Thulium-170 and Cesium-137 and these isotopes have the advantage of giving a largely nonenergetic emission.

Schrock & Selph [1963], Truong-Quang Minh [1965], Pike [1965] and Lahey [1977] used X-rays as an alternative to gamma-rays. With the development of improved X-ray sources, this method is becoming more popular. Schrock & Selph [1963] showed there are less restrictions in the utilisation of the X-ray method than in the gamma-ray method.

Piper [1974] discussed in his investigation the errors arising in radiation-attenuation void measurements. The main problems with the method are the extremely careful handling procedure required for radiation, which should be considered before an attempt to use these techniques is made, the fundamental inaccuracy due to the normal photon statistical fluctuations, which might be minimised by long counting time or strong sources, and certain effects of void orientation and fluctuations in void fraction with time.

2.3.3.2. Local Void Fraction Measurement

In order to analyse the precise structure of a two-phase flow accurately, local instantaneous measurement of void fraction, is

required. For this purpose several methods have been developed and generally require the insertion at the point of interest of a probe which detects changes in physical properties inherent in the two phases, e.g., electrical resistivity, thermophysical properties, or index of refraction. Of these the electrical probe and optical probe are probably the two best known.

The use of electrical probes was first proposed by Neal & Bankoff [1963] and Akagawa [1963], and later was used by Galaup [1975], Serizawa [1975] and Delhay & Achard [1977] etc. The void fraction is measured by detecting a signal caused by a difference in electric conductivity between liquid and gas. Therefore the prime requirement to be met when using an electrical probe in two-phase flow is that one phase has a significantly different electrical conductivity from the other. The electrical probe consists of two identical sensors or needles, whose tips are about 5 mm apart from each other. By making the probe face the flow, it is possible to detect the time during which the probe spends in each phase. The local void fraction α is defined as

$$\alpha = \frac{t_G}{t_G + t_L} = \frac{t_G}{T} \quad (2.14)$$

where t_G is the time gas or vapour is present at the probe tip and t_L is the time there is liquid. T is the total measurement time.

According to the way in which the sensor is energised, the ideal output signal of an electrical probe is either a binary-wave

sequence, or a sequence of bursts of constant-amplitude oscillations separated by zero-voltage zones. Actually, the output signal is misshapen with respect to the ideal signal because of the interface deformations. The signal is generally transformed into a binary sequence by setting a trigger level. Galaup [1975] used a level adjustment based on a comparison between the integrated void profile and the line void fraction obtained with a gamma-ray absorption method.

It is obvious that the electrical probe has various disadvantages such as being susceptible to electrical noise and is impracticable for a nonconductive fluid. For nonconductive fluids such as Freon, oil and liquefied natural gas, optical probes of small dimensions have been developed by Miller & Mitchie [1970], Danel & Delhaye [1971], Hinata [1972] and Delhaye & Galaup [1974]. More recently, a design successfully combining features of several of the earlier versions has been described by Abuaf & Jones [1978]. For illustration, the optical probe developed by Danel & Delhaye [1971] is given in Fig.2.7. It consists of a single optical fibre, 40 μm in diameter, a light source and phototransistor.

The principle of an optical probe is that it is sensitive to the changes in the refractive index of the surrounding medium and is thus responsive to the interfacial passages. The operational principle of an optical fibre probe is shown in Fig.2.8. It can be seen that if gas is present at the tip of the probe, the light passing down the glass rod from the light source, is reflected and a higher signal is produced by the phototransistor. If the liquid is present, the light

is refracted giving a lower signal. A typical output of signal from the phototransistor is in Fig.2.8. It should be noted that n_L and n_G are the refractive index of liquid and gas phase respectively. The local void fraction can be obtained in the same fashion as that described in the electrical probe method. To determine interface velocity, two consecutive probes are situated a known distance from each other in the flow direction.

Hsu [1963] and Delhaye [1968][1969] reported the use of a hot-wire anemometer for local void fraction measurement. A probe of this kind works on the principle of variation in the quantity of heat dissipated in the respective phases. The principal measurement from this probe is the statistical characteristic of two phase temperatures. However, if the measurement is combined with an electrical phase indicator, then the local void fraction may also be obtained.

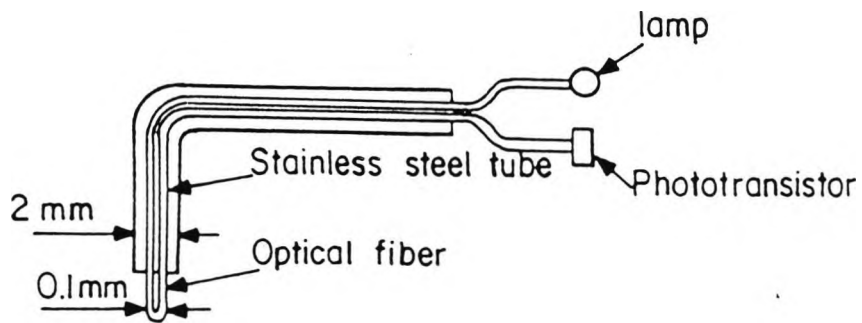


Fig.2.7. Danel & Delhaye Fibre Optic Probe

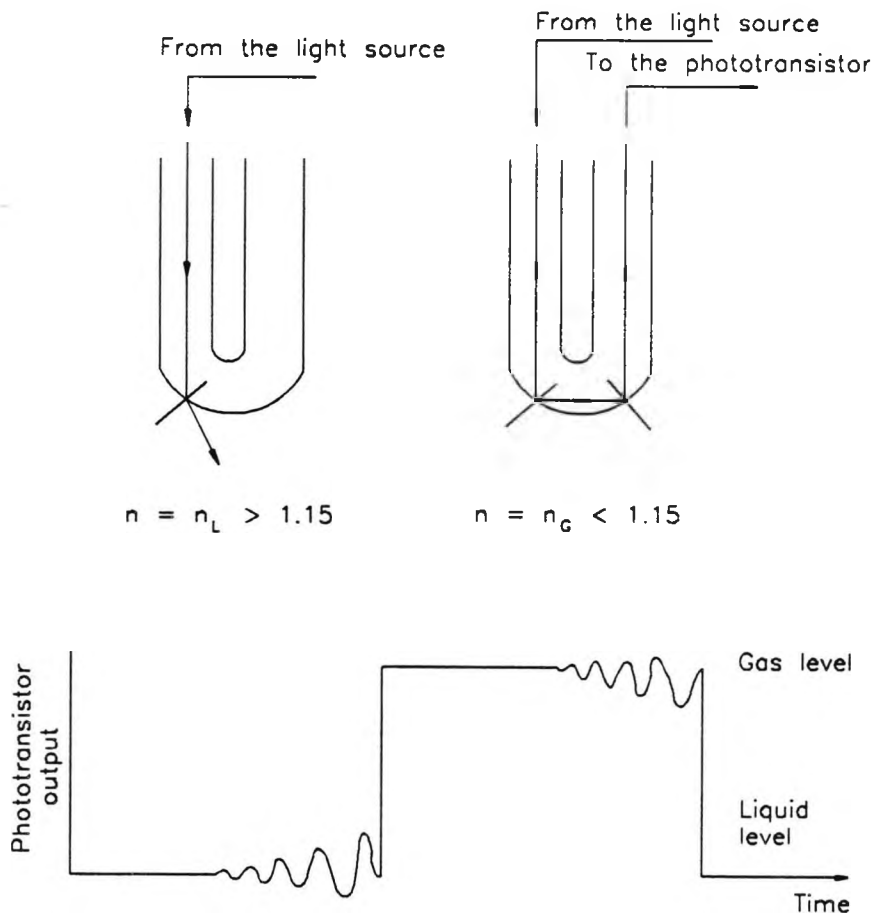


Fig.2.8. Operational Principle of Optical Method

CHAPTER 3

OBJECT OF THE RESEARCH

In view of the previous related work, the main purpose of this research project was to help develop an analytical approach suitable for the design of an efficient Lysholm screw expander, for low-grade heat recovery. Smith's experimental investigation of this type of machine indicated that the area most likely to improve the expander adiabatic efficiency appeared to be an improved rotor filling. This could only be achieved by a better inlet port design. The best first approach would be to treat the port as a straight one-dimensional flow nozzle and design for maximum adiabatic efficiency with uniform vapour and liquid distribution at exit. To achieve this the following programme was adopted:

1. To establish an analytical model for steady two-phase flow in a circular or axisymmetric duct of variable cross section.
2. To develop a numerical procedure to solve efficiently the coupled non-linear differential equations which arise from the analytical model.
3. To develop an optimisation procedure to obtain an inlet port profile with optimum adiabatic efficiency.
4. To develop a transformation procedure to alter the duct cross sectional shape from circular or axisymmetric to that required at the rotor inlet.
5. To use the analytical methods developed to design first a circular

duct and then its transformed version as the inlet port for a 163.2 mm asymmetric rotor screw expander.

6. To design and construct a test apparatus to measure the performance of both the circular and transformed ports.
7. To measure the performance of the port designs under steady flow conditions and compare it with that predicted.

The detailed analytical modelling of two-phase flow through the inlet port is carried out in Chapter 4 whereas its relevant numerical solution procedure is set out separately in Chapter 5. Following the work in these two chapters, Chapter 6 contains the inlet port design and optimisation study using the calculus of variations. Also in this chapter, the transformation procedure is evaluated. The experimental work is described in Chapter 7.

CHAPTER 4

THEORETICAL ANALYSIS

4.1. SUMMARY

The literature survey carried out in Chapter 2 has shown that two-phase flow of liquid-gas mixture is a complex process. Flow regimes and channel geometry have a marked effect on the nature of the processes. Moreover the majority of flow models proposed over the years are restricted in their availability to air-water two-component two-phase flow systems or water-steam one-component two-phase flow systems. There has been little research work in the field of two-phase flow where volatile organic fluids are employed as working fluids.

Since two-phase flow is complex, there is a general lack of systematic theoretical work which is applicable to the flashing flow through the inlet port of a Lysholm screw expander. To fill this gap, an attempt is made within the current chapter to develop a two-phase flow model appropriate for the current study. From what has been described in the literature survey, it would appear of interest to use a separated two-phase flow model, which should allow in a general way for thermal non-equilibrium between the liquid and gas phases, and for interphase relative motion. Such an approach, while more complicated than the homogeneous model, would offer greater insight into the flow character as well as giving quantitative predictions of the critical flow rate.

4.2. PHYSICAL MODEL

Thermodynamically, flashing results from suddenly lowering the pressure of a liquid until the bubble point is reached. Further lowering of the pressure will leave the liquid superheated or at a temperature higher than the saturation temperature corresponding to the pressure, and the liquid tends to convert to vapour to regain equilibrium. Under adiabatic conditions the vapour formed can obtain its latent heat of vaporisation only at the expense of the sensible heat of the remaining liquid. Equilibrium will be reached when the fraction of liquid converted to vapour has extracted enough energy from the residual liquid to cool it and both phases reach the saturation or equilibrium temperature.

Nucleation begins at a flow control valve upstream of the inlet port. In a previous Lysholm screw expander test by Smith [1985], an observation chamber with a glass window was placed between the control valve and the inlet port. The flow was visually observed to be a conglomerate of droplets and bubbles of very small diameters. Therefore, in the development of the separated flow model through the inlet port it is assumed that the liquid phase in the mixture is of discrete droplets and is well dispersed in a continuous gas continuum. This makes it quite convenient to model the transport processes between the two phases because a great amount of information is available for predicting the transport of droplets in a moving gas stream.

Fig.4.1 is a schematic diagram of the analytical flow model used

in the current analysis which shows that a spatially uniform mixture of liquid droplets and gas enters the inlet port at high pressure and low velocity and expands to low pressure and high velocity. Because of the difference in the density of the two phases, the gas velocity increases more rapidly than the liquid, thus exerting an interfacial drag force on the liquid-gas interface. Hence the liquid accelerates

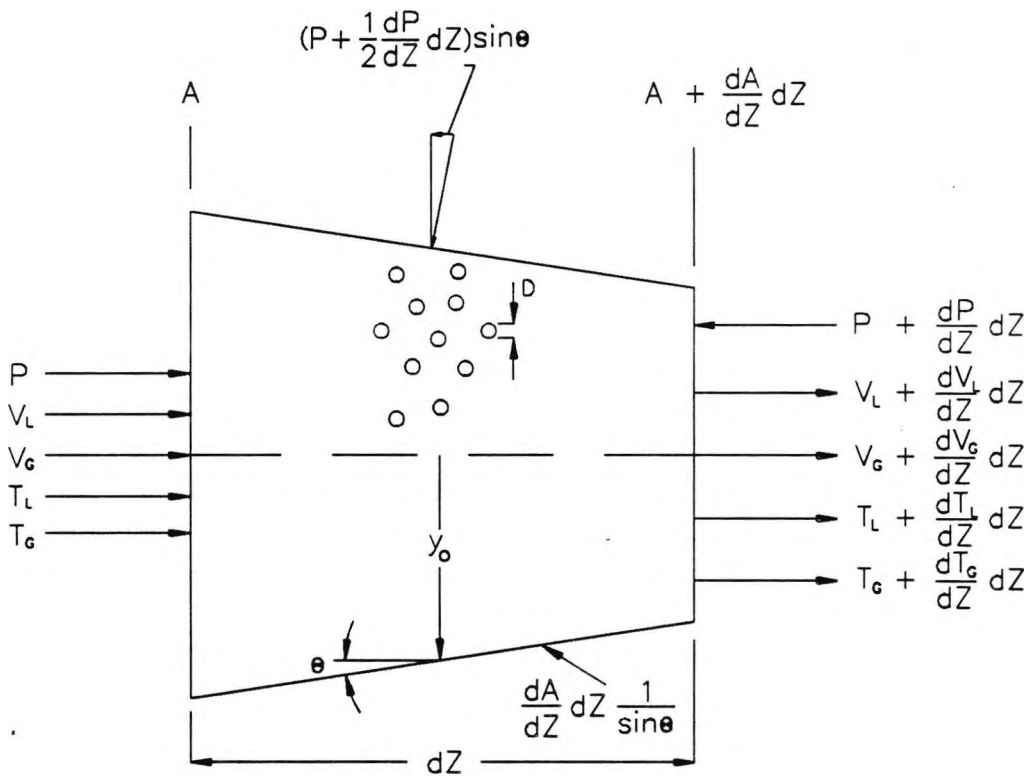


Fig.4.1. Schematic Diagram of Two-Phase Flow Model

as a result of

- (1) the decreasing pressure in the direction of flow
- (2) the drag forces exerted on them by the faster moving gas.

During the expansion of the two-phase mixture, thermal energy is

transferred between the liquid and the gas. The amount of heat transferred between the phases in a given period of time depends upon

- (1) the difference in temperature of the two phases
- (2) the amount of heat lost through the wall
- (3) the shape and size of the liquid droplets
- (4) the velocities of each of the fluids
- (5) the thermal characteristics of each of the individual phases including condensation and vaporisation.

4.2.1. Basic Assumptions

In the subject analysis here, separated flow was considered with the following basic assumptions:

1. The flow is steady and one-dimensional.
2. Apart from gravity, whose effects are small, there are no external forces acting on the two-phase mixture other than pressure and wall shear. There is no heat transfer to or from the mixture.
3. The two phases can have different temperatures as well as velocities. These may be evaluated by an appropriate interfacial relationship.
4. Mass transfer is limited by the heat transfer between the phases. Heat transfer includes conduction as well as convection, as appropriate.
5. Liquid is in the form of droplets which are uniformly distributed throughout the gas phase and all of the same diameter at any cross section of the flow channel. The droplets do not interact with each other and do not coalesce or shatter.
6. The droplets are large enough for the surface curvature to have

negligible effect on the vapour pressure of the liquid and for the surface energy to be negligible.

7. The thermal conductivity of the liquid is large compared to that of the gas phase so that the temperature is uniform throughout the droplet.
8. The effect of the presence of any non-condensable gas is negligible.

4.2.2. Equations Employed

There are six main unknown flow parameters to be determined in the analysis. These are: static pressure P , liquid and gas velocities V_L and V_G , liquid and gas temperatures T_L and T_G , and gas flow rate m_G . To obtain them the following conservation equations are to be employed:

a) for the two-phase mixture:

- (1) the continuity equation
- (2) the momentum equation
- (3) the energy equation

b) for the liquid droplets:

- (4) the drag equation
- (5) the heat transfer equation.

It should be noted that in the process of deriving the momentum equation for the two-phase mixture, the wall shear stress term will not be involved. Instead its influence on the flow behaviour is described in detail by a boundary layer momentum integral equation which is commonly used in single phase flow analysis.

4.3. DEVELOPMENT OF CONSERVATION EQUATIONS

4.3.1. The Continuity Equation For a Two-Phase Mixture

According to assumption 1, the flow under investigation is steady. With reference to the control volume cut out in Fig.4.1, the principle of conservation of mass, when applied to this control volume, therefore, states that the total mass flow rates into the control volume be equal to the total mass flow rates leaving the control volume if no sources and sinks are involved. Mathematically this principle can be expressed as:

$$\sum \dot{m}_{in} = \sum \dot{m}_{out} \quad (4.1)$$

where

$\sum \dot{m}_{in}$ is the summation of the mass flow rates entering the control volume

$$\sum \dot{m}_{in} = \rho_G V_G A_G + \rho_L V_L A_L \quad (4.2)$$

and

$\sum \dot{m}_{out}$ is the summation of the mass flow rates leaving the control volume

$$\begin{aligned} \sum \dot{m}_{out} = & \left(\rho_G + \frac{d\rho_G}{dZ} dZ \right) \left(V_G + \frac{dV_G}{dZ} dZ \right) \left(A_G + \frac{dA_G}{dZ} dZ \right) + \\ & \left(\rho_L + \frac{d\rho_L}{dZ} dZ \right) \left(V_L + \frac{dV_L}{dZ} dZ \right) \left(A_L + \frac{dA_L}{dZ} dZ \right) \end{aligned} \quad (4.3)$$

where Z is the coordinate in the flow direction.

Upon Substituting Eqns.(4.2) and (4.3) back to Eqn.(4.1) and eliminating the higher order terms, the continuity equation for two-phase mixture is obtained in differential form as follows:

$$\begin{aligned} \rho_G V_G \frac{dA_G}{dZ} + \rho_G A_G \frac{dV_G}{dZ} + V_G A_G \frac{d\rho_G}{dZ} + \\ \rho_L V_L \frac{dA_L}{dZ} + \rho_L A_L \frac{dV_L}{dZ} + V_L A_L \frac{d\rho_L}{dZ} = 0 \end{aligned} \quad (4.4)$$

where A_L and A_G are the cross sectional areas occupied by the liquid and gas phases, respectively. They can be written in terms of the total channel flow area A and void fraction α by the following relations:

$$A_L = (1 - \alpha)A \quad (4.5)$$

$$A_G = \alpha A \quad (4.6)$$

Eqn.(4.4) can be further rearranged in a more compact manner

$$\frac{d(\rho_G V_G A_G)}{dZ} + \frac{d(\rho_L V_L A_L)}{dZ} = 0 \quad (4.7)$$

It is obvious from the above equation that the two terms are the evaporation rate and condensation rate respectively. Therefore in the steady flow situation one can conclude the evaporation rate is equal to the negative of the condensation rate. Furthermore the integration of Eqn.(4.7) leads to

$$\dot{m}_t = \rho_G V_G A_G + \rho_L V_L A_L \quad (4.8)$$

where \dot{m}_t is the total flow rate.

4.3.2. The Momentum Equation For a Two-Phase Mixture

The principle of conservation of momentum states that the balance of forces exerted on the control volume, including both body forces and surface forces, be equal to the momentum changes accompanying the process. Mathematically it can be expressed in the axial direction as:

$$\sum F = \sum \dot{M}_{out} - \sum \dot{M}_{in} \quad (4.9)$$

The respective terms in the equation will be described and evaluated as follows:

$\sum F$ is the summation of forces acting on the control volume in the axial direction. Referring to Fig.4.1, it is seen that the forces on the element are those due to the pressure gradient and the wall shear. The wall shear is to be treated separately in the boundary layer momentum integral equation, as already pointed out. Therefore the forces on the element are

$$\begin{aligned} \sum F = & A \cdot P - (A + \frac{dA}{dZ}dZ)(P + \frac{dP}{dZ}dZ) + \\ & (P + \frac{1}{2} \frac{dP}{dZ}dZ) \sin\theta \frac{dA}{dZ}dZ \frac{1}{\sin\theta} \end{aligned} \quad (4.10)$$

$\sum \dot{M}_{in}$ is the summation of the momentum inflow rates to the control volume

$$\sum \dot{M}_{in} = \dot{m}_G V_G + \dot{m}_L V_L \quad (4.11)$$

where \dot{m}_G and \dot{m}_L are the gas and liquid flow rate at the control

volume inlet.

$\dot{\Sigma M}_{out}$ is the summation of the momentum outflow rates from the control volume

$$\begin{aligned} \sum \dot{M}_{out} = & (\dot{m}_G + \frac{d\dot{m}_G}{dZ}dZ)(V_G + \frac{dV_G}{dZ}dZ) + \\ & (\dot{m}_L + \frac{d\dot{m}_L}{dZ}dZ)(V_L + \frac{dV_L}{dZ}dZ) \end{aligned} \quad (4.12)$$

Thus the conservation momentum equation for two-phase mixture in differential form can be obtained simply by substituting Eqns.(4.10)-(4.12) into Eqn.(4.9) and eliminating higher order terms from the equation:

$$-A \frac{dP}{dZ} = \dot{m}_G \frac{dV_G}{dZ} + V_G \frac{d\dot{m}_G}{dZ} + \dot{m}_L \frac{dV_L}{dZ} + V_L \frac{d\dot{m}_L}{dZ} \quad (4.13)$$

Or rearranging the equation by moving all the terms on the right hand side to the left hand side, we have

$$A \frac{dP}{dZ} + \dot{m}_G \frac{dV_G}{dZ} + V_G \frac{d\dot{m}_G}{dZ} + \dot{m}_L \frac{dV_L}{dZ} + V_L \frac{d\dot{m}_L}{dZ} = 0 \quad (4.14)$$

4.3.3. The Energy Equation For a Two-Phase Mixture

According to assumption 2, the system under study is undergoing adiabatic flow. If this occurs without external work, then according to the principle of conservation of energy the enthalpy flowing into the control volume must be equal to that leaving it, i.e.

$$\sum H_{in} = \sum H_{out} \quad (4.15)$$

where

$\sum H_{in}$ is the summation of the enthalpies flowing into the control volume and with reference to Fig.4.1,

$$\sum H_{in} = \dot{m}_G \left(h_G + \frac{1}{2} V_G^2 \right) + \dot{m}_L \left(C_L T_L + \frac{P}{\rho_L} + \frac{1}{2} V_L^2 \right) \quad (4.16)$$

and

$\sum H_{out}$ is the summation of the enthalpies leaving the control volume and as shown in Fig.4.1,

$$\begin{aligned} \sum H_{out} = & \left(\dot{m}_G + \frac{d\dot{m}_G}{dZ} dZ \right) \left[\left(h_G + \frac{dh_G}{dZ} dZ \right) + \frac{1}{2} \left(V_G + \frac{dV_G}{dZ} dZ \right)^2 \right] + \\ & \left(\dot{m}_L + \frac{d\dot{m}_L}{dZ} dZ \right) \left[C_L \left(T_L + \frac{dT_L}{dZ} dZ \right) + \frac{1}{\rho_L} \left(P + \frac{dP}{dZ} dZ \right) + \frac{1}{2} \left(V_L + \frac{dV_L}{dZ} dZ \right)^2 \right] \end{aligned} \quad (4.17)$$

where h_G is the specific enthalpy of gas phase,

C_L is the specific heat of liquid phase,

By substituting Eqns.(4.16) together with Eqn.(4.17) back to Eqn.(4.15) and eliminating the higher-order terms from the resulting

equation, we have the energy equation for the two-phase mixture in differential form

$$\begin{aligned} (h_G + \frac{1}{2}V_G^2)\frac{d\dot{m}_G}{dZ} + \dot{m}_G\frac{dh_G}{dZ} + \dot{m}_GV_G\frac{dV_G}{dZ} + (C_L T_L + \frac{P}{\rho_L} + \frac{1}{2}V_L^2)\frac{d\dot{m}_L}{dZ} + \\ C_L\dot{m}_L\frac{dT_L}{dZ} + \frac{\dot{m}_L}{\rho_L}\frac{dP}{dZ} + \dot{m}_LV_L\frac{dV_L}{dZ} = 0 \end{aligned} \quad (4.18)$$

4.3.4. The Drag Equation For Liquid Droplets

The forces exerted on a single droplet, as discussed in section 4.2.1., consist of the pressure force resulting from the pressure gradient in the direction of the flow and the drag force caused by the relative motion of the two phases. Therefore applying the principle of conservation of momentum to the liquid droplets, using the boundary between the phases as the control volume, the momentum equation (better known as the drag equation) for the droplets can be written as

$$\dot{N}_d(F_P + F_D) = \dot{m}_L\frac{dV_L}{dt} = \dot{m}_LV_L\frac{dV_L}{dZ} \quad (4.19)$$

Each terms on the left hand side of the equation can be determined as follows.

F_P is the pressure force exerted on a single liquid droplet. The pressure force for a single droplet is evaluated in detail in Appendix C. Hence we have

$$F_P = -\frac{\pi D^3}{6} \frac{dP}{dZ} \quad (4.20)$$

where D is the droplet diameter.

F_D is the drag force exerted on a single droplet by the gas phase. From the standard drag equation we have

$$F_D = C_D \frac{\pi D^2}{4} \rho_G \frac{(V_G - V_L)|V_G - V_L|}{2} \quad (4.21)$$

where C_D is the drag coefficient.

\dot{N}_d is the number flow rate of liquid droplets. Given the liquid mass flow rate \dot{m}_L as well as the liquid density, the following relationship holds

$$\dot{N}_d = \frac{\dot{m}_L}{\frac{\pi D^3}{6} \rho_L} \quad (4.22)$$

Upon substituting Eqns.(4.20)-(4.22) into Eqn.(4.19), the drag equation for liquid droplets can be derived as follows

$$\rho_L V_L D \frac{dV_L}{dZ} + D \frac{dP}{dZ} - \frac{3C_D \rho_G}{4} (V_G - V_L)|V_G - V_L| = 0 \quad (4.23)$$

The purpose of employing the absolute value signs in the above equations is to make the drag force positive when $V_G > V_L$ and negative when $V_G < V_L$.

4.3.5. The Heat Transfer Equation For Liquid Droplets

For liquid droplets as a whole, the principle of conservation of energy states that the rate of heat transfer to or from the gas, using the boundary between the two phases as a control volume, should be equal to the rate of work done on the droplets due to friction plus the total rate of change of enthalpy in the process, or mathematically,

$$\delta\dot{Q} = d\dot{H} + \delta\dot{W} \quad (4.24)$$

Each term on both the left and right hand side of the equation can be determined as follows.

$\delta\dot{Q}$ in Eqn.(4.24) represents the heat transfer rate across the interface and is made up of two contributions: (1) convection due to the temperature difference between liquid and gas; (2) evaporation due to the latent heat supplied to the liquid being vaporised. Hence

$$-\delta\dot{Q} = h \cdot A_d \cdot \dot{N}_d \cdot (T_L - T_G) \cdot dt + h_{LG} \cdot d\dot{m}_G \quad (4.25)$$

where h is the heat transfer coefficient,

$A_d = \pi D^2$ is the surface area of a droplet,

h_{LG} is the latent heat,

$d\dot{m}_G$ is the amount of liquid vaporised.

$\delta\dot{W}$ in Eqn.(4.24) represents the rate of external work done on the liquid droplets by the viscous drag force and can be expressed as

$$-\delta\dot{W} = F_D \cdot \dot{N}_d \cdot dZ \quad (4.26)$$

where F_D is the drag force exerted on a single droplet. It has been obtained in the previous section in Eqn.(4.21). Upon substituting Eqns.(4.21) into Eqn.(4.26), it becomes

$$-\delta\dot{W} = C_D \frac{\pi D^2}{4} \rho_G \frac{(V_G - V_L)|V_G - V_L|}{2} \cdot \frac{\dot{m}_L}{\frac{\pi D^3}{6} \rho_L} \cdot dZ \quad (4.27)$$

$d\dot{H}$ is the total rate of enthalpy change of the liquid phase over the increment dZ and is simply given by

$$d\dot{H} = \dot{m}_L (C_L dT_L + \frac{dP}{\rho_L} + \frac{1}{2} dV_L^2) \quad (4.28)$$

Now that all the relevant terms in Eqn.(4.24) have been determined individually, the heat transfer equation for liquid droplets can be derived. Substituting the relevant equations deduced above and making use of the drag equation for liquid droplets, the heat transfer equation may be expressed as:

$$\dot{m}_L C_L \frac{dT_L}{dZ} + h_{LG} \frac{d\dot{m}_G}{dZ} - \frac{6h\dot{m}_L(T_G - T_L)}{\rho_L D V_L} = 0 \quad (4.29)$$

4.4. CONSTITUTIVE AND STATE EQUATIONS

Eqns.(4.4), (4.14), (4.18), (4.23) and (4.29) form a complete set of field equations for adiabatic two-phase flow in a variable area flow channel. To close the model, a set of constitutive and state equations are needed to describe the fluid properties as well as the

interfacial conditions between the two phases. This section describes the relations for the droplet diameter, drag coefficient and heat transfer coefficient. A relation for the wall shear stress will be developed separately in the following section.

4.4.1. Droplet Size

It is clear from the above conservation equations that the droplet size and its distributions are important for detailed mechanistic modelling of the two-phase flow of liquid droplet and gas mixture. As a consequence, it is of direct relevance to examine those factors which may affect the droplet size distribution.

Droplets can be generated in a number of different ways such as liquid jet breakup, droplet disintegration and droplet entrainment from a body of liquid. Weber [1931] studied the instability of liquid jets which disintegrated into smaller droplets through the action of aerodynamic forces and surface tension forces. A criterion for droplet breakup and disintegration can be expressed in terms of a dimensionless number, now called the Weber number, one form of which is

$$We = \frac{\rho_G(V_G - V_L)^2 D}{2\sigma} \quad (4.30)$$

where σ is the liquid surface tension. The Weber number may be considered as the ratio of stagnation pressure $\rho_G(V_G - V_L)^2/2$ to surface tension pressure $4\sigma/D$. Thus a droplet would be expected to flatten and break up at a sufficiently high value of We , which is

referred to as the critical Weber number. The implication is that a droplet diameter is limited to a value D for which We equals the critical Weber number. Thus if the critical Weber number is denoted by We_{cri} , the maximum diameter is calculated from

$$D_{max} = \frac{2\sigma We_{cri}}{\rho_G(V_G - V_L)^2} \quad (4.31)$$

It should be noted that the mode by which the breakup occurs depends on the initial droplet size and the flow condition. The above criterion for droplet size has been adopted and various critical Weber numbers were proposed. Crabtree [1961] showed after the study of the flow conditions of a droplet in a two-phase nozzle that the droplets would break up early in the accelerating process, and suggested a critical Weber number equal to 6. It was obtained by correlating the data for atomisation by gas streams within a factor of about two and was further verified experimentally by Morrell [1961] and Hanson [1963]. Netzer [1962] incorporated it into a two-phase nozzle programme and exit velocities computed from it agreed within 3% with measured values in a short air-water nozzle. The same value was also used by Elliott [1968] in a large nitrogen-water nozzle investigation and good agreement with experiment was attained.

As no other data could be found for smaller droplets, the average value of 6 was employed in this analysis to determine the droplet size. On this basis the maximum diameter that can exist at any cross section is given by

$$D_{max} = \frac{12\sigma}{\rho_G(V_G - V_L)^2} \quad (4.32)$$

4.4.2. Drag Coefficient

The drag coefficient correlations found in the literature were usually obtained from the plot of Reynolds number versus drag coefficient based on experimental observations. The Reynolds number referred to throughout this work is the droplet Reynolds number and is calculated by employing the relative velocity between phases and the droplet diameter. Thus this Reynolds number can be written as

$$Re = \frac{\rho_G(V_G - V_L)D}{\mu_G} \quad (4.33)$$

where μ_G is the gas viscosity and the velocity difference $(V_G - V_L)$ is often referred to as the slip velocity.

The relationship employed for computing droplet drag coefficient in the subject analysis is as follows:

For $Re \leq 0.1$

$$C_D = \frac{24}{Re} \quad (4.34)$$

For $0.1 < Re \leq 2 \times 10^4$

$$\ln C_D = 3.271 - 0.8893 \ln Re + 0.03417 \ln^2 Re + 0.001443 \ln^3 Re \quad (4.35)$$

For $Re > 2 \times 10^4$

$$C_D = 0.4569 \quad (4.36)$$

These correlations were originally developed for solid spheres in an air stream. Among them Eqn.(4.34) is given by Stokes Law while Eqn.(4.35) is a least square fit to Perry's C_D [1963] data. The last equation is the value of Eqn.(4.35) for $Re = 2 \times 10^4$. However the drag coefficient for a solid sphere should be valid for droplets as well especially if the droplets are not distorted and internal circulation is negligible.

4.4.3. Heat Transfer Coefficient

It is common practice in the study of heat transfer to use a dimensionless number - Nusselt number to correlate the heat transfer coefficient data from experiment. Here for two-phase flow consisting of liquid droplets and gas it is defined as

$$Nu = \frac{hD}{k_G} \quad (4.37)$$

where k_G is the gas thermal conductivity.

The heat transfer coefficient used in the subject analysis is that of Kreith [1965], which is valid when Pr is approximately 1.0.

For $Re \leq 0.1$

$$Nu = 2 \quad (4.38)$$

For $0.1 < Re \leq 25$

$$Nu = \frac{\rho_G C_G (V_G - V_L) D}{k_G} \left(\frac{2.2}{Re} + \frac{0.48}{\sqrt{Re}} \right) \quad (4.39)$$

For $Re > 25$

$$Nu = 0.37Re^{0.6} \quad (4.40)$$

where C_G is the gas specific heat and Re is the droplet Reynolds number as defined by Eqn.(4.33).

4.5. BOUNDARY LAYER MOMENTUM EQUATION

The conservation equations as derived in the previous sections provide for a solution for inviscid two-phase flow in a variable area flow channel. However, for viscous fluids or long flow channels, the wall shear stress is expected to be significant. Any model which attempts to ignore this term may lead to serious error in theoretical prediction. In this section the method is presented for calculating the wall shear stress term.

By analogy with single phase flow, the influence of the fluid viscosity on two-phase flow is confined to an extremely thin region known as the boundary layer, which is close to the solid wall of the flow channel. The remainder of the flow field, which is known as the free stream, can to a good approximation be treated as inviscid. In order to account for the wall shear stress effect, it is necessary to have a knowledge of those quantities which are related to the boundary layer such as the boundary layer displacement thickness and momentum thickness. These quantities can be obtained by solving the boundary layer momentum integral equation.

In the process of deriving the momentum integral equation for

two-phase flow, the following assumptions are adopted:

- (i). The two-phase mixture is treated as homogeneous within the boundary layer.
- (ii). The flow is in the turbulent region and the velocity profile within the boundary layer obeys a one-seventh power law.
- (iii). Density variation within the boundary layer is ignored.

To facilitate the development of the boundary layer momentum integral equation, we employ some mass-weighted mean properties for a two-phase mixture such as density and velocity in the light of assumption (i). These two quantities are defined as follows.

- (1) The mass-weighted mean velocity \bar{V} in the free stream:

$$\bar{V} = \frac{\dot{m}_G V_G + \dot{m}_L V_L}{\dot{m}_t} \quad (4.41)$$

- (2) The mass-weighted mean density ρ' in the free stream:

Given the total mass flow rate \dot{m}_t , total cross sectional area A and mass-weighted mean velocity \bar{V} , this quantity can be expressed as

$$\rho' = \frac{\dot{m}_t}{\bar{V} \cdot A} \quad (4.42)$$

It follows from assumption (i) that the boundary layer momentum integral equation for single phase flow can be used directly for two-phase flow. The equation employed in the subject analysis is based on the one developed by Kays [1966] for single phase flow with two-phase velocity \bar{V} and density ρ' replacing the single phase density and velocity in the original equation:

$$\frac{\tau_o}{\rho' \bar{V}^2} = \frac{d\theta}{dZ} + \theta \left[\left(2 + \frac{\delta^*}{\theta}\right) \frac{1}{\bar{V}} \frac{d\bar{V}}{dZ} + \frac{1}{\rho'} \frac{d\rho'}{dZ} + \frac{1}{R_o} \frac{dR_o}{dZ} \right] \quad (4.43)$$

where τ_o is the wall shear stress, δ^* is the boundary layer displacement thickness and θ is the boundary layer momentum thickness; R_o is the radius of revolution of the body. For duct flow it is simply the radius of the duct which is measured from the centre line to the channel wall. With reference to Fig.4.1, it is y_o . The thickness ratio δ^*/θ is frequently called the shape factor.

Eqn.(4.43) is an ordinary differential equation for θ as a function of Z , and this equation, although in a sense exact, also forms the basis for many approximate boundary layer solutions. The approximations generally arise as a result of some assumptions about the relationship between τ_o and θ , and also the thickness ratio.

(1) Shape Factor δ^*/θ :

The boundary layer displacement thickness δ^* is a measure of the displacement of the main stream due to the presence of the solid wall and its boundary layer, or mathematically,

$$\delta^* = \int_0^\delta \left(1 - \frac{\rho V}{\rho' \bar{V}}\right) dy \quad (4.44)$$

where δ is the boundary layer thickness,

ρ and V are the two-phase density and velocity within the boundary layer respectively.

Similarly, boundary layer momentum thickness is a measure of the

momentum flux decrement caused by the boundary layer,

$$\theta = \int_0^\delta \frac{\rho V}{\rho' \overline{V}} \left(1 - \frac{\rho V}{\rho' \overline{V}}\right) dy \quad (4.45)$$

According to assumption (ii), the one-seventh power relationship holds for the velocity distribution within the boundary layer. Hence

$$\frac{V}{\overline{V}} = \left(\frac{y}{\delta}\right)^{\frac{1}{7}} \quad (4.46)$$

This velocity profile can be substituted into the two equations for δ^* and θ . Noting from assumption (iii) that

$$\rho = \rho' \quad (4.47)$$

then the required integration can be performed to yield

$$\delta^* = \int_0^\delta \left[1 - \left(\frac{y}{\delta}\right)^{\frac{1}{7}}\right] dy = \frac{\delta}{8} \quad (4.48)$$

and

$$\theta = \int_0^\delta \left(\frac{y}{\delta}\right)^{\frac{1}{7}} \left[1 - \left(\frac{y}{\delta}\right)^{\frac{1}{7}}\right] dy = \frac{7\delta}{72} \quad (4.49)$$

Hence the shape factor δ^*/θ is simply

$$\frac{\delta^*}{\theta} = \frac{9}{7} \quad (4.50)$$

(2) Wall Shear Stress τ_0 :

It is convenient to correlate the wall shear stress against a

dimensionless parameter - friction coefficient C_f

$$C_f = \frac{\tau_o}{\frac{1}{2}\rho'V^2} \quad (4.51)$$

It follows that if the friction coefficient is known, the wall shear stress can be calculated. However, it is quite difficult in two-phase flow to obtain the friction coefficient and the majority of the data available were collected for single phase flow only. To overcome this, it was proposed by Martinelli & Nelson [1948] to relate the two-phase friction factor to an equivalent single phase friction factor by an empirical formula. Some investigators simply ignored the contribution of the gas phase to the wall shear stress, as in the annular flow regime. Eddington [1966] found that the wall shear stress in homogeneous two-phase flow equals that which would exist with pure liquid at the same free stream velocity and boundary layer thickness multiplied by the wetted wall fraction. This approach is adopted here and the following equation holds:

$$\tau_o = C_f \frac{1}{2}\rho'V^2 = C_{fL} \frac{1}{2}\rho_L V_L^2 \frac{A_L}{A} \quad (4.52)$$

where C_{fL} is the friction coefficient for the liquid phase alone,

$A_L/A = 1 - \alpha$ is the wetted wall fraction.

Eqn.(4.52) is then solved to exhibit the relationship between the two-phase friction coefficient C_f and the liquid phase friction coefficient as

$$C_f = C_{fL} \frac{\rho_L V_L^2 (1 - \alpha)}{\rho'V^2} \quad (4.53)$$

The liquid phase friction coefficient C_{fL} is from the Shultz-Grunow relation which is

$$C_{fL} = \frac{0.208}{(\log_{10} Re_{\delta} + 0.425)^{2.584}} \quad (4.54)$$

where Re_{δ} is referred to as the boundary layer Reynolds number and defined as follows

$$Re_{\delta} = \frac{\rho_L V_L \delta}{\mu_L} \quad (4.55)$$

Thus substituting the above relevant equations into Eqn.(4.43) and then making some necessary rearrangement, the final form of the boundary layer momentum integral equation is

$$\frac{d\theta}{dZ} = C_{fL} \frac{\rho_L V_L^2}{2\dot{m}_t \bar{V}^2} (1 - \alpha) - \theta \left[\frac{16}{7\bar{V}} \frac{d\bar{V}}{dZ} - \frac{1}{A} \frac{dA}{dZ} + \frac{1}{y_o} \frac{dy_o}{dZ} \right] \quad (4.56)$$

It should be pointed out that this equation must be solved together with other conservation equations to produce the momentum thickness θ and then the displacement thickness δ^* . Only when this is done, can the effect of the wall shear stress on the flow field be examined. Considering the definition of momentum thickness, one can write

$$\dot{m}_t \bar{V} - \dot{m}_t \bar{V}_{\delta} = 2\pi y_o \theta \frac{\dot{m}_t \bar{V}}{A} \quad (4.57)$$

where \bar{V}_{δ} is the mass-weighted mean velocity including the boundary layer. The equation can be recast to give \bar{V}_{δ} as

$$\bar{V}_\delta = \bar{V} \left(1 - 2\pi y_o \frac{\theta}{A} \right) \quad (4.58)$$

Therefore the quantities in the bracket on the right hand side of the equation can be taken as the velocity reduction factor due to the presence of the viscous force. Similarly from the definition of the displacement thickness, the flow rate is reduced to

$$\dot{m}_\delta = \dot{m}_t \left(1 - 2\pi y_o \frac{\delta^*}{A} \right) \quad (4.59)$$

where \dot{m}_δ is the mass flow rate including the boundary layer.

CHAPTER 5

NUMERICAL SOLUTION

5.1. SUMMARY

In the preceding chapter the conservation equations governing the liquid-gas adiabatic two-phase flow were derived from first principles. It is evident that these equations constitute a system of coupled first-order non-linear ordinary differential equations. These differential equations, once solved, can be used to fully describe the flow conditions through the flow channel under consideration.

Nonetheless, application of the two-phase flow equations to the analysis of a specific problem leads to great mathematical complexity in all but the simplest circumstances. It is generally not possible to obtain analytical solutions for practical problems in two-phase flow. For this reason, it has been necessary to develop numerical solution techniques for use with high speed computers. The Euler type integration schemes were often used by previous investigators. With these schemes the flow field was divided into a series of computational steps. At each computational step the differential equations were solved using those properties at the step inlet and the corresponding local derivatives of the variables were obtained. The values of the derivatives so determined were then applied over the whole step to obtain the properties at the exit of this step. This process was repeated until a termination criterion was reached.

Such an approach, described in detail elsewhere, immediately raises questions concerning accuracy. The numerical errors introduced by such approximations are of several different kinds. One arises from coarseness of resolution, and can be mitigated by the use of a step scale that is fine compared with the spatial scale for appreciable changes in the field variables. However the negative effect of this change is the increase in the consumption of computational time. Another is numerical instability, in which the calculated results oscillate around the desired solution with increasing amplitude, or otherwise drift away from the desired results. The well-known Runge Kutta method, despite its fourth order accuracy, may also run into numerical instability because of its 'explicit' nature.

In what follows an 'implicit' type finite difference scheme is presented which can avoid the aforementioned numerical difficulties. The main difference between the two schemes lies in the fact that, with the implicit scheme the properties at the exit of each computational cell are also involved in the iteration process while they are not in the previous scheme. Furthermore the discretization equations are obtained by integrating the differential equations over a control volume formed with two neighbouring computational grid points rather than from a Taylor series expansion approach. This method permits a larger computational step to be taken without affecting stability.

5.2. DERIVATION OF THE DISCRETIZATION EQUATIONS

This section is concerned with transforming the conservation equations into a form suitable for numerical solution. This is achieved by replacing the differential equations with difference equations. The difference equations are then solved for a finite number of computational cells which represent the entire flow field.

The basic concept can best be illustrated in Fig.5.1. The spatial domain of interest is divided into a series of connected control volumes or computational cells. As indicated in the figure, a one-dimensional channel has been subdivided into a total number of $N-1$ computational steps with grid point 1 coinciding with the channel inlet and N the channel exit. The grid points are related to the axial distance Z along the flow path by

$$Z_1 < Z_2 < \dots < Z_i < \dots < Z_N$$

and each step size can be calculated by taking the difference of the axial positions of the two neighbouring grid points.

It should be emphasised that for the grid points shown above, it is not necessary that the step sizes are equal. Indeed, the use of nonuniform grid spacing is often desirable, for it enables the grid points to be concentrated in regions where pressure gradients are likely to be steep and so enhance economy. The number of grid points needed for given accuracy and the way they should be distributed in the calculation domain are matters which depend on the nature of the problem to be solved.

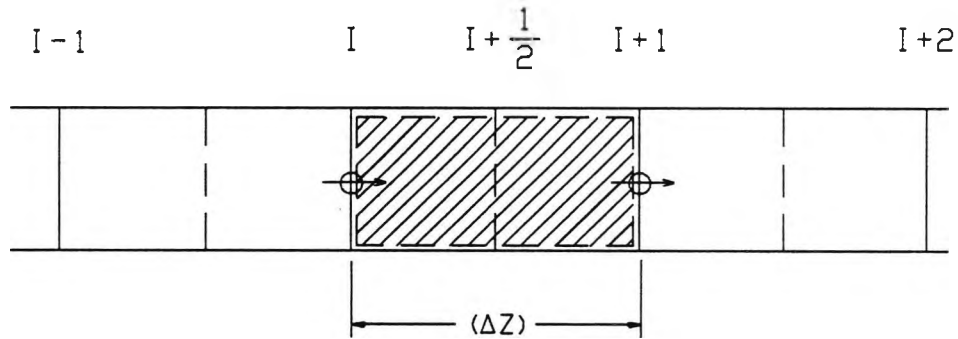


Fig.5.1. Discretisation of Flow Field

An algebraic, finite-difference counterpart of the differential equation will now be derived for the representative cluster of grid points. The procedure is as follows: firstly the differential equations will be integrated, as far as formal calculus allows, over the control volume from grid point i to its forward neighbouring grid point $i+1$ and with a step size ΔZ . Then the remaining integrals can be replaced by algebraic approximations. In the solution process, the pressure P , mass-weighted mixture velocity \bar{V} , slip ratio s , dryness fraction x and liquid temperature T_L are conveniently chosen as a set of primary dependent variables.

At this point, it is convenient to introduce a new dimensionless parameter s known as the slip ratio in two-phase flow. The introduction of the slip ratio makes the discretisation equations more compact. Slip ratio is one of those parameters which distinguish

two-phase flow from single phase flow. There are two types of definition for it in the literature. Some investigators use it as the ratio of vapour velocity to liquid velocity. Others use it as the ratio of the slip velocity to the mass-weighted two-phase mixture velocity. The latter definition is chosen in this study and is expressed as

$$s = \frac{V_G - V_L}{\bar{V}} \quad (5.1)$$

where \bar{V} has been defined and used in the previous chapter.

1. The Momentum Equation for a Two-Phase Mixture

The momentum equation for a two-phase mixture evaluated in the last chapter can be rewritten here as

$$A \frac{dP}{dZ} + \dot{m}_G \frac{dV_G}{dZ} + V_G \frac{d\dot{m}_G}{dZ} + \dot{m}_L \frac{dV_L}{dZ} + V_L \frac{d\dot{m}_L}{dZ} = 0 \quad (5.2)$$

It was known from the last chapter that the mass-weighted two-phase mean velocity \bar{V} is related to the liquid and gas velocities by

$$\dot{m}_t \bar{V} = \dot{m}_G V_G + \dot{m}_L V_L \quad (5.3)$$

Differentiation of the above equation with respect to the independent variable Z leads to the following relationship

$$\dot{m}_t \frac{d\bar{V}}{dZ} = \dot{m}_G \frac{dV_G}{dZ} + V_G \frac{d\dot{m}_G}{dZ} + \dot{m}_L \frac{dV_L}{dZ} + V_L \frac{d\dot{m}_L}{dZ} \quad (5.4)$$

And the total flow area A can be expressed as the sum of the individual flow areas occupied respectively by the liquid and gas phases, i.e.

$$A = A_L + A_G = \frac{\dot{m}_L}{\rho_L V_L} + \frac{\dot{m}_G}{\rho_G V_G} \quad (5.5)$$

Furthermore, given the slip ratio s defined by Eqn.(5.1) and the dryness fraction x , the two individual velocities V_L and V_G can be related to the two-phase velocity \bar{V} as

$$V_L = (1 - xs)\bar{V} \quad (5.6)$$

$$V_G = [1 + (1 - x)s]\bar{V} \quad (5.7)$$

Hence if Eqn.(5.6)-(5.7) is substituted into Eqn.(5.5), it takes the following form

$$A = \left[\frac{1 - x}{\rho_L(1 - xs)} + \frac{x}{\rho_G[1 + (1 - x)s]} \right] \frac{\dot{m}_t}{\bar{V}} \quad (5.8)$$

Combine the Eqn.(5.4) with Eqn.(5.2) and then replace the flow area A in the resulting equation with Eqn.(5.8). After rearrangement the momentum equation for two-phase mixture can be recast as

$$\bar{V} \frac{d\bar{V}}{dZ} + \left[\frac{1 - x}{\rho_L(1 - xs)} + \frac{x}{\rho_G[1 + (1 - x)s]} \right] \frac{dP}{dZ} = 0 \quad (5.9)$$

To obtain the finite difference form of the momentum equation, Eqn.(5.9) is integrated over the control volume under consideration,

as previously described. With reference to Fig.5.1, the integration limit is from Z to $Z + \Delta Z$. Thus

$$\int_Z^{Z+\Delta Z} \left\{ \bar{V} \frac{d\bar{V}}{dZ} + \left[\frac{1-x}{\rho_L(1-xs)} + \frac{x}{\rho_G[1+(1-x)s]} \right] \frac{dP}{dZ} \right\} dZ = 0 \quad (5.10)$$

It is not difficult to find that the above equation can be conveniently rearranged as follows

$$\int_{\bar{V}}^{\bar{V}+\Delta\bar{V}} \bar{V} d\bar{V} + \int_P^{P+\Delta P} \left[\frac{1-x}{\rho_L(1-xs)} + \frac{x}{\rho_G[1+(1-x)s]} \right] dP = 0 \quad (5.11)$$

The evaluation of the first integral is quite straightforward. In the process of evaluating the second integral, all quantities are taken outside the integral and evaluated at the step mid-position (denoted by the subscript m). With this in mind, performing the integration in the above equation and rearranging leads to the finite difference form of the mixture momentum equation as follows

$$\Delta \bar{V}^2 = -2 \left[\frac{(1-x_m)}{\rho_{L_m}(1-x_m s_m)} + \frac{x_m}{\rho_{G_m}[1+(1-x_m s_m)]} \right] \Delta P \quad (5.12)$$

2. The Energy Equation for a Two-Phase Mixture

In a similar manner, the energy equation for a two-phase mixture derived in Chapter 4 can be simplified with the help of the dryness fraction to the following form

$$\left[h_{LG} + \frac{1}{2}(V_G^2 - V_L^2) \right] \frac{dx}{dZ} + x \left[\frac{dh_G}{dZ} + V_G \frac{dV_G}{dZ} \right] + (1-x) \left[C_L \frac{dT_L}{dZ} + \frac{1}{\rho_L} \frac{dP}{dZ} + V_L \frac{dV_L}{dZ} \right] = 0 \quad (5.13)$$

which is then integrated over the control volume under consideration

$$\int_Z^{Z+\Delta Z} \left\{ \left[h_{LG} + \frac{1}{2}(V_G^2 - V_L^2) \right] \frac{dx}{dZ} + x \left[\frac{dh_G}{dZ} + V_G \frac{dV_G}{dZ} \right] + (1-x) \left[C_L \frac{dT_L}{dZ} + \frac{1}{\rho_L} \frac{dP}{dZ} + V_L \frac{dV_L}{dZ} \right] \right\} dZ = 0 \quad (5.14)$$

On performing the indicated integration, as was done for the two-phase momentum equation, and rearranging by moving Δx to the left hand side of the obtained equation, we have

$$\Delta x = - \frac{1}{h_{LG_m} + \frac{1}{2}(V_{G_m}^2 - V_{L_m}^2)} \left[x_m (\Delta h_G + \frac{1}{2} \Delta V_G^2) + (1-x_m) (C_{L_m} \Delta T_L + \frac{1}{\rho_{L_m}} \Delta P + \frac{1}{2} \Delta V_L^2) \right] \quad (5.15)$$

which is the finite difference form of the energy equation for two-phase mixture.

3. The Droplet Drag Equation

The drag equation for liquid droplets derived in Chapter 4 can be simplified by using the slip ratio to

$$\rho_L V_L D \frac{dV_L}{dZ} + D \frac{dP}{dZ} - \frac{3}{4} \rho_G C_{Ds} |s| \bar{V}^2 = 0 \quad (5.16)$$

It was known that $V_L = (1 - xs) \cdot \bar{V}$. Differentiation of it with respect to Z leads to the relationship

$$\frac{dV_L}{dZ} = (1 - xs) \frac{d\bar{V}}{dZ} - x\bar{V} \frac{ds}{dZ} - s\bar{V} \frac{dx}{dZ} \quad (5.17)$$

By substituting the relationship for dV_L/dZ into Eqn.(5.16), the droplet drag equation now takes the following form

$$\rho_L V_L D \left[(1 - xs) \frac{d\bar{V}}{dZ} - x\bar{V} \frac{ds}{dZ} - s\bar{V} \frac{dx}{dZ} \right] + D \frac{dP}{dZ} - \frac{3}{4} \rho_G C_{Ds} |s| \bar{V}^2 = 0 \quad (5.18)$$

This differential equation is integrated over the control volume from Z to $Z + \Delta Z$

$$\int_Z^{Z+\Delta Z} \left\{ \rho_L V_L D \left[(1 - xs) \frac{d\bar{V}}{dZ} - x\bar{V} \frac{ds}{dZ} - s\bar{V} \frac{dx}{dZ} \right] + D \frac{dP}{dZ} - \frac{3}{4} \rho_G C_{Ds} |s| \bar{V}^2 \right\} dZ = 0 \quad (5.19)$$

Evaluating the integral expression and then rearranging Δs to the left hand side of the resulting equation, we have

$$\Delta s = \frac{1 - x_m s_m}{2\bar{V}_m^2 x_m} \Delta \bar{V}^2 - \frac{s_m}{x_m} \Delta x + \frac{1}{\rho_{Lm} (1 - x_m s_m) \bar{V}_m^2 x_m} \Delta P - \frac{3\rho_{Gm} C_{Dm} s_m |s_m|}{4\rho_{Lm} D_m (1 - x_m s_m) x_m} \Delta Z \quad (5.20)$$

which is the finite difference form of the droplet drag equation.

4. The Droplet Heat Transfer Equation

The heat transfer equation for liquid droplets derived in the last Chapter is simply carried over as

$$\dot{m}_L C_L \frac{dT_L}{dZ} + h_{LG} \frac{d\dot{m}_G}{dZ} - \frac{6h\dot{m}_L(T_G - T_L)}{\rho_L D V_L} = 0 \quad (5.21)$$

which can be modified by substituting $\dot{m}_L = (1 - x)\dot{m}_t$ and $\dot{m}_G = x\dot{m}_t$. After making further rearrangement, the above equation becomes

$$(1 - x)C_L \frac{dT_L}{dZ} + h_{LG} \frac{dx}{dZ} - \frac{6h(1 - x)(T_G - T_L)}{\rho_L D(1 - xs)\bar{V}} = 0 \quad (5.22)$$

which can then be integrated over ΔZ

$$\int_Z^{Z+\Delta Z} \left\{ (1 - x)C_L \frac{dT_L}{dZ} + h_{LG} \frac{dx}{dZ} - \frac{6h(1 - x)(T_G - T_L)}{\rho_L D(1 - xs)\bar{V}} \right\} dZ = 0 \quad (5.23)$$

Upon integrating the equation over the control volume and solving for ΔT_L , we have

$$\Delta T_L = \frac{1}{C_{L_m}} \left[\frac{6h(T_{G_m} - T_{L_m})\Delta Z}{\rho_{L_m} D(1 - x_m s_m)\bar{V}_m} - \frac{h_{LG_m} \Delta x}{1 - x_m} \right] \quad (5.24)$$

which is the finite difference form of the droplet heat transfer equation.

5. The Boundary Layer Momentum Integral Equation

The last equation to be discretised is the boundary layer momentum integral equation. The equation derived in last chapter can be directly carried over and integrated over the control volume from Z to $Z + \Delta Z$ as follows

$$\int_Z^{Z+\Delta Z} \left\{ \frac{d\theta}{dZ} - C_{fL} \frac{\rho_L (1 - xs)^2 \bar{V}^2}{2\dot{m}_t} (1 - \alpha) + \theta \left[\frac{16}{7\bar{V}} \frac{d\bar{V}}{dZ} - \frac{1}{A} \frac{dA}{dZ} + \frac{1}{y_o} \frac{dy_o}{dZ} \right] \right\} dZ = 0 \quad (5.25)$$

After evaluating the integral expressions, we have the following equation

$$\Delta\theta = C_{fL_m} \frac{\rho_{L_m} (1 - x_m s_m)^2 \bar{V}_m^2}{2\dot{m}_t} (1 - \alpha_m) \Delta Z + \theta_m \left[\frac{16}{7\bar{V}_m} \Delta\bar{V} - \frac{\Delta A}{A_m} + \frac{\Delta y_o}{y_{o_m}} \right] = 0 \quad (5.26)$$

which is the finite difference form of the boundary layer momentum integral equation.

5.3. SOLUTION PROCEDURE

With the finite difference form of the governing differential equations in hand, the solution can be achieved numerically from grid point 2 forward to the last grid point N . However, the nature of the problem constitutes an initial value problem, i.e. the flow conditions at grid point 1 which corresponds to the port inlet must be specified beforehand in order to initiate the solution procedure.

What can be classified as initial values for the solution under consideration include the following quantities: initial pressure P_0 , initial liquid velocity V_{L0} and temperature T_{L0} , initial gas velocity V_{G0} , initial dryness fraction x_0 and droplet diameter D_0 . For the sake of simplicity it is postulated that the thermodynamic and hydrodynamic equilibrium condition between the two phases is satisfied at the flow channel inlet. Consequently, the inlet liquid and vapour temperatures are readily available as the saturation temperature corresponding to the specified initial pressure.

Besides the initial values discussed above, the solution procedure requires that the channel geometry should be specified too. For those with a circular cross section, it can be prescribed as a variation of the channel diameter with the axial distance which is measured from the port inlet. Whereas for flow channels of a non-circular shape, the channel diameter should be replaced by its hydraulic mean diameter. Having said this, it should be noted that we will be faced with a problem of finding an optimum inlet port profile in the following chapter. In this case the flow channel geometry is not known a priori but forms part of the numerical solution procedure. For the sake of differentiation the former is referred to as the geometry specified mode and the latter the geometry optimised mode.

The solution procedure adopted in the analysis can be best illustrated by selecting an arbitrary computational step, say from grid point i to grid point $i+1$. Let it be further assumed that the computation has progressed successfully to the grid point i and all

the quantities at this point have been determined. The work is to determine the quantities at its forward grid point $i+1$. For this purpose the following steps are employed:-

1. The starting point for the numerical solution procedure is to make an initial guess of the variable changes across the computational step under consideration for iteration. Which are selected as primary variables for direct involvement in the iteration depends to a greater degree on if the flow channel geometry is prescribed or is to be optimised. In the geometry specified mode, the following variables: pressure, liquid velocity, liquid temperature and vapour mass flow rate are iterated. Whereas in the geometry optimised mode the liquid velocity, liquid temperature, vapour velocity and vapour mass flow rate are iterated. A reasonable initial guess of the variable changes for the computational step from grid point i to $i+1$ is based on that of the computed variable changes in the immediate preceding computational step from grid point $i-1$ to i . The initial guesses of the variable changes are denoted by subscript *guess*.

2. On the basis of the initial guesses of the variable changes, the primary variable values at grid point $i+1$ can be calculated from the following relationship

$$\begin{aligned}
 V_L(i+1) &= V_L(i) + (\Delta V_L)_{guess} \\
 \dot{m}_G(i+1) &= \dot{m}_G(i) + (\Delta \dot{m}_G)_{guess} \\
 P(i+1) &= P(i) + (\Delta P)_{guess} \\
 T_L(i+1) &= T_L(i) + (\Delta T_L)_{guess}
 \end{aligned}$$

which is valid for the geometry specified mode. While for the geometry optimised mode the relationship

$$V_G(i+1) = V_G(i) + (\Delta V_G)_{guess}$$

should take the place of the pressure relationship. Those other than the above primary variables, can be calculated by the relevant relationship. It follows that the quantities at the step mid-position can be obtained as arithmetic mean of the quantities at the grid points i and $i+1$ by assuming a linear variation across the step. They are in turn used to evaluate the auxiliary properties appearing in the discretisation equations, such as drag coefficient and latent heat.

3. The differential equations in the finite difference form, i.e. Eqns. (5.12), (5.15), (5.20) and (5.24) are solved by substituting in the right hand side of the equations all the quantities having the subscript m with the above calculated values at the step mid-position. As regards the step variable changes appearing on the right hand side of the equations, the guessed variable changes should be used. It should be noted that the droplet diameter D is an exception, which is assumed to be constant throughout the whole computational step under consideration. To be specific, the Weber number is computed at the start of the step using the values obtained from the preceding step. If this newly calculated Weber number is found to be less than the critical Weber number, the droplet diameter remains unchanged from the last step. If a critical breakup is found to have occurred, a new droplet diameter is calculated from the breakup criterion and prevails throughout the computational step.

4. The solution of the finite difference equations leads to a new set

of variable changes which are, to distinguish them from those initial guessed variable changes, denoted by a subscript *cal*. At this point, a functional FNORM is defined as follows:

$$FNORM = \sum_{n=1}^4 FF^2(n) \quad (5.27)$$

where

$$\begin{aligned} FF(1) &= (\Delta V_L)_{guess} - (\Delta V_L)_{cal} \\ FF(2) &= (\Delta \dot{m}_G)_{guess} - (\Delta \dot{m}_G)_{cal} \\ FF(3) &= (\Delta P)_{guess} - (\Delta P)_{cal} \\ FF(4) &= (\Delta T_L)_{guess} - (\Delta T_L)_{cal} \end{aligned}$$

if the computation is in the geometry specified mode. While for the geometry optimised mode, FF(3) is

$$FF(3) = (\Delta V_G)_{guess} - (\Delta V_G)_{cal}$$

Obviously the functional FNORM is a square sum of the differences of the guessed variable changes and their corresponding calculated variable changes. Given a set of guessed variable changes, there is a set of calculated variable changes and subsequently FNORM. It is noted that both FNORM and all its components $FF^2(n)$ ($n=1, \dots, 4$) must always be positive or, at the extreme, zero. It follows therefore that a necessary condition for the functional FNORM to be rendered zero is that each $FF(n)$ ($n=1, \dots, 4$) in Eqn.(5.27) must be zero. In other words, the guessed variable changes are equal to their corresponding calculated ones, which means that the required iteration has converged. Thus the functional FNORM being zero is used as a convergence criterion for the required iteration.

5. If the convergence criterion is not satisfied, then the newly obtained calculated variable changes are used as a new set of guessed variable changes and the iteration returns to steps 2-4. This process is repeated until the solution converges. Nonetheless, this direct iteration algorithm is not an efficient way of achieving convergence and is not usually used. We noticed within step 4 that the solution procedure is in fact a standard problem in the field of non-linear programming and several numerical algorithms are well-established in the literature. A well-known algorithm is that based on the simplex (Secant) method and is adopted in this solution procedure. It has the advantage over other methods in that it is reliable and there is no need for tedious evaluation of variable derivatives. The details of this algorithm can be found in Appendix B.

6. Once the convergence criterion is satisfied, the computation at the current step is terminated and the quantities at the exit of the step become known. With these essential quantities for free-stream flow the boundary layer momentum integral equation Eqn.(5.26) is then solved, resulting in the boundary layer momentum thickness and the displacement thickness at the grid point. The velocity obtained above from free-stream flow theory is then modified to take account of the boundary layer effect. Up till this point the computation at the current step from grid point i to grid point $i+1$ is completed and the calculation proceeds to next computational step.

7. The above processes are repeated until the computation reaches the port exit. At this point it can be said that the solution procedure is completed. However for critical flow rate more work is required.

The critical flow rate is the maximum flow rate that can be attained in a given flow channel under given flow conditions at the inlet and the pressure at the exit. Therefore if a mass flow rate is too large, the computation would not be able to reach the port exit. Based upon this a numerical search routine is devised to iterate the choking flow rate. To start with, a mass flow rate is estimated, eventually causing choking at the port exit plane. Fig.5.2 illustrates the block diagram of this search routine.

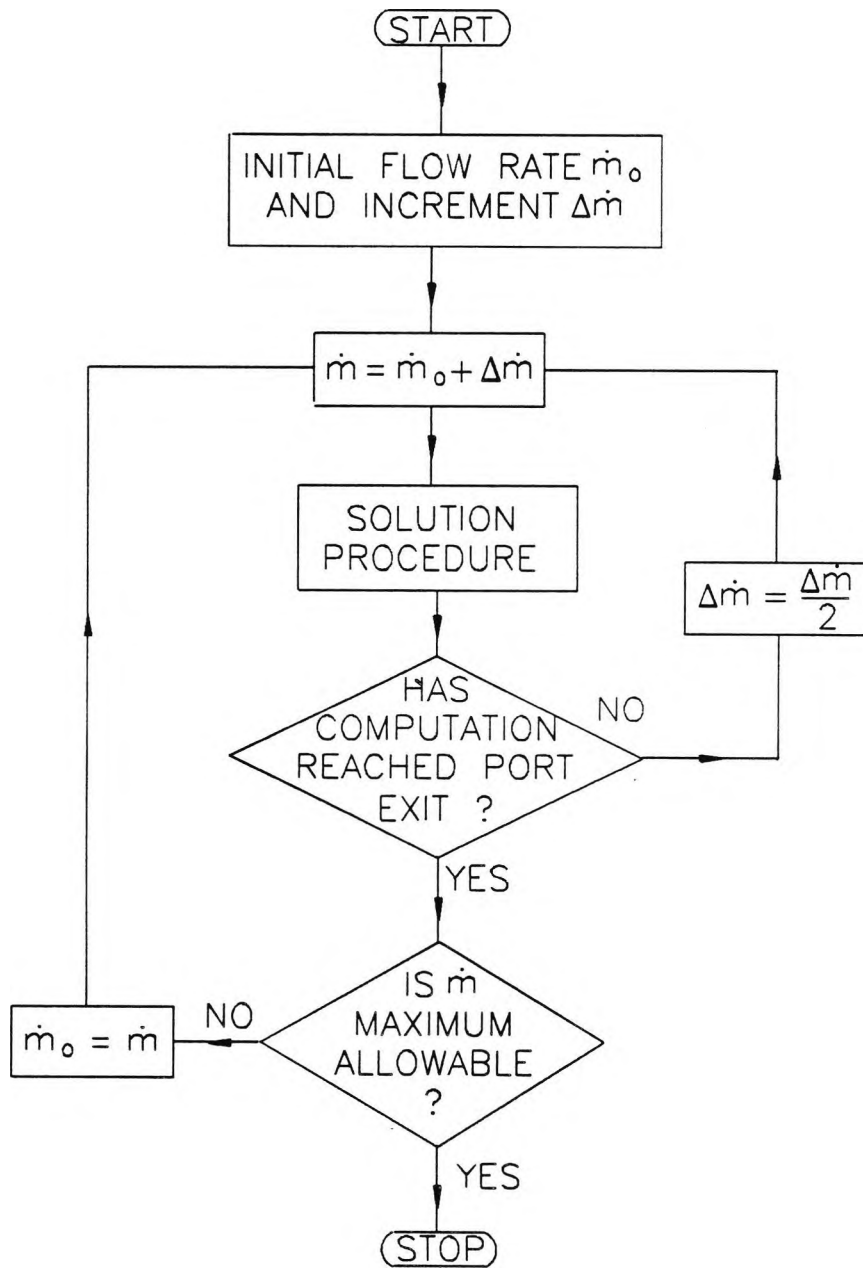


Fig.5.2. Block Diagram of Choking Flow Rate Search

CHAPTER 6

INLET PORT DESIGN AND OPTIMISATION

6.1 SUMMARY

As was previously pointed out, one of the main objectives of this investigation was to establish a strategy for optimal design of the inlet port profile. In the preceding two chapters two-phase flow of the liquid and gas through the inlet port was analysed and a numerical solution procedure was established. With the flow field equation solved we are in a position to embark upon the inlet port design and optimisation.

The importance of having a sound mathematical foundation for the optimisation method to be chosen was recognised at the outset of this investigation. It was found that the problem in question fits in with a well-known isoperimetric problem in the classical calculus of variations. The calculus of variations technique has been used widely in the rocket engine industry for the maximum-thrust nozzle design. To be more specific, the concept of maximum-thrust nozzle design subject to an isoperimetric constraint was originally introduced by Guderley and Hantsch [1955]. Then, a greatly simplified version of the procedures, which makes use of special properties of the functions involved, was achieved by Rao [1958]. More recently Guderley & Armitage [1965] formulated the problem for the design of conventional axisymmetric nozzles using a more general approach which permits selection of the geometric constraint. The additional potential of the Guderley-Armitage approach was realised when the

method was extended by Hoffman and Thompson [1967] to include the effects of gas-particle flows, and by Hoffman [1967] to include the effects of non-equilibrium reacting flows. The use of the method in the design of thrust nozzles with water and nitrogen as the working fluid was due to Elliott [1968]. A detailed examination of these various works showed that their main difference is in the computation of the basic flow field and not in the method itself.

The layout of the present chapter is as follows. Firstly, a brief introduction to the theory of calculus of variations is made, which provides a necessary theoretical background for the formulation of the one-dimensional optimisation problem with particular application to two-phase flow in the inlet port of a Lysholm screw expander. This is then used to generate an optimum inlet port profile under a specified flow condition and subject to an isoperimetric constraint. The last section deals with geometrical transformation in which the optimum inlet port obtained is modified to take into account the geometrical constraints set by the screw expander rotor.

6.2. THE THEORY OF THE CALCULUS OF VARIATIONS

In contrast to the ordinary theory of maxima and minima the calculus of variations is concerned with the maxima and minima of a functional expression where an entire function must be determined. Thus the unknown of the calculus of variation is not a discrete number of points but rather a discrete number of curves, surfaces or hypersurfaces, depending on the nature of the problem.

6.2.1. Solution of the Simplest Problem

The simplest problem of the calculus of variations in one independent variable is concerned with the extremization of a particular type of functional, that is, a line integral having the form

$$I(T) = \int_{x_i}^{x_f} F(x, T, \dot{T}) dx \quad (6.1)$$

where x denotes the independent variable, T the dependent variable and \dot{T} the derivative dT/dx . F is an arbitrarily specified function of the arguments x , T and \dot{T} and is called the fundamental function. The subscripts i and f refer to the initial and final points, respectively. The formulational procedure is to determine the function $T(x)$, hence the function $F(\cdot)$ that extremizes $I(T)$. The methodology is formal (Weinstock [1952]) and requires the definition of a one-parameter family of function $\phi(x)$ that lies arbitrarily close to the solution $T(x)$. A convenient form is

$$\phi(x) \equiv T(x) + \varepsilon \cdot \Phi(x) \quad (6.2)$$

where $\Phi(x)$ is arbitrary in $x_i < x < x_f$, but $\Phi(x_i) = 0 = \Phi(x_f)$, and ε is a parameter that controls the "closeness" of $\phi(x)$ and $T(x)$ for each $\Phi(x)$. Specifically, for all $\Phi(x)$, there is a value of $-\varepsilon_0 \leq \varepsilon \leq \varepsilon_0$ such that the distance between $\phi(x)$ and $T(x)$ may be made arbitrarily small, i.e.,

$$|\phi(x) - T(x)| < \delta \quad (6.3)$$

where δ is (arbitrarily) small.

Determining the extremum of $I(T)$ in Eqn.(6.1) is now replaced by seeking the stationary value of $I(\phi, \epsilon)$

$$I(\phi, \epsilon) \equiv \int_{x_i}^{x_f} F(x, \phi(\epsilon), \phi_x(\epsilon)) dx \quad (6.4)$$

with respect to the arbitrary parameter ϵ . It is important to note that once the functional form is achieved, the distance between $\phi(x)$ and $T(x)$ vanishes on setting $\epsilon = 0$. Therefore, the formulation statement is

$$\left. \frac{dI}{d\epsilon} \right|_{\epsilon=0} \equiv 0 \quad (6.5)$$

Using Eqn.(6.4) and (6.2), and noting that the limits of integration are constants, Eqn.(6.5) becomes

$$\begin{aligned} \left. \frac{dI}{d\epsilon} \right|_{\epsilon=0} &= \int_{x_i}^{x_f} \left[\frac{\partial F}{\partial \phi} \frac{\partial \phi}{\partial \epsilon} + \frac{\partial F}{\partial \phi_x} \frac{\partial \phi_x}{\partial \epsilon} \right] dx \\ &= \int_{x_i}^{x_f} \left[\frac{\partial F}{\partial \phi} \Phi(x) + \frac{\partial F}{\partial \phi_x} \frac{d\Phi}{dx} \right] dx \\ &= \int_{x_i}^{x_f} \left[\frac{\partial F}{\partial \phi} - \frac{d}{dx} \left(\frac{\partial F}{\partial \phi_x} \right) \right] \Phi(x) dx + \left. \frac{\partial F}{\partial \phi_x} \Phi(x) \right|_{x_i}^{x_f} \end{aligned} \quad (6.6)$$

The final form in Eqn.(6.6) is achieved by means of integration by parts. The last term vanishes identically, as $\Phi(x_i) = 0 = \Phi(x_f)$. Since $\Phi(x)$, $x_i < x < x_f$, is completely arbitrary, Eqn.(6.6) can be rendered zero in a general way only if the integrand in brackets vanishes identically. Then setting $\epsilon = 0$ in Eqn.(6.2) yields that the extremum of $I(T)$ occurs for $F(\bullet)$ satisfying the partial differential equation

$$L(F) = \frac{\partial F}{\partial T} - \frac{d}{dx} \left[\frac{\partial F}{\partial T_x} \right] = 0 \quad (6.7)$$

which is the well-known Euler-Lagrange equation, a necessary condition for Eqn.(6.1) to be rendered an extremum. Its general solution has the form

$$T = T(x, C_1, C_2) \quad (6.8)$$

where the constants C_1 and C_2 must be determined so that the extremum function satisfies the prescribed end points.

For completeness, the multidimensional Euler-Lagrange equation is written as

$$L(F) = \frac{\partial F}{\partial T} - \nabla \cdot \left[\frac{\partial F}{\partial (\nabla T)} \right] = 0 \quad (6.9)$$

which determines the function $F(\mathbf{x}, T, \nabla T)$ that corresponds to the extremum of

$$I(T) = \int_{R^n} F(\mathbf{x}, T, \nabla T) d\mathbf{x} \quad (6.10)$$

where R^n is the n-dimensional region spanned by the \mathbf{x} (x_i , $1 \leq i \leq n$) coordinate system.

6.2.2. Solution of the Isoperimetric Problem

The isoperimetric problem of the calculus of variations in one independent variable is a modification of the simplest problem

discussed above and is concerned with the extremization of the functional

$$I(T) = \int_{x_i}^{x_f} f(x, T, \dot{T}) dx \quad (6.11)$$

subject to an isoperimetric constraint which is

$$K = \int_{x_i}^{x_f} \phi(x, T, \dot{T}) dx \quad (6.12)$$

where f and ϕ are functions of the arguments within the parentheses and K denotes an arbitrarily specified constant. It is noted that the isoperimetric constraint is one of a rather loose nature, since it affects the choice of $T(x)$ integrally rather than locally. Obviously, there exist infinite $T(x)$ which yield the prescribed value for the integral in Eqn.(6.12). Of these it is desired to find that particular one which extremizes the functional in Eqn.(6.11).

The solution to such a problem can be found by employing an undetermined constant λ , called a Lagrangian multiplier. To be precise, multiplying Eqn.(6.12) by the Lagrangian multiplier and then summing it with Eqn.(6.11) the following relationship is formed

$$I' = \int_{x_i}^{x_f} f(x, T, \dot{T}) dx + \lambda \left[\int_{x_i}^{x_f} \phi(x, T, \dot{T}) dx - K \right] \quad (6.13)$$

It is known from the variational theory that if the function $T(x)$ is chosen to be consistent with the isoperimetric constraint

expressed by Eqn.(6.12), the behaviour of the functional in Eqn.(6.13) is identical with that of the functional in Eqn.(6.11) irrespective of the value attributed to the Lagrangian multiplier. In other words, the problem of extremizing the functional Eqn.(6.11) subject to the constraint of Eqn.(6.12) is identical with that of extremizing the functional Eqn.(6.13) subject to the same constraint. Hence the extremal problem is ultimately equivalent to the extremization of the functional

$$I' = \int_{x_i}^{x_f} F(x, T, \dot{T}) dx \quad (6.14)$$

in which the fundamental function F is a linear combination of the integrands of the functional being extremized and the isoperimetric constraint

$$F = f + \lambda \phi \quad (6.15)$$

Because of the analogy between the functional expressed by Eqn.(6.14) associated with the isoperimetric problem and that associated with the simplest problem, the extremum of $I(T)$ occurs for $F(\bullet)$ satisfying Euler-Lagrange equation. Therefore Eqn.(6.15) can be substituted into Eqn.(6.7) leading to the following general solution

$$T = T(x, C_1, C_2, \lambda) \quad (6.16)$$

where C_1 and C_2 are integration constants as in the simplest problem. If these constants are determined in such a way that the boundary conditions are satisfied, it can be shown that they obey the following functional relationships

$$C_1 = C_1(\lambda) \quad C_2 = C_2(\lambda) \quad (6.17)$$

Hence it follows that the ensemble of curves which are consistent with the Euler-Lagrange equation and the boundary conditions, but not necessarily with the isoperimetric constraint, is the one-parameter family

$$T = T(x, \lambda) \quad (6.18)$$

The particular value of the Lagrange multiplier which defines the extremum should be determined in such a way that it satisfies the isoperimetric constraint. The extension of the treatment to the case of several isoperimetric constraints is immediate and is omitted for the sake of brevity.

6.3. INLET PORT OPTIMISATION PROBLEM FORMULATION

In the previous two-phase flow analysis through an inlet port, it was clear that with a pressure field known, the velocity field can be directly obtained by solving the momentum equations. Thus the pressure can be conveniently employed as an independent variable when the optimisation problem involves both pressure and velocity field calculation. This was tackled as an inverse problem by Marble [1963]. With this in mind, the optimisation problem for two-phase flow in an inlet port can be stated as follows. Given the pressures at port inlet and the exit, what axial pressure distribution would produce the maximum thrust for a port of fixed length?

The thrust from an inlet port is defined as

$$I = \frac{1}{2} \dot{m}_t V_e^2 \quad (6.19)$$

where V_e is two-phase mixture mean velocity at the inlet port exit, which can be attained by integration of Eqn.(5.9) over the pressure range from the inlet to the exit, i.e.

$$V_e^2 = V_i^2 + \int_{P_i}^{P_e} \left[\frac{1-x}{\rho_L(1-xs)} + \frac{x}{\rho_G[1+(1-x)s]} \right] dP \quad (6.20)$$

where the subscripts i and e have been used to denote the values of variables at the port inlet and exit, respectively. As the inlet velocity V_i is small relative to the exit velocity, it is often ignored. Thus the above equation can be substitute into Eqn.(6.19) leading to a functional

$$I = \frac{1}{2} \dot{m}_t \int_{P_i}^{P_e} \left[\frac{1-x}{\rho_L(1-xs)} + \frac{x}{\rho_G[1+(1-x)s]} \right] dP \quad (6.21)$$

It is evident that the main cause of the thrust losses in the inlet port is the interfacial shear stress or drag resulting from the liquid and gas phase slip. Therefore Eqn.(6.21) may be written as

$$I = C \int_{P_i}^{P_e} f\left[P, s(P), \frac{ds}{dP}\right] dP \quad (6.22)$$

in which

$$f\left[P, s(P), \frac{ds}{dP}\right] = \frac{1-x}{\rho_L(1-xs)} + \frac{x}{\rho_G[1+(1-x)s]} \quad (6.23)$$

Having defined the functional to be optimised it is necessary to consider the constraints imposed on the optimisation. In the current problem it is an isoperimetric constraint which may be written as

$$L = \int_{P_i}^{P_e} \phi\left[P, s(P), \frac{ds}{dP}\right] dP \quad (6.24)$$

in which the integrand has the following expression

$$\phi\left[P, s(P), \frac{ds}{dP}\right] = \frac{4D}{3\rho_G|s|sC_D\bar{V}^2} \left[1 + \frac{1}{2}\rho_L(1-xs)^2 \frac{d\bar{V}^2}{dP} - \rho_L x(1-xs)\bar{V}^2 \frac{ds}{dP} - \rho_L(1-xs)s\bar{V}^2 \frac{dx}{dP} \right] \quad (6.25)$$

It is obtained by integrating the droplet drag equation over the pressure range from P_i to P_e .

The functional as expressed by Eqn.(6.22) is of the general form appropriate for treatment by the techniques of elementary variational methods. Consider the pressure distribution as unknown, and ask for the distribution function $s(P)$ that leads to the maximum thrust for the expansion ratio P_i/P_e subject to the isoperimetric constraint as expressed by Eqn.(6.24).

However numerical estimates show that for most cases of practical interest the variations in both dx/dP and ds/dP are slow over a small

increment in a two-phase inlet port. Consequently the expression for ϕ can be simplified by dropping the two terms containing dx/dP and ds/dP without loss of accuracy. Hence

$$\phi[P, s(P), \frac{ds}{dP}] = \frac{4D}{3\rho_G |s| s C_D \bar{V}^2} \left[1 + \frac{1}{2} \rho_L (1 - xs)^2 \frac{d\bar{V}^2}{dP} \right] \quad (6.26)$$

As was discussed in the previous section, the optimum solution to this isoperimetric problem can be found by constructing a fundamental function

$$F = f + \lambda \phi \quad (6.27)$$

and subsequently solving the Euler - Lagrange equation Eqn.(6.7) with P replacing x and s replacing T respectively. Since both functions f and ϕ do not involve the term ds/dP but only $s(P)$, the Euler - Lagrange equation is just

$$\frac{\partial F}{\partial s} = 0 \quad (6.28)$$

Upon substituting the required expressions into this equation and performing the indicated differentiation, the optimum slip ratio $s_o(P)$ is given implicitly in the following cubic equation

$$s_o^3 + \lambda \frac{4\rho_L(1 - xs)^2 D}{3\rho_G \bar{V}^2 C_D} \left[\frac{cx(1 - x)s_o + bC'_D}{2x(1 - x)(a - 1)} \right] = 0 \quad (6.29)$$

where

$$a = \frac{(1 - xs)^2 \rho_L}{[1 + (1 - x)s]^2 \rho_G} \quad (6.30)$$

$$b = \frac{x(1 - xs)^2 \rho_L}{[1 + (1 - x)s] \rho_G} + (1 - x)(1 - xs) - 1 \quad (6.31)$$

$$c = a \left[\frac{2[1 + (1 - x)s]x}{(1 - xs)(1 - x)} + 1 \right] + 1 \quad (6.32)$$

and

$$C'_D = 1.0 \quad Re \leq 0.1611 \quad (6.33)$$

$$C'_D = 1.1107 + 0.06854 \ln Re + 0.004329 \ln^2 Re \quad (6.34)$$

$$0.1611 < Re \leq 4.709 \times 10^3$$

$$C'_D = 2.0 \quad Re > 4.709 \times 10^3 \quad (6.35)$$

The above equation has been incorporated in our solution procedure and is referred to as the geometry optimised mode. A brief mention of it was made in the last chapter. Within this mode Eqn.(6.29) is used to replace the droplet drag equation for the slip ratio. At each grid point the equation is solved numerically by a bisectional method for solution of non-linear equations. The droplet drag equation is instead combined with the continuity equation for two-phase mixture to produce the inlet port contour corresponding to this optimum slip ratio. More specifically, the droplet drag equation Eqn.(5.20) is rearranged to give the increment in axial distance ΔZ as follows

$$\Delta Z = \frac{4D}{3\rho_{G_m}|s_m|s_m C_{D_m} \bar{V}_m^2} \left[\Delta P + \frac{1}{2} \rho_{L_m} (1 - x_m s_m)^2 \Delta \bar{V}^2 - \rho_{L_m} x_m (1 - x_m s_m) \bar{V}_m^2 \left(\frac{s_m \Delta s}{x_m} + \Delta s \right) \right] \quad (6.36)$$

while the channel cross-sectional area is calculated from the continuity equation

$$A = \left[\frac{1-x}{\rho_L(1-xs)} + \frac{x}{\rho_G[1+(1-x)s]} \right] \frac{\dot{m}_t}{\bar{V}} \quad (6.37)$$

The application of the optimisation routine to a particular design problem is the main task of the following section.

6.4. INLET PORT DESIGN PROCEDURE

The optimisation equation established for a two-phase inlet port was used to design an inlet port for a new Lysholm screw expander to replace the original reversed compressor used in the TCU test facility. The rotors of this new Lysholm screw expander were 163.2 mm in diameter and 269.28 mm in length. The flow conditions on which the design was based were chosen to be identical with that projected in the new Lysholm screw expander operating at its design condition. This was obtained from a computer program which analysed the performance limits imposed by the boiler and feed pump on the experimental trilateral flash cycle system in the TCU thermodynamics test laboratory. Details of the feed pump and its characteristics can

be found from Figs.7.3 and 7.4. in the following chapter. To summarise, the flow condition for the inlet port design is listed below:

Total mass flow rate	=	14.55	kg/s
Static pressure at inlet	=	7.0611	bar
Dryness fraction at inlet	=	0.0739	
Mixture velocity at exit	=	20.0	m/s

In parallel with the current inlet port study, a layout design of the new Lysholm screw expander was carried out by a designated screw manufacturer. Fig.6.1 is a schematic of this layout design from which a framework for the inlet port size could be ascertained. It shows that the required inlet port could not exceed 445 mm in length and that its inlet diameter was confined to 4 inch I.D. More importantly, because of the meshing requirement of the male and female rotors, the port exit cross section is irregular in shape as shown in Fig.6.2 instead of circular. These constraints had to be considered in the inlet port design.

To start with, the design of a circular inlet port was performed based on the method presented in the previous section. As described in Chapter 5, the programme was first set to the geometry optimised mode for port profile and as such, required the input of a Lagrange multiplier apart from the flow condition specified. Furthermore, an initial droplet diameter of 0.2 mm was prescribed which would cause eventual droplet critical breakup in the flow channel. It should be noted that the Lagrangian multiplier used in the programme has the units of acceleration (m/s^2).

The first requirement was to establish the relationship between the efficiency and a port length. For this purpose a series of values of Lagrange multipliers was set out which covered the lengths of practical interest. The results are presented in Fig.6.3 - effect of inlet port length on efficiency and Fig.6.4 - relationship between Lagrange multiplier and port length.

An inspection of the curve in Fig.6.3 reveals that, as the port length is increased starting from about 220 mm, the inlet port efficiency rises accordingly. The trend continues until it reaches a length of about 450 mm. At such a port length, the corresponding efficiency is 89.07%, the highest that could possibly be achieved under the given inlet and exit flow conditions. Beyond this value any further increase in length leads instead to a fall in efficiency. The reason for this is that the losses experienced in the inlet port is the combination of the wall shear stress and the interfacial drag caused by phase slip. Generally speaking, if the inlet port is short then the loss attributed to the phase slip is dominant. Since any increase in length would tend to reduce the phase slip, the efficiency is improved. While in a long inlet port the loss attributed to the wall shear stress is dominant. The longer the flow channel, the greater the effect of the wall shear stress. Therefore any increase in length would tend to reduce the efficiency. In other words, too short a port would have a low efficiency because of large slip, and too long a port would have a low efficiency too because of large wall shear stress. It follows, therefore, that there exists a trade-off between minimising the loss by the phase slip and that by wall shear stress.

At this point, a decision was made as to which inlet port length should be adopted for the current work. It should be remembered that the screw expander layout design restricts the maximum allowable length to 445 mm. At such a value of the port length the efficiency attained is found to be nearly the maximum efficiency 89.07%. With this in mind a decision was made that the port length should be taken as 445 mm. It is known from Fig.6.4 that this corresponds to a Lagrange multiplier of about 42.0 m/s^2 . Taking it as an input to the program, the optimum inlet port contour was obtained and is given in Fig.6.5.

An inspection of the contour indicates some interesting features. Firstly it is observed that the area changes from inlet to exit are fairly smooth, an expected result from the optimisation work aimed at minimising the phase slip. Of more importance is the realisation that the contour can be distinctively divided into two sections in terms of its area variation rate. The first section has a sharp area contraction and is approximately 50 mm long from the inlet. By contrast the second section, which occupies the rest of the contour, has a much more gradual or literally little area variation. On the whole the configuration of the inlet port is convergent.

Having observed the above features of the contour, it was thought that the contour could be modified somehow to turn it into a practical one, which could then be tested in the experiment. In the first place, since the area variation of the second section is small, it might be possible to replace it with a straight line in parallel with the axis. This would make it much easier to manufacture. It was

calculated from Fig.6.2 that the cross-sectional area of the port exit is 4560.0 mm^2 , equivalent to a 3 inch (76.2 mm) I.D. pipe. For this reason, 3 inch I.D was chosen for this section. Secondly it was found that the contour of the first section could be approximated reasonably well by two arcs of equal radius. The dimensions and exact locations of the two arcs can be seen in Fig.6.5. They are arranged in such a way that the second arc is tangent to both the first one and the straight line. This arrangement would eliminate discontinuity in the contour. The final practical inlet port contour obtained is shown in Fig.6.5.

With the final inlet port contour obtained, the remainder of the design process involved examination of its performance under a wide range of flow conditions. As a result, the computer program was then set to the geometry specified mode. A series of area versus axial distance data $A(Z)$ were read off the contour line to make up the input table. Based on the same initial droplet diameter of 0.2 mm, the computational results were obtained and these are given in Table 6.1. It shows in general that the efficiency of the inlet port had not been affected by the proposed modification.

Some typical computational results of the two-phase flashing flow through the inlet port are illustrated in Figs.6.6-6.9. These include the axial static pressure distribution (Fig.6.6), the liquid and gas velocity distribution (Fig.6.7), the axial cross-sectionally averaged void fraction distribution (Fig.6.8) and the droplet diameter distribution (Fig.6.9).

6.5. TRANSFORMATION PROCEDURE

In the preceding section, an inlet port contour was obtained by using optimisation theory to maximise the adiabatic efficiency subject to an isoperimetric constraint. It was then modified from a practical point of view. However it must be remembered that the required inlet port exit is not circular, but the one depicted in Fig.6.2. As a result some further work was needed in order that the designed inlet port could be utilised in the Lysholm screw expander.

This added complication could be resolved by conducting a linear geometrical transformation on the second portion of the circular inlet port already obtained so that both requirements that the inlet is circular while the exit is irregular were satisfied. By linear transformation there is no area variation and hence no difference between the circular and the transformed inlet ports in terms of axial cross-sectional area distribution. It was hoped that judging from this, the flow field in the transformed inlet port would not differ very much from that in the circular inlet port, and that the model developed in Chapter 4 could then be used to predict the flow in this inlet port. For convenience of description the circular inlet port is referred to as No.1 inlet port, while the one yet to emerge from linear transformation is referred to as No.2 inlet port.

The main reason that the second section was selected for transformation is that it is long compared to the first section. It was expected that the geometrical variation would be smooth. With reference to Fig.6.1, the inlet and exit planes are not in parallel

to each other. For this reason the transformation process was divided into two stages: transformation between two parallel cross sections was conducted first; It was then extended to the situation when the two planes are not in parallel.

6.5.1. Transformation between Two Parallel Cross Sections

The linear transformation of geometry between two parallel cross sections is shown schematically in Fig.6.10. The two sections are of equal area and L length apart in space. The left one is denoted 1-1 with its centroid at O_1 . Similarly, the right one is denoted 2-2 with its centroid at O_2 . The straight line linking the two centroids O_1O_2 is perpendicular to both cross sections and represents the axis of the flow channel. In the process of transformation, both Cartesian and cylindrical coordinate systems are employed. Since the shape of both cross sections are prescribed, any points on the respective perimeters can be expressed explicitly using either of the coordinate system.

The process in which an intermediate cross section is generated by means of linear transformation can be illustrated by employing an arbitrary plane a-a. It rotates around O_1O_2 from 0° to 360° . As the cross section 1-1 and 2-2 are parallel, it is obvious that this plane is perpendicular to both cross sections. Let's assume for the moment that the rotational angle θ relative to the abscissa X is between 0° and 90° . As shown in the diagram, plane a-a intersects cross section 1-1 at A_1 and cross section 2-2 at A_2 . A quadrilateral $O_1A_1A_2O_2$ is then formed within a-a.

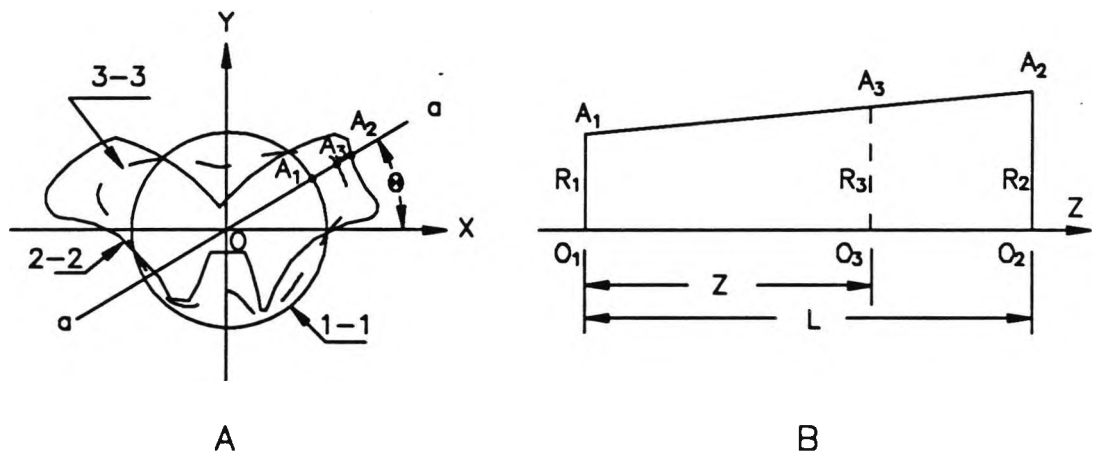


Fig.6.10. Transformation between Two Parallel Cross Sections

It is further assumed that the intermediate cross section of interest, denoted 3-3, lies at a distance Z from 1-1. As shown in Fig.6.10, line A_1A_2 intersects the cross section at A_3 . It follows that this point is one of the desired point on the intermediate cross section, and that the task is to find its coordinate. With reference to Fig.6.10(A), A_1 and A_2 are expressed in cylindrical coordinate as $(\theta, R_1, 0)$ and (θ, R_2, L) , while A_3 is expressed as (θ, R_3, Z) . As 1-1 and 2-2 are given the two radius R_1 and R_2 are known. The only unknown parameter is R_3 -the radius of the point A_3 .

The radius R_3 can easily be determined by examining the geometrical relation revealed in Fig.6.10(B). Mathematically it can be expressed as:

$$\frac{\overline{O_3A_3} - \overline{O_1A_1}}{\overline{O_1O_3}} = \frac{\overline{O_2A_2} - \overline{O_1A_1}}{\overline{O_1O_2}} \quad (6.38)$$

or

$$\frac{R_3 - R_1}{Z} = \frac{R_2 - R_1}{L} \quad (6.39)$$

from which R_3 can be written in terms of R_1 and R_2 as:

$$R_3 = R_1 + \frac{R_2 - R_1}{L} Z \quad (6.40)$$

This relation forms the basis for the linear transformation of geometry between two parallel cross sections. To obtain any cross section situated at a distance Z , the plane $a-a$ is rotated for a full circle from 0° to 360° . Corresponding to each angle θ , R_1 and R_2 can be determined. Then using Eqn.(6.40) R_3 is evaluated. In this way a sufficient number of points can be generated and hence the shape of the intermediate cross section required.

6.5.2. Transformation between Two Nonparallel Cross Sections

The transformation process can now be extended to where the two cross sections are not parallel but inclined to each other by a small angle α . As shown in Fig.6.11, the left cross section 1-1 is perpendicular to the axis O_1O_2 with an inclination angle α with respect to the horizontal, whereas the right cross section is in the vertical position. It is obvious that the relationship obtained in the previous section is no longer applicable. To circumvent this

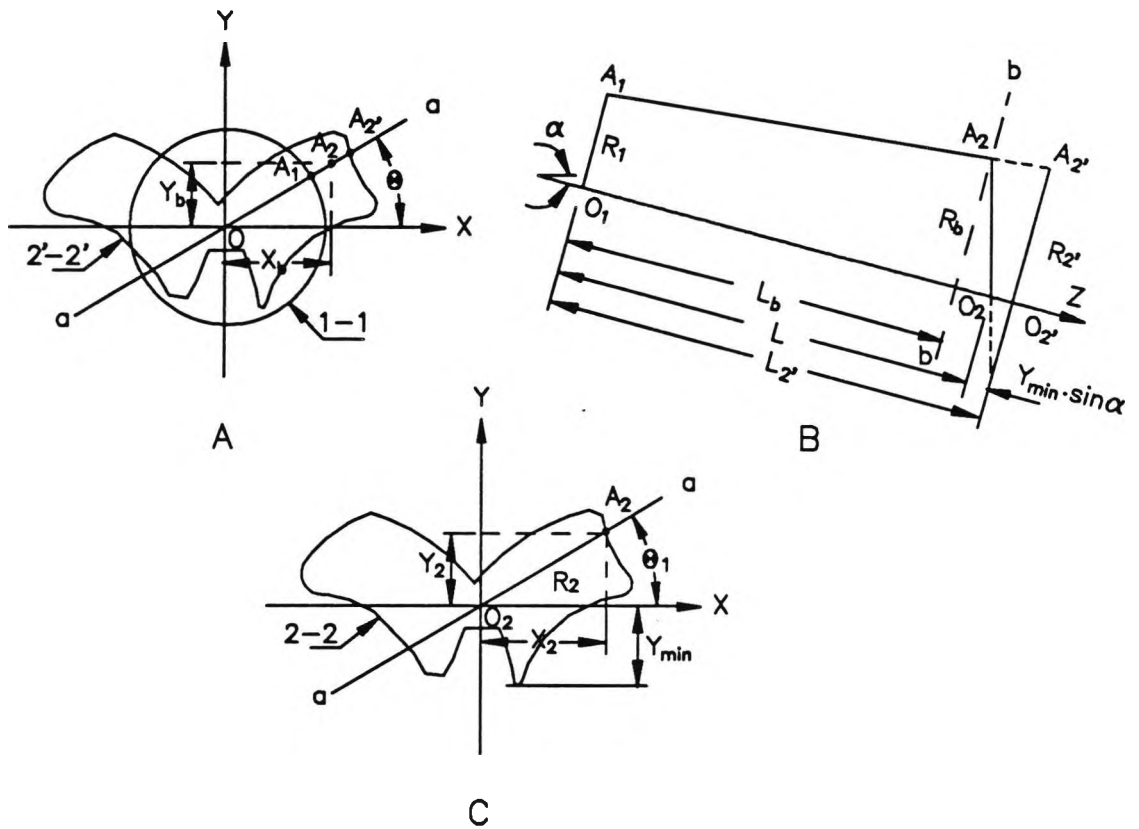


Fig.6.11. Transformation between Two Nonparallel Cross Section

difficulty, the cross section 2-2 is first projected onto a plane parallel to 1-1. The main problem is to find a suitable plane onto which 2-2 can be projected. It is found that the most convenient and suitable plane is the one which passes through the lowest point on 2-2 (measured in terms of its Y coordinate) but is also normal to the axis O_1O_2 . It is denoted 2'-2' in Fig.6.11.

As in Part 1, an arbitrary plane a-a is employed to rotate about the axis O_1O_2 . At an angle θ it intersects 1-1 at point A_1 and 2-2 at A_2 respectively. If a straight line is drawn such that it not only passes through A_1 and A_2 , but also intersects $2'-2'$, then this intersection point must be a point of the projected cross section $2'-2'$. For consistency this point is designated as A_2' . It is clear that its coordinates need to be determined.

As the geometrical relationship in Fig.6.11 shows, the plane a-a is perpendicular to both 1-1 and $2'-2'$, but not to 2-2. Thus it follows that the angle formed between the intersection line O_2A_2 and the X axis is not equal to θ . If this angle is denoted as θ_1 , then the following relations hold:

$$\begin{cases} X_2 = R_2 \cdot \cos \theta_1 \\ Y_2 = R_2 \cdot \sin \theta_1 \end{cases} \quad (6.41)$$

where (X_2, Y_2) and (R_2, θ_1) are the Cartesian and cylindrical coordinates of A_2 in plane 2-2. Since the cross section 2-2 is prescribed, there exists a unique R_2 corresponding to each angle θ_1 and hence X_2, Y_2 .

It should be noted that as plane a-a rotates around the axis, the angle θ_1 varies with θ . It is important to determine the relationship between the two angles. For this purpose another plane b-b is employed to pass through A_2 while perpendicular to the axis O_1O_2 . If it is further assumed that the coordinate of A_2 is (X_b, Y_b) in plane b-b, they can be expressed in terms of its X and Y coordinates in

plane 2-2 as:

$$\begin{cases} X_b = X_2 = R_2 \cdot \cos \theta_1 \\ Y_b = Y_2 \cdot \cos \alpha = R_2 \cdot \sin \theta_1 \cdot \cos \alpha \end{cases} \quad (6.42)$$

and

$$L_b = L - X_2 \cdot \sin \theta_1 \cdot \sin \alpha \quad (6.43)$$

where L_b is the distance between 1-1 and b-b.

In view of the fact that b-b is perpendicular to O_1O_2 and A_2 is a point within it, it must be true that if a line is drawn from A_2 perpendicularly towards O_1O_2 , this line must be contained within b-b as well. As a matter of fact, it is the intersection line of the two planes a-a and b-b. The angle of the line with respect to the X axis in b-b is θ . Hence one can write

$$\theta = \arctan \frac{Y_b}{X_b} = \arctan(\tan \theta_1 \cdot \cos \alpha) \quad (6.44)$$

$$R_b = \sqrt{X_b^2 + Y_b^2} = R_2 \sqrt{\cos^2 \theta_1 + \sin^2 \theta_1 \cdot \cos^2 \alpha} \quad (6.45)$$

where R_b is the radius of point A_2 from point O_2 in plane b-b.

On the basis of the above preparatory work, the point A_2' can be located in relation to A_1 and A_2 . As all the following lines O_1A_1 , $A_1A_2A_2'$, $O_2'A_2'$ and $O_2'O_1$ are all in the plane a-a, their relationship can be readily seen in Fig.6.11(B). If R_1 is again used for line O_1A_1 while R_2' for $O_2'A_2'$, the following linear relation exists:

$$\frac{R_{2'} - R_1}{L_{2'}} = \frac{R_b - R_1}{L_b} \quad (6.46)$$

where

$$\begin{aligned} L_{2'} &= \overline{O_1O_2} + Y_{min} \cdot \sin \alpha \\ &= L + Y_{min} \cdot \sin \alpha \end{aligned} \quad (6.47)$$

It should be noted that Y_{min} in the above equation is the minimum absolute Y coordinate of all the points on the cross section 2-2. Upon some manipulation and substitution one can write

$$\begin{aligned} R_{2'} &= \frac{R_b - R_1}{L_b} (L + Y_{min} \cdot \sin \alpha) + R_1 \\ &= \frac{R_b - R_1}{L - R_2 \cdot \sin \theta_1 \cdot \sin \alpha} (L + Y_{min} \cdot \sin \alpha) + R_1 \end{aligned} \quad (6.48)$$

Eqn.(6.48) and Eqn.(6.44) form the basis for projecting the cross section 2-2 to plane 2'-2' and the procedure can be described as follows: In the cross section 2-2 an angle θ_1 is set out and then its corresponding radius R_2 is determined. Using Eqn.(6.44) the angle θ can be evaluated. This in turn produces a radius R_1 from the cross section 1-1. Then Eqn.(6.48) can be utilised to give $R_{2'}$. Hence the projected point of cross section 2-2 on plane 2'-2' can be located. If the angle θ_1 is rotated continuously for a full circle, the whole cross section 2-2 can then be projected onto plane 2'-2'.

With the cross section 2-2 projected to a plane parallel to the

cross section 1-1, the remainder of the transformation simply involves determining any intermediate cross section between two parallel cross sections, as described in section 6.5.1.

CHAPTER 7

EXPERIMENTAL DETAILS

7.1. SUMMARY

Two inlet port designs were built in order to evaluate the accuracy of the design procedure developed. The first was of circular cross section throughout its length. The second was similar but transformed, as described in Section 6.5, to end in the shape appropriate for a Lysholm screw expander. These were tested in a large closed circuit test loop, modified to accommodate them in place of a complete Lysholm screw expander. A specially designed computer controlled traversing fibre optic probe was used to measure the void fraction distribution at the port exit. A description of the system and its components is given together with the start-up, running and shut-down procedure.

7.2. DESCRIPTION OF THE TEST RIG

Fig.7.1 is a photographic view of the test rig used for the experimental investigation. The corresponding schematic diagram is shown in Fig.7.2. The rig is designed for use with organic working fluids such as common refrigerants and operates in a closed loop. The main components are the feed pump, fluid heater, control valve, test section and condenser. As shown in Fig.7.2, liquid refrigerant passes through the feed pump at around 40°C via a filter drier, where any moisture is removed, to a shell and tube heat exchanger where its temperature is raised to about 110°C by exchanging heat with

saturated steam which condenses on the shell side. The steam is supplied by the laboratory boiler at 14 bar and 195°C and is throttled as necessary to obtain the required fluid temperature. The hot liquid then proceeds to the control valve where it is throttled to the required pressure and dryness fraction before flowing into the test section in which it expands in the test section. It is then condensed by exchanging heat with cooling water in the condenser. The condensed refrigerant finally returns to the feed pump where the cycle begins again.

The test rig is accommodated in the Thermo-Fluids Engineering Research Centre Main Engine Testing Laboratory, City University. It is constructed on two levels so that the heat exchangers, pumps and auxiliary fittings are located in a basement area while the items to be tested are set up in a test cell, on the floor above, to which the hot high pressure fluid was admitted and from which the expanded fluid is returned. The rig construction material is largely carbon steel and the piping is assembled using flange type fittings to the relevant British Standards. The primary pipework bores ranges between 1" and 8" for various sections of the circuit.

The working fluid used in the experiment was Refrigerant 113 (Trichlorotrifluoroethane), which has a critical temperature of 214.1°C and a critical pressure of 33.7 bar. Its molecular weight is 187.39. The test rig was designed for a maximum working fluid temperature of 150°C. The normal operating pressure of the system was less than 7 bar.

Details of the main components of the rig are as follows:

7.2.1. Main Feed Pump

The main feed pump is of the CEHQ type and supplied by Sihi-Ryaland Pumps Ltd. As shown in Fig.7.3, the CEHQ pump combines a centrifugal suction stage impeller with one or more self-priming lateral channel stages. The suction branch is arranged in the horizontal plane with the discharge branch arranged vertically. The rotating element is carried on a substantial shaft which is manufactured in 13% chrome steel or special alloy steel. The shaft runs in an external grease lubricated ball bearing at the drive end and in well-dimensioned internal sleeve bearing positioned behind the suction stage. The material used for the impeller is gunmetal, while the casing and bearing frame is cast iron.

The designed flow rate of the feed pump is 21.24 m^3 per hour and a graph of the pump characteristics is given in Fig.7.4. It exhibits an inverse relationship between the required discharge pressure and the fluid flow rate through the pump. It can be seen that the discharge pressure is in the range of 6 to 20 bar gauge. The feed pump is driven by a motor with a rated power input of 37 KWe and at a standard speed of 1450 rpm. The whole unit, comprising the feed pump and the motor, is bolted to a steel frame on the basement floor.

7.2.2. Fluid Heater

The heater is a shell and tube heat exchanger with a rated

capacity of 600 kWth. The fluid flows horizontally inside the tubes and is heated by steam supplied to the outside of the tubes. The type of heater used is BEU and has 4 passes. The fluid temperature at the heater exit is regulated by the amount of the steam supplied by the gas fired laboratory boiler. The designed heating duty of this boiler is 900kWth.

7.2.3. Flow Control Valve

A 2 inch Type 767-EB series Fisher "plus bore" valve is fitted upstream of the test section to control the flow. It is air operated and is designed for process flow control applications. It is of air-to-open operation and a conventional spring-opposed diaphragm actuator operating from a 3-15 lb/in (0.21-1.03bar) regulated supply controls its movement. The valve is fitted with a V-ported plug which has a modified parabolic characteristic and seats onto a replaceable seat ring giving a shut-off flow of 0.1% of valve capacity. The valve gland packing consists of the well-proven Fisher spring loaded PTFE V-rings with PTFE and felt wiper rings for extended life. The Bonnet which supports the actuator yoke is rigidly bolted to the valve body and sealed by a fully retained gasket. The constructional material is carbon steel.

7.2.4. Condenser

Like the fluid heater, the condenser is of shell and tube heat exchanger design of the BEU type. It is employed for the cooling of the primary fluid after it leaves the test section. Heat removal is

to the cooling water which circulates inside the tubes. The rated capacity of the condenser is 600 KWth. Because the boiling and condensing heat transfer coefficients are large, the unit is relatively compact.

7.3. DESCRIPTION OF THE INLET PORTS

Two experimental inlet ports were built with contours as described in Chapter 6. They had identical area versus axial distance distribution but different exit cross sectional shapes. For convenience of description they are denoted as No.1 and No.2 inlet port respectively. Their details are as follows:

Fig.7.5 is a scale drawing of No.1 inlet port with detailed dimensions. The material is carbon steel. As shown in the drawing, the inlet port has an entrance diameter of 4" from which it gradually converges to a diameter of 3" over an axial distance of 1.94" from the port inlet. This is then followed by a straight pipe section of 3" diameter bore. The length of the straight section, as measured from the two centres, is 405 mm. Throughout its whole length the cross section of No.1 inlet port is circular. Fig.7.1 shows No.1 inlet port in-situ on the test rig.

Fig.7.6 is a schematic drawing of No.2 inlet port. It has the same converging section as No.1 inlet port. However this is followed by a transformed section which is also 405 mm long. Here its cross section is gradually changed from circular at the inlet to an irregular one at the exit. The procedure for obtaining intermediate

cross sections was given in the previous chapter. Due to the complexity of its cross sectional shape, No.2 inlet port was cast using a wood pattern, which was hand made from the drawings generated using the transformation procedure. The casting was carried out by the Stockton Casting Co.Ltd and the construction material is SG iron to BS.2789 GR:420/12. A 6" flange (BS1560:Part 2:1970) was cast at each end. Fig.7.7 shows No.2 inlet port in-situ on the test rig.

These figures also show the location of the pressure tapplings provided for the measurement of pressure profile along each of the ports. In all, seven pressure tapplings of 4.0 mm inner diameter were drilled at the bottom of the test section with axes perpendicular to the wall which, if extended, would intersect the pipe centre line. At the point of break-through the hole was circular. The edges were flush with the internal surface of the pipe wall and made as sharp as possible. To ensure the elimination of all burrs or wire edges at the inner edge, rounding was permitted but was kept as small as possible. No irregularity was allowed to appear inside the connecting hole, on the edges of the hole drilled in the pipe wall, or on the pipe wall close to the pressure tapping.

7.4. INSTRUMENTATION

The following parameters were measured or monitored during the test programme, to provide experimental data for comparison with the theoretical analysis:

1. System Pressures
2. System Temperatures

3. Working fluid flow rate
4. Local void fraction distribution at the port exit
5. Cooling water flow rate

The detailed location of each measurement can be seen in Fig.7.2, and the instrumentation employed for measuring the above parameters is described below.

7.4.1. System Pressures

The system pressures at various locations around the test loop were measured by the strain-gauge type pressure transducers. They operate by detection of flexing of a diaphragm to which the system fluid has access through the tapping hole. The pressure transducers employed in the experiment had a sensitivity of about 0.3% full scale and a response time of 10-100 μ s. The maximum working temperature was approximately 160 °C. The locations where the pressure measurements were made can be found in Figs.7.2, 7.5 and 7.6.

Generally speaking, pressure transducers can be categorised into two groups according to whether they are used for measuring absolute pressure or differential pressure. As its name suggests, the absolute pressure transducer can produce a straightforward absolute pressure value at the point of measurement and has the advantage of being direct. However, elaborate calibration is usually required for it in order to maintain accuracy. As a result, it is sometimes more convenient and accurate to use a differential pressure transducer, referenced to a common source. Both types of pressure transducers

were used in the test and were initially calibrated by means of a dead weight tester, the pressure being sampled and calculated with a FORTRAN programme run on a Compulog Four data logger. Frequent calibration of pressure transducers was considered necessary because of the possibility of a significant change in their characteristic which could have been caused by excessive pressures. The measurement ranges as well as the errors of the pressure transducers used are tabulated in Table 7.1. It was found that their accuracies were within ± 0.01 bar.

7.4.2. System Temperatures

The system temperatures at various locations were measured using platinum resistance temperature detectors (RTD) of the Pt.100 wire-wound type. Inside this the platinum winding was partially supported by a high temperature adhesive, inside a ceramic tube. The specification was based on BS1907 (provisional 1980) & DIN43760-1980. The lead was sheathed with 6 mm diameter stainless steel braid and sealed in the test rig with a stainless steel compression union of sliding fitting. The temperature element was duplex, i.e. a type "T" thermocouple plus a Pt.100 RTD. The RTD's tolerance band for this application was Band 5 in tolerance grade Class "A". Therefore the temperature measurement can be accurate to within $\pm 0.1^{\circ}\text{C}$. However it must be borne in mind that they were used to measure bulk temperatures and on this basis the measured values were probably accurate to only ± 0.25 to $\pm 0.5^{\circ}\text{C}$.

7.4.3. Working Fluid Flow Rate

A turbine flow meter was installed upstream of the heater for the measurement of volumetric flow rate through the system. A flow meter of this type is considered to be insensitive to changes in the density of flowing fluid. The flow meter is type M9F/1500/250B and manufactured by Bestobell Meterflow Ltd. The materials are stainless steel BS970-316S16 throughout, with the exception of the rotor which is BS2S143 stainless steel, and bearings which are of the Tungsten carbide high chrome/high cobalt journal type, unlubricated. According to the manufacturer, the M9 type meters are intended for use on general purpose application and where maximum bearing life is required. Prior to being dispatched water calibration was carried out as standard on the manufacturer's own calibration rig. The normal metering range is from 15 I.G.P.M.(Imperial Gallon Per Minute) min. to 150 I.G.P.M. max. The allowable operating temperature range is between -15°C to $+175^{\circ}\text{C}$. It has a response time better than 0.05 sec. A full flow filter drier set was fitted upstream of the flow meter to protect the meter from large foreign bodies or excessive quantities of particles. The meter was calibrated to within $\pm 1.0\%$ accuracy according to the manufacturers data sheet.

7.4.4. Cooling Water Flow Rate

The cooling water flow rate in the condenser was measured using an orifice plate. The geometry of the orifice plate used in this test is 45.06 mm diameter orifice and 102.26 mm pipe diameter. The pressure tappings adopted for this flow meter are in accordance with

the standard corner tapings by which the flow calculation was based on BS1042(1981). The maximum flow which could be measured was 25,000 KG/hr. The maximum pressure differential permitted was specified to be 250 mbar. The flow had a tendency to fluctuate with this meter but the readout was on a time average basis. As a consequence, the accuracy of the measurement was in the order of $\pm 1\%$.

7.4.5. Local Void Fraction

It was revealed in the literature survey that a fibre optic probe was best suited for the local void fraction measurement in a non-conductive fluid. Hence it was adopted in the current experimental investigation. It was further recognised at the very outset of the experimental preparation that to scan the entire port exit cross section manually would be both complex and time consuming. Moreover the fluid of interest was a refrigerant which had to be retained in a completely sealed containment. A remotely controlled automatic traversing system was considered to be the best means of fast scanning under these conditions. For this reason a probe traversing system was designed and constructed for the experiment.

7.4.5.1. Fibre Optic Probe

The probe used was a modified version of a standard unit made by RBI of Grenoble, France. It used a single fibre with a tip diameter of 50 μm and had a response of less than 0.1 μs . The probe was made according to the specifications given in Fig.7.8. As shown in the diagram, the rigid stainless steel casing which retains the fibre is

10 mm in diameter and 250 mm in length to enable the probe to be attached to its traversing system well downstream of the plane of measurement. This is followed by a 700 mm long flexible sheathed cable which is leak proof. A 1 inch bore flange is fitted at its end to ensure that no leakage of refrigerant is possible. It is bolted to a corresponding flange welded to a 90 degree bend of a 4" pipe.

A constant 5V DC electric supply was provided to the optic probe light source and the signal developed from it was processed on line by a high speed signal processing module installed in one of the free slots of an IBM/AT type computer. The program for this operation was written in Pascal and assembly language. The executable code of the program was named MEASURE.EXE after it was successfully compiled and linked. The output of the program was the integrated void fraction over various time intervals ranging from 1 to 100 seconds.

The probe was pressure tested up to 15 bars and calibrated by the manufacturer before delivery. The maximum fluid velocity in the flow channel was restricted to 30 m/s with recommendation that the incidence angle between the probe axis and the main flow should not exceed 15° with respect to the horizontal. This was considered necessary to avoid physical damage to the tip of the probe. It was further recommended that the turbulence level in the test region should not be too high. The fluid used had also be perfectly clean, with no solid particles larger than 50 μm present. For this reason a fine filter was fitted prior to the test section for screening out dry particles.

7.4.5.2. Probe Traversing System

The complete probe traversing system comprised a mechanical traversing unit, a stepper motor controller unit and a microcomputer. A photographic view of the system, with the fibre optic probe unit included, is given in Fig.7.9.

Fig.7.10 is a front view of the mechanical traversing unit used to move the probe across the test section. The overall dimension of the unit is 450x395x120 mm and was originally designed to accommodate an 8" bore pipe to measure the void fractions across the new Lysholm screw expander exit. In the current experiment, however, only 4" and 6" bore pipes were used. Flange fittings were therefore provided to allow for these reduced diameters. The construction material of the unit was carbon steel except for the shafts and the bevel gears which were of stainless steel. Based on a stress analysis, the wall thickness of the unit was chosen to be 20 mm so that it could withstand up to 22 bar pressure, in accordance with the rig safety requirement.

The operation of the mechanical traversing unit can be described with the aid of Fig.7.10. As shown in the figure, the probe movement is controlled by two horizontal shafts. The upper is a screw shaft which moves the probe holder horizontally, while the lower is a spline shaft, which rotates a vertical screw shaft via a pair of bevel gears to move the holder up or down along a pair of guide rods on which it slides. Each drive shaft is rotated by a separate externally mounted stepper motor and leakage between it and the

casing is prevented by a pair of lip seals. By combining the motions of the two motors it was possible to traverse the probe to any position within a cross section of up to 8 inch diameter. The probe holder assembly is comprised of three main components, namely a screw shaft carriage, a probe holder carriage and a bevel gear carriage. The dimensions of the three components are given in Fig.7.11.

To minimise friction and backlash between the screw and nut, ball bearing screw and spline shafts were chosen on the assumption that rolling friction is much less than of sliding. It led to smaller motors, smaller drive components and above all less power than with the conventional screw shaft. It also provided the system stiffness required for accuracy and reliability. The top shaft (Model R-0502) has a nominal diameter of 0.5 inch and 0.5 lead. With every turn of the shaft, the ball nut moves horizontally by 0.5 inch. Since the probe holder is fixed to it, the probe would traverse horizontally the same distance. The vertical shaft (Model R-0308) has a nominal diameter of 3/8 inch and 0.125 lead. Hence every turn would cause the probe to traverse vertically by 0.125 inch. The tooth ratio of the bevel gears was 1:2, thereby with every turn of the spline shaft the probe would traverse vertically by 0.25 inch.

Fig.7.12 is a schematic of the stepper motor controller unit. It shows that the unit is made up of two stepper motors, a stepper motor controller and a microcomputer. The two stepper motors were supplied by McLennan Servo Supplies Ltd. and both were of their 34HS Series. The 34HS series stepper motor is bi-directional and has a 0.9° (1.8° optional) step angle with a tolerance within 5.0%. The selection of

correct motors was important, since too small a motor would not provide the required torque while too a big motor would considerably increase cost and size. It depended largely on the starting torque needed to overcome load and friction caused by the seal assembly and bevel gears. When the unit had been assembled, the starting torques were measured. This was done by attaching a torque arm of fixed length to each shaft and then increasing the load on the arm incrementally until the shaft was just about to rotate. It was found that the starting torque was 97.5 Ncm for vertical movement and 10.1 Ncm for horizontal movement. Based on these measurement results, the two motors selected were a type 34HS109 for No.1 motor and a type 34HS311 for No.2 motor. The former can provide a torque up to 100 Ncm, while the latter can provide a torque up to 300 Ncm. Both were fitted with a 5:1 reduction gearhead to reduce the speed and provide the desired performance margin. As R-113 might dissolve oil off the drive in operation, the friction would be higher and hence higher working torques might be needed. The precision with which the probe holder traversed in both directions was found to be within 1.0 mm for every 100.0 mm of traverse.

All instructions to the stepper motors from the computer were handled and translated by a McLennan stepper motor controller which consists of a PM214 RS232 serial interface, a PM212 Intelligent data buffer (IDB), a channel select module, a power supply unit and two PM164 motor translators. The modules were supplied in kit form and were subsequently mounted on a standard 19 inch EURORACKS with the power supply unit occupying the upper deck and the rest the lower deck. A 19 inch packflat instrument case was used to hold the rack

and a small fan (Radio Spares) was provided inside the rear of the case for cooling purpose. Each component was connected in accordance with the diagram given in Fig.7.13. The controller was interfaced to a serial port (COM1) of an IBM/AT computer via an RS232 link. The link was fitted with a 15 pin RS232 female plug on the controller side, and a 25 pin RS232 male plug on the computer side. The two motors were connected to the controller by screwing the coloured motor leads to the correct motherboard sockets as shown in Fig.7.13.

The PM212 IDB unit was a microprocessor based module capable of interpreting and executing the instructions initiated from the microcomputer, and then instructing the motors to carry out the right movement. It was provided with 8 preset trimmers which could be used to select eight different motor rotational speeds, up to a maximum rate of 20,000 steps/sec. The speed '0' represented the fastest speed and the speed '7' the slowest. When a speed setting of '0' to '6' was selected the IDB started the motor at the base speed and accelerated it to the desired slew speed. A deceleration programme was provided at the end of each movement to ensure there would be no loss of steps.

The program for control of the stepper motor movement was written in Basic language. It issued a series of movement instructions to the IDB unit. The program was stored in executable format as MOTOR.EXE, which received instructions from a data file MOTOR.DAT. The basic movement instructions given to the computer were in the form of a message which defined:

- i) the axis required

ii) the speed required

iii) the traversing distance required

A summary of the main instructions used is listed below.

INSTRUCTION	FUNCTION
01Z	Initialise the drive axis
01P0	Set the current motor position zero
01W0000	Select No.1 motor as current motor
01W0001	Select No.2 motor as current motor
01S3	Select preset speed '3'
01M500	Move current motor forward 500 steps
01M-500	Move current motor 500 steps in reverse
wait	Pause for a preset period
end	Halt the operation

7.4.5.3. Programming

Fig.7.14 is a block diagram of a complete computer system for use in obtaining local void fractions in the inlet port. All programming operations were carried out on the IBM/AT computer which was equipped with an Intel 80286 main processor and 80287 math co-processor. The computer alternately controlled the traversing unit and high speed signal processing module. The computer had an enhanced graphics card (EGA) and an EGA monitor. The main processor speed was 12 MHz. As mentioned earlier, the stepper motor controller was interfaced to the computer via an RS232 link using COM1 port. In accordance with the switch settings in the controller's PM214 RS232 serial interface, the COM1 was configured to the following parameters: 9600 bps baud rate, even parity, 7 data bits, 1 stop bit. The COM2 port was used by the high speed signal processing module.

The programmings involved were:

1) control the motors to move the fibre optic probe to a

designated point given its coordinates;

- 2) pause for a sufficient amount of time for fluid to settle down;
- 3) process the signal at this point to get the local void fraction, and when it was done, move to next point.

The above operations were repeated until all the points were scanned in the cross section. To achieve these, basically three programs were required and could be described as: motor control, signal processing and coordinating. The first two have been mentioned. The last one, which coordinates the probe traversing and signal processing operations, is the most important in the sense that it would ensure the whole scan could be performed automatically.

Fig.7.15 shows a flow chart of how the probe traversing unit and the signal processing operations were coordinated. The input for this program defined the cross section to be traversed and the coordinates of the points at which void fraction measurements were taken. The program first checked if the controller was connected properly or not. If it did, then a time constant for the fibre optic probe was specified from the keyboard and was stored in a data file TC.DAT. This would later be retrieved for use by the signal processing program MEASURE.EXE. Each time before the probe was traversed to a new point, the program would examine whether the current point was the last one to be scanned. If it was not, then the program MOTOR.EXE was called to move the probe to next point. When the probe had been moved to the required position, the program MEASURE.EXE was called and the signal from the probe was processed for this point. The output was stored in a temporary data file, RESULTAT. It should be noted that the movement instructions were obtained from a data file

MOTOR.DAT which was updated for each point. Since the data file RESULTAT was only temporary and updated at each point, a permanent data file TAPE1 was used to store the output for all the points. As soon as the signal processing was completed at each point, the content of RESULTAT was appended to TAPE1. The above operations were repeated until all the points were scanned.

7.4.6. Data Logging System

All the measurements from the rig, except for the local void fraction, were logged through a Compulog Four data logger system. Compulog Four is a microcomputer based data acquisition and control system made by Intercole Systems Ltd. It was capable of handling up to 80 channels of analog signals and up to 20 status signals from the test rig. The analog signals, developed either from the pressure transducers or from the RTD's etc., were transmitted to the data logger and transformed into a digital signal using built-in digital voltmeters. Each signal was allocated a channel number and connected to the data logger on a one channel per one connector basis. The corresponding relationship between each measurement and channel is given in the instrumentation schedule in Table 7.1.

The data was transferred via an RS232 link to an IBM/AT computer for post processing and storage. Fig.7.16 is a schematic diagram of the complete data logging system used during the rig operation.

7.5. EXPERIMENTAL PROCEDURES

On completion of the rig construction, the unit was thoroughly checked against the piping and instrumentation drawings. All instrument elements were checked against the design data for correctness of location, connection, labelling and range of measurement. Control valves were tested for proper response to their control indices and for proper action on air failure. Moreover, hydrostatic tests were carried out on new or repaired equipment items and pipings to prove the strength of the body materials and welds. These were conducted by filling the equipment involved with liquid and then building up pressure with a portable test pump. Having accomplished this work, the test could be carried out. The following describes the proper procedures for the start up preparation, start up and shut down of the test rig.

7.5.1. Preparations for Start Up

The main work involved in the preparation for start up was to ensure the system was thoroughly dry and clean. Moisture and foreign matter, if present in the system, could seriously damage the equipment, in particular the fibre optic probe unit. The effects of moisture in a system using a halocarbon refrigerant are both mechanical and chemical. Since water is only slightly soluble with halocarbon refrigerants, moisture would generally appear as free water. The moisture absorbed into the refrigerant can combine with the refrigerant to form highly corrosive acids, which can attack internal parts of the system. Air and moisture are closely associated

and when air exists in the system, moisture is usually present. Therefore the presence of moisture within the system must be minimised and as a general rule it is considered desirable to keep the maximum water content to below 4 parts per million at all times. To achieve this requirement, the system is fitted with filter drier units. Steps were taken to minimise the ingress of moisture into the system.

Dehydration, or removal of water or moisture from the system after it had been installed was accomplished by evacuation method. This method consisted basically of applying a deep vacuum to the refrigerant containing portions of the system after the system had been thoroughly leak tested and made pressure tight. During the evacuation procedure, as the pressure within the system was reduced, the vaporising temperature of any water or moisture within the system was also reduced. The heat required to vaporise the water was supplied by the metal of the refrigerant containing portions of the system. At normal conditions a sizable temperature difference exists between these metal temperatures and the boiling points of water under vacuum conditions.

It should be noted, however, that under normal circumstances, a possibility existed for freezing water inside the system. Such moisture of free water might be removed by what was known as the double evacuation procedure. In this method, the system pressure was first reduced to approximately 100 torr and then the vacuum pump stopped. At about 5 torr any free water present would freeze. The vacuum was then broken by charging with oxygen free dry nitrogen. The

nitrogen was allowed to flow into the system until the pressure reached just above zero gauge pressure. The nitrogen supply should then be isolated from the system which was again evacuated. Since dry nitrogen could hold a large quantity of moisture before becoming saturated, it became an effective vehicle for carrying in vapour form, any remaining moisture for the vacuum pump. Moisture removal was progressively more complete when the system was swept twice or more times with dry nitrogen as explained above.

To be considered dry and free of moisture, a refrigerant system must be capable of sustaining a pressure of 1/2 torr or better for 24 hours with the vacuum pump isolated. If the pressure was pulled down to 1/2 torr and it rose to no more than 2 torr in 24 hours, then the system might be considered to be adequately dry and leak tight.

7.5.2. Starting Procedure

The test loop was ready for initial start up with the liquid receiver charged with the refrigerant. This was already completed for testing of the Lysholm screw expander. In addition, the following services were made available:

- i) Steam to heater
- ii) Cooling water to condenser
- iii) Air to control panel and air sets

The following steps were carried out before start-up:

- (1) Ensure that all valves in the following categories were closed.
 - (a) Instrument bleed valves

- (b) Start-up bypass valves
 - (c) Drain valves
 - (d) Vent valves
 - (e) Charge connections
 - (f) Bypass valve for filter/drier
- (2) Ensure that all other hand operated valves were open, especially feed pump discharge valve.
- (3) Ensure that all air actuated valves and solenoid valves were closed prior to start up.
- (4) The control valve on the cooling water line to the condenser should be half opened by manual adjustment of the controller output, and the cooling water pump started. When a stable water flow was achieved, this flow control loop was put into automatic at the desired flow rate.
- (5) The control valve on the main feed pump recirculating line should then half opened by manual adjustment of the controller. The main feed pump was then started by operating the panel start/stop push-button. This filled the heater, and the lines through the start-up loop with refrigerant liquid.
- (6) Gradually open the steam control valve, by manual adjustment of controller. Continue until the temperature of the refrigerant leaving the heater has reached the desired value. At this point the temperature controller can be put into automatic.
- (7) The test section inlet temperature controller was then adjusted and put into automatic.
- (8) Gradually close the start-up bypass control valve. The measured fluid flow was then entering the test section. The flow control valve was then put into automatic control at the desired flow rate.

7.5.3. Shut-Down Procedure

A normal shut down procedure involved the termination of operations under planned conditions. When shutting down, steps was taken to prevent equipment damage from expansion, contraction, thermal shock or abnormal pressure or vacuum. The operations could be described as follows.

- (1) Bypass flow of refrigerant around the test section by opening flow bypass valve.
- (2) Shut off steam flow to heater.
- (3) Let the refrigerant circulate for a time, and when it had cooled down sufficiently stop the feed pump.
- (4) Shut off flow of cooling water.

CHAPTER 8
RESULTS AND DISCUSSION

8.1. SUMMARY

In this chapter the two most important parameters in the study of two-phase flow, the pressure and void fraction obtained from the experiment, are presented. They are compared in detail with predictions from the theoretical model. It is shown that the agreement between the analytical and experimental results is well within the limits of experimental error.

8.2. TEST CONDITIONS

The two experimental inlet ports described in the previous chapter were tested under a wide range of flow conditions in order to provide sufficient data for comparison with the results from the theoretical analysis. For this purpose a total of twenty four test runs was planned and carried out - shared equally by the two inlet port systems. The flow conditions for them were made identical. The range of flow conditions which the experiments covered can be summarised as follows:

Mass flow rate	: 5.37 - 11.33 Kg/s
Inlet pressure	: 3.43 - 5.49 Bar (abs)
Inlet temperature	: 90 - 110 °C
Inlet Dryness fraction	: 0.07 - 0.47

The detailed flow conditions planned for the port inlet are given in Table 8.1. These were based on a thermodynamic analysis of the test rig taking into account the restrictions imposed by the feed pump and heater boiler capacities. In practice it was found that some of the planned flow conditions were hard to achieve. For instance certain fluid mass flow rates had to be raised above those planned so that the working fluid could remain in the single phase state prior to the main flow control valve. The main causes for this will be given in the next section. As a result, the flow conditions for which the two inlet ports were actually run are recorded in Table 8.2 for No.1 inlet port and Table 8.3 for No.2 inlet port respectively. They show some deviation from the planned flow conditions.

8.3. STEADY STATE CONDITION AND DATA COLLECTION PROCEDURE

In order to make any sensible comparison of experimental and theoretical results, it is important to ensure that a steady state condition should be established throughout the test loop prior to each data recording, and that such a steady state, once established, should be properly maintained throughout the whole period of the probe traversing operation.

It was realised at the outset of the experiment that it was not possible to achieve a complete steady state throughout the test loop. There are two main reasons for this. The first of these is that the gas-fired boiler with 600 KW capacity was operated on a periodic basis, there being a constant temperature fluctuation of ± 2 °C in the steam supplied to the heat exchanger. It follows that a similar

temperature fluctuation existed on the fluid side of the heat exchanger. Secondly the test rig was initially designed for a much greater heat input, which means that the size of the test rig is possibly too large for the current work. One direct consequence of this is the slow response of the fluid in the loop to the control instructions. A long warm-up period was also needed at the start of every test run. It was not uncommon for a number of hours to elapse before the first test recording could be attempted. This limited the number of tests which could be run each day.

Basically there are two methods to ascertain whether the flow in the test loop had reached a steady state or not. The first of these was purely of a qualitative nature and simply involved making direct and visual observations of the pressure readings on the digital meters connected to the pressure transducers, and then logging the data from the data logger at a regular interval. By contrast the second method was of quantitative nature and more complex. It involved a detailed heat balance analysis on the condenser. The procedure could be described as follows: The amount of heat rejected by the working fluid and that absorbed by the cooling water were calculated. Once the two values were found to agree to within a desired accuracy, it was then believed that steady state had been established throughout the test loop.

Test conditions in the test loop were set and maintained by a Foxboro controller with the exception of the heater boiler. The controller could be operated either in auto or manual mode. Ideally the controller should always be set to auto mode, which ensures that

the fluctuation within the loop be kept to an acceptable limit. However, it was found during testing that this mode did not seem to perform as well as was desired and occasionally the operating conditions drifted from their set point. The test then had to be repeated. Finally, manual control had to be adopted, thereby slowing the whole testing process.

In addition to the difficulties associated with the setting of test conditions, excessive pressure fluctuations were observed in the inlet port region from the digital meter connected to the high accuracy differential pressure transducer. Moreover, some of the desired test conditions, most notably the working fluid flow rate, were hard to achieve. It was further realised that the fluid flow rates had to be raised higher than planned in order to maintain the fluid in the single phase state prior to the throttle valve. This was essential for the dryness fraction at the port inlet to be determined.

After failing to achieve the planned test conditions, a serious attempt was made to discover the cause for this as well as the presence of excessive pressure fluctuation in the test section. It was found that by relocating the fine mesh filter between the exit of the control valve and the entrance of the inlet port instead of before the control valve, a much steadier flow in the test section was observed from the digital meter. More importantly, the operation to set and maintain the planned flow conditions in the test loop became much easier. One possible explanation for this improvement was that the filter itself acted as a 'flow damper' which could

significantly reduce the effect of high turbulence and swirls caused by the presence of the control valve.

Once a desired steady state had been achieved throughout the test loop, the flow condition data were collected from the data logger and then transferred via data link to the IBM/AT microcomputer for storage and post processing. The main parameters logged were pressures along the inlet port, temperatures at inlet and exit of the port, as well as fluid and cooling water flow rates. This was followed immediately by traversing the fibre optic probe across the exit plane for local void fraction measurement. Upon completion of the probe traverse operation, the flow conditions around the loop were logged and stored again. Having satisfied that the heat balances calculated from these two data recordings were within acceptable limit and the temperatures did not fluctuate by more than $\pm 2^{\circ}\text{C}$ throughout the traversing operation, the current test was accepted as a good one. The test conditions summarised in Tables 8.2 and 8.3 for the two inlet ports are the arithmetic average of these two data recordings.

8.4. COMPARISON OF EXPERIMENTAL AND COMPUTED PRESSURE DISTRIBUTIONS

Upon completion of the experiment, the pressure distributions obtained experimentally were compared with the numerically calculated ones to establish the validity of the separated two-phase flow model proposed in Chapter 4. For this purpose It was found both convenient and straightforward to present the results of the comparison graphically, with pressure distribution non-dimensionalised using the

inlet pressure values against the axial distance measured from the port inlet. In each graph the experimentally determined pressures are indicated by the discrete points, whereas the numerically calculated pressure distributions are represented by a continuous line.

The numerical pressure distributions were computed from the test data summarised in Table 8.2 for No.1 inlet port and Table 8.3 for No.2 inlet port respectively. In addition to the test data it was made clear throughout the theoretical work in chapter 4 and 5 that an initial droplet diameter must also be prescribed in order that the computation could be initiated. The criterion for the choice of this initial droplet diameter is such that it would eventually lead to droplet breakup when expanding through the inlet port. Based on this criterion, an initial droplet diameter of 0.2 mm was found sufficient to cause droplet breakup through No.1 inlet port. Hence it was used throughout the computation of the pressure distributions for No.1 inlet port. Using the droplet breakup criterion it was found that the droplet breakup would generally occur at a distance of 3 inch to 5 inch from the inlet.

The pressure distribution results for No.1 circular inlet port were examined first as a basis for comparison. They are presented in Figs.8.1-8.12 respectively for the twelve test runs numbered R.113-C1 to R.113-C12. With regard to these figures it must be pointed out that the present scaling scheme is adopted for illustrative purposes only, due to the low values of overall pressure drops across the inlet port at the current inlet/exit area ratio. The scheme may be a bit misleading because the actual difference in pressure between the

theory and experiment is much smaller than that shown. Having said this, it can be seen that the predicted pressure distributions show remarkably close agreement with the experimental ones throughout the majority of the test runs, numerically the mean error (relative) for the twelve runs being well within 1.0%. The best agreement is found for those test runs having two nominal pressures of 4.3773 bar and 5.4965 bar at the port inlet (see Figs.8.7 - 8.12). At 3.4368 bar nominal inlet pressure, small discrepancies are observed between the predicted and experimental values in some of the intermediate pressure points and the overall pressure drop. In some cases the error is almost one percent above the mean error value. These appear to correspond mainly to those test runs with higher dryness fraction at the port inlet.

In view of the above observations it must be further pointed out that the poorer agreement obtained in some intermediate pressure points is probably due to the accuracy of the pressure transducers used for these points. Two types of pressure transducers had been employed in the current experiment. One is differential and the other is absolute. The pressure at the port exit was measured by a high precision differential pressure transducer, whereas the rest were measured by various absolute pressure transducers. It is generally believed that the differential pressure transducer produces more accurate measurement than the absolute one. Furthermore, the absolute pressure transducers must be properly calibrated prior to use or serious error could be introduced into the measurement. Ideally the experiment should be repeated to avoid the measurement error. However the time factor precluded the repetition of the experiment for these

particular points.

The comparisons made above with respect to the No.1 inlet port pressure results indicate that the developed separated two-phase flow model is adequate and accurate in predicting the pressure distributions through an inlet port of circular cross section, and as such that in general the assumptions incorporated in the model are justified. The question then was, could the model be used also to predict the pressure distribution through the No.2 inlet port with the same degree of accuracy? Although this inlet port had a cross sectional area distribution identical to that of the No.1 inlet port, its cross-sectional shape is highly irregular.

In order to answer this question, the pressure distributions in No.2 inlet port were predicted using the same two-phase flow model. One difference to be noted in relation to the model is the friction coefficient between the fluid and the solid wall. It was mentioned in the last chapter that owing to its complex shape this inlet port was made from cast iron. It is known that the cast iron possesses a higher surface roughness than the material for the No.1 inlet port, which is commercial steel, and that in the turbulent region the wall shear stress is directly affected by the degree of surface roughness. The liquid skin friction coefficient for this inlet port was taken from Vennard & Street [1976] and is applicable to wholly rough pipe. It is expressed as follows:

$$\frac{1}{\sqrt{C_{fL}}} = 1.14 + 2.0 \log \frac{d}{e} \quad (8.1)$$

where

e is the pipe roughness coefficient and is 0.26mm for cast iron.
 d is the diameter of the pipe and for irregular cross section,
a hydraulic diameter should be used.

Based on this new liquid friction coefficient, the theoretical pressure distribution results were computed and these are presented together with the experimental results in Figs.8.13-8.24. In the process of computation it was found that an initial droplet diameter of 0.2mm could no longer cause droplet breakup throughout every test runs. Instead in some cases the initial droplet diameter had to be increased to 0.5mm and in others a reduction was necessary. The initial droplet diameter chosen for each test run ranged from 0.5 mm to 0.1 mm and can be seen in the corresponding graphs.

The comparison between the two results shows that the theoretical analysis generally predicts a slightly smaller overall total pressure drop than the experimental values. Although the agreement is not as good as that for No.1 inlet port, in terms of the mean relative error the agreement is found to be still within 1.0%. Very satisfactory agreement is achieved for those test runs with relatively lower inlet dryness fractions, with the best result corresponding to the test run R.113-B1 (see Fig.8.13). This test run has an inlet dryness fraction of 0.07615. On the other hand the agreement becomes progressively worse as the dryness fraction at the port inlet increases. However even in the test runs where the overall total pressure drop agreements are relatively poor, there is a general agreement in the convergent portion of the inlet port.

That the moderate discrepancy is observed between the predicted pressure distributions and the experimental values in some test runs is not really surprising in view of the fact that the theory assumes the flow field is one-dimensional while the real flow is hardly one-dimensional, due to the complex geometrical variation in the flow channel. This effect appears to be greater as the gas content or the two-phase velocity increases in the flow channel. The other factor can be attributed to the presence of a stronger phase separation phenomenon as opposed to that associated with No.1 inlet port. The local void fraction distribution measurement, carried out at the port exit plane using the fibre optic probe, reveals that this is quite the case. Details of the void fraction measurement result can be seen in the next section. Stronger phase separation leads to a larger interfacial shear stress and hence a higher overall pressure drop across the inlet port.

8.5. LOCAL VOID FRACTION MEASUREMENT RESULTS

With steady state condition achieved throughout the test loop for each set test condition, local void fraction measurement was initiated across the exit plane of the inlet port. The local void fraction thus obtained was then utilised to calculate the cross-sectionally averaged void fraction and to construct the isovoid diagram. The latter serves as an useful and important indication of how liquid and gas phases distribute over the cross section under study.

The fibre optic probe was positioned approximately 5 to 10 mm

further behind the exit plane. The main purpose for this arrangement was to protect the probe tip, which is extremely fragile, from any accidental damage should something unexpected happen while the traversing operation was in progress. For No.1 inlet port the void fraction measurements were carried out at a total number of 54 points over the exit plane, with a complete traversing time of roughly 30 minutes. It must be pointed out that such traversing time also includes (1) that time it takes for fluid to settle down locally every time the probe is traversed to a new position. Sufficient time must be allocated for this; (2) that time it takes to carry out on-line data acquisition and signal processing operation. In the case of No.2 inlet port, the measurements were carried out at a total number of 73 points, with a complete traversing time of roughly 45 minutes.

To ensure that the traversing and positioning operations of the fibre optic probe across the exit plane were smooth and accurate, the two stepper motors were set to run at their lowest rotational speeds. The other benefit of this arrangement is that, the disturbance to the flow locally which might be introduced by the movement of the probe in the test section, could be minimised. Besides, maximum torque could also be provided to the motors. On the other hand, the disadvantage of this arrangement is that too much traversing time was required. It appears from the operating experience gained so far that higher motor speeds can be used. The traversing time would thereby be greatly reduced and more data points could be taken. This option should certainly be considered in any future experiment.

The numerical procedure to compute the cross-sectionally averaged

void fraction of the inlet port exit can be described as follows:

The cross section is subdivided into a number of segments of small size. These segments can be either triangular or rectangular in shape, the choice of which depends very much on whether they can appropriately fit the boundary geometry. The vertices of the segments are made to coincide exactly with those points at which the local void fractions are measured by the probe. From the literature it is known that the definition of the cross-sectionally averaged void fraction is given as

$$\bar{\alpha} = \frac{\int \alpha dA}{\int dA} \quad (8.2)$$

which can be approximated numerically as:

$$\bar{\alpha} = \frac{\sum \alpha_i A_i}{\sum A_i} \quad (8.3)$$

where α_i is the local void fraction at the centre of the segment of i and A_i its corresponding cross-sectional area. The void fractions at the centre of each segment are obtained by interpolation of those at the vertices of each segments.

In what follows the detailed local void fraction measurement results are presented in the isovoid diagrams. For convenience of presentation and discussion, the local void fraction measurement

results for the two inlet ports are dealt with separately.

8.5.1. Results for No.1 Inlet Port

It can be seen that the geometry of the No.1 inlet port exit is symmetric about the vertical axis through its centre. As a result it is reasonable to assume that the local void fraction distribution on the exit plane of this inlet port is also similarly symmetric. For this reason it was decided that only half of the exit cross section would be traversed by the fibre optic probe. More data points could therefore be measured in a given time and thus a more accurate estimate of the average void fraction made. The exact locations of the points at which the local void fractions were measured can be found in Fig.8.25. The maximum horizontal and vertical traversing distances between two neighbouring points are 6 millimetres.

The detailed local void fraction measurement results for No.1 inlet port are presented in Figs.8.26-8.37. As is apparent from these diagrams, there generally exists a uniform distribution of the void fractions across the inlet port exit plane throughout a majority of the test runs, with little variation in void fraction from the centre to the wall. Those having significant variations are seen to be associated only with those test conditions where the inlet dryness fraction is low. An example of these is test run R.113-C1 which has an inlet dryness fraction of 0.0837. In this case the highest void fraction is observed to be at the top of the cross section, whereas the lowest is at the bottom. It appears that phase separation has occurred. The difference between the highest and the lowest void

fractions in each test run range from 15% to only 1%.

The fact that the phase separation seems to have occurred at lower inlet dryness fractions is not really surprising since the test section was not positioned vertically but at a 15° angle to the horizontal. Therefore in certain situations the effect of gravity on phase distribution were quite significant and had to be taken into consideration. It is particularly true when the fluid velocity through the inlet port was low. It is often the case that low inlet dryness fraction leads to low velocity and hence buoyancy force dominates as opposed to the accelerational force. Consequently the lighter component of the two-phase mixture, gas or vapour phase, tends to drift to the top of the flow channel and the heavier component, the liquid phase, then tends to settle down to the bottom. This phenomenon is clearly illustrated in the isovoid diagrams by the different colours which are associated with various levels of void fractions.

After thoroughly examining the void fraction distributions in a wide range of test conditions, the cross-sectionally averaged void fractions were evaluated. These were then compared with those found from the theoretical predictions and are plotted against the dryness fraction at the port inlet. Figs.8.38-8.40 show the results for three nominal inlet pressures, i.e., 5.4965, 4.3773 and 3.4368 bar. It can be seen that the predicted void fractions are in very good agreement with the experimental ones. The error of the prediction is found to be 2.13 percent for 3.4368 bar inlet pressure, 1.75 percent for 4.3773 bar and 2.5 percent for 5.4965 bar. It should be noted that

due to the low vapour/liquid density ratio of the refrigerant, the average void fraction is much higher for a given dryness fraction than in air-water or water-steam two phase mixtures.

8.5.2. Results for No.2 Inlet Port

In contrast to No.1 inlet port, this inlet port has a much more complex and irregular geometrical shape at its exit, and no symmetry of any sort exists. Consequently the entire cross section of the exit plane was traversed by the fibre optic probe. For accurate results to be obtained, more measurement points are necessary than for No.1 inlet port. On the other hand more points means longer traversing time. A total of 73 measurement points were selected and their locations are illustrated in Fig.8.41.

The detailed measurement results are presented for 12 test runs in Figs.8.42-8.53 respectively. The traverse shows clearly the effect of gravity on the phase distribution under all flow conditions. The highest void fraction regions are at the top and, as can be seen, these extend further downwards as the dryness fraction increases. It is also observed the rate of change of void fraction is greatest at regions where the change of the port cross sectional profile is the sharpest.

The comparisons are made of the cross-sectionally averaged void fraction predicted with the experimental results. These are given in details in Figs.8.54-8.56 respectively for three nominal pressures. It can be seen that the agreements are close, except at low dryness

fractions. The average relative error is 4.55 percent for the twelve runs, slightly higher than that for No.1 inlet port. This is believed to be caused by the coarse mesh used for the calculation of the average void fraction. The agreement would be improved if more measurement points had been used.

CHAPTER 9

CONCLUSIONS

In the theoretical investigation of flashing flow of organic working fluid through an inlet port of a Lysholm screw expander. A one-dimensional separated two-phase flow model has been developed. The model allows in a general way for both hydrodynamic and thermodynamic non-equilibrium phenomena associated with any two-phase flow, although in the case of one-component two-phase flow, the thermodynamic equilibrium is normally assumed.

In the experimental investigation, two inlet ports have been tested. The main parameters measured include the static pressure distributions along the flow channel and the local void fraction profiles at the inlet port exit plane. These data have been used to validate the theoretical model.

In the light of detailed comparison of the theoretical and experimental results, the following was concluded:

1. As far as the circular inlet port is concerned, the prediction from the two-phase separated flow model agrees well with the experimental measurements, both in terms of pressure distribution along the flow channel and cross-sectionally averaged void fraction at the port exit. The local void fraction at the port exit appears to be uniformly distributed, although higher void fraction tends to be near the top and lower void fraction tends to be near the bottom, because of the gravitational effect.

2. As far as the irregular inlet port is concerned, the agreement between the theoretical prediction and the experimental measurement is satisfactory if the flow through the channel is relatively low. While for higher flow, some discrepancies may be expected. This is believed to be caused by two-dimensional effect of the flow channel having a variable cross sectional shape. Furthermore, it is no longer true that the flow is uniformly distributed, as is apparent from the relevant isovoid diagrams.

3. The analysis and the computational method developed for the optimisation of inlet port shape are generally satisfactory as a design tool for use in producing an optimum efficiency inlet port for a two-phase Lysholm screw expander.

4. The fibre optic probe, which was adopted in the experiment for the measurement of local void fraction, proved to be very reliable and sensitive. It is believed that the whole traversing and sampling system developed can be used more generally to obtain void profiles in flow channels of irregular cross section.

REFERENCES AND BIBLIOGRAPHY

- Abuaf, N., Jones, O.C. and Zimmer, G.A., "Optical Probe for Local Void Fraction and Interface Velocity Measurement", Rev.Sci.Instrum, 1978.
- Akagawa, K., "A Study on Fluctuating Characteristics of the Void Fraction in Gas-Liquid Two-Phase Flow", Trans. Japan Soc. Mech. Engrs 29, 924-931, 1963.
- Ardron, K.H., "A Two-Fluid Model for Critical Vapour-Liquid Flow", Int.J.Multiphase Flow 4, 323-337, 1978.
- Ardron, K.H. and Ackerman, M.C., "Studies of the Critical Flow of Subcooled Water in a Pipe", CEGB, Berk., England, RD/B/N 4299, 1978.
- Ardron, K.H. and Furness, R.A., "A Study of the Critical Flow Models Used in Reactor Blowdown Analysis", Nucl.Eng Design 39, 1976.
- Arnold, C.R. and Hewitt, G.F., "Further Developments in the Photography of Two-Phase Gas-Liquid Flow", AERE-R5318, 1967.
- Austin, A.L., Sourcebook on the Production of Electricity from Geothermal Energy (Ed: J. Kestin), U.S.Dept. of Energy, 1980.
- Austin, A.L., Higgins, G.H. and Howard, J.H., "The Total Flow Concept for Recovery of Energy from Geothermal Hot Brine Deposits", LLL Report UCRL-51366, 1973.
- Baker, O., "Simultaneous Flow of Oil and Gas", Oil Gas J., 53, 1954.
- Bilicki, Z. and Kestin, J., "Two-Phase Flow in a Vertical Pipe and the Phenomenon of Choking: Homogeneous Diffusion Model", Int.J.Multiphase Flow, Vol.9, 1983.
- Biphase Energy System, "The Biphase Turbine: An Economical Mean to Alternative Energy", 1982.
- Boure, J.A., "On A Unified Presentation of the Non-Equilibrium Two-Phase Flow Model", ASME Symp. Vol. on Non-Equilibrium Two-Phase Flows, 1975.
- Chisholm, D., "Pressure Gradients during the Flow of Incompressible Two-Phase Mixtures through Pipes, Venturis and Orifice Plates", British Chemical Engineering, 12, 9, Sept, p.455, 1967.
- Chisholm, D., "Prediction of Pressure Drop at Pipe Fitting during Two-Phase Flow", 13th Int.Inst.Refrigeration Conf., Washington, 1971.
- Chisholm, D. and Sutherland, L.A., "Prediction of Pressure Gradients in Pipeline Systems during Two-Phase Flow", Instn.Mech.Engrs.Symp. on Two-Phase Flow Systems, University of Leeds, Paper 4, 1969.
- Cooper, K.D., Hewitt, G.F. and Pinchin, B., "Photography of Two-Phase Flow", AERE-R4301, 1963.

- Crabtree, D.L., "Investigation of the Influence of the Design Parameters on the Flow Characteristics of the Drive Nozzle of a Gas-Driven Jet Pump", MS Thesis, Purdue University, Lafayette, Ind., 1961.
- Danel, F and Delhaye, J.M., "An Optical Probe for Measuring Local Voidage in Two-Phase Flow", *Measures*, 99-101, Aug-Sept 1971.
- Delhaye, J.M., "Measurement of the Local Void Fractions in Two-Phase Air-Water Flow with a Hot-Film Anemometry", CEA-R-3465(E), 1968.
- Delhaye, J.M., "Hot-Film Anemometry in Two-phase Flow". Proc. 11th Nat. ASME/AIChE Heat Transfer Conf. on Two-Phase Flow Instrumentation, Minneapolis, 1969.
- Delhaye, J.M. and Achard, J.L., "On the Use of Averaging Operators in Two-Phase Flow Modelling", *Symp. on Thermal & Hydraulic Aspects of Nuclear Reactor Safety*, Vol.1, ASME, 1977.
- Delhaye, J.M. and Galaup, J.P., "Measurement of Local Void Fraction in Freon 12 with A 0.1 mm Optical Fibre Probe", *European Two Phase Flow Meeting*, June 1974, Harwell, Paper A6, 1974.
- Dipippo, R., "International Developments in Geothermal Power Production", *Geothermal Resources Council BULLETIN* May 1988.
- Eckert, E.R.G., and Drake, R.M., "Heat and Mass Transfer", McGraw-Hill Book Company, Inc., New York, 1959.
- Eddington, R.B., "Investigation of Supersonic Shock Phenomena in a Two-Phase (Liquid-Gas) Tunnel", *AIAA Paper No.66-87*, 1966.
- Elliott, D.G., "Theory and Tests of Two-Phase Turbines", *Jet Propulsion Laboratory Publication 81-105*, 1982.
- Elliott, D.G. and Weinbery, E., "Acceleration of Liquids in Two-Phase Nozzles", *Technical Report 32-987*, Jet Propulsion Laboratory, California Institute of Technology, July, 1968.
- Galaup, J.P., "Contribution a l'Etude des Methodes de Mesure en Ecoulement Diphasique", *These de Docteur*, Universite Scientifique et Medicale de Grenoble, 1975.
- Govier, G.W., Radford, B.A. and Dunn, J.S.C., "The Upwards Vertical Flow of Air-Water Mixtures, I. Effects of Air and Water Rates on Flow Pattern, Holdup and Pressure Drop", *Canadian J.Chem.Eng.*, 35, 1957.
- Griffith, P. and Wallis, G.B., "Two-Phase Slug Flow", *Trans. A.S.M.E.*, 83, Series C, 307, 1961.
- Guderley, G. and Armitage, J.V., "General Approach to Optimum Rocket Nozzles", Chapter 11, *Theory of Optimum Aerodynamic Shapes*, Edited by A.Miele, Academic Press, New York, 1965.
- Guderley, G. and Hantsch, E., "Beste Formen für Achsensymmetrische Überschallschubdüsen", *Zeitschrift für Flugwissenschaften*, Vol.3, No.9, 1955.

- Hanson, A.R., Domich, E.G. and Adams, H.S., "Shock Tube Investigation of the Breakup of Drops by Air Blasts", *Physics of Fluids*, Vol.6, No.8, pp.1070-1080, 1963.
- Harlow, F.H. and Amsden, A., "A Numerical Fluid Mechanics Calculation Method for All Flow Speeds", *Journal of Computational Physics*, Vol.8, No.2, 1971.
- Henry, R.E., "A Study of One-and Two-Component, Two-Phase Critical Flows at Low Qualities", ANL-7430, 1968.
- Henry, R.E., "An Experimental Study of Low Quality, Steam-Water Critical Flow at Moderate Pressure", ANL-7740, 1970.
- Hetsroni, G. (Editor-in-Chief), "Handbook of Multiphase System", Hemisphere, 1982.
- Hewitt, G.F., "Measurement of Two-Phase Flow Parameters", Academic Press, New York, 1978.
- Hewitt, G.F. and Roberts, D.N., "Studies of Two-Phase Flow Patterns by Simultaneous X-Ray and Flash Photography", AERE-M2159, 1969.
- Hinata, S., "A Study on the Measurement of the Local Void-Fraction by the Optical Fibre-Glass Probe", *Bull. Japan. Soc. Mech. Engrs.* 15, 1972.
- Hoffman, J.D., "A General Method for Determining Optimum Thrust Nozzle Contours for Chemically Reacting Gas Flows", *AIAA Journal*, Vol.5, No.4, April 1967.
- Hoffman, J.D. and Thompson, H.D., "A General Method for Determining Optimum Thrust Nozzle Contours for Gas-Particle Flows", *AIAA Journal*, Vol.5, No.10, Oct. 1967.
- Hooker, H.H. and Popper, G.F., "A Gamma-Ray Attenuation Method for Void Fraction Determinations in Experimental Boiling Heat Transfer Test Facilities", ANL-5766, 1958.
- House, P.A., "Helical Rotor Expander Application for Geothermal Conversion", LLL Report UCRL-52043, 1976.
- Hsu, Y.Y. and Graham, R.W., "Transport Process in Boiling and Two-Phase System", McGraw-Hill Book Company, 1976.
- Hsu, Y.Y., Simon, F.F. and Graham, R.W., "Application of Hot-Wire Anemometry for Two-Phase Flow Measurements such as Void Fraction and Slip Velocity", *Multiphase Flow Symp.* ASME, Philadelphia, 1963.
- Isbin, H.S., Moy, J.E. and Dacruz, J.R., "Two-Phase, Steam-Water Critical Flow", *AIChE*, 3, 361-365, 1957.
- Isbin, H.S., Rodriguez, H.A., Larson, H.C. and Pattie, B.D., "Void Fractions in Two-Phase Flow", *AIChE Jnl.* 5 (4), 427-432, 1959.
- Ishii, M., "Thermo-Fluid Dynamic Theory of Two-Phase Flow", Eyrolles, Paris, 1975.

- Ishii, M. and Zuber, N., "Drag Coefficient and Relative Velocity in Bubbly, Droplet or Particulate Flows", *AIChE Journal*, Vol.25, 1979.
- Johnson, H.A. and Abou-Sabe, A.H., "Heat Transfer and Pressure Drop for Turbulent Flow of Air-Water Mixtures in A Horizontal Pipe", *Trans. ASME*, 977-987, 1952.
- Jones, A.B. and Zuber, N., "The Interrelation between Void Fraction Fluctuation and Flow Patterns in Two-Phase Flow", *Int. J. Multiphase Flow*, Vol.2, 273-306, 1975.
- Kataoka, I., Ishii, M. and Mishima, K., "Generation and Size Distribution of Droplet in Annular Two-Phase Flow", *Trans. ASME, Journal of Fluids Eng.*, Vol.105, 1983.
- Kays, W.M., "Convective Heat and Mass Transfer", McGraw-Hill, 1966.
- Kreith, F., "Principle of Heat Transfer", 2nd Edition. International Textbook Company, Scranton, Pa., 1965.
- Lahey, R.T. USNRC sponsored instrumentation research at Rensselaer Polytechnic Institute (RPI), US Nuclear Regulatory Commission, Proceedings of Meeting of Review Group on Two-Phase Flow Instrumentation, January 1977. NUREG-0375, (Paper No I.2), 1977.
- Liles, D.R. and Reed, W.M.H., "A Semi-Implicit Method for Two-Phase Fluids Dynamics", *Journal of Computational Physics*, Vol.26, 1978.
- Lockhart, R.W. and Martinelli, R.C., "Proposed Correlation of Data for Isothermal Two-Phase Two-Component Flow in Pipes", *Chem. Eng. Prog.* 45, 39, 1949.
- Lysholm, A., "Screw Rotor Machine", U.S. Patent No. 3,314,598, 1967.
- Marble, F.E., "Nozzle Contours for Minimum Particle-Drag Loss", *AIAA Journal*, Vol.1, No.12, 1963.
- Martinelli, R.C. and Nelson, D.B., "Prediction of Pressure Drop during Forced Circulation Boiling of Water", *Trans. ASME*, Vol.70, 1948.
- Martindale, W.R. and Smith, R.V., "Separated Two-Phase Flow in a Nozzle", *Int. J. Multiphase Flows*, Vol.8, No.3, 1982.
- McKay, R.A., and Sprankle, R.S., "Helical Rotary Screw Expander Power System", *Conf. on Res. for Dev. of Geothermal Energy Resources*, Rept. NSF-RA-N-74-159, Pasadena, 1974.
- McQuillan, K.W. and Whalley, P.B., "Flow Patterns in Vertical Two-Phase Flow", *Int. J. Multiphase Flow*, Vol.11, pp.161-175, 1985.
- Miller, N. & Mitchie, R.E., "Measurement of Local Voidage in Liquid /Gas Two-Phase Flow System", *J. Br. Nucl. Energy Soc.* 9, 94-100, 1970.
- Miropolsky, Z.L. and Shneyerova, R.I., "Heat Engineering and Hydrodynamics. 1. Measuring the Volumetric Content of Steam-Generating Elements by means of Gamma Radiation", USAEC Report No AEC-tr-4206,

1, 1960.

Mishima, K.M. and Ishii, M., "Flow Regime Transition Criteria for Upward Two-Phase Flow in Vertical Tubes", Int.J.Heat Mass Transfer 27, 723-737, 1984.

Morrell, G., "Critical Conditions for Drop and Jet Shattering", NASA TN D-677. NASA, Washington, Feb. 1961.

Neal, L.G. and Bankoff, S.G., "A High Resolution Resistivity Probe for Determination of Local Void Properties in Gas-Liquid Flow", AIChE Journal 9, 1963.

Netzer, D.W., "Calculations of Flow Characteristics of Two-Phase Flow in Annular Converging-Diverging Nozzles", Report No. TM-62-3. Jet Propulsion Center, Purdue University, Lafayette, Ind., June 1962.

Perry, J.H., Chilton, C.H. and Kirkpatrick, S.O., "Chemical Engineer's Handbook", 4th Edition, McGraw-Hill Book Co., Inc., New York, 1963.

Pike, R.W., Wilkins, B. and Ward, H.C., "Measurement of the Void Fraction in Two-Phase Flow by X-Ray Attenuation", AIChE Journal 11, 1965.

Piper, T.C., "Dynamic Gamma Attenuation Density Measurements", Aerojet Nuclear Company, ANCR-1160, 1974.

Rao, G.V.R., "Exhaust Nozzle Contour for Optimum Thrust", Jet Propulsion, Vol.28, No.6, 1958.

Richter, H.J., "Separated Two-Phase Flow Model: Application to Critical Two-Phase Flow", Int.J.Multiphase Flow, Vol. 9, 1983.

Schrock, V.E. and Selph, F.B., "Reactor Heat Transients Research. An X-Ray Densitometer for Transient Steam-Void Measurement", U. California. Inst. Eng. Research Report No SAN-1005, TID-4500, 1963.

Serizawa, A., Kataok, A.I and Michiyoshi, I., "Turbulence Structure of Air Water Bubbly Flow 1. Measuring Techniques", Int. J. Multiphase Flow, 12 (3), 221-233, 1975.

Smith, I.K., "A Method for Converting Geothermal Energy", Israeli Patent No.64582, 1981.

Smith, I.K., "PROJECT SPHERE: An Assessment of the Practicability of the Trilateral Wet Vapour Cycle for Recovery of Power from Low grade Heat Sources", Thermo-Fluids Engineering Research Centre Report, The City University, 1985.

Smith, I.K., "A Comparison of Three Surface Plant Options for the Conversion of Geothermal Energy from HDR", IRD 86/17, 1986.

Smith, R.V., "Choking Two-Phase Flow Literature Summary and Idealized Design Solution", Nat.Bureau of Standards, Tech.Note No.179, 1963.

Sozzi, G.L. and Sutherland, W.A., "Critical Flow of Saturated and Subcooled Water at High Pressure", ASME Non-Equilibrium Two-Phase

Flows Symp., pp19-26, 1975.

Sprankle,R.S., "Electrical Power Generating Systems", U.S. Patent 3,751,673, August 1973.

Sprankle,R.S., "Throttling Means for Geothermal Stream", U.S.Patent 3,977,818, 1976.

Steidel,R.F., Weiss,H. & Flower,J.E. "Characteristics of the Lysholm Engine as Tested for Geothermal Applications in the Imperial Valley", J.Eng for Power,vol.104, pp231-240, Jan 1982.

Steltz,W.G., "The Critical and Two-Phase Flow of Steam", J.Eng.Power, Trans.ASME 83, 1961.

Taitel,Y., Bornea,D. and Dukler,A.E., "A Model for Predicting Flow Regime Transitions in Horizontal and near Horizontal Flow", AIChE J., 22, 47-55, 1976.

Taniguchi,H., "Analytical and Experimental Investigation of Two-Phase Flow Screw Expanders for Power Generation", Tran. of ASME, J. of Eng. for Gas Turbines & Power, Vol.110, 1988.

Thomas,D.G., "Quarterly Progress Report on Blow Down Heat Transfer, Separate-Effects Programme", ORNL/NUREG/TX-109, 1977.

Truong Quang Minh and Huyghe,J., "Measurement of Average Thickness Liquid Film Two-Phase, Two-Component Flow in the Annular Dispersed Regime", CEN Grenoble, Report No 54, 1965.

Vennard,J.K and Street,R.L., "Elementary Fluid Mechanics", John Wiley & Sons, Inc., 1976.

Wallis,G.B., "Use of the Reynolds Flux Concept for Analysing One-Dimensional Two-Phase Flow", Int.J.Heat Mass Transfer, Vol.11, 1968.

Wallis,G.B., "One-Dimensional Two-Phase Flow", McGraw-Hill, 1969.

Weber,C., Zeit.fur Angew.Math., 11, 106, 1931.

Weinstock,R., "Calculus of Variations", McGraw-Hill, 1952.

Weisman,J., Duncan,D., Gibson,J. and Crawford,T., "Effects of Fluid Properties and Pipe Diameter on Two-Phase Flow Patterns in Horizontal Lines", Int.J.Multiphase Flow, Vol.5, pp.437-462,1979.

Wilson,S.S. & Radwan, M.S., "Appropriate Thermodynamics for Heat Engine Analysis and Design", Int.J.Mech.Eng.Educ., Vol.5, No.1, 1977.

Zaludek,F.R., "Steam-Water Critical Flow from High Pressure Systems", GE Report HW80535, 1964.

APPENDIX A

COMPUTER PROGRAM DOCUMENTATION AND LISTING

A1.1. INTRODUCTION

This appendix details the computer program TPSFS (Two-Phase Separated Flow Study) used for the analysis of two-phase flashing flow in the inlet port of a circular cross section. The program was written in Fortran 77 and was initially run on the City University Computer Unit's Honeywell mainframe computer. Unfortunately this system was taken out of service in June 1987, and a GOULD minicomputer with Unix operating system was installed. When the program was transferred to this system two main problems were encountered. Firstly, great effort was made to get the numerical procedure to solve a system of non-linear equations converge but in vain. This was believed to be largely caused by the machine accuracy. Secondly the machine was amazingly slow in compilation and execution of the program. After one month's frustrating debugging and rearranging of the program no apparent improvement was made. It was therefore decided to resort to the Cray 2 supercomputer (presently Cray X-MP) at the University of London Computer Centre (ULCC). It proved to be a successful move and no serious problems were encountered. For a typical run the CPU time taken was 30 seconds. The job can be submitted in batch to Cray X-MP or run in interactive mode on the ULCC Amdahl. The program should be linked with IMSL library which contains the routine ZSCNT for solving a system of nonlinear equations. Similar routines from other libraries may also be used.

A1.2. PROGRAM STRUCTURE

The general structure of the program TPSPS is illustrated by the flow chart in Fig.A.1.

A1.3. LIST OF SUBROUTINES

A1.3.1. DROPDIA

This routine is for the calculation of droplet diameter at each computational step. As described in the theoretical analysis, a critical Weber number was utilised. This number was taken as 6 and later when new breakup criteria are available which provide better agreement between prediction and experiment, they can be incorporated into the program within this routine. The input data defining the state of the fluid and at which droplet diameter is to be evaluated are in the call statement argument list as follows:

VG,VL,SURFT,RHOG (Input)

and

DD (Output)

A1.3.2. FRIC

This subroutine is used to evaluate the wall shear stress; in it the friction factor is calculated and the boundary layer momentum equation is solved. The input data defining the geometry of the port and fluid properties at nodal point K and K+1 are taken from FRC and BL commons. The output of boundary layer thickness, velocity and area reduction factors are transferred through BL common.

A1.3.3. PROPSC

This is the routine for the thermodynamic and transport properties required by the computation. Two methods are available for them in this subroutine, either by table interpolation or by directly solving equation of state. The thermodynamic and transport property evaluation program by Smith uses Lee-Kesler and Martin-Hou equation of state and covers over 90 organic working fluids and water. This program can be conveniently linked as a property library to the two-phase flow program. The main subroutines available from Smith's property program are the following:

ENTH(I,P,T,IX,X,K) for specific enthalpy

ENTR(I,P,T,IX,X,K) for specific entropy

VOL(I,P,T,IX,X,K) for specific volume

TSAT(P) for saturation temperature

TRANS(I,P,T,IX,X,CP,VIS,CO,PRA,SURFT,K) for transport properties

where

- I - An integer which indicates whether the equation of state has been solved. When equation of state is not solved, use I = 1 or I = 2
- IX - An integer indicating the states
 - IX = 1 Superheated
 - IX = 2 Saturated
 - IX = 3 Subcooled
- X - Dryness fraction
- K - An integer

CP - Specific heat
VIS - Viscosity
CO - Conductivity
PRA - Prantle number
SURFT - Surface tension

For those fluids whose properties cannot be evaluated correctly from the equation of state, their properties can be obtained by an appropriate interpolation of relevant property data from the table prepared in the block DATA statements. The call statement argument list for the subroutine PROPSC is

P, ISTATE (input data)

and

TT, HG, HL, RHOG, RHOL, MUG, WG (output).

where integer ISTATE tells the program to use Smith's property subroutine when ISTATE = 2 or use interpolation when ISTATE = 1.

A1.3.4. FCN

The FCN is the most important subroutine in the program and is used to solve the conservation equations of frictionless flow. It is one of the parameter argument list in the numerical minimisation subroutine ZSCNT and is declared EXTERNAL in the calling program. As described in the solution procedure in Chapter 5, for iterations at each step an initial set of variable changes such as $(\Delta P)_{i,i+1}$ are guessed. On the basis of these guessed variable changes, the routine FCN is used to obtain the corresponding calculated variable changes by solving the relevant conservation equations. In other words there should be a set of calculated variable changes corresponding to a set

of guessed variable changes by FCN. Therefore the call statement argument list is

NEQ	Number of variable changes to be iterated	(input)
XGS(NEQ)	Guessed variable changes	(input)
FF(NEQ)	A set which defines the difference between guessed variable changes and their corresponding calculated ones.	(output)

The input data defining the step inlet conditions are taken from the main subroutine PSTPSC argument list. They will remain unchanged while the XGS(NEQ) are varied according to a specific route dictated by the optimisation subroutine ZSCNT. When the iteration is converged the step exit conditions are passed back to the main program by CHAN common.

A1.3.5. OSLIP

In this subroutine the optimum slip ratio given in Chapter 6 is evaluated numerically by a bisection method.

A1.3.6. INPUT

Most of the program input is read from this routine and can be listed as follows:

IOPT	An integer which specifies type of the calculation required.
IOPT = 1	flow area is specified.
IOPT = 3	optimisation is required.
NSTEP	Number of computational steps.
ISRCH	Specifies whether scan of flow rate is needed.
ISRCH = 0	No scan (Default)
ISRCH = 1	Scan is needed.

NUIN Input data units.
 NUIN = 1 SI units.
 NUIN = 2 English units.

NUOUT Output data units.
 NUOUT = 1 SI units.
 NUOUT = 2 English units.

NWDTH An integer which controls wide or narrow printout.
 NWDTH = 0 Wide printout.
 NWDTH = 1 narrow printout.

NSP Number of steps per printout.

KCHK Print search details at node point KCHK.

NSIG Number of significant figures of accuracy in the iteration procedure.

DMTO Initial increment for flow rate search.

DMTMIN Fractional change in mass flow rate at which to end search.

PO Static pressure at port exit.

XGO Dryness fraction at port exit.

DO Droplet diameter at port exit.

VO Mixture velocity at port exit.

MTO Mass flow rate through the port; In NSRCH = 1 case it is taken as initial value for scanned mass flow rate.

The following four inputs are needed only when IOPT = 3 :

IEXIT Specifies whether pressure or velocity is known at port exit.
 IEXIT = 1 Port exit pressure is given.
 IEXIT = 3 Port exit velocity is given.

PEXIT Port exit pressure.
 VEXIT Port exit mixture velocity.
 LAMDA Lagrangian multiplier.
 ISTATE An integer which specifies whether the properties are taken from table or evaluated from equation of states.
 ISTATE = 1 From table input.
 ISTATE = 2 Equation of state.

A1.3.7. PRNTAB

This is a printout routine in which all the important input and flow parameters calculated at nodal points are printed. The parameter list of the routine is:

AREA, DD, P, T, MG, VB, VG, VL, X, NWDTH, NX

where all the above parameters are declared array of size NX except NWDTH, which controls wide or narrow printout. It is called only once before the computation starts in the main program to transmit array storage. It should be noted that it has another entry point through the entry statement ENTRY PRINT1(J) where J is the nodal point number. This subroutine is called whenever the flow parameters need to be printed at a particular point.

A1.3.8. ZSCNT

It is the IMSL non-linear equation solver which is based on a secant method. It finds the values of XGS(1) to XGS(NEQ) that zero the values of FNORM to NSIG places. The calling statement argument list is

FCN, NSIG, N, ITMAX, PAR, XGS, FNORM, WK, IER

where IER is the error parameter (output) and can take any of the

following three values:

IER = 0 indicates that the iteration has succeeded.

IER = 129 indicates that the routine has failed to converge within ITMAX iterations. The user may increase ITMAX or try a new initial guess XGS.

IER = 130 indicates the algorithm was unable to improve in the returned value of XGS. This situation arises when the solution cannot be determined to NSIG digits due to errors in the function values. It may also indicate that the routine is trapped in the area of a local minimum. The user may try a new initial guess.

A1.4. GLOSSARY OF PRINCIPAL FORTRAN NOTATION

FORTRAN Name and Dimension	Description
AEFF	Effective flow area
AREA(NX)	Cross-sectional area of the port
DAFRIC	Area reduction due to the boundary layer
DD(NX)	Droplet diameter
DMAX	Maximum droplet diameter
DMMAX	Max gas flow rate change allowed for each step
DPMAX	Max pressure change allowed for each step
DVFRIC	Velocity reduction due to the boundary layer
DVMAX	Max velocity change allowed for each step
FDPREV(NEQ)	Calculated variable changes. If ZSCNT does not converge, assign it to XGS(NEQ)
FNORM	Used by ZSCNT and defined as $FNORM = FF(1)**2 + FF(2)**2 + \dots + FF(NEQ)**2$
IER	Error flag for subroutine ZSCNT

ITMAX	Max number of iterations in the solution procedure
KLAST	Last obtainable point
KTHT	Throat step number
LPORT	Port total length
MG(NX)	Vapour mass flow rate
MT	Total mass flow rate
MZ(2)	Conversion factor for mass flow rate
NEQ	Number of simultaneous equations to be solved
N1	Flag set during manual pressure search mode
NFAIL	Maximum mass flow rate search fail flag
NMIN	Minimum pressure flag
NX	Array size
P(NX)	Pressure
P2MIN	Minimum pressure guess allowed
PMIN	Minimum pressure in the port
PZ(2)	Conversion factor for pressure between SI and English units
RHOG(NX)	Vapour density
RHOL(NX)	Liquid density
RU	Universal gas constant
T(NX)	Temperature
VF	1 + DVFRIC
VG(NX)	Vapour velocity
VL(NX)	Liquid velocity
VSK	Slip velocity at node K
VZ(2)	Conversion factor for velocity
WEC	Critical Weber number
WG	Molecular weight

WK(100)	Work vector for ZSCNT
X(NX)	Distance measured from port inlet
XG	Dryness fraction
XGS(NEQ)	Guessed variable changes across each step
XSCALE(NEQ)	Scaling factors
XZ(2)	Conversion factor for distance

A1.5. PROGRAM LISTING

```

C ** ** ** ** ** ** ** ** ** ** ** ** ** ** ** ** ** **
C
C ** ** ** **          PROGRAM TPSFS          ** ** ** **
C
C ** ** **          BY Z.G. XU          ** ** **
C
C ** ** **          MAY, 1987          ** ** **
C
C ** ** **          ** ** **          ** ** **          ** ** **
C
C ** ** **          LAST MODIFICATION MADE OCT.1989          ** ** **
C
C
C          IMPLICIT DOUBLE PRECISION (A-H,L-M,O-Z)
C
C          PARAMETER (NX=50,NEQ=3)
C
C          DIMENSION AREA(NX),DD(NX),MG(NX),P(NX),RHOG(NX),T(NX)
C          DIMENSION SIG(NX),VG(NX),VL(NX),X(NX),V(NX),VB(NX)
C          DIMENSION XGS(NEQ),XSCALE(NEQ),FDPREV(NEQ),WK(100),PAR(1)
C          DIMENSION PZ(2),MZ(2),XZ(2),VZ(2)
C
C          EXTERNAL FCN
C
C          COMMON /CONST/RU,MT,V,ISTATE /SIG/SIGK /CHK/KCHK,K /MODE/NMODE
C          COMMON /BOUND/DVMAX,DMMAX,DPMAX,P2MN /XSCL/XSCALE,FDPREV
C          COMMON /PRNT/NUOUT,NP,KTHT,KK,N3
C          COMMON /BL/AREAK,DA,DAFRIC,DVFRIC,THETA
C          COMMON /EXIT/P2G,T2G,MG2G,VB2G,VG2G,VL2G,X2G,AREA2G,RHOG2G
C          COMMON /ADD/NOPT,NISEN,LAMDA
C
C ***** CONVERSION FACTORS AND CONSTANTS *****
C
C          DATA PZ/1D0,6894.7572D0/,MZ/1D0,0.45359237D0/
C          DATA XZ/1D0,2.54D-2/,VZ/1D0,0.3048D0/
C          PI=3.14159D0
C          ITMAX=200
C          DVMAX=50D0
C          DMMAX=0.5D0
C          DPMAX=1D5
C          P2MN=1.33D4
C
C          CALL PRNTAB(AREA,DD,P,T,MG,VB,VG,VL,X,NWIDTH,NX)
C
C ***** DEFAULT INPUTS *****
C
C          PO=706D3
C          DO=2D-4
C          XGO=0.0739D0
C          MTO=14.55D0
C          VO=4.0D0
C          PE=100D3
C          DMT0=0.05D0
C          THETA0=1D-4
C          DMTMIN=1D-10
C          IOPT=1

```

```

NSTEP=50
NSRCH=0
NWDTH=1
NSP=1
NINPT=1
NUIN=1
NUOUT=1
KCHK=0
NPX=0
NSIG=12
KBPS=0
DMGS1=0.18D-2
NBUF=0
NISEN=0
VEXIT=20.0D0
LAMDA=1.0D2

```

C

C ***** TAKE INPUTS *****

C

```

15 CALL INPUT(NX, IOPT, NSTEP, ISRCH, NUIN, NUOUT, NSP,
$           KCHK, NSIG, DMT0, DMTMIN, ISTATE, PO, XGO,
$           DO, VO, MTO, IEXIT, PE, VEXIT, LAMDA)

```

C

C ***** UNITS CONVERSION *****

C

```

MT=MTO*MZ(NUIN)
P(1)=PO*PZ(NUIN)
DD(1)=DO*XZ(NUIN)
VOX=VO*VZ(NUIN)
VEX=VEXIT*VZ(NUIN)
PEX=PE*PZ(NUIN)

```

C

```

CALL PROPS(P(1), T(1), HG1, HL1, RHOG1, RHOL1, MUG1, WG1)

```

C

C ***** PRESCRIBED AREA FOR IOPT=1 *****

C

```

IF (IOPT.EQ.1) CALL SHAPE (X, AREA, NSTEP)

```

C

C ***** PRESCRIBED PRESSURE FOR IOPT=3 *****

C

```

21 IF (IOPT.EQ.3) THEN
  IF (IEXIT.EQ.2) THEN
    PEX=P(1)+(VOX**2-VEX**2)/(2*(XGO/RHOG1+(1-XGO)/RHOL1))
  END IF
  NOPT=1
  DP=(PEX-P(1))/(NSTEP-1)
  DO 19 K=2, NSTEP
    P(K)=P(1)+DP*(K-1)
19 CONTINUE
END IF

```

C

C ***** OPTIONAL SCAN OF FLOW RATE *****

C

```

18 N2=0
   DMT=DMT0
   NFAIL=0

```

```

        MBASE=MTO-DMT
        IF (NSRCH.EQ.1) PRINT 20
20    FORMAT (/26X,'FLOW RATE SEARCH',/12X,
        $      'MTO,          LAST K   LAST P   MIN K       MIN P'//)
C
25    IF (NSRCH.EQ.1) THEN
        IF (NFAIL.EQ.1) DMT=DMT/2.0
        MTO=MBASE+DMT
        MT=MTO*MZ(NUIN)
    END IF
C
C ***** INITIALIZATION *****
C
        RHOG(1)=RHOG1
        SIG(1)=SIGK
        MG1=MT*XGO
        MG(1)=MG1
        ML1=MT-MG1
        R1=ML1/MG1
C
        IF (IOPT.GT.1) AREA(1)=MG1*(1/(RHOG1*VOX)+R1/(RHOL1*VOX))
C
        VB(1)=MG1/AREA(1)*(1/RHOG1+R1/RHOL1)
        VG(1)=VB(1)
        VL(1)=VB(1)
        X(1)=0.0
        IF (NOPT.NE.1) DELTX=X(2)
        DO 30 K=1,NEQ
            XGS(K)=ODO
30        XSCALE(K)=1D0
C
        IF (IOPT.EQ.1.AND.NPX.NE.2) THEN
            RHOMX1=1D0/((1D0-XGO)/RHOL1+XGO/RHOG1)
            V2GS=VB(1)*AREA(1)/AREA(2)
            XGS(1)=V2GS-VL(1)
            XGS(3)=0.5*RHOMX1*(VB(1)**2-V2GS**2)
            XGS(2)=DMGS1
        END IF
C
        NP=0
        IF (IOPT.EQ.1) NMODE=1
        IF (IOPT.EQ.3) NMODE=2
        KTHT=0
        IER=0
        N1=0
        NMIN=0
        THETA=1D-6
        DAFRIC=ODO
        DVFRIC=ODO
C
        DO 100 K=1,NSTEP
C
            KK=K
            KLAST=K
            IF (K.EQ.NPX) NMODE=2
            IF (K.EQ.NPX) N1=1

```

```

      IF (K.EQ.1.AND.NSRCH.EQ.0) CALL PRINT1(KK)
      IF (K.EQ.1) GO TO 100
C
C ***** DROPLET DIAMETER *****
C
      IF (IOPT.EQ.1) THEN
      DD(K)=DROPDIA(VG(K-1),VL(K-1),SIG(K-1),RHOG(K-1),DD(K-1))
      ELSE
      DD(K)=DD(K-1)
      END IF
C
C ** TELL STEP SUBROUTINE WHAT VARIABLES TO READ AND WRITE THIS STEP **
C ** FOR PRESCRIBED-AREA OPTION, CORRECT AREA FOR PREVIOUS FRICTION **
C
      IF (NMODE.EQ.1) AEPF=AREA(K)*(1D0+DAFRIC)
C
      CALL PSTPSC(P(K-1),T(K-1),MG(K-1),VB(K-1),VG(K-1),
$           VL(K-1),X(K-1),DD(K),
$           P(K),T(K),MG(K),VB(K),VG(K),
$           VL(K),X(K),AEPF,RHOGK)
C
C *** SET THE GUESSES FOR THE VARIABLE CHANGES IN THIS STEP ***
C
      IF (K.GT.2) THEN
      DO 35 J=1,3
      XSCALE(J)=1D0/FDPREV(J)
35      XGS(J)=1D0
      END IF
C
C ***** OPTIONAL MANUAL PRESSURE SEARCH AT K=NPX *****
C
40  IF (N1.GT.0) THEN
C
      IF (N1.EQ.1) THEN
      PRINT *, ' ENTERING SPECIFIED-PRES MODE AT K=',K
      PRINT *, ' ENTER PRESSURE '
      PRINT *, ' ENTER 0.0 TO GO TO NEXT K-STEP '
      PRINT *, ' ENTER -1.0 TO RESUME PRESCRIBED A(X) RUN '
      PRINT *, ' ENTER -2.0 TO RETURN TO START '
      N1=2
      END IF
C
C ***** ENTER PRESSURE *****
C
      PRINT 45,K
45  FORMAT(/' ENTER P(',I3,')')
      READ *,PK
      IF (PK.LT.-1) GO TO 15
      IF (PK.LT.0) PRINT *, ' RESUMING PRESCRIBED-AREA RUN '
      IF (PK.LT.0) NMODE=1
      IF (PK.LE.0) GO TO 100
      P(K)=PK*PZ(NUIN)
      IF (K.GT.2) THEN
      XGS(1)=FDPREV(1)
      XGS(2)=FDPREV(2)
      XGS(3)=FDPREV(3)

```

```

        END IF
C
        END IF
C
C ***** END OF OPTIONAL MANUAL PRESSURE SEARCH *****
C
        IF (K.EQ.KCHK.AND.NMODE.EQ.1) PRINT 50
50  FORMAT (//10X, 'DVL', 17X, 'DMG', 18X, 'DP',16X,'FNORM',/)
        IF (K.EQ.KCHK.AND.NMODE.EQ.2) PRINT 51
51  FORMAT (//10X, 'DVL', 17X, 'DMG', 17X, 'DVG',16X,'FNORM',/)
C
C ***** SOLVE FOR THE EXIT CONDITIONS AT THIS STEP *****
C
C      ZSCNT IS THE IMSL NON-LINEAR EQUATION SOLVER. IT FINDS
C      THE VALUES OF XGS(1) TO XGS(3) THAT ZERO THE VALUES OF
C      YY(1) TO YY(3) IN PSTPSC TO NSIG PLACES.
C
        CALL ZSCNT(PCN,NSIG,NEQ,ITMAX,PAR,XGS, FNORM,WK, IER)
C
        P(K)=P2G
        T(K)=T2G
        MG(K)=MG2G
        VB(K)=VB2G
        VG(K)=VG2G
        VL(K)=VL2G
        X(K)=X2G
        AEFF=AREA2G
        RHOGK=RHOG2G
C
        SIG(K)=SIGK
        RHOG(K)=RHOGK
C
        IF (NMODE.EQ.2) AREA(K)=AEFF/(1D0+DAFRIC)
        IF (N3.EQ.1) AREA(K)=AEFF
        AREAK=AREA(K)
        DA=AREA(K)-AREA(K-1)
        DAFSV=DAFRIC
        DVFSV=DVFRIC
        IF (NISEN.EQ.1) GO TO 52
        IF (N1.EQ.0) CALL FRIC
C
C ***** STORE MINIMUM PRESSURE POINT, IF ANY *****
C
52  IF (P(K).GT.P(K-1).AND.NMIN.EQ.0.AND.K.GT.KBPS) THEN
        NMIN=K-1
        PMIN=P(NMIN)/PZ(NUIN)
        END IF
C
C ** IF SEARCHING FOR MTO, PRINT LAST STEP REACHED AND RETURN FOR NEW MTO **
C
        IF (NSRCH.EQ.1.AND.K.GT.KBPS) THEN
C
                IF (IER.GT.0) THEN
                        IF (N2.EQ.0) PRINT *, 'INITIAL MTO GUESS TOO LARGE'
                        IF (N2.EQ.0) GO TO 15
                        KM1=K-1

```

```

        PLAST=P(KM1)/PZ(NUIN)
        IF (NMIN.EQ.0) PRINT 55,MTO,KM1,PLAST
55      FORMAT(1X,F22.18,I6,F13.2,I6,F13.2)
        IF (NMIN.GT.0) PRINT 55,MTO,KM1,PLAST,NMIN,PMIN
        NFAIL=1

C
        IF (DMT/2.LT.MT*DMTMIN) THEN
            NSRCH=0
            MTO=MBASE
            GO TO 15
        END IF

C
        GO TO 25
    END IF

C
    IF (K.EQ.NSTEP) THEN
        N2=1
        PE=P(K)/PZ(NUIN)
        IF (NMIN.EQ.0) PRINT 55,MTO,K,PE
        IF (NMIN.GT.0) PRINT 55,MTO,K,PE,NMIN,PMIN
        MBASE=MTO
        GO TO 25
    END IF

C
        GO TO 100
    END IF

C
C ***** PRINT LAST CONDITIONS IF COULD NOT REACH EXIT *****
C
    IF (IER.GT.0.AND.K.GT.KBPS) THEN
        PRINT *, ' ZSCNT IER=', IER
        PRINT *, ' LAST ATTAINABLE POINT:'
        WRITE(13,201) IER
201    FORMAT(' ZSCNT IER=',I3)
        WRITE(13,202)
202    FORMAT(' LAST ATTAINABLE POINT:')
        KLAST=K-1
        CALL PRINT1(KLAST)
        GO TO 105
    END IF

C
C ***** PRINT MINIMUM-PRESSURE CONDITIONS, IF ANY *****
C
    IF (NMIN.EQ.K-1) THEN
        WRITE(5,203)
        WRITE(13,203)
203    FORMAT(' MINIMUM-PRESSURE POINT:')
        CALL PRINT1(NMIN)
    END IF

C
C ***** SAVE THROAT CONDITIONS *****
C
    IF (AREA(K).LT.AREA(K-1)) THEN
        KTHT=K
        DAF'THT=DAFRIC
        DVFTHT=DVFRIC

```

```

        END IF
C
C ***** PRINT CONDITIONS AT EACH STEP *****
C
        IF (K.EQ.NSTEP) PRINT *, 'PORT EXIT:'
C
        IF (MOD(K-1,NSP).EQ.0.OR.K.GE.NSTEP
$ .OR.K.EQ.KCHK-1.OR.N1.EQ.2.OR.K.EQ.NPX-1) CALL PRINT1(KK)
C
C ***** PRINT THROAT CONDITIONS *****
C
        IF (KTHT.GT.0.AND.K.EQ.NSTEP) THEN
            PRINT 60
        60    FORMAT(// ' THROAT CONDITIONS:')
            WRITE(13,60)
            DAFRIC=DAFTHT
            DVFRIC=DVFTHT
            CALL PRINT1(KTHT)
        END IF
C
C ** SEARCH FOR NEXT PRESSURE IF EXIT VELOCITY IS GIVEN **
C
        IF (NEXIT.EQ.2) THEN
            IF (K.EQ.NSTEP.AND.ABS(V(K)-VEXIT).LT.1.0D-2) GO TO 100
            IF (K.EQ.NSTEP.AND.V(K).LT.VEXIT) THEN
                PE=PE+DP/10.0
                PEX=PE*PZ(NUIN)
                NBUF=1
                GO TO 105
            END IF
            IF (V(K).GT.VEXIT) THEN
                PE=P(K-1)+DP*(VEXIT-V(K-1))/(V(K)-V(K-1))
                PEX=PE*PZ(NUIN)
                NBUF=1
                GO TO 105
            END IF
        END IF
C
        IF (N1.EQ.2) GO TO 40
C
        100 CONTINUE
        IF (NEXIT.EQ.2.AND.NISEN.NE.1) NBUF=0
        105 CONTINUE
C
C ***** EVALUATE ISENTROPIC PROPERTIES *****
C
        IF (NBUF.EQ.0) THEN
            NISEN=1
            NDRIVE=2
            NBUF=1
            NEXIT=1
            VREAL=V(NX)
            PJET1=0.5*MT*V(NX)*V(NX)
            PRINT 112
        112    FORMAT('1',35X,'ISENTROPIC FLOW CALCULATION RESULT')
            WRITE(13,112)

```

```

        GO TO 18
    END IF
C
C ***** EVALUATE PREFORMANCE PARAMETERS *****
C
    IF (NEXIT.EQ.2.AND.NBUF.EQ.1) GO TO 21
C
    VRATIO=VREAL/V(NX)
    PJET2=0.5*MT*V(NX)*V(NX)
    EFFI=PJET1/PJET2
    WRITE(6,113) VRATIO
113  FORMAT(///25X,'VELOCITY RATIO AT EXIT',5X,'=',F13.7)
    WRITE(6,114) EFFI
114  FORMAT(/25X,'THRUST EFFICIENCY',10X,'=',2PF13.7,'%')
    WRITE(13,113) VRATIO
    WRITE(13,114) EFFI
    WRITE(4,115) MT,EFFI,T(1),T(NX)
115  FORMAT(F13.7,2PF13.7,OPF13.7,OPF13.7)
    WRITE(4,116) MG(1)/MT,MG(NX)/MT
116  FORMAT(2F13.7)
C
    REWIND 13
C
    PRINT*,'IF CONTINUE,READ 1 OR 2'
    READ(5,*) NECHO
    IF (NECHO.EQ.1) GO TO 15
C
    GO TO 15
C
999  STOP
C
    END
C ** ** ** ** ** ** ** ** ** ** ** ** ** ** ** ** ** ** ** ** ** ** ** ** ** ** ** ** ** ** ** ** ** ** ** ** ** ** ** ** ** ** ** **
C ** ** ** ** ** ** ** SUBROUTINE FOR PROGRAM INPUT ** ** **
C ** ** ** ** ** ** ** ** ** ** ** ** ** ** ** ** ** ** ** ** ** ** ** ** ** ** ** ** ** ** ** ** ** ** **
C
    SUBROUTINE INPUT(NX,IOPT,NSTEP,ISRCH,NUIN,NUOUT,NSP,
$                    KCHK,NSIG,DMTO,DMTMIN,ISTATE,PO,XGO,
$                    DO,VO,MTO,IEXIT,PE,VEXIT,LAMDA)
C
    IMPLICIT DOUBLE PRECISION (A-H,L-M,O-Z)
C
    ICHAN=5
    IF (ICHAN.NE.5) OPEN(ICHAN,FILE='GPES539.INPUTDAT')
    READ(ICHAN,*) IOPT
    READ(ICHAN,*) NSTEP
    READ(ICHAN,*) ISRCH
    READ(ICHAN,*) NUIN
    READ(ICHAN,*) NUOUT
    READ(ICHAN,*) NSP
    READ(ICHAN,*) KCHK
    READ(ICHAN,*) NSIG
    READ(ICHAN,*) DMTO
    READ(ICHAN,*) DMTMIN
    READ(ICHAN,*) ISTATE
    READ(ICHAN,*) PO

```

```

READ(ICHAN,*) XGO
READ(ICHAN,*) DO
READ(ICHAN,*) VO
READ(ICHAN,*) MTO
C
IF (IOPT.EQ.3) THEN
  READ(ICHAN,*) IEXIT
  IF (IEXIT.EQ.1) READ(ICHAN,*) PE
  IF (IEXIT.EQ.2) READ(ICHAN,*) VEXIT
  READ(ICHAN,*) LAMDA
END IF
C
IF (NSTEP.GT.NX) THEN
  PRINT*, 'INCREASE NX TO ',NSTEP
  STOP
END IF
C
RETURN
END
C
C ** ** ** ** ** ** ** ** ** ** ** ** ** ** ** ** ** ** ** ** ** ** **
C
C ** ** SUBROUTINE FOR DISCRETISATION EQUATIONS ** **
C
C ** ** ** ** ** ** ** ** ** ** ** ** ** ** ** ** ** ** ** ** ** **
C
SUBROUTINE PSTPSC(P1,T1,MG1,VB1,VG1,VL1,X1,DD,
$ P2,T2,MG2,VB2,VG2,VL2,X2,AREA2,RHOG2)
C
  IMPLICIT DOUBLE PRECISION (A-H,L-M,O-Z)
C
  PARAMETER (NE=3)
C
  DIMENSION XGS(NE),PF(NE),XSCALE(NE),XCALC(NE),PAR(1),
$ FDPREV(NE)
C
  COMMON /CONST/RU,MT /MODE/NMODE /BOUND/DVMAX,DMMAX,DPMAX,P2MN
  COMMON /FRC/MUL2,RRHOG2,RHOL2,VVG2,VVL2,R2,B2,DX,DVBSQ,VBSQM
  COMMON /XSCL/XSCALE,FDPREV /CHK/KCHK,K
  COMMON /EXIT/P2G,T2G,MG2G,VB2G,VG2G,VL2G,X2G,AREA2G,RHOG2G
  COMMON /ADD/NOPT,NISEN,LAMDA
C
C ***** STEP INLET PROPERTIES *****
C
  CALL PROPSC(P1,T1,HG1,HL1,RHOG1,RHOL1,MUG1,WG1)
C
  A1=VG1/VB1
  B1=VL1/VB1
  S1=(VG1-VL1)/VB1
  VB1SQ=VB1**2
  ML1=MT-MG1
  R1=ML1/MG1
  DIVSQ=VG1**2-VL1**2
  FXX=3D2
  DPGS=ODO
  DVGGS=ODO

```

```

KSTOP=0
JSTOP=0
C
RETURN
C
ENTRY FCN (XGS,FF,NEQ,PAR)
C
NEQ=NEQ
PPP=PAR(1)
C
C ***** GUESSED END QUANTITIES *****
C
DVLGS=XGS(1)/XSCALE(1)
DMGGS=XGS(2)/XSCALE(2)
IF (NMODE.EQ.1) DPGS=XGS(3)/XSCALE(3)
IF (NMODE.EQ.2) DVGGS=XGS(3)/XSCALE(3)
VL2=VL1+DVLGS
MG2=MG1+DMGGS
ML2=MT-MG2
R2=ML2/MG2
IF (NMODE.EQ.1) P2=P1+DPGS
C IF (NMODE.EQ.2) P2 IS AN INPUT FROM THE CALL
C
C ***** IF ZSCNT TRIES AN EXCESSIVE GUESS, RETURN WITH A LARGE ERROR *****
C
IF (ABS(DVLGS).GT.DVMAX.OR.ABS(DMGGS).GT.DMMAX.
$ OR.ABS(DVGGS).GT.DVMAX.
$ OR.ABS(DPGS).GT.DPMAX.OR.P2.LT.P2MN.OR.R2.LE.0) THEN
IF (K.NE.KSTOP) THEN
C PRINT *, 'GUESS OUTSIDE BOUNDS AT K=',K
C IF (ABS(DVLGS).GT.DVMAX) PRINT *, ' DVLGS=',DVLGS
C IF (ABS(DMGGS).GT.DMMAX) PRINT *, ' DMGGS=',DMGGS
C IF (ABS(DPGS).GT.DPMAX) PRINT *, ' DPGS=',DPGS
C IF (ABS(DVGGS).GT.DVMAX) PRINT *, ' DVGGS=',DVGGS
C IF (P2.LT.P2MN) PRINT *, ' P2=',P2
C IF (R2.LE.0) PRINT *, ' R2=',R2
KSTOP=K
END IF
FF(1)=1D2
FF(2)=1D2
FF(3)=1D2
IF (K.EQ.KCHK) PRINT 85,XGS
IF (K.EQ.KCHK) PRINT 86,FF,FXX
RETURN
END IF
C
C ***** STEP EXIT PROPERTIES *****
C
CALL PROPSC(P2,T2,HG2,HL2,RHOG2,RHOL2,MUG2,WG2)
C
C ***** EXIT GAS VELOCITY *****
C
IF (NMODE.EQ.1) VG2=1/(RHOG2*(AREA2/MG2-R2/(RHOL2*VL2)))
IF (NMODE.EQ.2) VG2=VG1+DVGGS
C
IF (VG2.LE.0D0) THEN

```

```

C      IF (K.NE.JSTOP) PRINT *, 'LIQ FLOW AREA .GT.PORT AREA AT K=',K
      JSTOP=K
      FF(1)=1D2
      FF(2)=1D2
      FF(3)=1D2
      IF (K.EQ.KCHK) PRINT 85,XGS
      IF (K.EQ.KCHK) PRINT 86,FF,FX
      RETURN
END IF

C
      VB2=(VG2+R2*VL2)/(1+R2)
      VB2SQ=VB2**2
      S2=(VG2-VL2)/VB2
      A2=VG2/VB2
      B2=VL2/VB2

C
C ***** MEAN QUANTITIES *****
C
      AM=(A1+A2)/2
      BM=(B1+B2)/2
      PM=(P1+P2)/2
      TM=(T1+T2)/2
      RM=(R1+R2)/2
      VBM=(VB1+VB2)/2
      VBSQM=(VB1SQ+VB2SQ)/2
      VGM=(VG1+VG2)/2
      VLM=(VL1+VL2)/2
      SM=(VGM-VLM)/VBM
      ASM=ABS(SM)

C
      CALL PROPC(PM, TM, HGM, HLM, RHOGM, RHOLM, MUGM, WGM)

C
C ***** DELTAS *****
C
      DP=P2-P1
      DR=R2-R1
      DVBSQ=VB2SQ-VB1SQ
      IF (NOPT.NE.1) DX=X2-X1

C
C ***** DROPLET DRAG COEFFICIENT *****
C
      REM=RHOGM*DD*ABS(VGM-VLM)/MUGM
      CDM=CD(REM)
      ASCDM=ASM*CDM

C
C ***** MOMENTUM EQUATION *****
C
      Z1=(1D0+RM)*DVBSQ/2D0
      Z2=-1.0D0/(AM*RHOGM)
      Z3=-RM/(BM*RHOLM)

C
      IF (NMODE.EQ.1) THEN
        DP=Z1/(Z2+Z3)
        P2=P1+DP
      END IF

C

```

```

      IF (NMODE.EQ.2) THEN
        DVBSQ=2DO*(Z2+Z3)*DP/(1DO+RM)
        VB2=SQRT(VB1**2+DVBSQ)
      END IF
C
C ***** SLIP RATIO FOR ISENTROPIC FLOW *****
C
      IF (NISEN.NE.1) GO TO 70
      S2=0.0DO
      GO TO 80
C
C ***** SLIP RATIO WHEN PRESSURE PROFILE IS OPTIMIZED *****
C
70  IF (NOPT.EQ.1) THEN
      VG2=VB2*A2
      VL2=VB2*B2
      RE=RHO2*DD*ABS(VG2-VL2)/MUG2
      IF (RE.EQ.0.) RE=1.0D-6
C
      CALL OSLIP(A2,B2,CDM,DD,DP,R2,RE,RHOL2,RHO2,VB2,S2)
C
      SM=(S1+S2)/2.
      ASM=ABS(SM)
      VB2SQ=VB2**2
      VBSQM=(VB1SQ+VB2SQ)/2
      AA=4.0*DD/(3.0*RHO2*SM*ASCDM*VBSQM)
      BB=DP+BM*BM*RHOLM*DVBSQ/2.0+BM*RHOLM*VBSQM*SM*DR/(1.+RM)**2
C
C ***** CHANGE IN DISTANCE *****
C
      X2=X1+AA*(BB-BM*RHOLM*VBSQM*(S2-S1)/(1.0+RM))
      DX=X2-X1
      GO TO 80
      END IF
C
C ***** CHANGE IN SLIP *****
C
      AA=BM*(1+RM)*DVBSQ/(2*VBSQM*DX) +
$      (1+RM)*DP/(BM*RHOLM*VBSQM*DX)
      BB=0.75*RHO2*ASCDM*(1+RM)/(BM*RHOLM*DD)-DR/((1+RM)*DX)
      PWR=MIN(700, BB*DX)
      S2=(AA-(AA-BB*S1)/EXP(PWR))/BB
C
80  B2=1-S2/(1+R2)
      VL2=B2*VB2
      DVL=VL2-VL1
      A2=1+R2*S2/(1+R2)
      VG2=A2*VB2
      DVG=VG2-VG1
      VLM=(VL1+VL2)/2
C
C ***** CHANGE IN GAS FLOW RATE *****
C
      E1=0.5*MG1*VG1**2+0.5*ML1*VL1**2
      E2=0.5*MG2*VG2**2+0.5*ML2*VL2**2
      H1=MG1*HG1+ML1*HL1

```

```

      DKE=E2-E1
C
      H2=H1-DKE
C
      MG2=(H2-ML2*HL2)/HG2
      DMG=MG2-MG1
C
C ***** FLOW AREA FOR PRESCRIBED P(X) CASE *****
C
      IF (NMODE.EQ.2) AREA2=MG2*(1/(RHOG2*VG2)+R2/(RHOL2*VL2))
C
C ***** COMPARISON OF CALCULATED AND GUESSED QUANTITIES *****
C
      XCALC(1)=XSCALE(1)*DVL
      XCALC(2)=XSCALE(2)*DMG
      IF (NMODE.EQ.1) XCALC(3)=XSCALE(3)*DP
      IF (NMODE.EQ.2) XCALC(3)=XSCALE(3)*DVG
      FDPREV(1)=DVL
      FDPREV(2)=DMG
      IF (NMODE.EQ.1) FDPREV(3)=DP
      IF (NMODE.EQ.2) FDPREV(3)=DVG
      FF(1)=XCALC(1)-XGS(1)
      FF(2)=XCALC(2)-XGS(2)
      FF(3)=XCALC(3)-XGS(3)
C
      IF (K.EQ.KCHK) THEN
          FNORM=FF(1)**2+FF(2)**2+FF(3)**2
          IF (NMODE.EQ.1) PRINT 85,DVLGS,DMGGS,DPGS
          IF (NMODE.EQ.2) PRINT 85,DVLGS,DMGGS,DVGGS
          IF (NMODE.EQ.1) PRINT 86,DVL,DMG,DP,FNORM
          IF (NMODE.EQ.2) PRINT 86,DVL,DMG,DVG,FNORM
      END IF
C
      85 FORMAT (3(E20.11))
      86 FORMAT (3(E20.11),E18.9/)
C
C ***** VALUES TO BE SAVED FOR NEXT STEP *****
C
      RRHOG2=RHOG2
      VVG2=VG2
      VVL2=VL2
      P2G=P2
      T2G=T2
      MG2G=MG2
      VB2G=VB2
      VG2G=VG2
      VL2G=VL2
      X2G=X2
      AREA2G=AREA2
      RHOG2G=RHOG2
C
      RETURN
      END
C

```

```

C ** ** ** ** ** ** ** ** ** ** ** ** ** ** ** ** ** ** ****
C
C ** ** ** ** **   PRINTOUT SUBROUTINE ** ** ** ****
C
C ** ** ** ** **   ** ** ** **   ** ** **   ** ** **
C
C
C   SUBROUTINE PRNTAB(AREA, DD, P, T, MG, VB, VG, VL, X, NWDTH, NX)
C
C   IMPLICIT DOUBLE PRECISION (A-H, L-M, O-Z)
C
C   DIMENSION AREA(NX), DD(NX), P(NX), T(NX), VB(NX)
C   DIMENSION VG(NX), VL(NX), X(NX), MG(NX), V(50)
C   DIMENSION PZ(2), XZ(2), VZ(2), TZ1(2), TZ2(2), AZ(2), DZ(2)
C
C   COMMON /CONST/RU, MT, V
C   COMMON /PRNT/NU, NP, KTHT, K, N3 /BL/AREAK, DA, DAFRIC, DVFRIC
C
C   ***** SCALING FACTORS AND CONVERSION FACTORS FOR OUTPUT *****
C
C   DATA PZ/1D3,6894.7572D0/,XZ/1D-3,2.54D-2/,VZ/1D0,0.3048D0/
C           KPA      PSIA          MM      IN          M/S      FT/S
C   DATA TZ1/1D0,1.8D0/,TZ2/0D0,459.67D0/,AZ/1D-4,6.4516D-4/
C           K      R          K      F          CM2      IN2
C   DATA DZ/1D-3,2.54D-2/
C           MM      IN          KG/M3      LB/FT3
C
C   RETURN
C
C   ENTRY PRINT1(J)
C
C   IF (MOD(NP,40).EQ.0.AND.NU.EQ.1.AND.NWDTH.EQ.0) PRINT 50
C   IF (MOD(NP,40).EQ.0.AND.NU.EQ.1.AND.NWDTH.EQ.1) PRINT 51
C   IF (MOD(NP,40).EQ.0.AND.NU.EQ.2.AND.NWDTH.EQ.0) PRINT 55
C   IF (MOD(NP,40).EQ.0.AND.NU.EQ.2.AND.NWDTH.EQ.1) PRINT 56
C
C   IF (MOD(NP,40).EQ.0.AND.NU.EQ.1.AND.NWDTH.EQ.0) WRITE(13,50)
C   IF (MOD(NP,40).EQ.0.AND.NU.EQ.1.AND.NWDTH.EQ.1) WRITE(13,51)
C   IF (MOD(NP,40).EQ.0.AND.NU.EQ.2.AND.NWDTH.EQ.0) WRITE(13,55)
C   IF (MOD(NP,40).EQ.0.AND.NU.EQ.2.AND.NWDTH.EQ.1) WRITE(13,56)
C
C   CALL PROPSC(P(J),T(J),HG,HL,RHOG,RHOL,MUG,WG)
C
C   ML=MT-MG(J)
C   XG=MG(J)/MT
C   R=ML/MG(J)
C   RV=(MG(J)/RHOG)/(ML/RHOL)
C   VF=1D0+DVFRIC
C   V(J)=VB(J)*VF/VZ(NU)
C
C   IF (NWDTH.EQ.0) PRINT 65,J,P(J)/PZ(NU),X(J)/XZ(NU),
C   $   VB(J)*VF/VZ(NU),VG(J)*VF/VZ(NU),VL(J)*VF/VZ(NU),
C   $   T(J)*TZ1(NU)-TZ2(NU),XG,AREA(J)/AZ(NU),
C   $   DD(J)/DZ(NU),R,RV,DAFRIC,DVFRIC
C
C   IF (NWDTH.EQ.1) PRINT 65,J,P(J)/PZ(NU),X(J)/XZ(NU),
C   $   VB(J)*VF/VZ(NU),VG(J)*VF/VZ(NU),VL(J)*VF/VZ(NU),
C   $   T(J)*TZ1(NU)-TZ2(NU),XG,AREA(J)/AZ(NU)

```

```

      IF (NWDTH.EQ.0) WRITE(13,65) J,P(J)/PZ(NU),X(J)/XZ(NU),
$     VB(J)*VF/VZ(NU),VG(J)*VF/VZ(NU),VL(J)*VF/VZ(NU),
$     T(J)*TZ1(NU)-TZ2(NU),XG,AREA(J)/AZ(NU),
$     DD(J)/DZ(NU),R,RV,DAFRIC,DVFRIC
C
      IF (NWDTH.EQ.1) WRITE(13,65) J,P(J)/PZ(NU),X(J)/XZ(NU),
$     VB(J)*VF/VZ(NU),VG(J)*VF/VZ(NU),VL(J)*VF/VZ(NU),
$     T(J)*TZ1(NU)-TZ2(NU),XG,AREA(J)/AZ(NU)
C
      NP=NP+1
C
      IF (MOD(NP,10).EQ.0) PRINT *, ' '
C
      RETURN
C
50  FORMAT('1',9X,'P',8X,'X',7X,'VBF',5X,'VGF',5X,'VLF',
$        6X,'T',6X,'XG',8X,'A',7X,'DD',6X,'R',7X,'RV',
$        4X,'DAFRIC  DVFRIC',/9X,'KPA',
$        7X,'MM',1X,3(5X,'M/S'),6X,'K ',
$        13X,'CM2',7X,'MM',21X,'PCT',6X,'PCT',/)
51  FORMAT('1',9X,'P',8X,'X',7X,'VBF',5X,'VGF',5X,'VLF',
$        6X,'T',6X,'XG',8X,'A',/9X,'KPA',
$        7X,'MM',1X,3(5X,'M/S'),6X,'K ',
$        13X,'CM2'/)
55  FORMAT('1',10X,'P',8X,'X',6X,'VBF',5X,'VGF',5X,'VLF',
$        6X,'T',6X,'XG',8X,'A',7X,'DD',7X,'R',6X,'RV',
$        4X,'DAFRIC  DVFRIC',/9X,'PSIA',
$        6X,'IN',1X,3(4X,'FT/S'),6X,'F ',
$        13X,'IN2',6X,'MILS',21X,'PCT',7X,'PCT',/)
56  FORMAT('1',10X,'P',8X,'X',6X,'VBF',5X,'VGF',5X,'VLF',
$        6X,'T',6X,'XG',8X,'A',/9X,'PSIA',
$        6X,'IN',1X,3(4X,'FT/S'),6X,'F ',
$        13X,'IN2'/)
65  FORMAT(1X,I3,F9.1,F9.3,4(F8.1),F8.4,F10.4,3(F8.2),2(2PF9.3))
C
      END
C
C ** ** ** ** ** ** ** ** ** ** ** ** ** ** ** ** ** ** ** ** ** ** **
C ** ** ** **   FRICTION SUBROUTINE * ** ** **
C ** ** ** **   ** ** ** ** ** ** ** ** ** ** **
C
      SUBROUTINE FRIC
C
      IMPLICIT DOUBLE PRECISION (A-H,L-M,O-Z)
C
      COMMON /FRC/MUL,RHOG,RHOL,VG,VL,R,B,DX,DVBSQ,VBSQ
      COMMON /BL/AREA,DA,DAFRIC,DVFRIC,THETA
C
      PI=3.14159D0
      CFL0=0.208/0.425**2.585
      RA=RHOL*VL/(R*RHOG*VG)
      RHOMX=RHOL/(1.0+RA)
      DELTA=THETA*72./7.
      RDELTA=RHOL*VL*DELTA/MUL

```

```

IF (RDELTA.GE.1) CFL=0.208/((DLOG10(RDELTA)+0.425)**2.585)
IF (RDELTA.LT.1) CFL=CFL0
CF=R*B*CFL/(1.0+R)
DTHETA=0.5*R*B*CF*DX/(1.0+R)-THETA*(8.0*DVBSQ/(7.0*VBSQ)
$   -0.5*DA/AREA)
C
IF (THETA+DTHETA.GT.THETA/2) THETA=THETA+DTHETA
C   (LIMIT THETA REDUCTION TO 1/2 FOR STABILITY EARLY IN THE NOZZLE)
DELST=9.0*THETA/7.0
C
RAD=SQRT(AREA/PI)
DAFRIC=-2.0*DELST/RAD
DVFRIC=-2.0*THETA/RAD
C
RETURN
END
C
C **   **   **   **   **   **   **   **   **   **   **   **
C
C **   **   **   SUBROUTINE FOR INLET PORT SHAPE   **   **   **
C
C **   **   **   **   **   **   **   **   **   **   **   **
C
SUBROUTINE SHAPE(X,AREA,NSTEP)
C
IMPLICIT DOUBLE PRECISION (A-H,L-M,O-Z)
C
DIMENSION X(NSTEP),AREA(NSTEP)
C
PI=3.14159D0
C
N1=10
DO 10 I=1,N1
X(I)=0.97*0.0254/(N1-1)*(I-1)
AREA(I)=PI*((2*0.0254)**2-X(I)*X(I))
10 CONTINUE
C
N2=10
DO 20 I=11,N1+N2
X(I)=0.97*0.0254+0.97*0.0254/N2*(I-10)
AREA(I)=SQRT((2*0.0254)**2-(1.94*0.0254-X(I))**2)
AREA(I)=3.5*0.0254-AREA(I)
AREA(I)=PI*AREA(I)*AREA(I)
20 CONTINUE
C
N3=30
DO 30 I=21,N1+N2+N3
X(I)=1.94*0.0254+0.405/N3*(I-20)
AREA(I)=PI*(1.5*0.0254)**2
30 CONTINUE
C
RETURN
END
C

```

```

C ** ** ** ** ** ** ** ** ** ** ** ** ** ** ** ** ** ** ** ** ** **
C
C ** SUBROUTINE FOR OPTIMIZATION OF PRESSURE PROFILE ** **
C
C ** ** ** ** ** ** ** ** ** ** ** ** ** ** ** **
C
SUBROUTINE OSLIP(A,B,CDM,DD,DP,R,RE,RHOL,RHOG,VB,S2)
C
IMPLICIT DOUBLE PRECISION(A-H,L-M,O-Z)
C
COMMON /ADD/NOPT,NISEN,LAMDA
C
CE=4.0*DD*LAMDA*B*B*RHOL/(3.0*RHOG*VB*VB*CDM)
DE=B*B*RHOL/(A*A*RHOG)
EE=B*B*RHOL/(A*RHOG*(1.0DO+R))+B*R/(1.0DO+R)-1.0DO
FE=DE*(2.0*A/(B*R)+1.0)+1.0
GE=R/(1.0+R)**2
C
IF (RE.LE.0.1611) CDE=1.0
IF (RE.GT.0.1611.AND.RE.LE.4.709D3) CDE=1.1107+
$ 0.06854*DLOG(RE)+0.004329*DLOG(RE)**2
IF (RE.GT.4.709D3) CDE=2.0
C
C *** USE BISECTIONAL METHOD TO FIND THE ROOT ***
C
XO=-0.05D0
X1=2.0D0
SIGO=1.0
SIG1=1.0
FXO=(FE*GE*XO+EE*CDE)/(2.0*GE*DE)
IF (FXO.LT.0.) SIGO=-SIGO
FXO=-DP*CE**(1./3.)/ABS(DP)*SIGO*(SIGO*FXO)**(1./3.)-XO
5 FX1=(FE*GE*X1+EE*CDE)/(2.0*GE*DE)
IF (FX1.LT.0.) SIG1=-SIG1
FX1=-DP*CE**(1./3.)/ABS(DP)*SIG1*(SIG1*FX1)**(1./3.)-X1
IF (FXO.EQ.SIGN(FXO,FX1)) STOP
10 X2=XO-FXO*(XO-X1)/(FXO-FX1)
SIG2=1.0
FX2=(FE*GE*X2+EE*CDE)/(2.0*GE*DE)
IF (FX2.LT.0.0) SIG2=-SIG2
FX2=-DP*CE**(1./3.)/ABS(DP)*SIG2*(SIG2*FX2)**(1./3.)-X2
IF (FXO.NE.SIGN(FXO,FX2)) GO TO 30
20 DELTA=ABS(X2-XO)
XO=X2
FXO=FX2
GO TO 40
30 DELTA=ABS(X2-X1)
X1=X2
FX1=FX2
C
C NORMALIZE THE CHANGE IF ABS(X2) GREATER THAN 1.0
C
40 IF (ABS(X2).GT.1.0) DELTA=DELTA/ABS(X2)
IF (DELTA.GT.1.0D-10) GO TO 10
S2=X2
C

```


COMMON /CONST/RU,MT,V,ISTATE /SIG/SIG /PRC/MUL

C

```
DATA TX/ .2793700D+03, .3203800D+03, .3428500D+03, .3577900D+03,
$ .3693500D+03, .3789200D+03, .3871600D+03, .3944500D+03,
$ .4010000D+03, .4069800D+03, .4124800D+03, .4223800D+03,
$ .4311100D+03, .4389600D+03, .4460900D+03, .4526500D+03/
DATA PX/ .2000000D+05, .1000000D+06, .2000000D+06, .3000000D+06,
$ .4000000D+06, .5000000D+06, .6000000D+06, .7000000D+06,
$ .8000000D+06, .9000000D+06, .1000000D+07, .1200000D+07,
$ .1400000D+07, .1600000D+07, .1800000D+07, .2000000D+07/
DATA ROGX/
$ .9502813D+00, .7365940D+01, .1418649D+02, .2092926D+02,
$ .2769316D+02, .3450656D+02, .4142502D+02, .4842615D+02,
$ .5558644D+02, .6289308D+02, .7037298D+02, .8583691D+02,
$ .1022495D+03, .1197605D+03, .1385041D+03, .1589825D+03/
DATA ROLX/
$ .1622498D+04, .1499250D+04, .1440922D+04, .1400560D+04,
$ .1367989D+04, .1340483D+04, .1315789D+04, .1293661D+04,
$ .1273885D+04, .1253133D+04, .1234568D+04, .1204819D+04,
$ .1166861D+04, .1133789D+04, .1102536D+04, .1070664D+04/
DATA HGX/
$ .2561911D+06, .2846800D+06, .2978600D+06, .3065400D+06,
$ .3131600D+06, .3185600D+06, .3231400D+06, .3271100D+06,
$ .3306100D+06, .3337400D+06, .3365600D+06, .3414400D+06,
$ .3454900D+06, .3488700D+06, .3516600D+06, .3539200D+06/
DATA HLX/
$ .9858333D+05, .1421300D+06, .1629800D+06, .1771500D+06,
$ .1882900D+06, .1976500D+06, .2058000D+06, .2131000D+06,
$ .2197400D+06, .2258600D+06, .2315600D+06, .2419700D+06,
$ .2513700D+06, .2600100D+06, .2680800D+06, .2757100D+06/
DATA MUGX/
$ .9874000D-05, .1089000D-04, .1146000D-04, .1186000D-04,
$ .1218000D-04, .1246000D-04, .1271000D-04, .1294000D-04,
$ .1317000D-04, .1347000D-04, .1357000D-04, .1397000D-04,
$ .1438000D-04, .1481000D-04, .1527000D-04, .1577000D-04/
DATA MULX/
$ .8874000D-03, .5155000D-03, .4045000D-03, .3495000D-03,
$ .3134000D-03, .2864000D-03, .2643000D-03, .2443000D-03,
$ .2269000D-03, .2109000D-03, .1959000D-03, .1683000D-03,
$ .1438000D-03, .1227000D-03, .1053000D-03, .9156000D-04/
DATA SIGX/
$ .1937000D-01, .1475000D-01, .1233000D-01, .1077000D-01,
$ .9594000D-01, .8639000D-02, .7833000D-02, .7133000D-02,
$ .6515000D-02, .5960000D-02, .5458000D-02, .4578000D-02,
$ .3827000D-02, .3176000D-02, .2606000D-02, .2102000D-02/
```

C

```
IF (ISTATE.EQ.1) THEN
TT=TSAT(P)
RHOG=VOL(1,P,TT,1,X,1)
HG=ENTH(2,P,TT,1,X,1)
CALL TRANSP(2,P,TT,1,X,CPG,MUG,COG,PRAG,SIG,1)
RHOL=VOL(1,P,TT,3,X,2)
HL=ENTH(2,P,TT,3,X,2)
CALL TRANSP(2,P,TT,3,X,CPL,MUL,COL,PRAL,SIG,2)
```

C

```
ENDIF
```

```

      IF (ISTATE.EQ.2) THEN
C
      IF (P.LT.PX(1).OR.P.GT.PX(NX1)) THEN
          PRINT *, 'OUT OF RANGE IN PROPSC AT P=', P
          STOP
      END IF
C
      NORD=2
C
      CALL SLUP1(P, TT, YDOT, PX, TX, NX1, NORD)
      CALL SLUP2(P, RHOG, PX, ROGX)
      CALL SLUP2(P, RHOL, PX, ROLX)
      CALL SLUP2(P, HG, PX, HGX)
      CALL SLUP2(P, HL, PX, HLX)
      CALL SLUP2(P, MUG, PX, MUGX)
      CALL SLUP2(P, MUL, PX, MULX)
      CALL SLUP2(P, SIG, PX, SIGX)
C
      ENDIF
C
      WG=RHOG*RU*TT/P
C
      RETURN
      END
C
C **      **      **      **      **      **      **      **      **      **      **      **
C
C **      **      **      SUBROUTINE FOR TABLE INTERPOLATION      **      **      **
C
C **      **      **      **      **      **      **      **      **      **      **      **
C
      SUBROUTINE SLUP1(X, Y, YDOT, XS, YS, LN, MORD)
C
      IMPLICIT DOUBLE PRECISION (A-H, O-Z)

      DIMENSION XS(LN), YS(LN)
      DATA ZERO/0.0DO/, ONE/1.0DO/
C
      N=LN
      M=MORD+1
      K=N
      L=1
C
      BEGIN BINARY SEARCH FOR APPROPRIATE SUBINTERVAL
10      J=(K+L)/2
          IF (X-XS(J))15, 35, 20
15      K=J
          GO TO 25
20      L=J
25      IF (IABS(K-L)-1)10, 30, 10
30      J=MAX0(K, L)
C
      SET INDEXES OF SUB-INTERVAL CONTAINING POINT GIVEN
C
      (ALSO INSURE INDEXES ARE WITHIN THOSE ALLOWED, I.E., 1 TO N)
35      NN=MAX0(1, J-M/2)
          MM=MINO(N, NN+M-1)
          NN=MM-M+1

```

```

C      ENTRY SLUP2(X,Y,XS,YS)
C
40  Y=ZERO
    YDOT=ZERO
    DO 90 J=NN,MM
      T=YS(J)
      K=0
      DO 60 I=NN,MM
        IF (I-J)45,60,45
45  R=X-XS(I)
      IF (R)55,50,55
50  R=ONE
      K=1
      IF (MORD)55,55,90
55  T=T*R/(XS(J)-XS(I))
60  CONTINUE
      IF (K)70,70,65
65  YDOT=YDOT+T
      GO TO 90
70  Y=Y+T
C      IS THE DERIVATIVE REQUESTED AT THE GIVEN POINT
      IF (MORD)75,75,90
75  DO 85 I=NN,MM
      IF (I-J)80,85,80
80  YDOT=YDOT+T/(X-XS(I))
85  CONTINUE
90  CONTINUE
C
100 RETURN
    END

```

APPENDIX B

THE SECANT METHOD FOR SIMULTANEOUS NONLINEAR EQUATIONS

The secant method is concerned with a computational procedure for the solution of a system of simultaneous nonlinear equations

$$f_i(\mathbf{x}) = 0 \quad \text{for } i=1, \dots, n \quad (\text{B.1})$$

where $\mathbf{x} = (x_1, \dots, x_n) \in E_n$ and each f_i is a computable function of \mathbf{x} . The f_i is supposed to have second-order derivatives, but no derivatives are calculated. The detailed iterative procedure can be described in the following steps:

1) An initial guess of \mathbf{x} is made.

2) The $n+1$ "trial solutions" $\mathbf{x}^1, \dots, \mathbf{x}^{n+1}$ are generated in the neighbourhood of initial guess \mathbf{x} . On the basis of these "trial solutions" the objective functions $f_i(\mathbf{x}^j)$ are calculated.

3) Let

$$\bar{\mathbf{x}} = \sum_{j=1}^{n+1} \pi_j \mathbf{x}^j \quad (\text{B.2})$$

where π_j must satisfy the relationship

$$\sum_{j=1}^{n+1} \pi_j = 1 \quad (\text{B.3})$$

and should be found from the following algebraic equations

$$\sum_{j=1}^{n+1} \pi_j f_i(\mathbf{x}^j) = 0 \quad \text{for } i=1, \dots, n \quad (\text{B.4})$$

4) A new set of trial solutions can be obtained by replacing, with $\bar{\mathbf{x}}$, some \mathbf{x}^j for which $\|\mathbf{x}^j\|$ is minimal, where

$$\|\mathbf{x}\| = \sum_{i=1}^n |f_i(\mathbf{x})|^2 \quad (\text{B.5})$$

5) The procedure is terminated when the convergence criterion is satisfied or a specified number of iterations has been exceeded. Numerically the convergence criterion is that the minimal of $\|\mathbf{x}^j\|$ should be zero to within a specified accuracy. Then \mathbf{x}^j for which $\|\mathbf{x}^j\|$ is minimal is taken as the root of the simultaneous nonlinear equations (B.1).

APPENDIX C

PRESSURE FORCE ON A SPHERICAL DROPLET

Consider a single spherical droplet of liquid travelling in a faster moving expanding gas. The force exerted on this spherical droplet as a result of static pressure variation around it can be determined by considering a small portion of the surface area of the droplet dA as shown in Fig.C.1. A pressure forces P acts upon this area dA . Suppose the droplet has a radius r , then we have

$$dA = r \cdot d\theta \cdot (r \cdot \sin \theta \cdot d\phi) \quad (C.1)$$

and

$$Z = r \cdot \sin \theta \cdot \cos \phi \quad (C.2)$$

It is further assumed that the pressure variation across the droplet is linear in the direction of flow, i.e. Z-direction. Hence

$$P = \frac{dP}{dZ} Z \quad (C.3)$$

and

$$P_Z = P \cdot \sin \theta \cdot \cos \phi \quad (C.4)$$

which is the pressure force acting in the negative direction in the quadrant shown in the figure. Then,

$$dF_Z = -P_Z dA \quad (C.5)$$

Then substituting dA , Z as well as Eqn.(C.3) and (C.4) into the above equation leads to the following relationship:

$$dF_z = -\frac{dP}{dZ} \cdot r^3 \cdot \sin^3 \theta \cdot d\theta \cdot \cos^2 \phi \cdot d\phi \quad (\text{C.6})$$

The pressure force acting upon the droplet can therefore be obtained by integrating Eqn.(C.6) over the whole droplet:

$$\begin{aligned} F_z &= -\frac{dP}{dZ} \cdot r^3 \int_0^\pi \int_0^{2\pi} (\sin^3 \theta \cdot d\theta) \cos^2 \phi \cdot d\phi \\ &= -\frac{4}{3}\pi r^3 \frac{dP}{dZ} \\ &= -(\text{volume of droplet}) \frac{dp}{dZ} \end{aligned} \quad (\text{C.7})$$

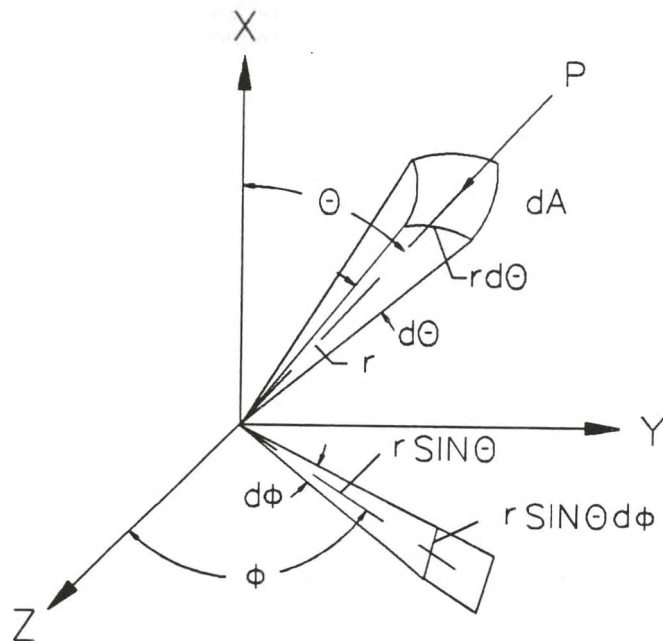


Fig.C.1. Differential Surface Area of a Spherical Droplet

APPENDIX D

FIGURES

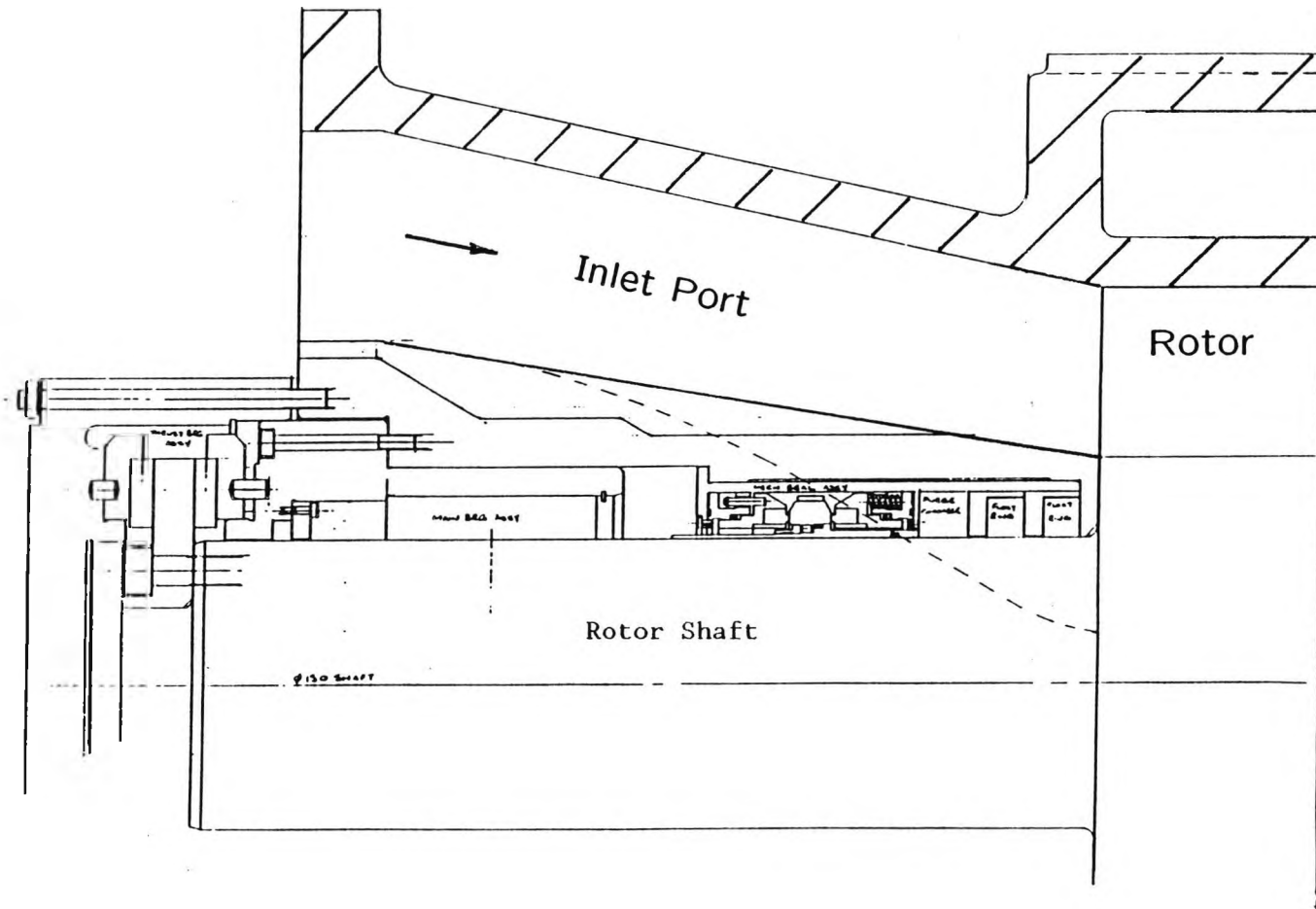


Fig.6.1. Layout of the New Lysholm Screw Expander Inlet Port

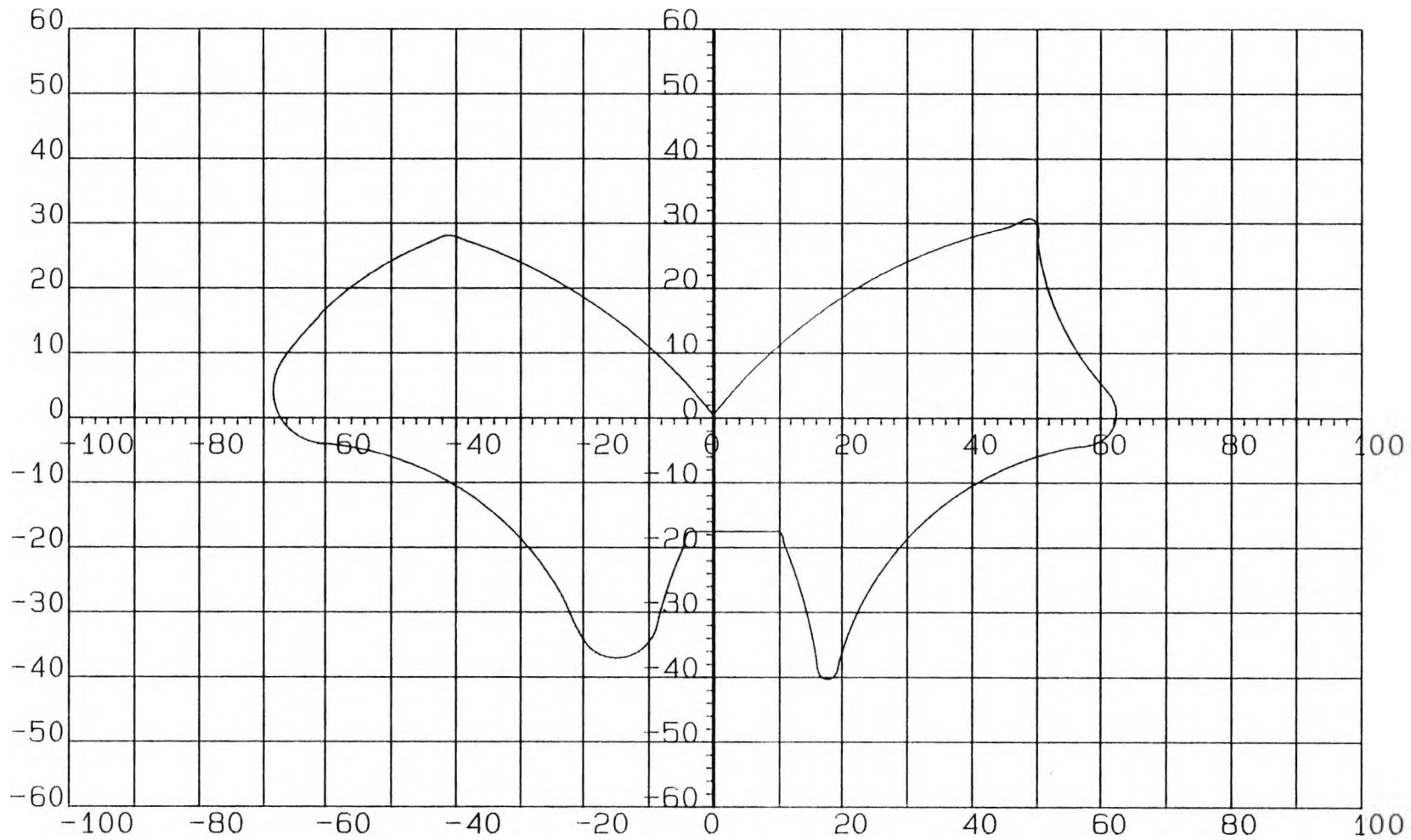


Fig.6.2. Inlet Port Exit Cross-Section

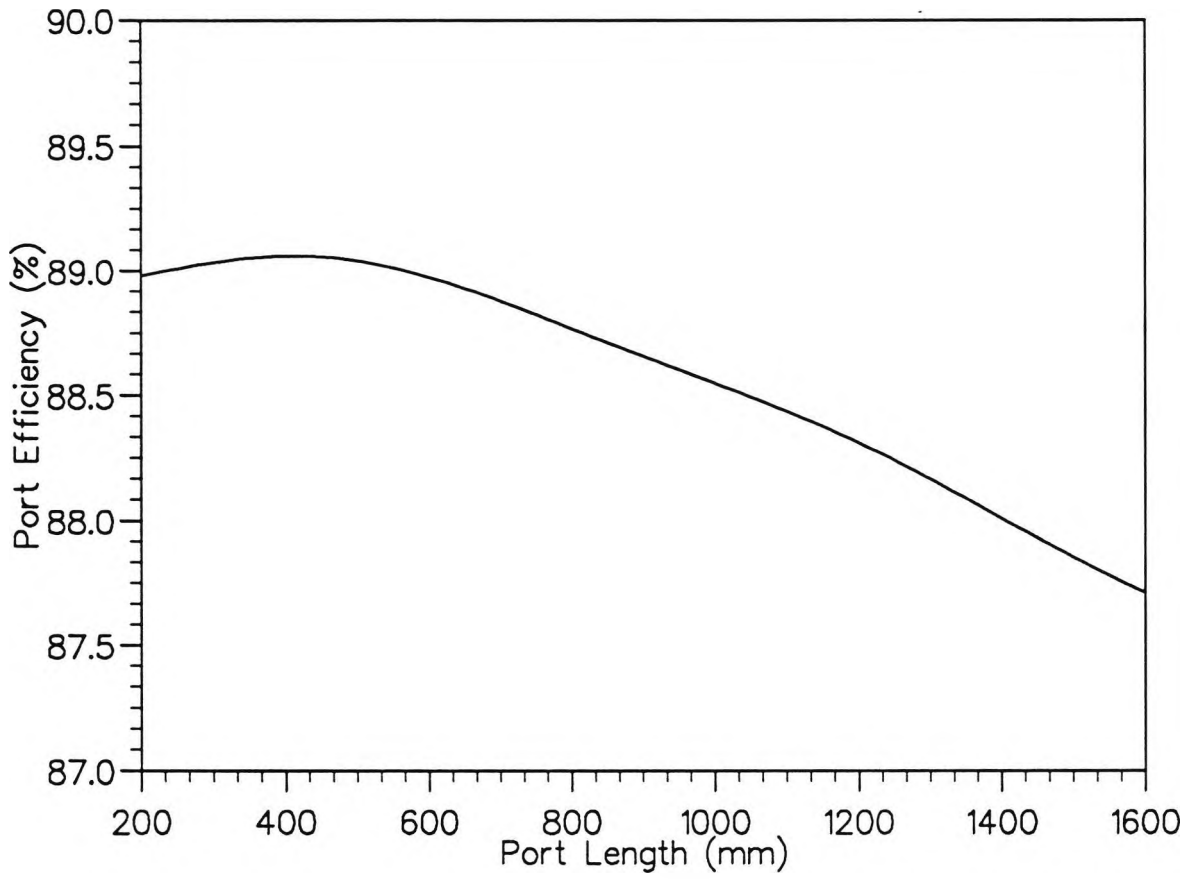


Fig.6.3. Effect of Inlet Port Length on Efficiency

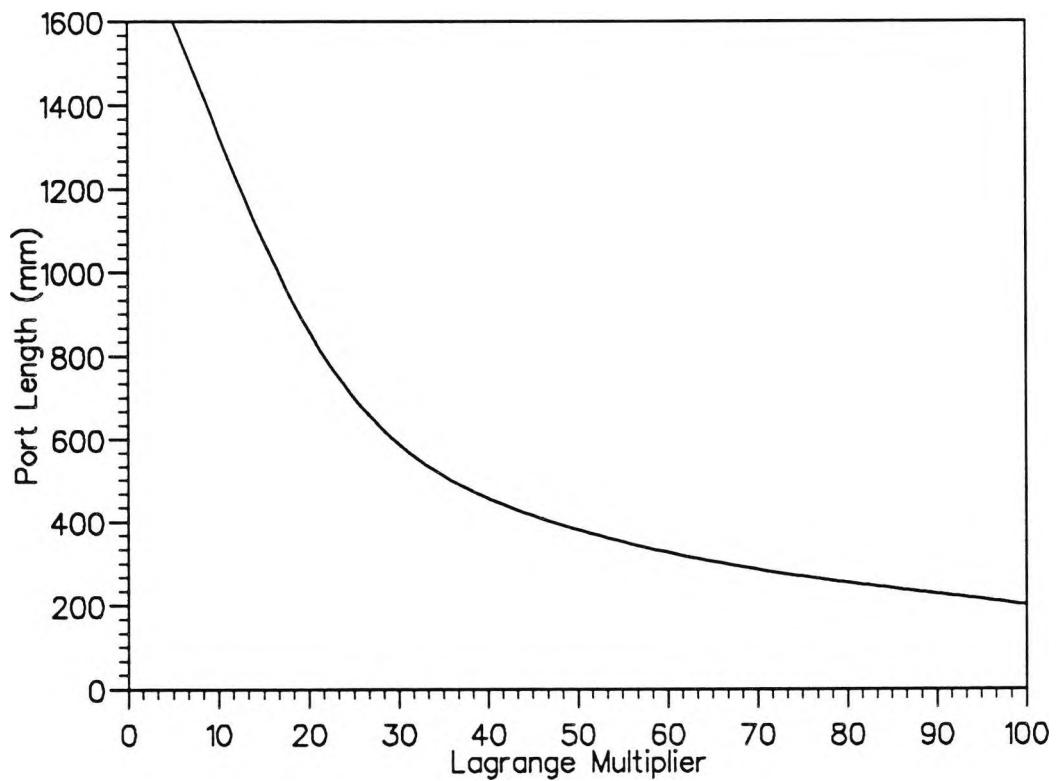


Fig.6.4. Relationship between Lagrange Multiplier and Port length

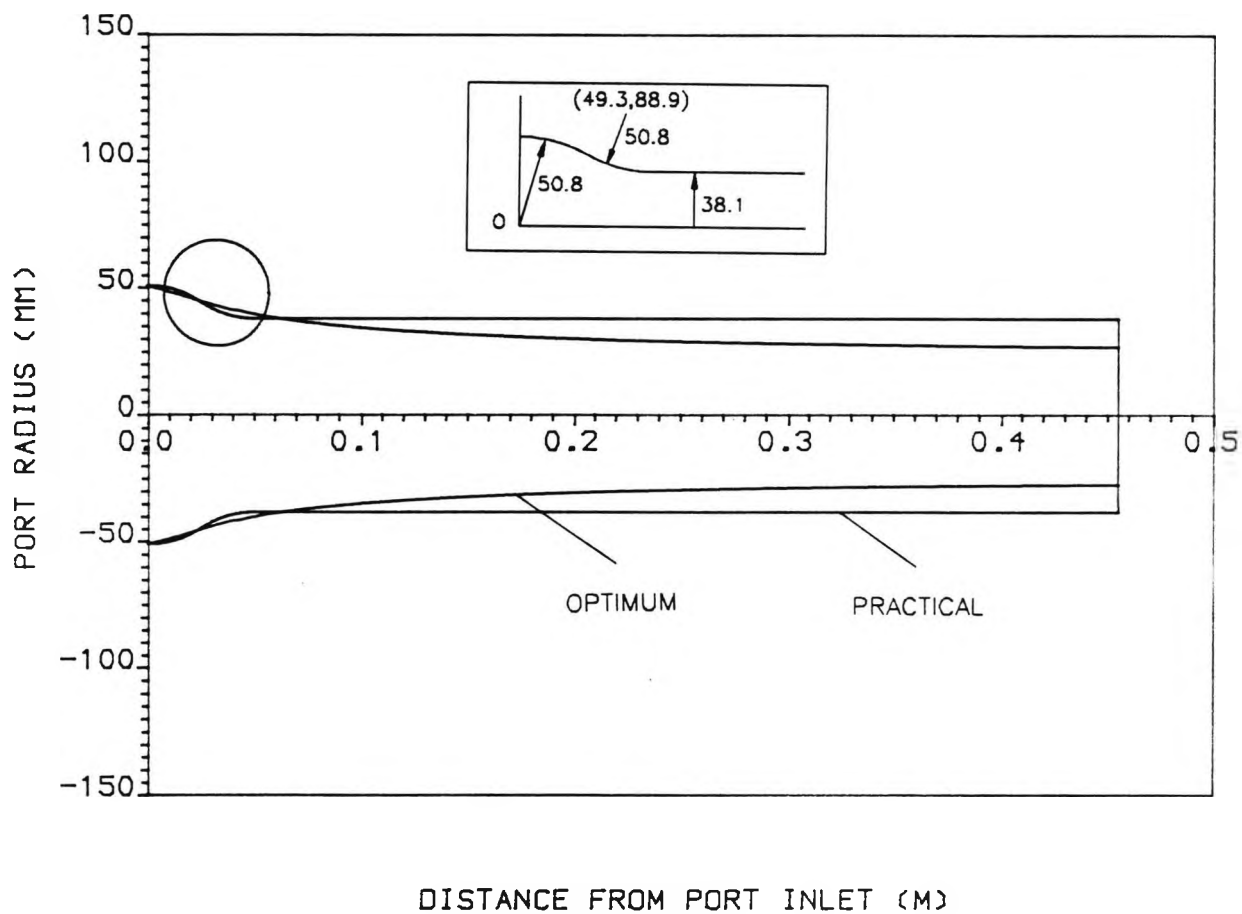


Fig.6.5. Optimum and Practical Inlet Port Contours

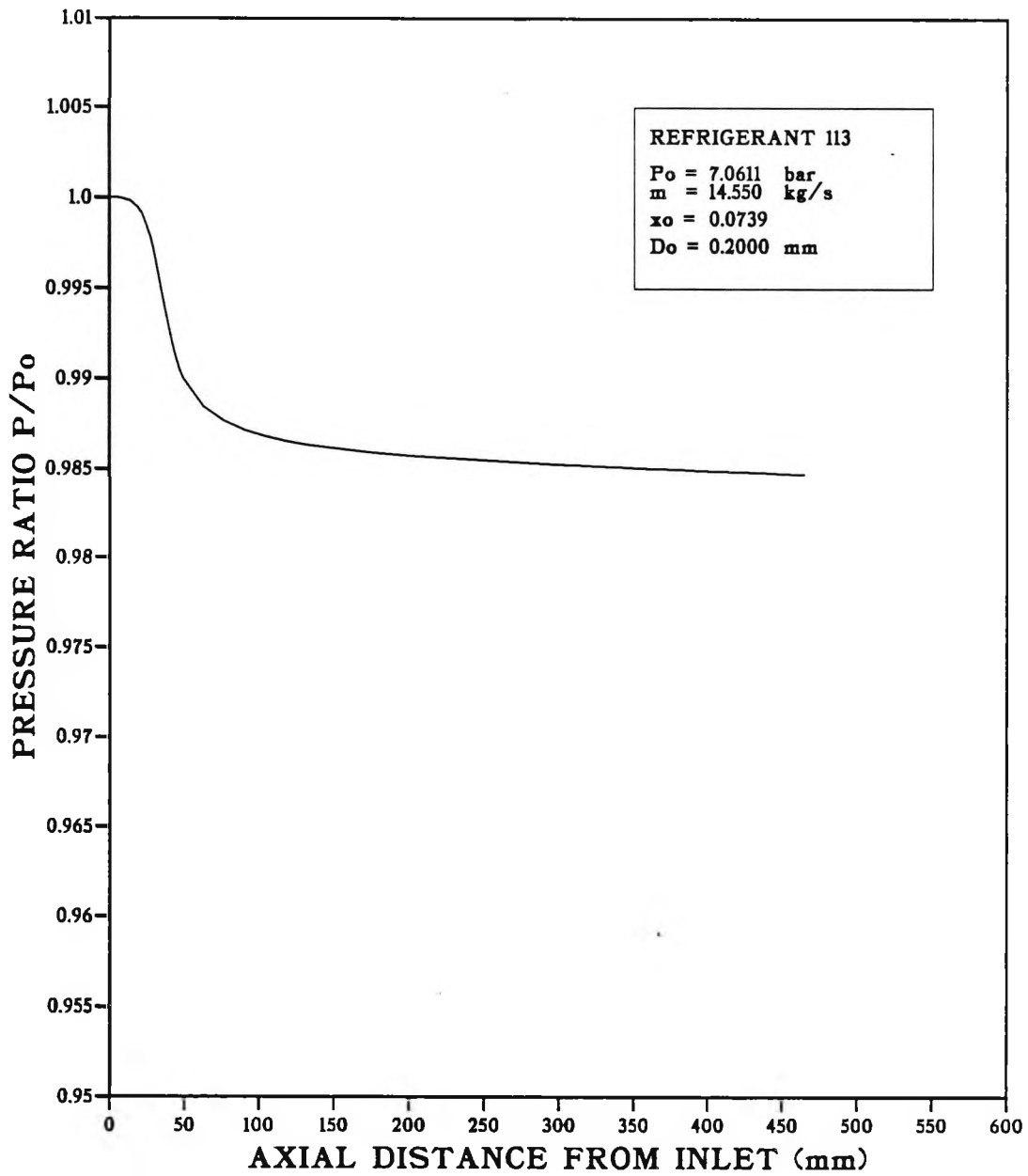


Fig.6.6. Axial Pressure Distribution

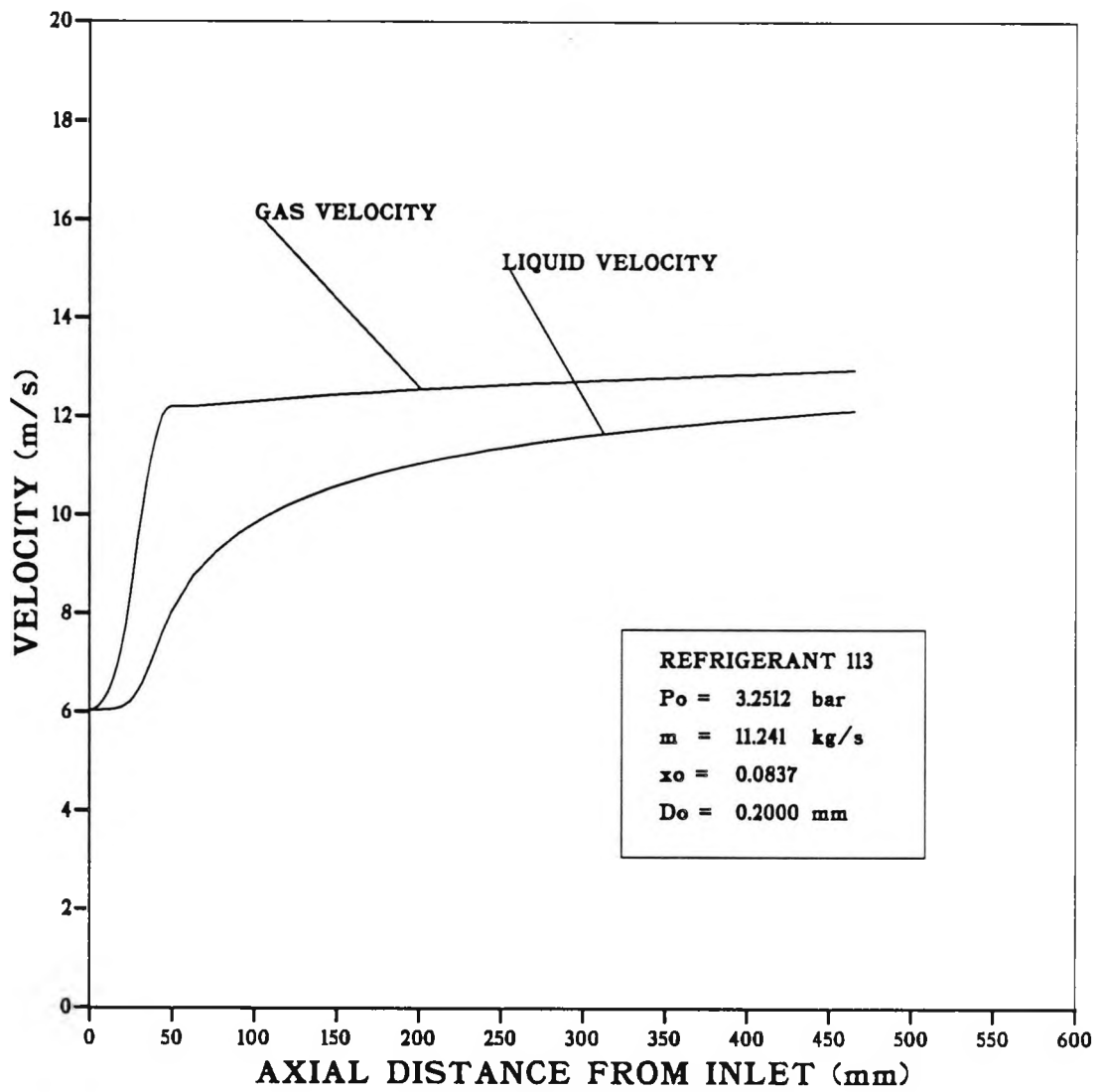


Fig.6.7. Liquid and gas Velocity Distributions

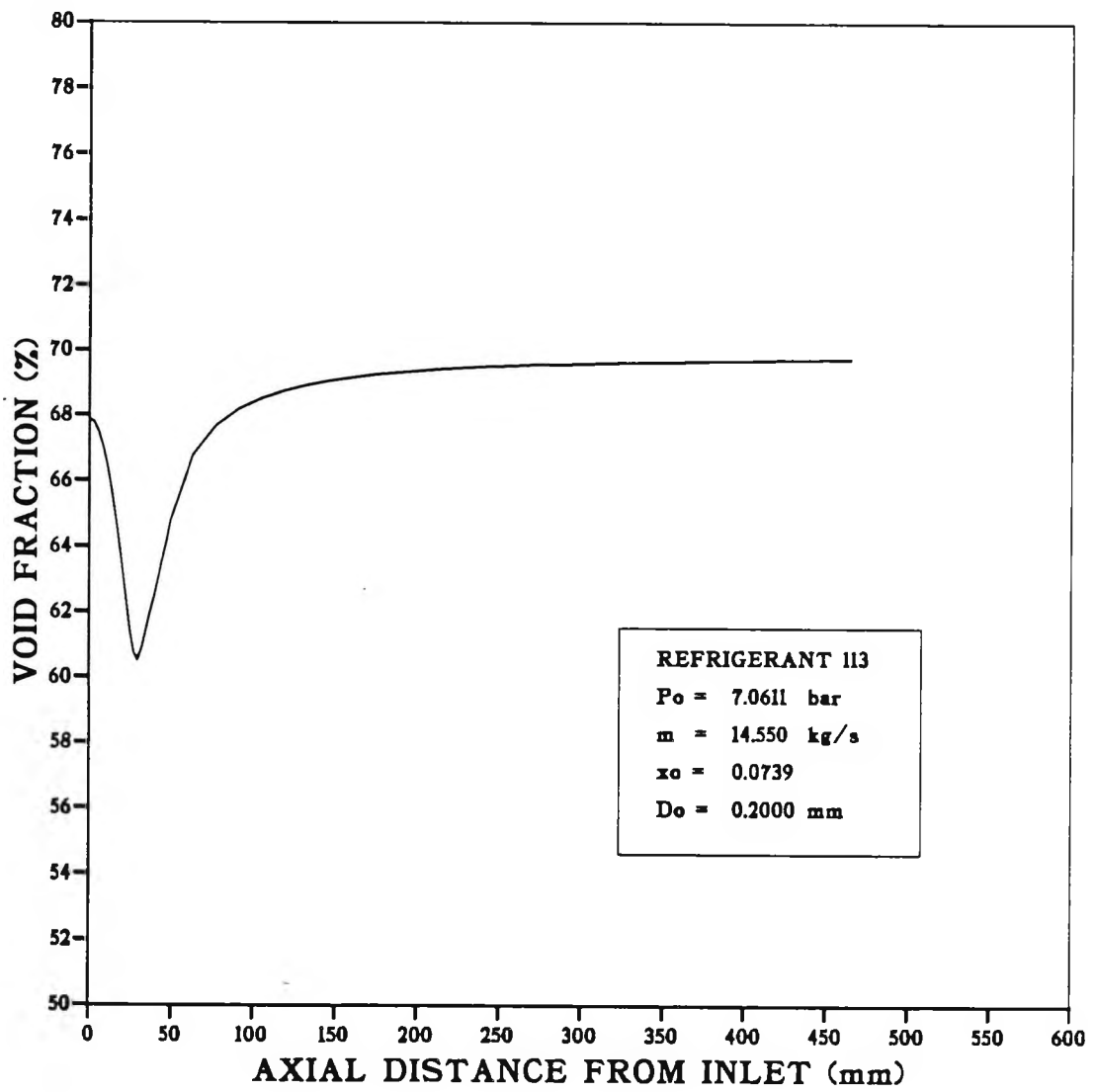


Fig.6.8. Averaged Void Fraction Distribution

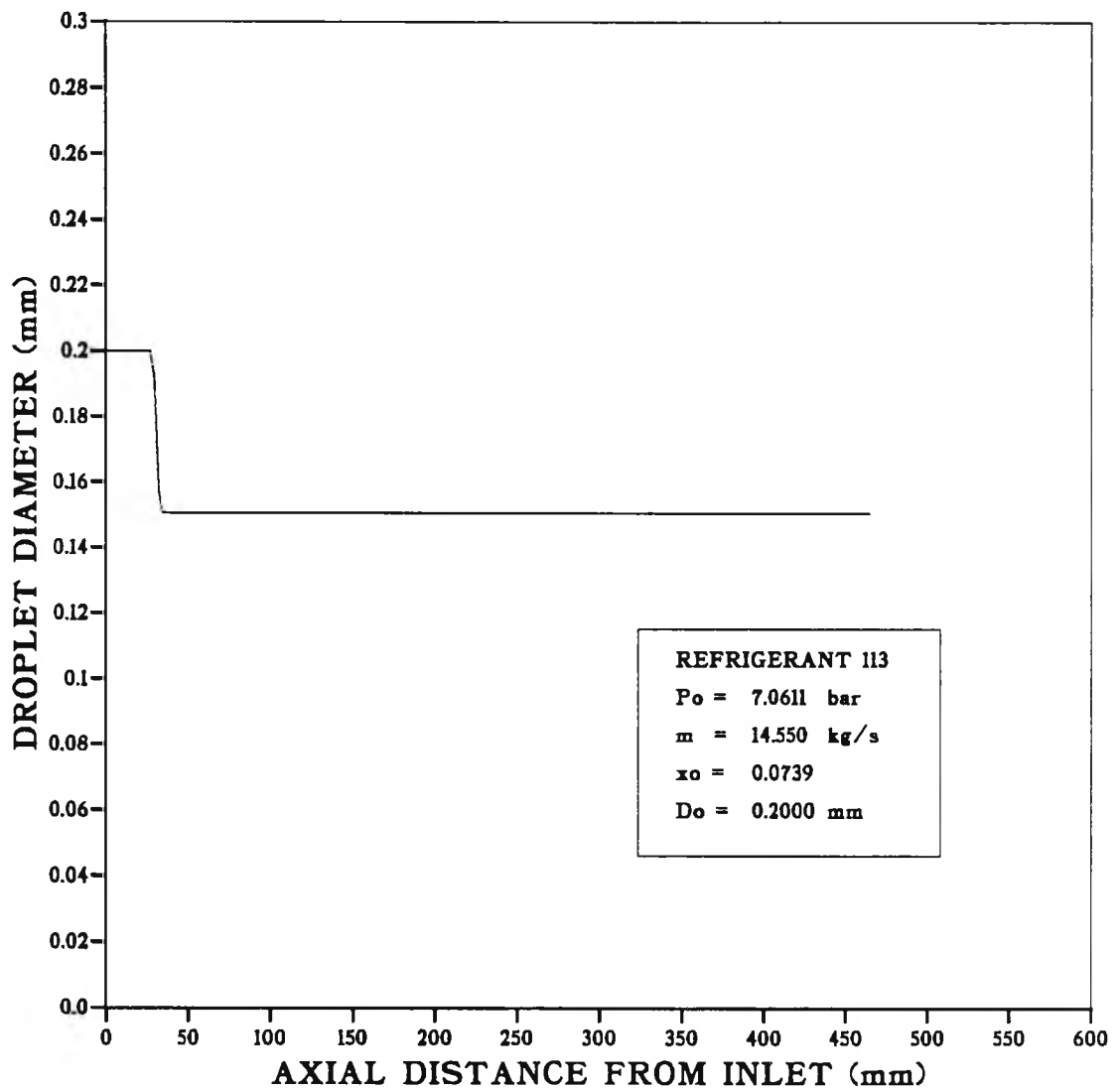


Fig.6.9. Droplet Diameter Distribution

Table 6.1. Computational Results for Practical Inlet Port

FLOW CONDITIONS AT INLET					EFFICIENCY (%)
PRESSURE (Bar)	TEMPERATURE (°C)	DRYNESS FRACTION	VELOCITY (m/s)	MASS FLOW RATE (kg/s)	
7.061	121.8	0.0739	4.0	14.55	86.9
7.061	121.8	0.2572	8.3	11.55	89.5
6.435	117.3	0.111	3.8	9.8097	86.1
6.417	117.2	0.3852	10.7	9.4822	91.4
5.331	108.6	0.1794	4.2	6.2595	85.9
5.182	107.4	0.2748	8.4	8.25	88.5
4.536	101.5	0.4019	11.4	6.95	89.2
3.2385	89.5	0.2995	11.2	6.6086	86.5

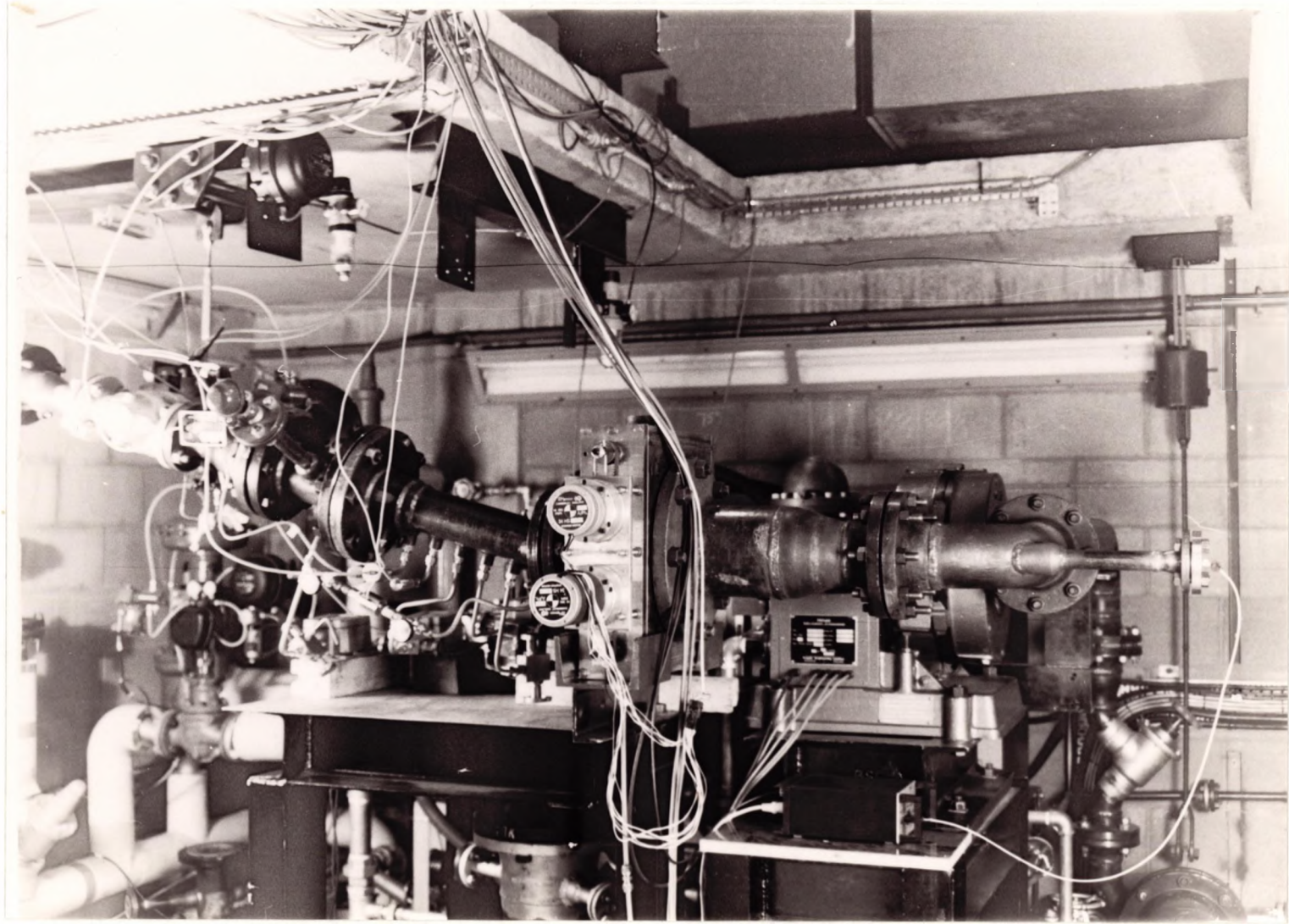


Fig.7.1. A Photographic View of the Test Rig

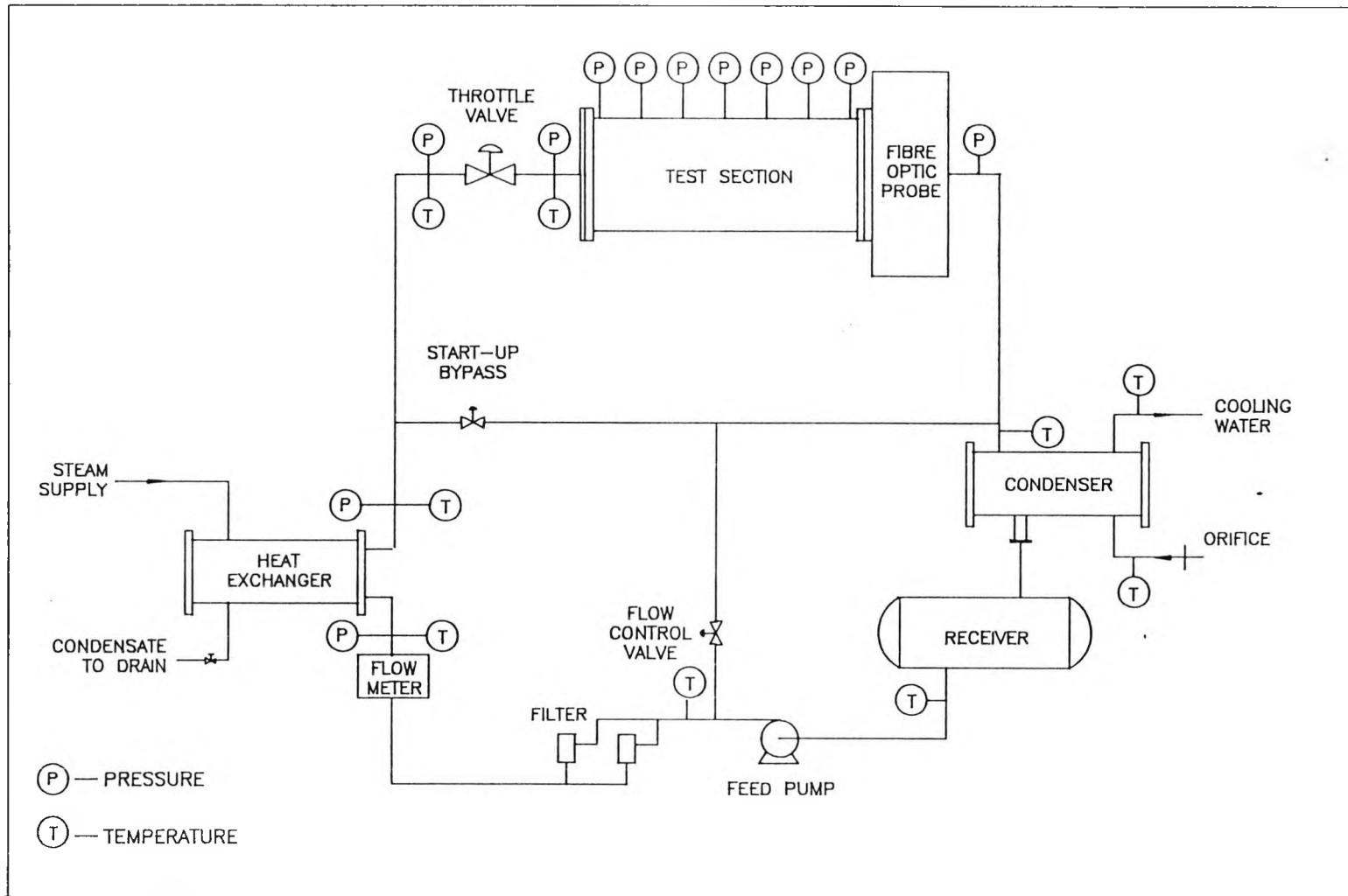


Fig.7.2. Schematic Diagram of the Test Rig

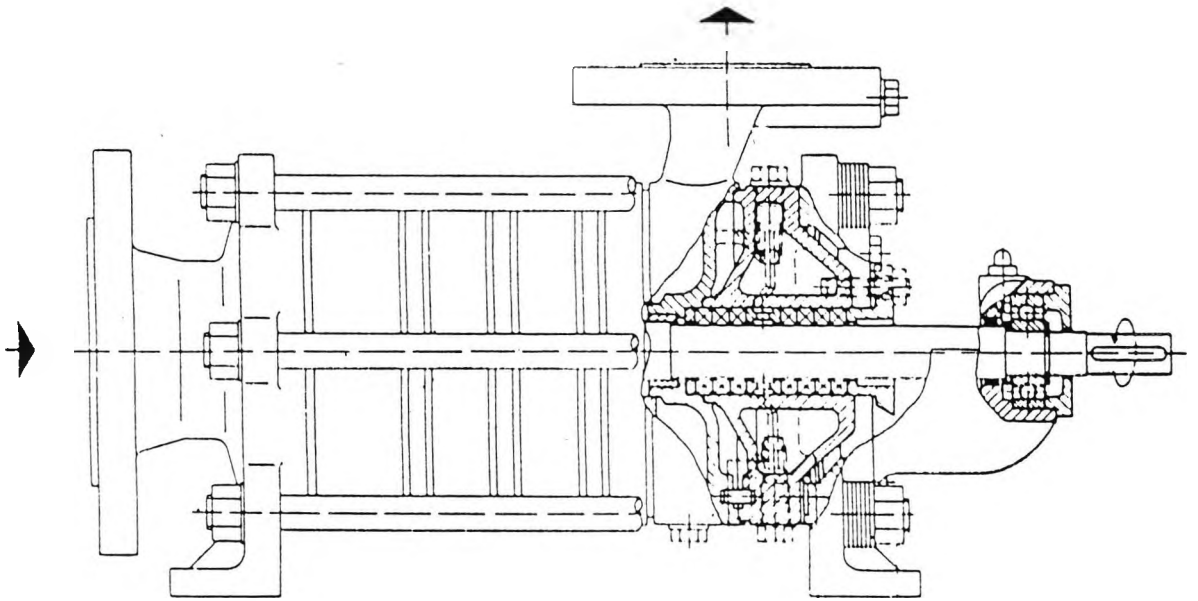


Fig.7.3. Schematic of the Feed Pump

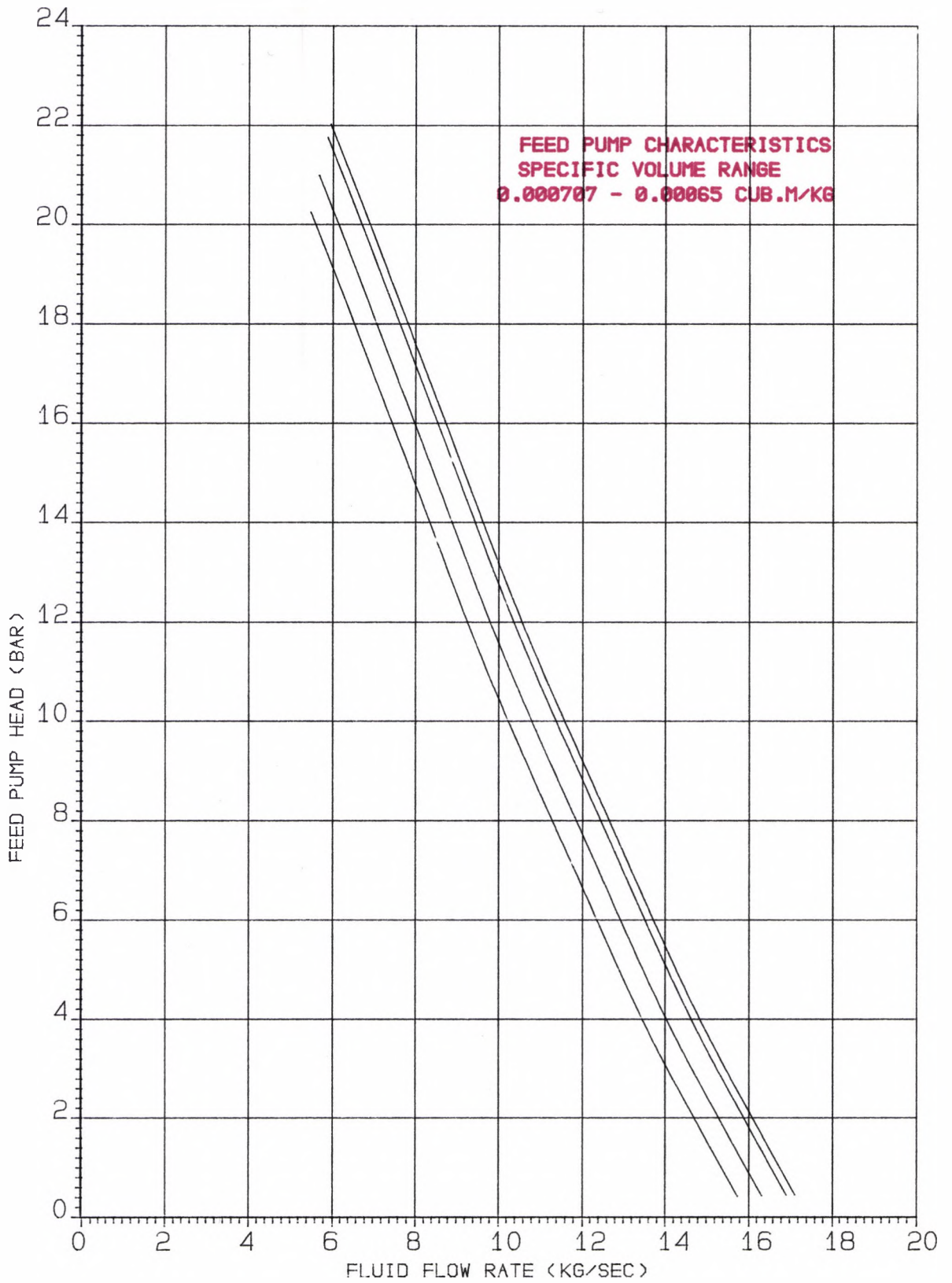


Fig.7.4. Feed Pump Characteristic

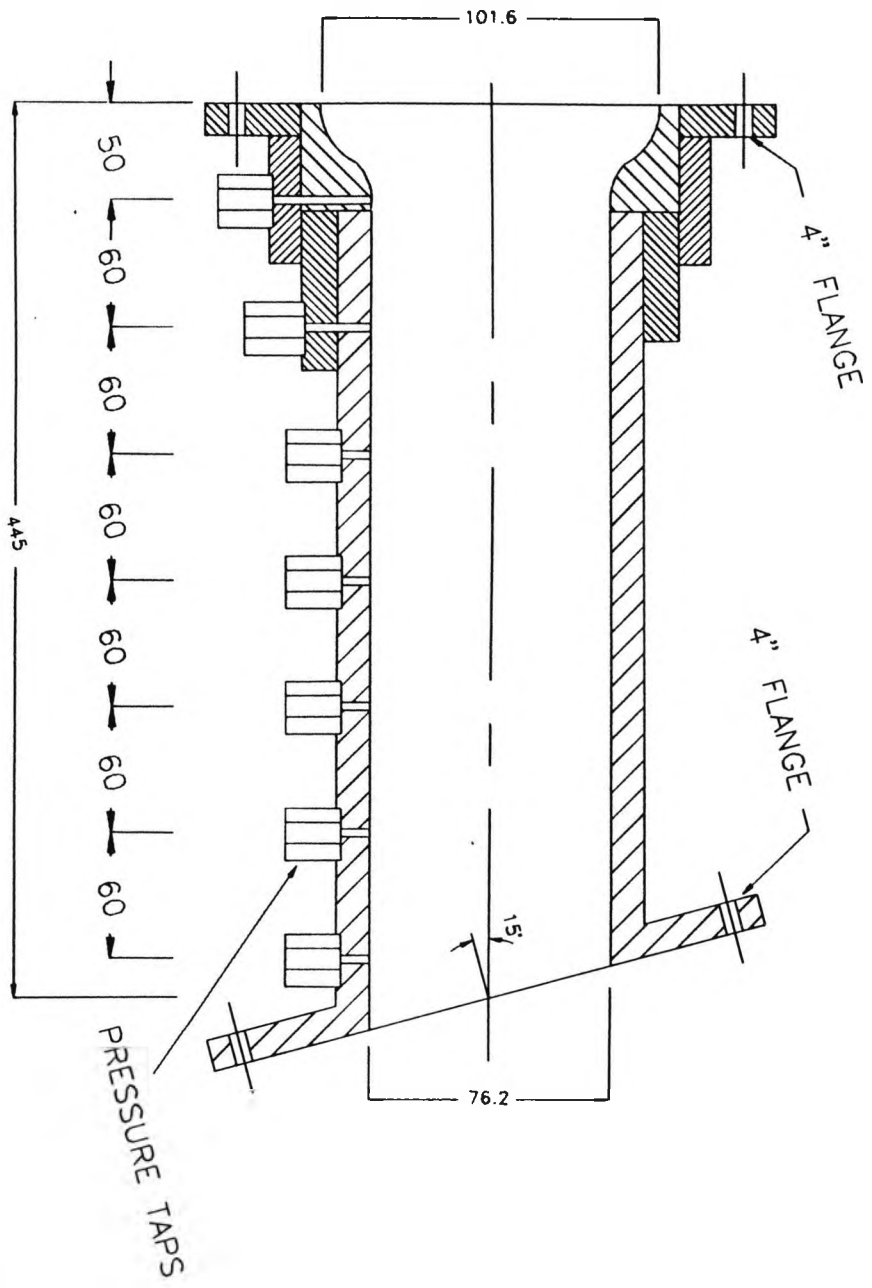


Fig. 7.5. Scale Drawing of No. 1 Inlet Port

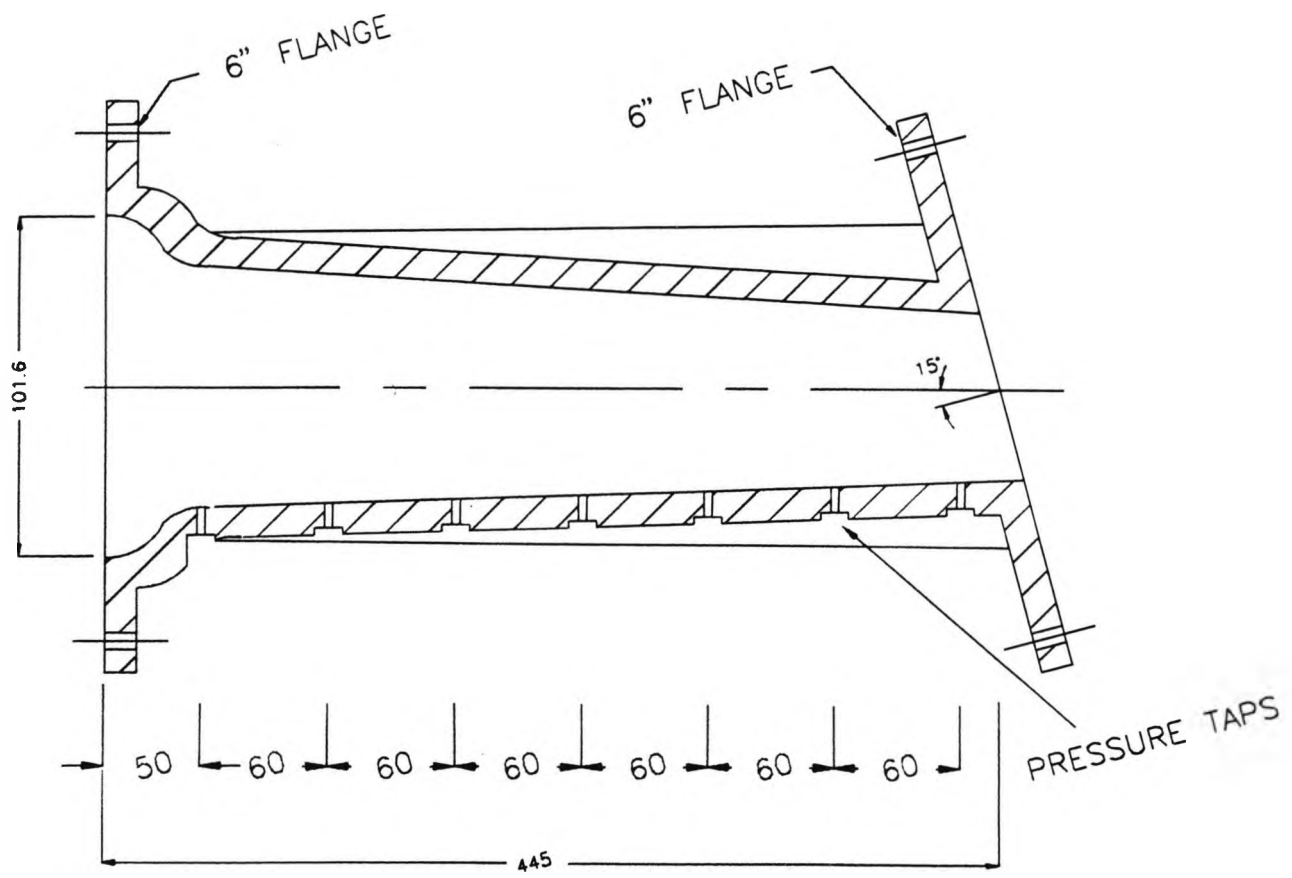


Fig.7.6. Schematic Drawing of No.2 Inlet Port

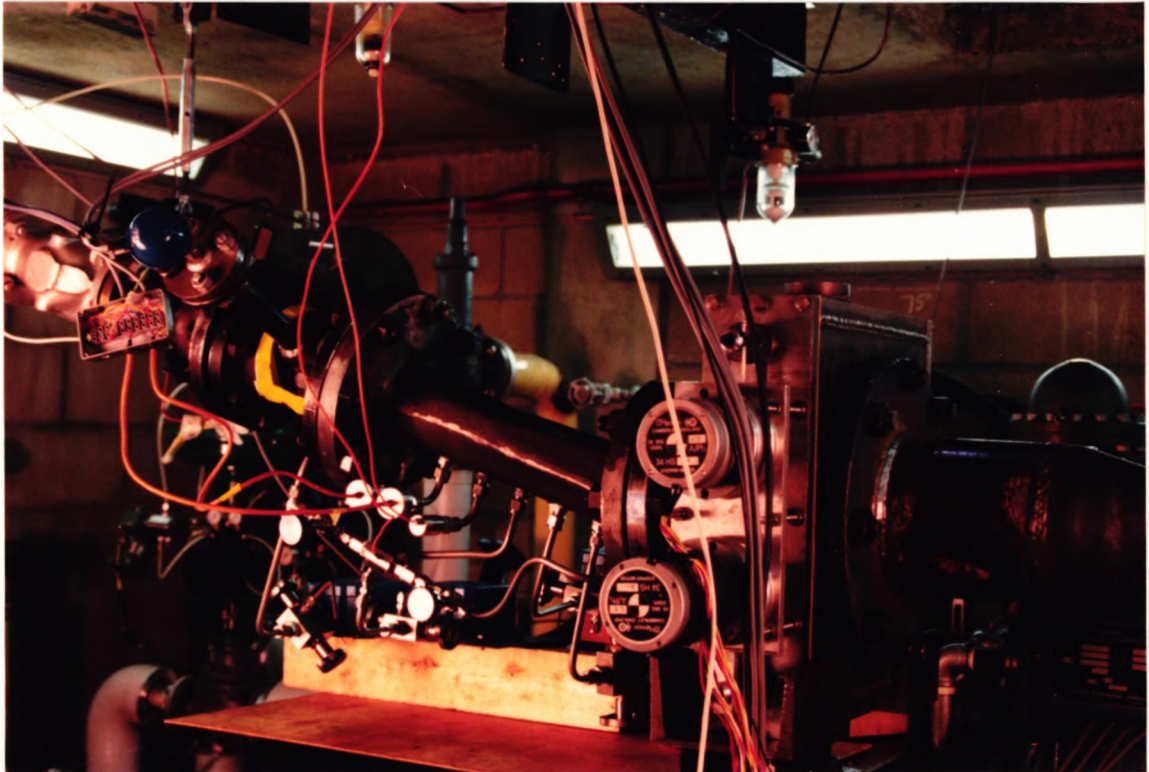


Fig.7.7. No.2 Inlet Port in Situ

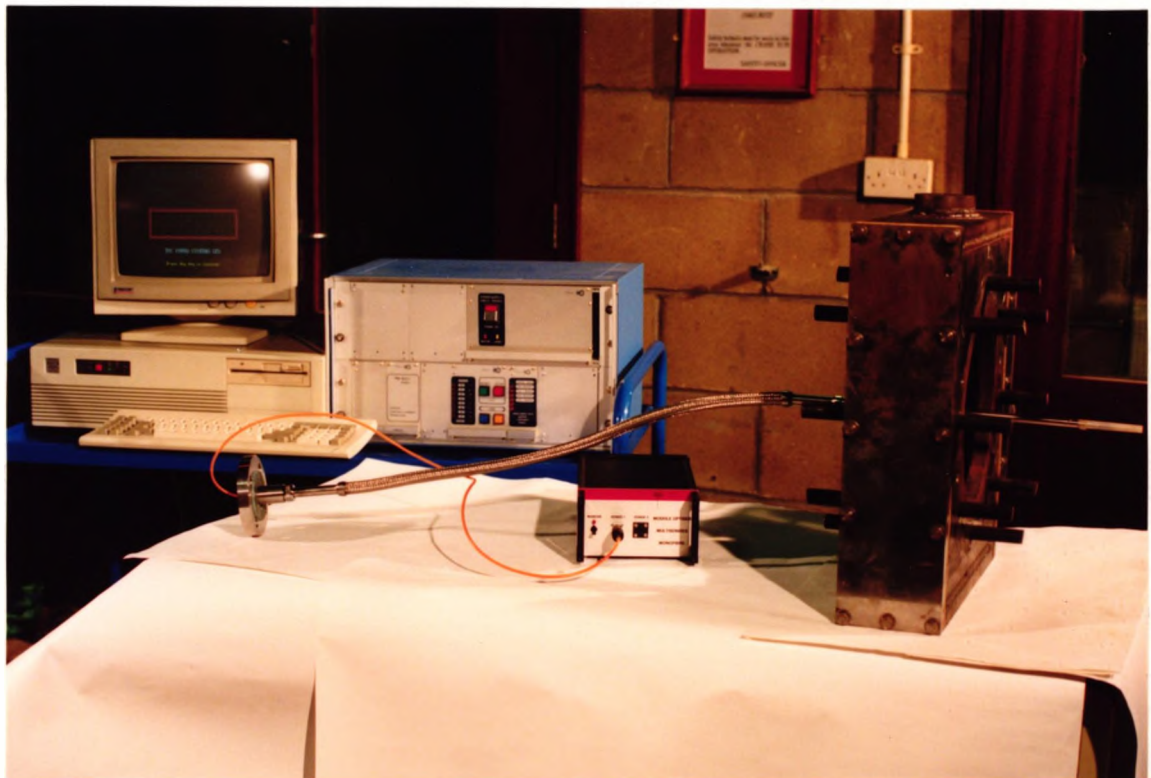


Fig.7.9. Void Fraction Unit and Probe Traversing System

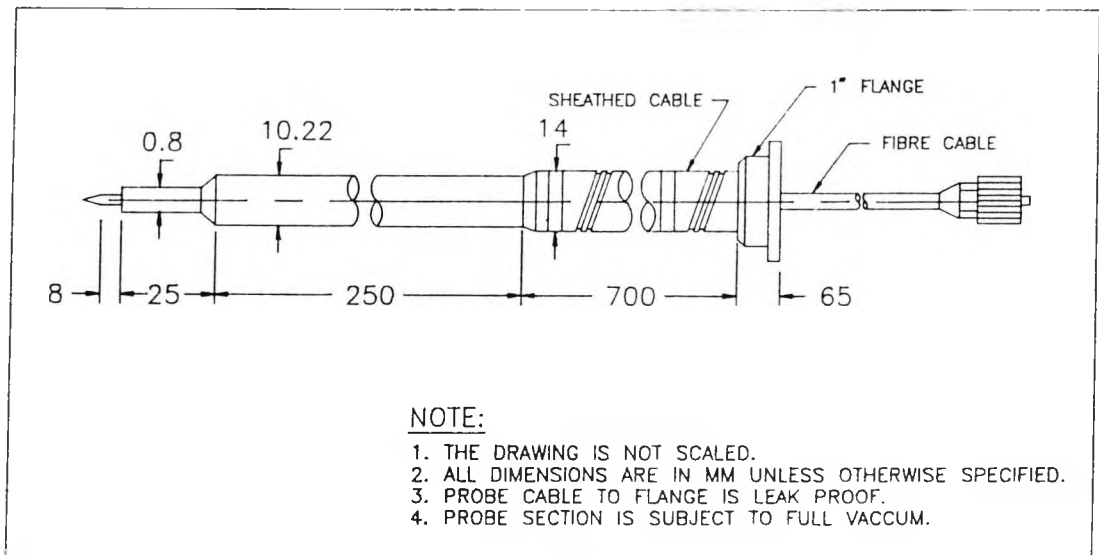


Fig.7.8. Dimensions of the Fibre Optic Probe

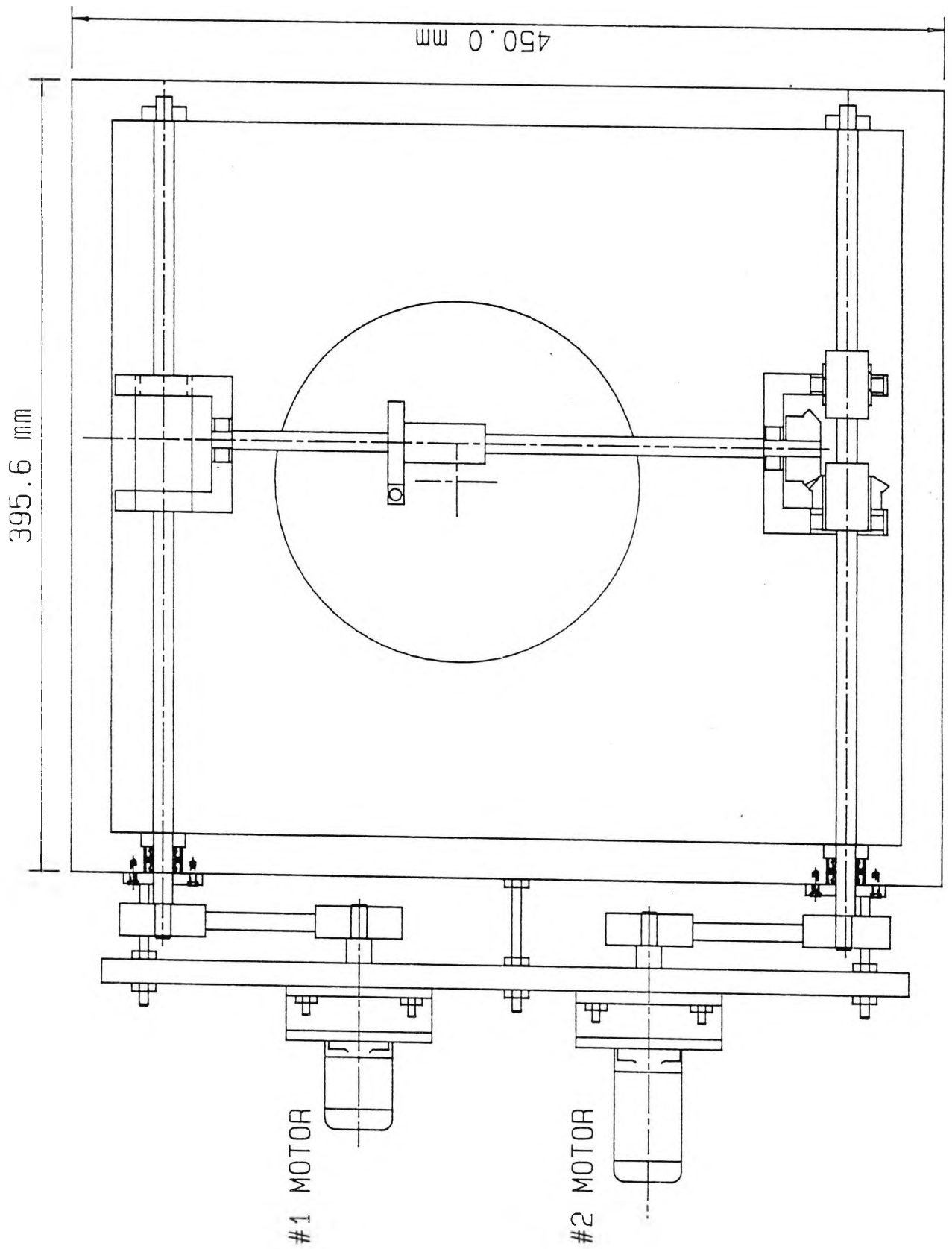
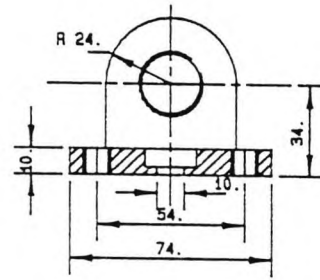
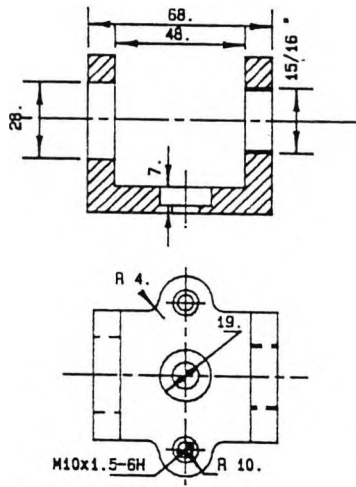
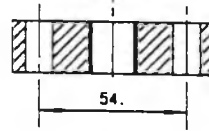
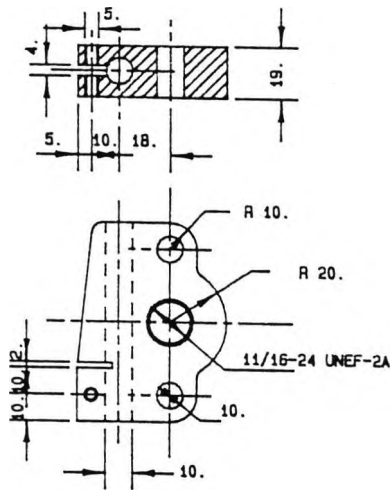


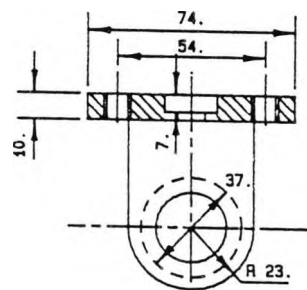
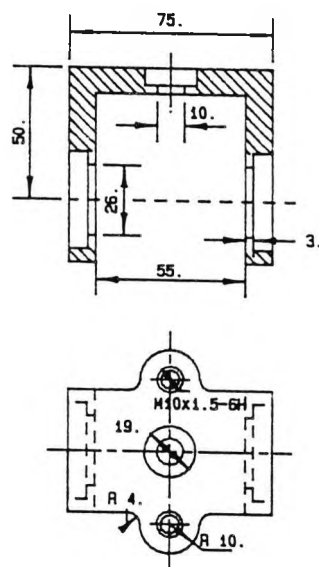
Fig.7.10. Front View of Mechanical Traversing Unit



(1) BALL SCREW SHAFT CARRIAGE



(2) PROBE HOLDER



(3) BEVEL GEAR CARRIAGE

Fig.7.11. Components of Mechanical Traversing Unit

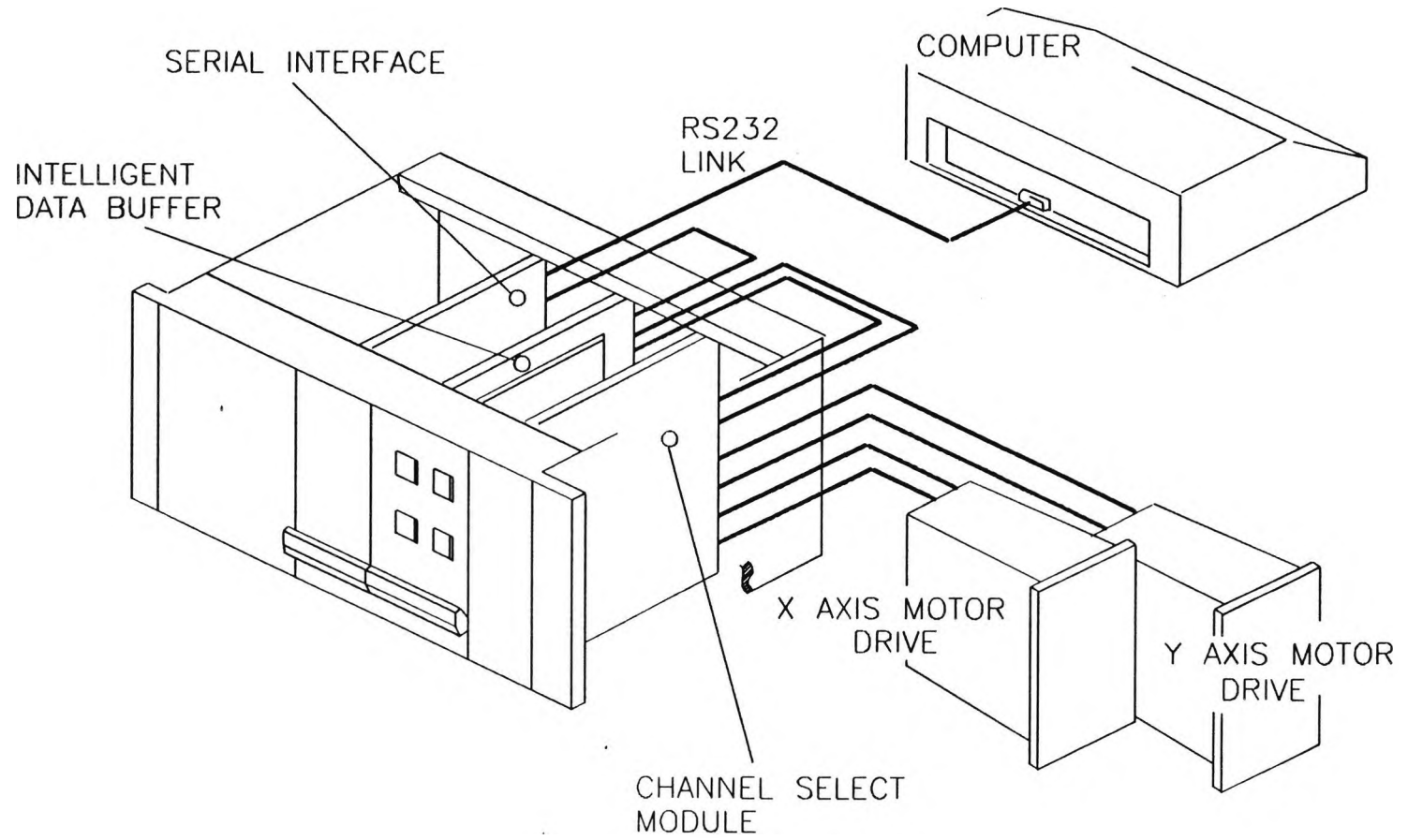


Fig.7.12. Schematic of Stepper Motor Controller Unit

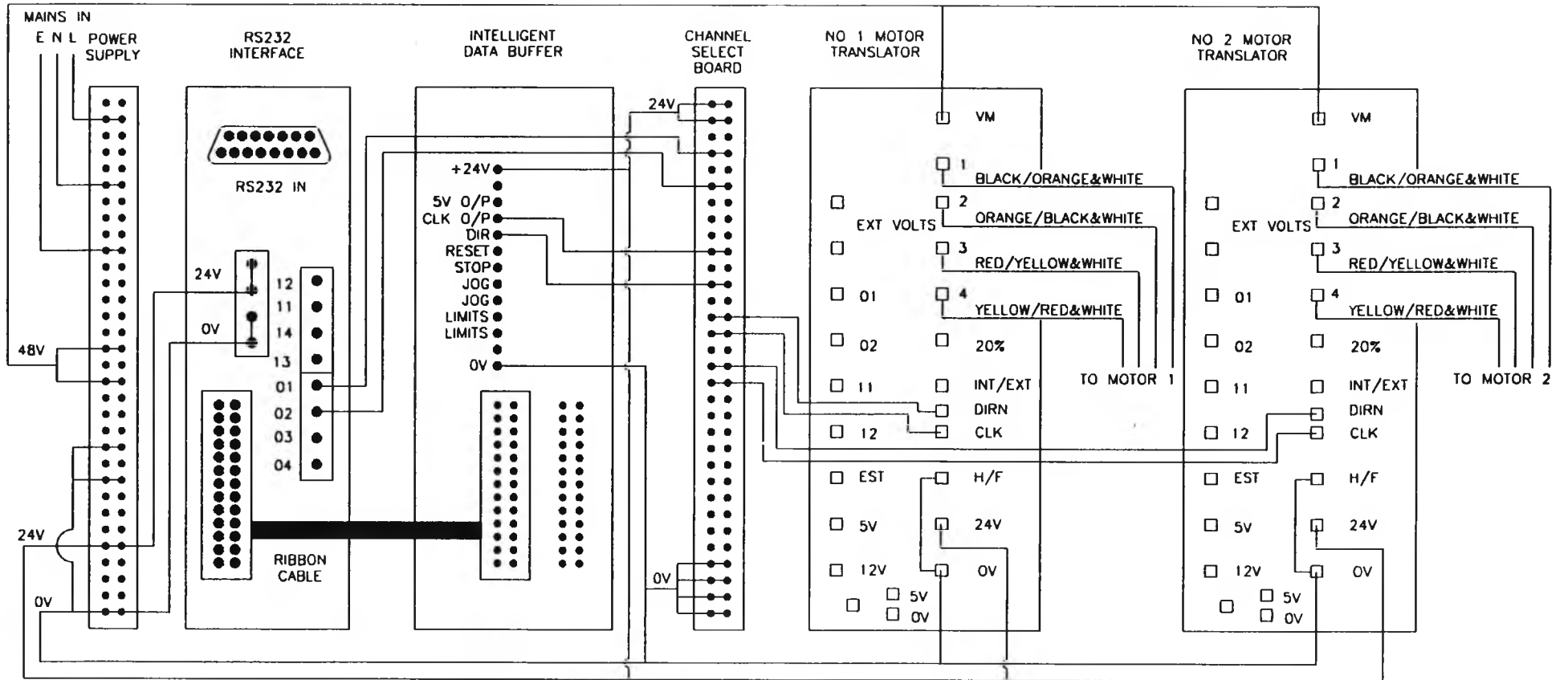


Fig.7.13. Stepper Motor Controller Connection Diagram

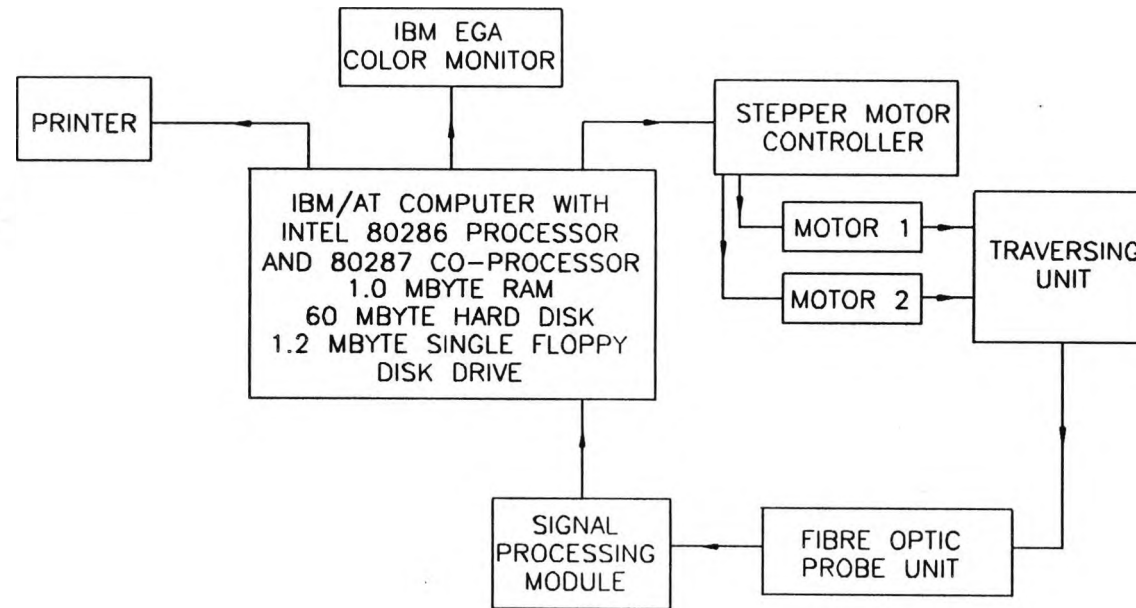


Fig.7.14. Block Diagram of Motor Control & Signal Processing Operation

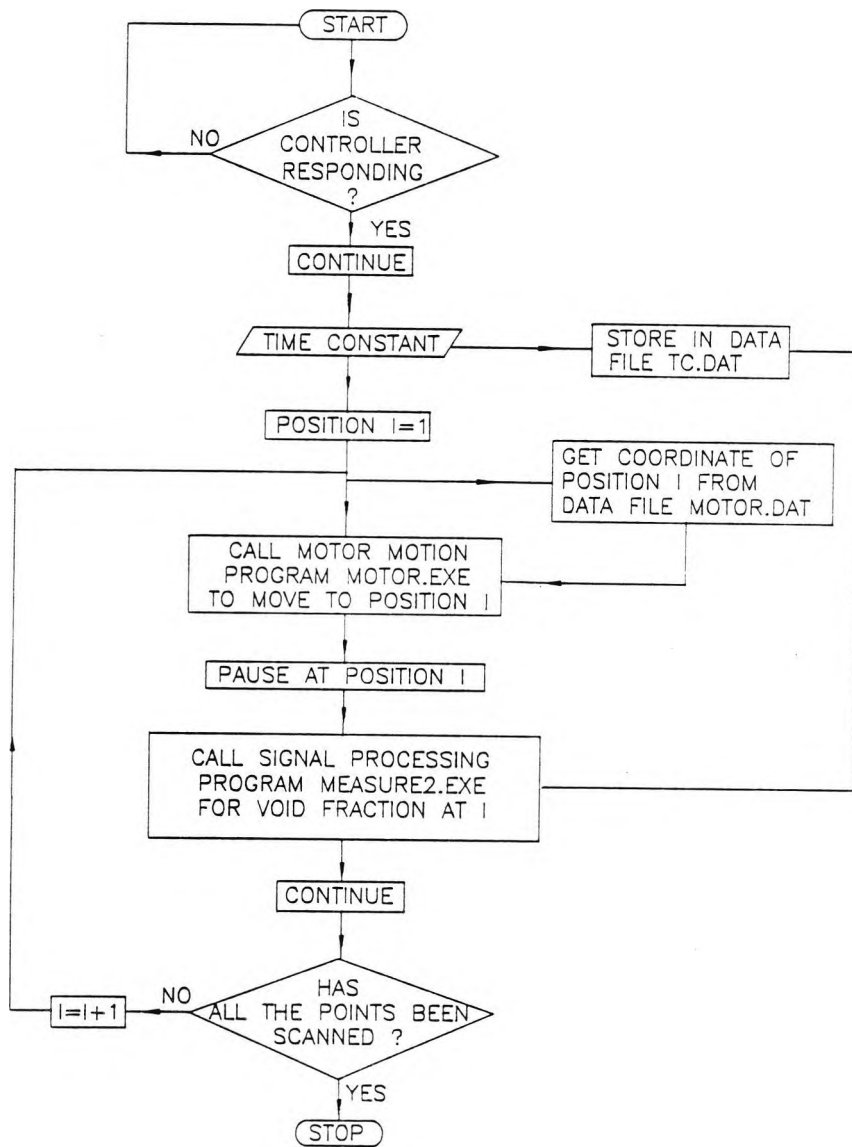


Fig.7.15. Flow Chart of Probe Movement & Signal Processing Program

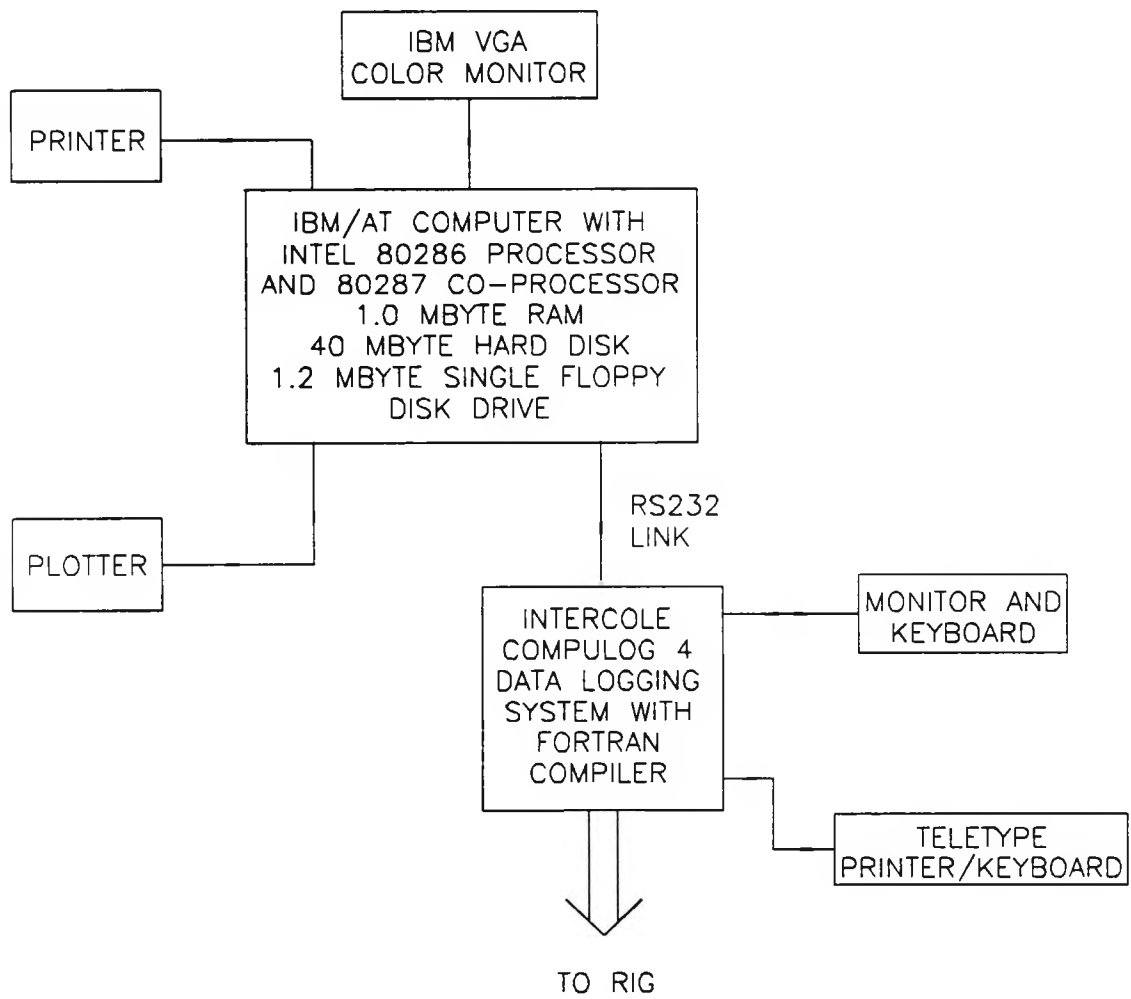


Fig.7.16. Schematic Diagram of Data Logging System

Table 7.1. Instrumentation Schedule

PARAMETER	SENSOR	TYPE	RANGE	CHANNEL NO.	ERROR %
TEMPERATURE					
Heater Inlet	RTD	Platinum	0-200°C	00	±0.25+ 0.0002t*
Heater Exit	"	"	"	10	"
Control Valve Inlet	"	"	"	11	"
Condenser Exit	"	"	"	08	"
Feed Pump:					
Inlet	"	"	"	01	"
Exit	"	"	"	09	"
Cooling Water:					
Exit	"	"	"	06	"
Inlet	"	"	"	07	"
PRESSURE					
Heater Inlet	Transducer	Strain Gauge	0-20bar	20	0.52
Heater Exit	"	"	0-20bar	21	0.09
Control Valve Inlet	"	"	0-20bar	22	0.08
Inlet Port Inlet	"	"	0-15bar	23	0.21
Test Section 1	"	"	0-200psi	30	1.42
Test Section 2	"	"	0-200psi	31	1.65
Test Section 3	"	"	0-15bar	32	0.27
Test Section 4	"	"	0-15bar	24	0.09
Test Section 5	"	"	0-5 bar	25	1.49
Test Section 6	"	"	0-5 bar	26	0.86
Test Section 7	"	"	0-0.5bar	34	1.39
Condenser Top	"	"	0-15bar	27	0.38
Feed Pump Inlet	"	"	0-15bar	28	0.28
FLOW RATE					
Working Fluid	Turbine Flow Meter		0-17.5kg/s	18	±1.0
Cooling Water	Orifice Plate		0-7.0 kg/s	19	±1.0

Table 8.1. Summary of Planned Refrigerant 113 Test Data

TEST RUN NO.	PRESSURE (Bar)	TEMPERATURE (°C)	DRYNESS FRACTION	MASS FLOW RATE (Kg/s)
R.113-1	3.4368	90.0	0.0762	10.6508
R.113-2	3.4368	90.0	0.1534	9.0734
R.113-3	3.4368	90.0	0.2317	7.8885
R.113-4	3.4368	90.0	0.3113	6.9648
R.113-5	3.4368	90.0	0.3924	6.2233
R.113-6	3.4368	90.0	0.4751	5.6135
R.113-7	4.3773	100.0	0.1606	7.8885
R.113-8	4.3773	100.0	0.2428	6.9648
R.113-9	4.3773	100.0	0.3265	6.2233
R.113-10	4.3773	100.0	0.4119	5.6135
R.113-11	5.4965	110.0	0.2555	6.2233
R.113-12	5.4965	110.0	0.3440	5.6135

Table 8.2. Summary of Test Conditions for No.1 Inlet Port

TEST RUN NO.	PRESSURE (Bar)	TEMPERATURE (°C)	DRYNESS FRACTION	MASS FLOW RATE (Kg/s)
R.113-C1	3.2512	89.0	0.0837	11.2414
R.113-C2	3.5014	92.0	0.1364	10.2188
R.113-C3	3.1760	88.7	0.2321	7.5687
R.113-C4	3.2385	89.5	0.2995	6.6086
R.113-C5	3.2405	89.7	0.3839	5.9702
R.113-C6	3.2713	90.2	0.4580	5.3684
R.113-C7	4.0835	98.7	0.1744	9.9420
R.113-C8	4.1818	99.8	0.2391	9.4052
R.113-C9	4.1929	100.0	0.3109	7.7889
R.113-C10	4.1637	99.7	0.4077	7.2860
R.113-C11	5.2138	109.5	0.2552	10.1294
R.113-C12	5.3105	110.4	0.3287	9.1030

Table 8.3. Summary of Test Conditions for No.2 Inlet Port

TEST RUN NO.	PRESSURE (Bar)	TEMPERATURE (°C)	DRYNESS FRACTION	MASS FLOW RATE (Kg/s)
R.113-B1	3.3502	90.0	0.0778	11.3330
R.113-B2	3.5358	92.4	0.1318	10.2559
R.113-B3	3.2113	88.8	0.2264	7.6610
R.113-B4	3.2321	89.2	0.3115	6.7355
R.113-B5	3.2218	89.2	0.3886	5.9769
R.113-B6	3.2963	90.0	0.4544	5.4247
R.113-B7	4.0691	98.4	0.1794	10.0515
R.113-B8	4.2788	100.5	0.2331	9.4031
R.113-B9	4.1751	99.8	0.3237	7.8409
R.113-B10	4.1950	100.1	0.4021	7.2628
R.113-B11	5.2479	109.7	0.2498	10.1509
R.113-B12	5.1833	109.2	0.3299	9.2090

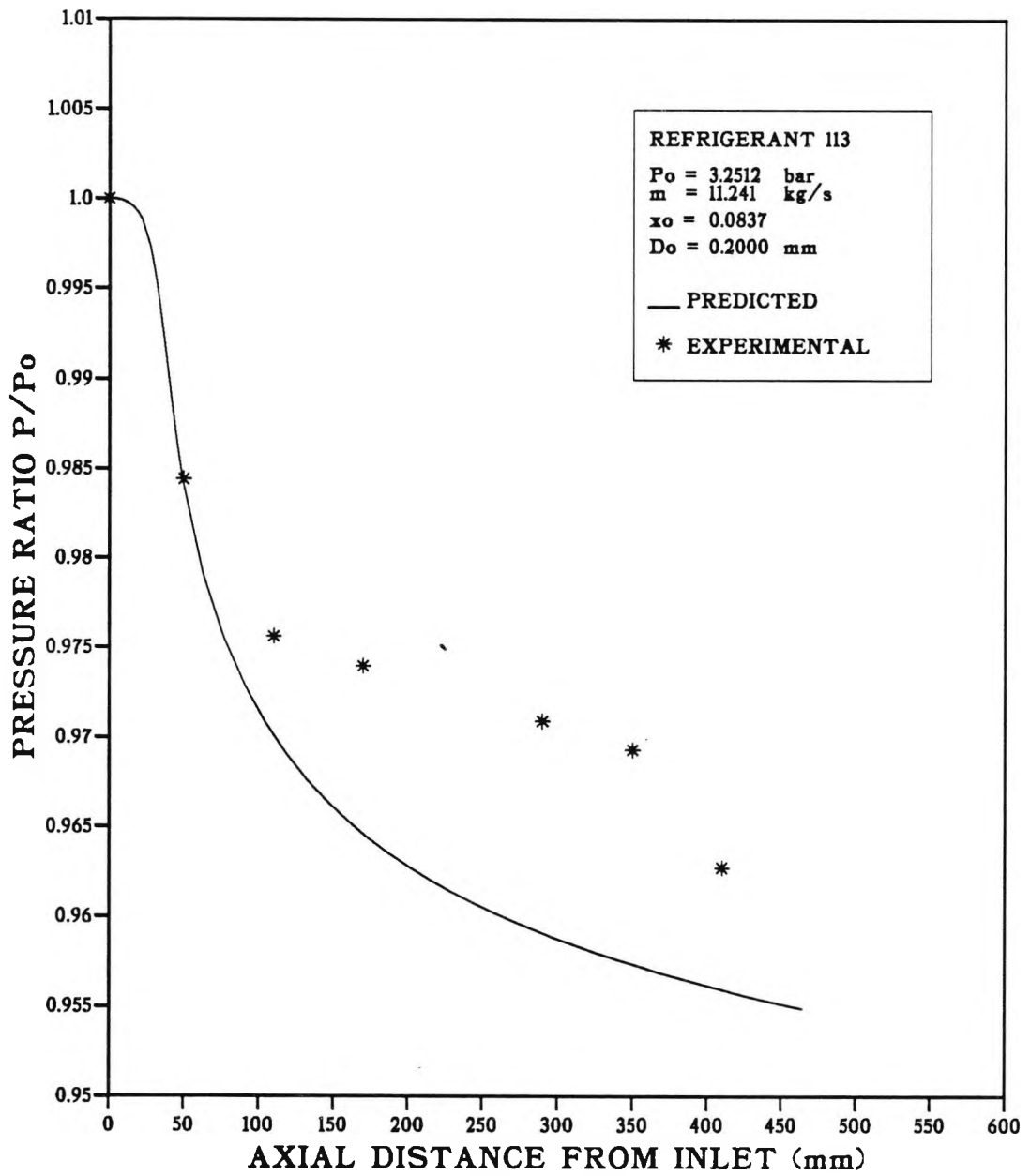


Fig.8.1. Experimental and Computed Pressure Distributions
(Test Run: R.113-C1)

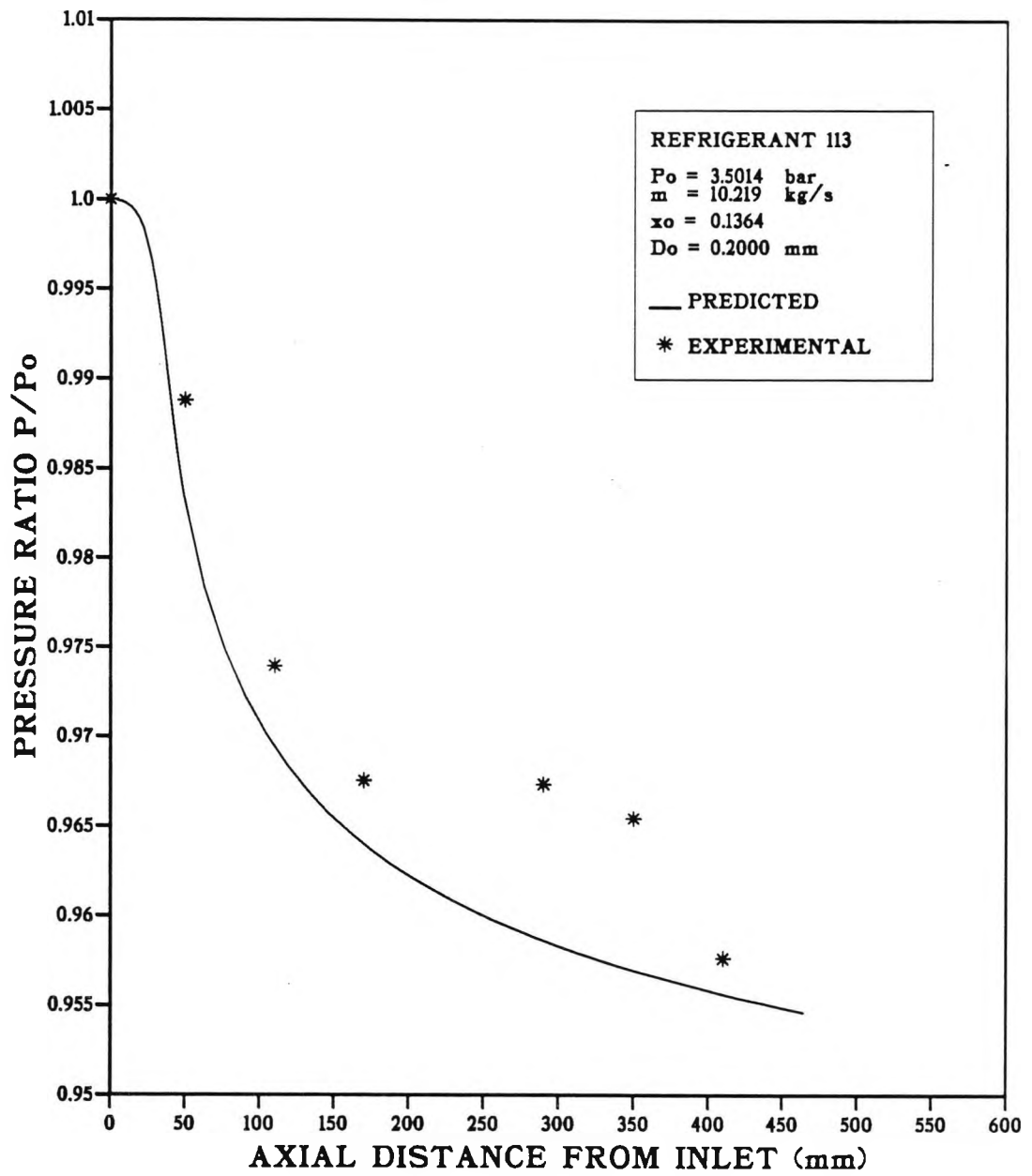


Fig.8.2. Experimental and Computed Pressure Distributions
 (Test Run: R.113-C2)

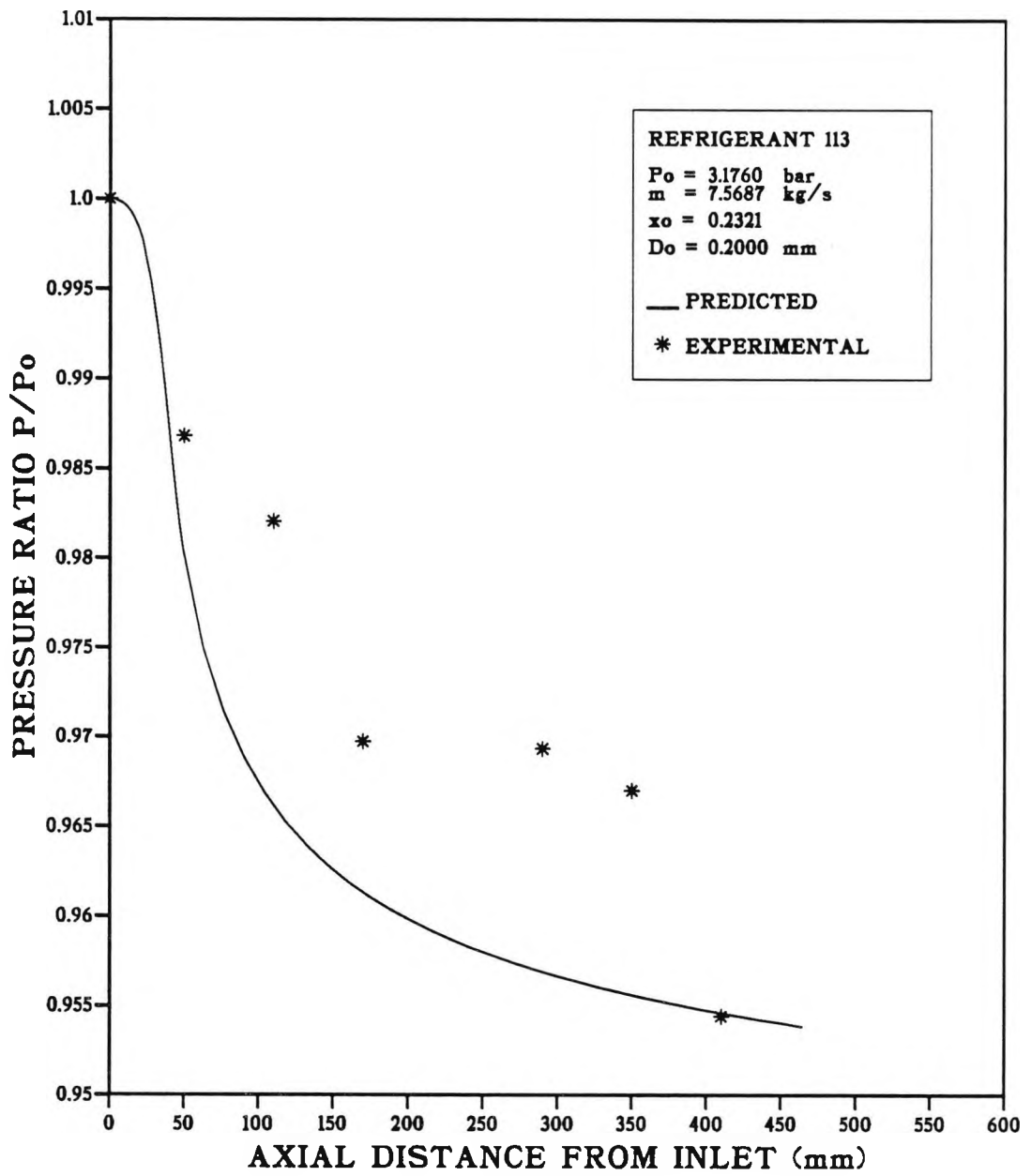


Fig.8.3. Experimental and Computed Pressure Distributions
 (Test Run: R.113-C3)

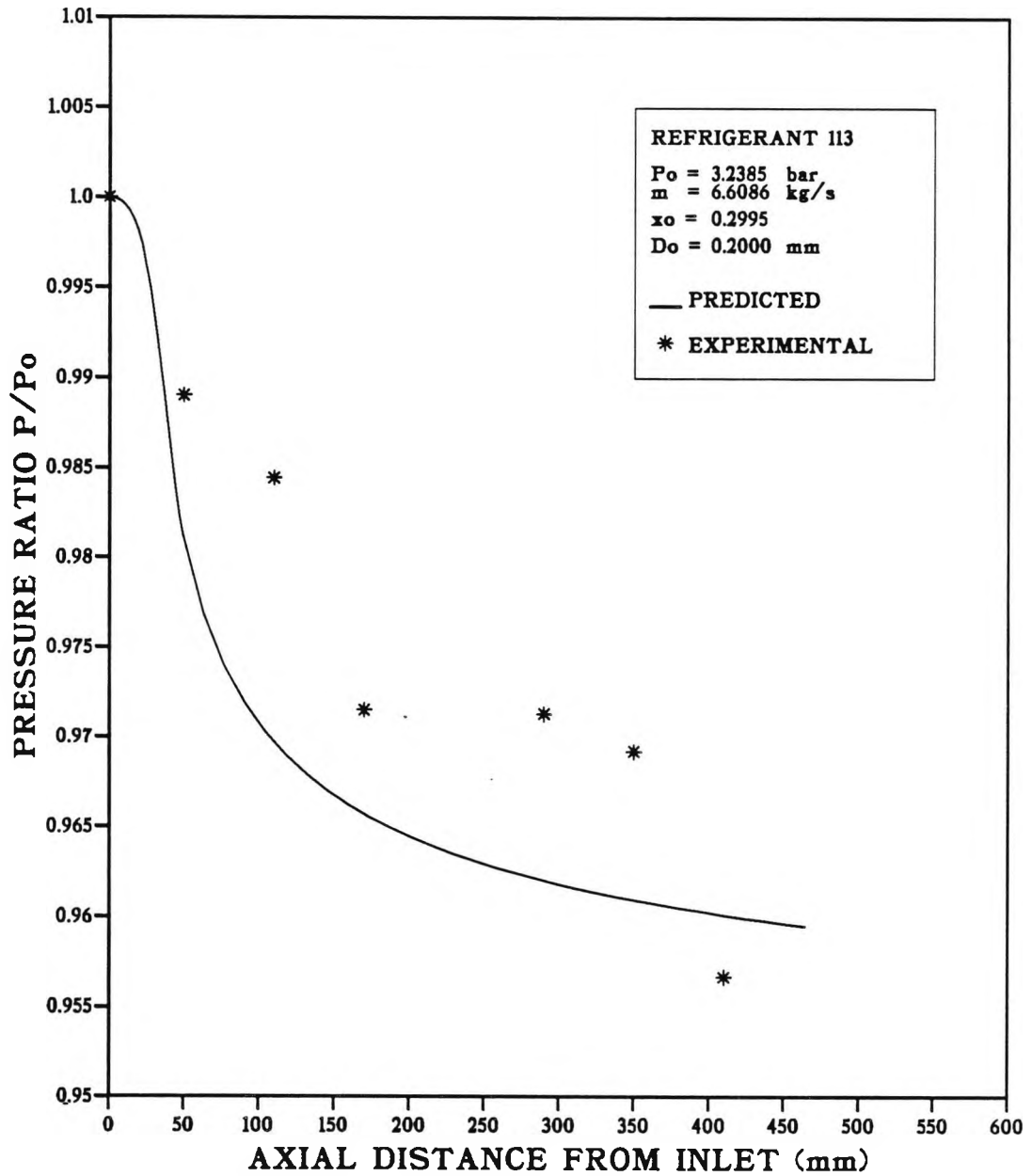


Fig.8.4. Experimental and Computed Pressure Distributions
 (Test Run: R.113-C4)

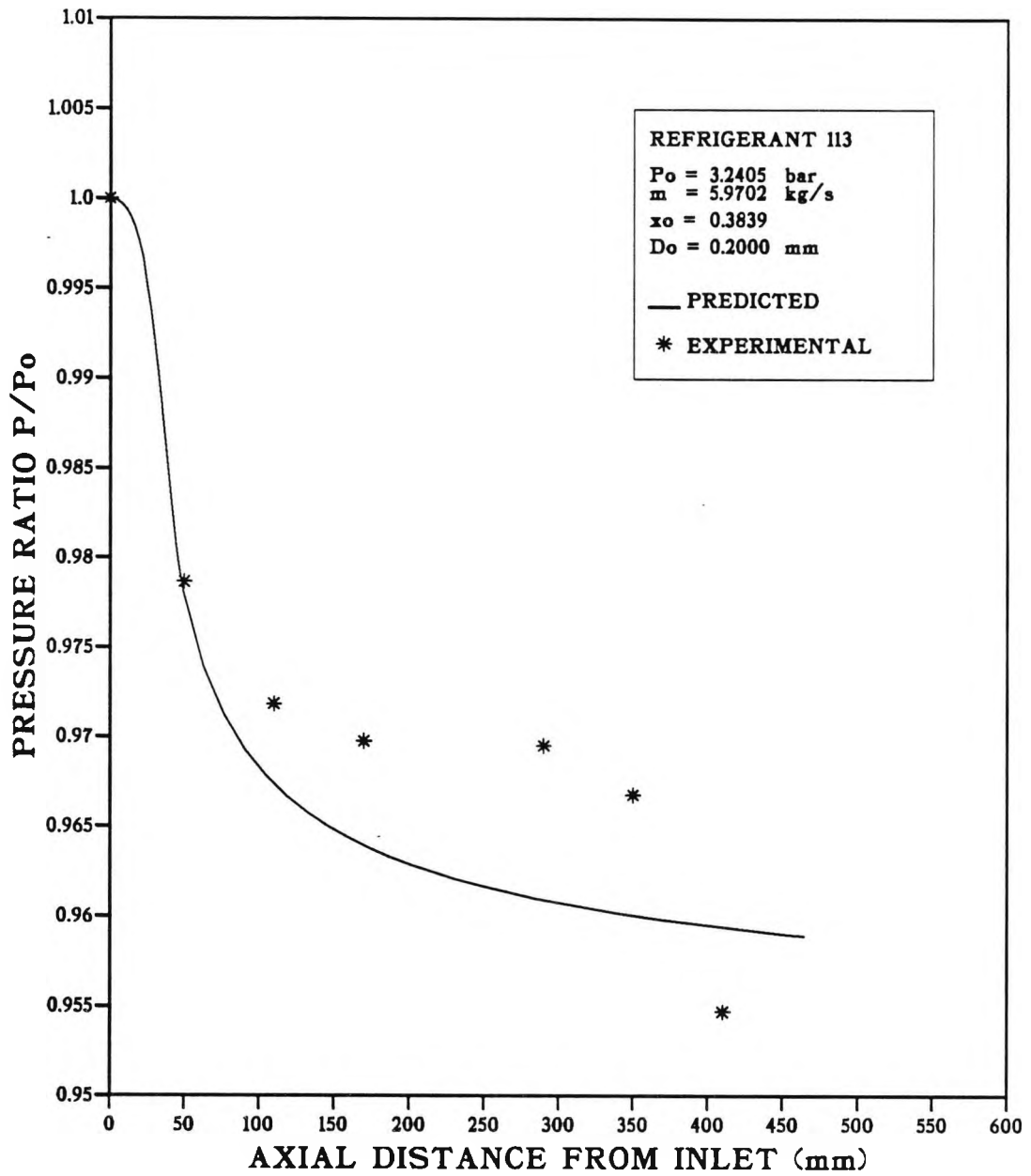


Fig.8.5. Experimental and Computed Pressure Distributions
(Test Run: R.113-C5)

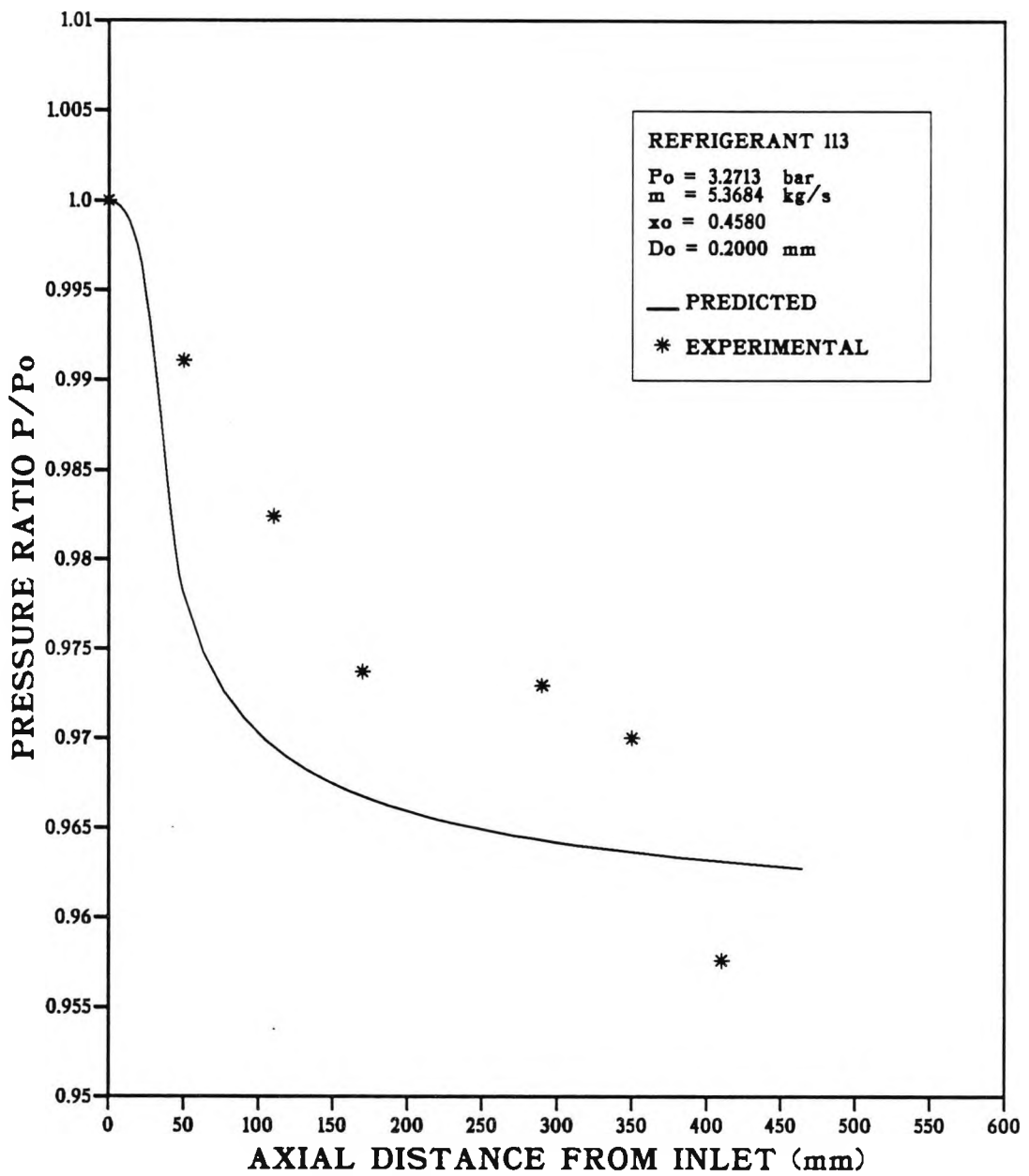


Fig.8.6. Experimental and Computed Pressure Distributions
(Test Run: R.113-C6)

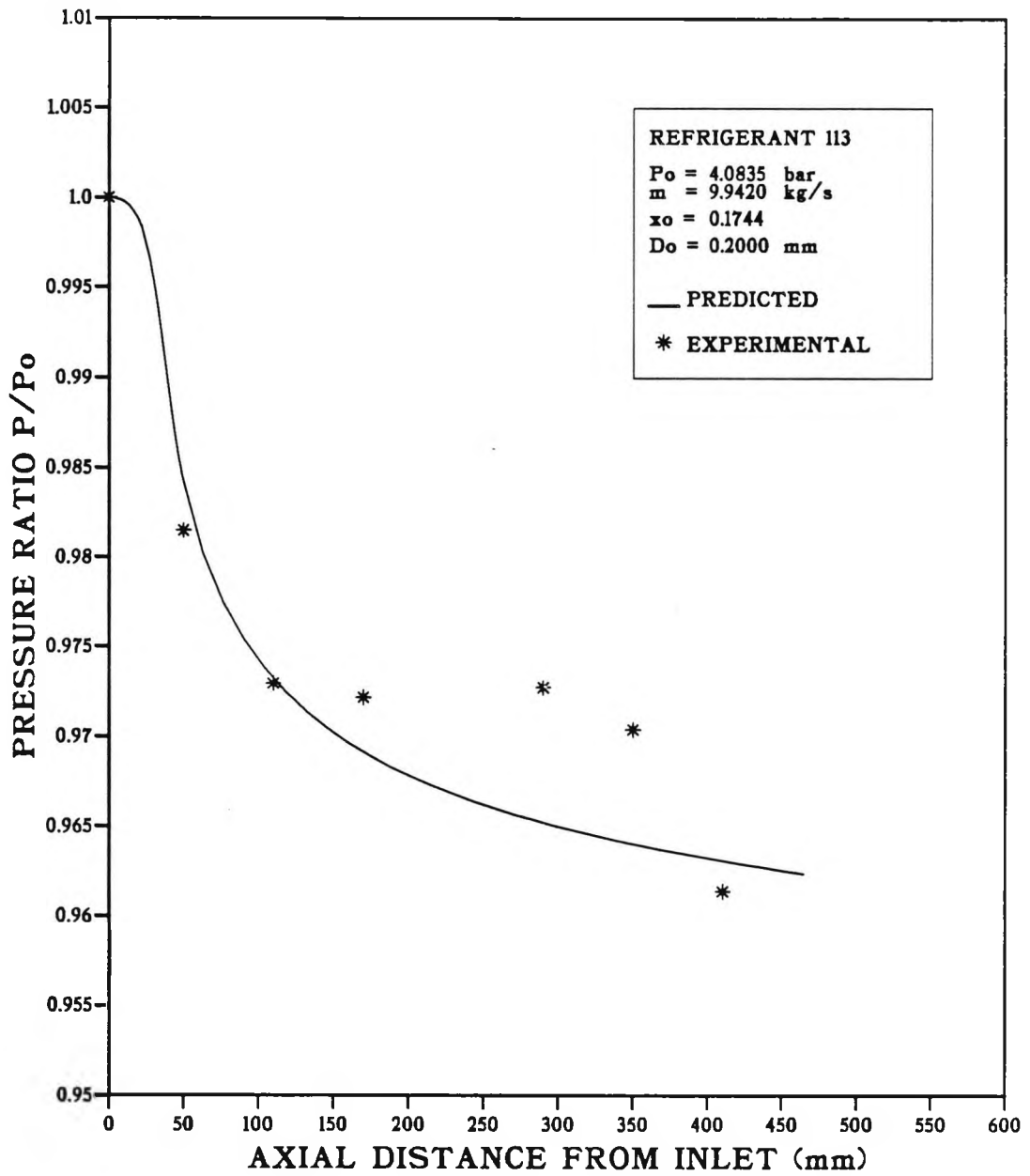


Fig.8.7. Experimental and Computed Pressure Distributions
(Test Run: R.113-C7)

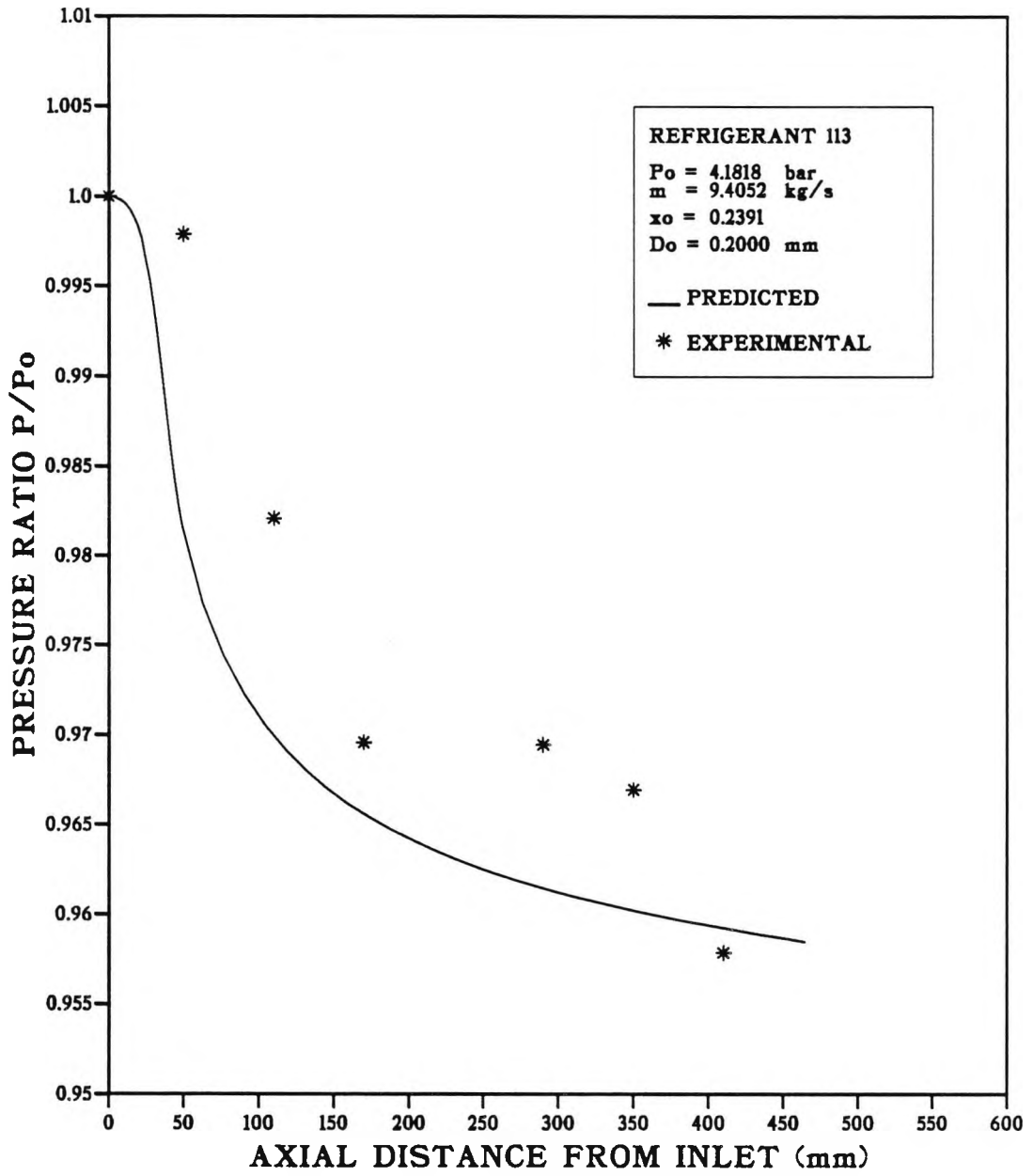


Fig.8.8. Experimental and Computed Pressure Distributions
 (Test Run: R.113-C8)

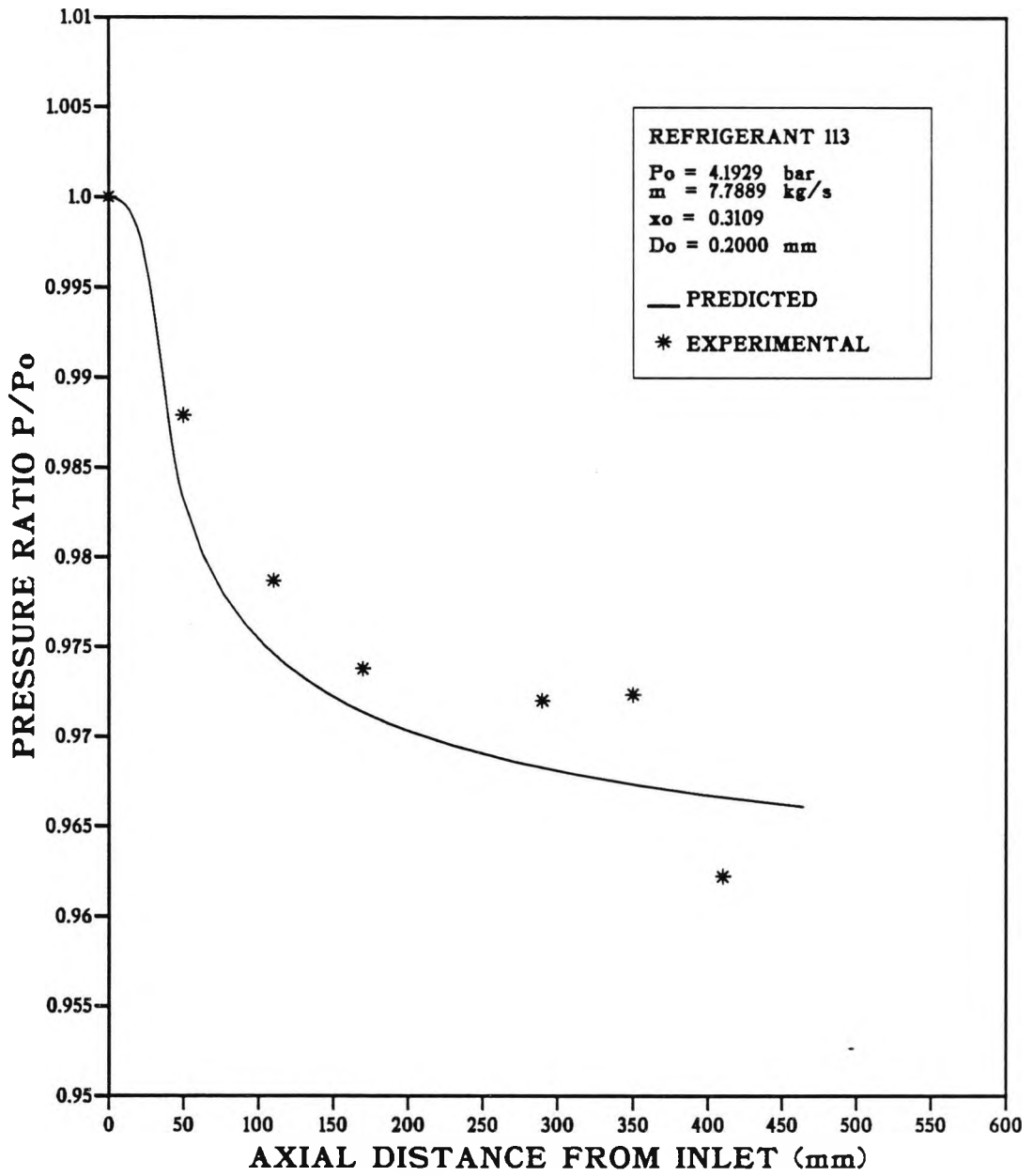


Fig.8.9. Experimental and Computed Pressure Distributions
 (Test Run: R.113-C9)

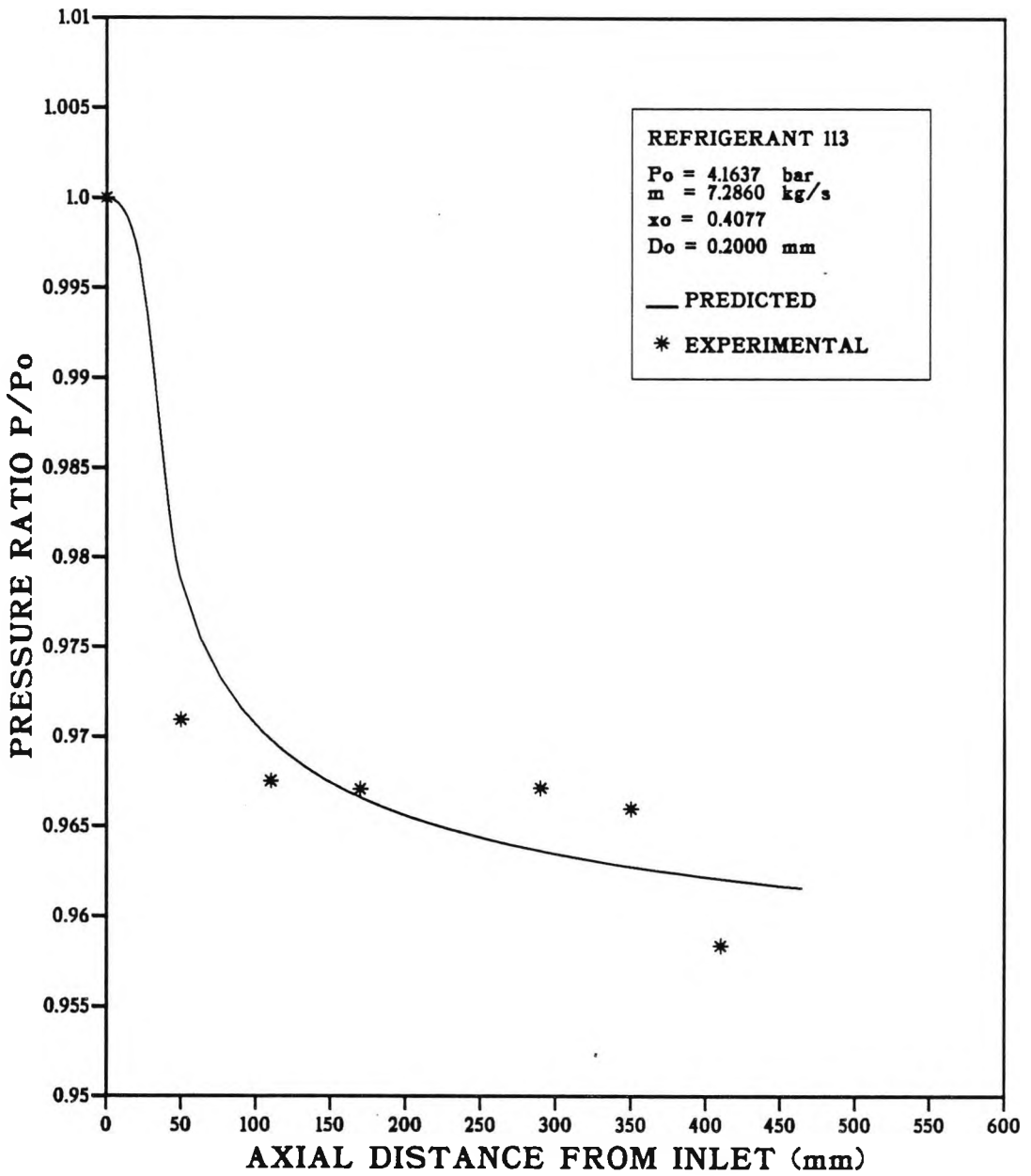


Fig.8.10. Experimental and Computed Pressure Distributions
(Test Run: R.113-C10)

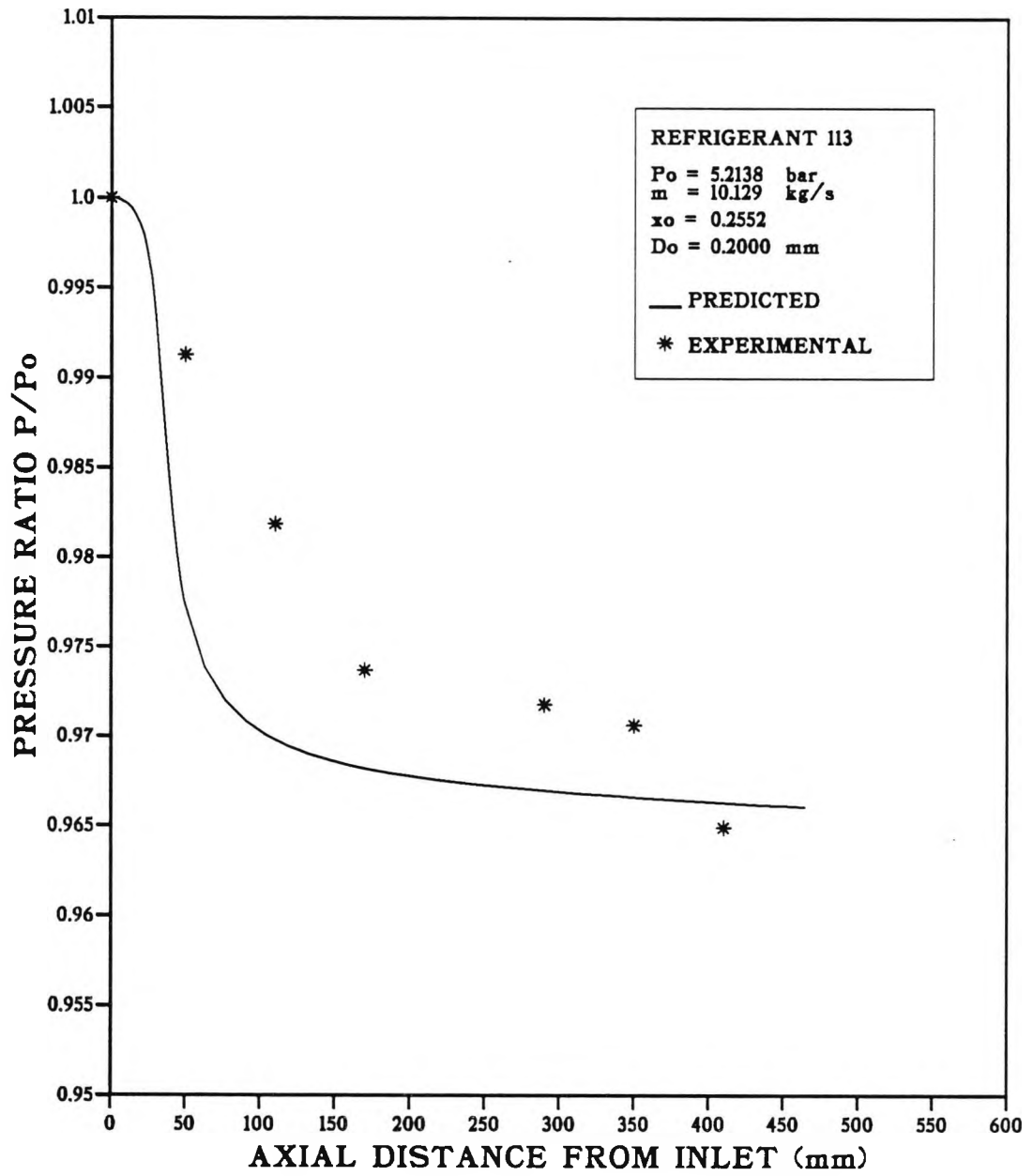


Fig.8.11. Experimental and Computed Pressure Distributions
(Test Run: R.113-C11)

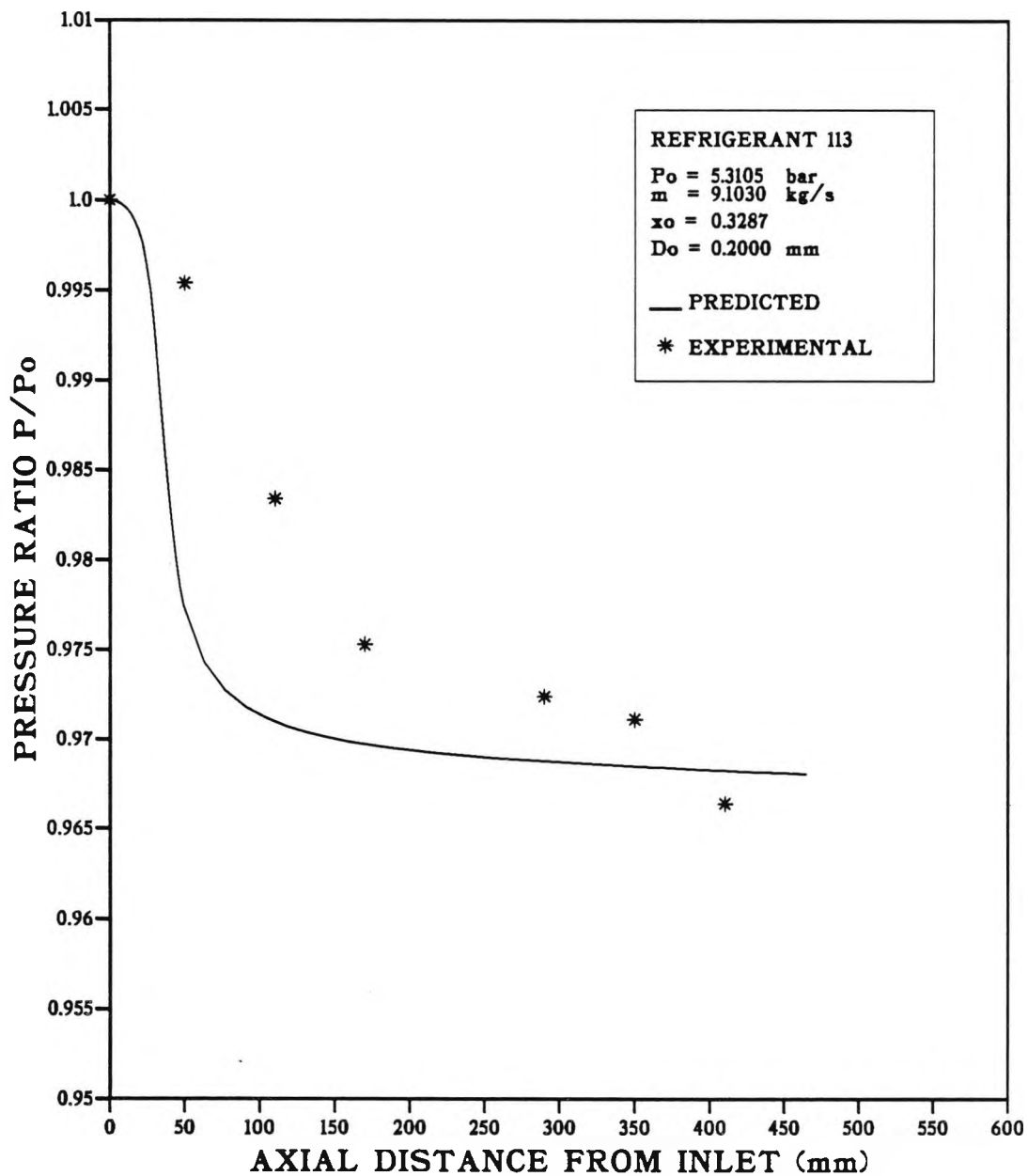


Fig.8.12. Experimental and Computed Pressure Distributions
 (Test Run: R.113-C12)

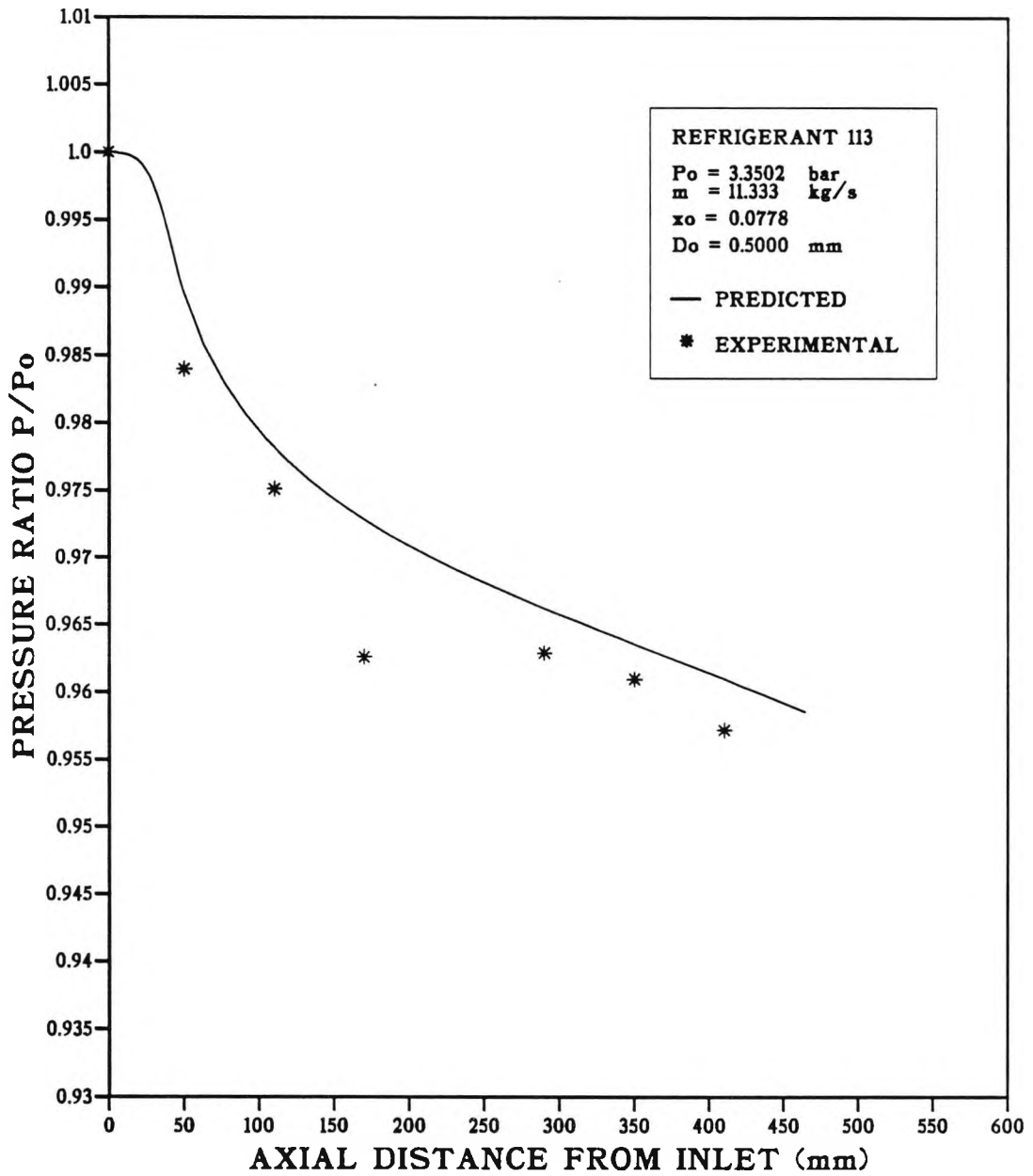


Fig.8.13. Experimental and Computed Pressure Distributions
(Test Run: R.113-B1)

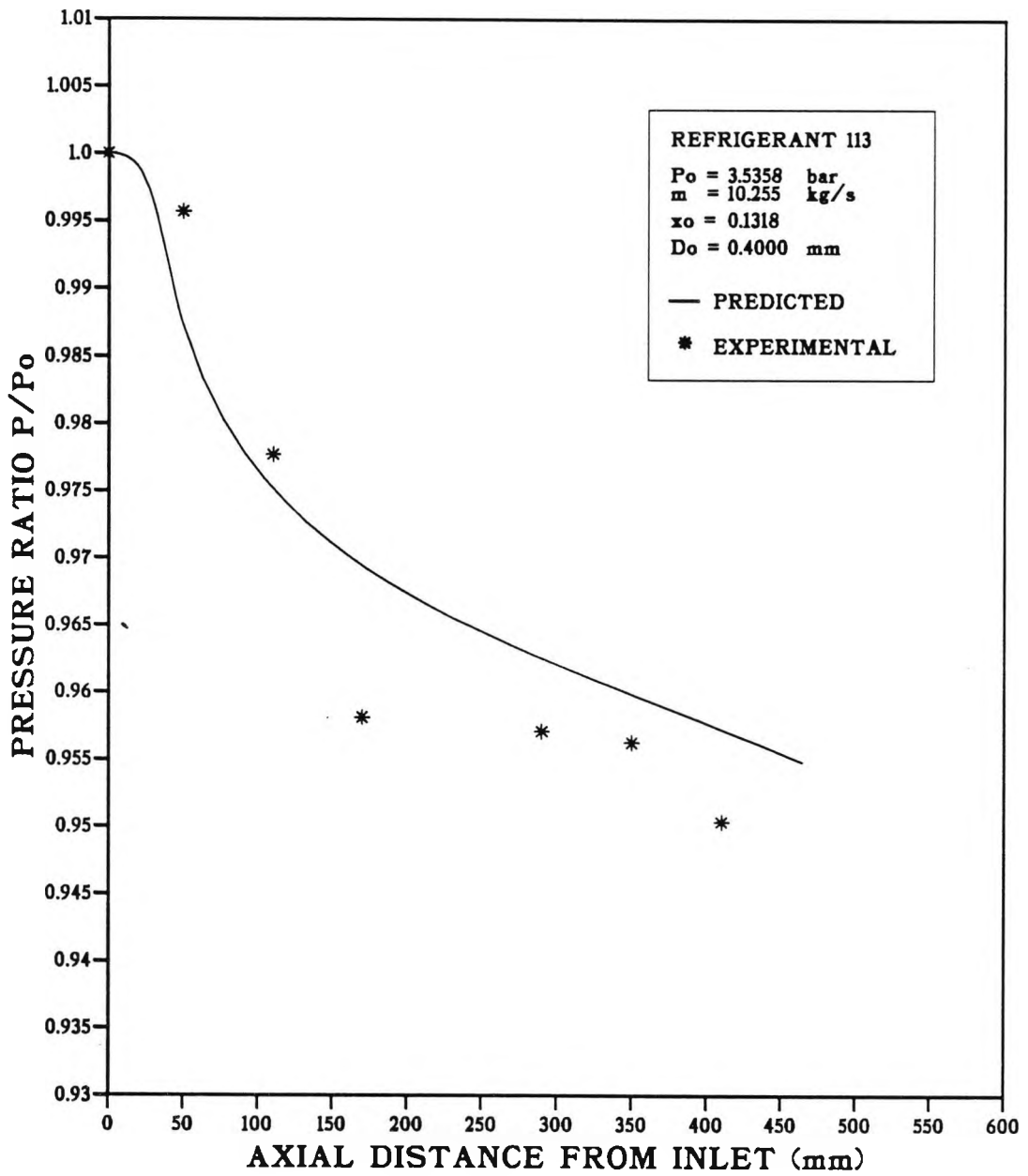


Fig.8.14. Experimental and Computed Pressure Distributions
 (Test Run: R.113-B2)

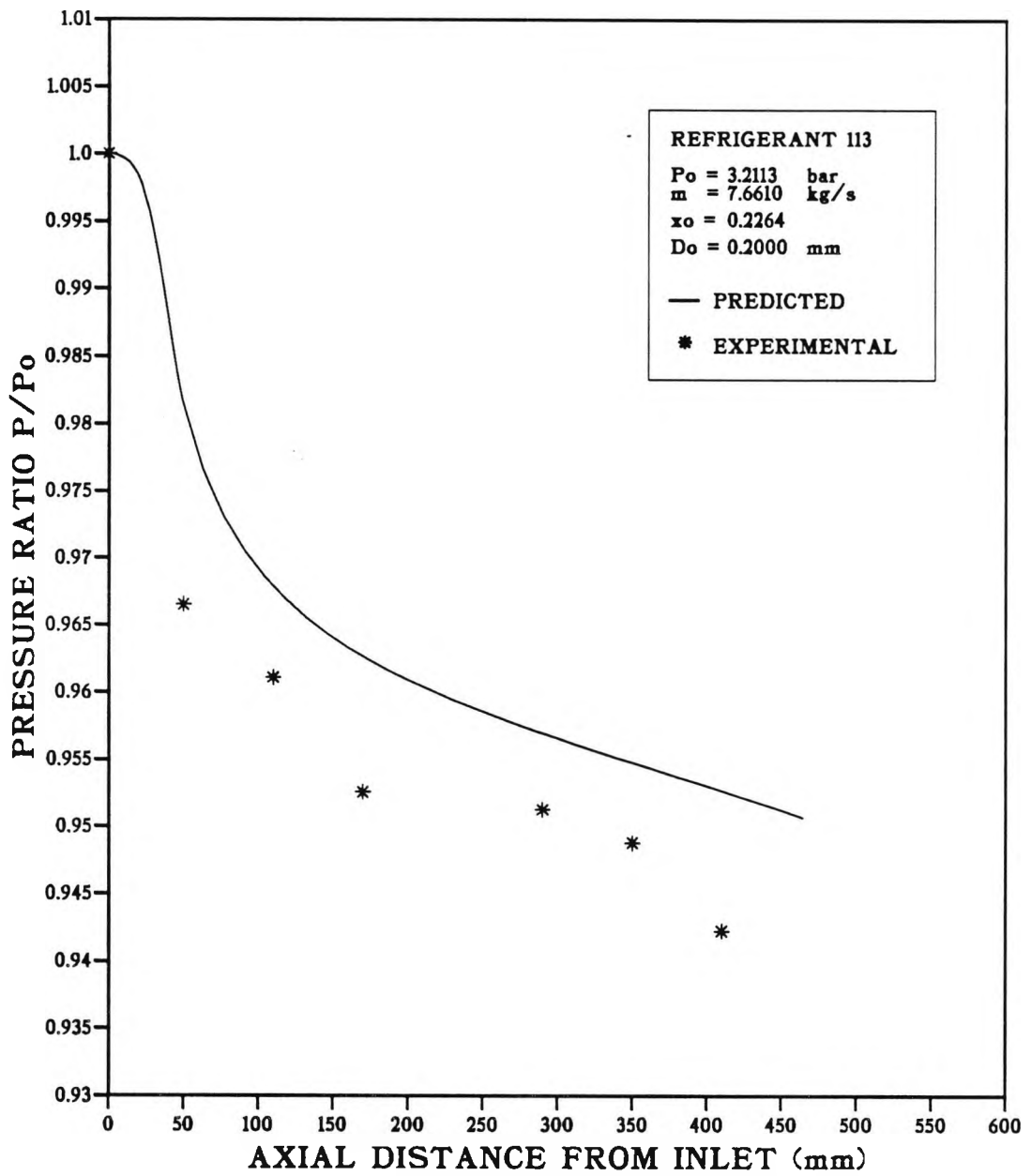


Fig.8.15. Experimental and Computed Pressure Distributions
 (Test Run: R.113-B3)

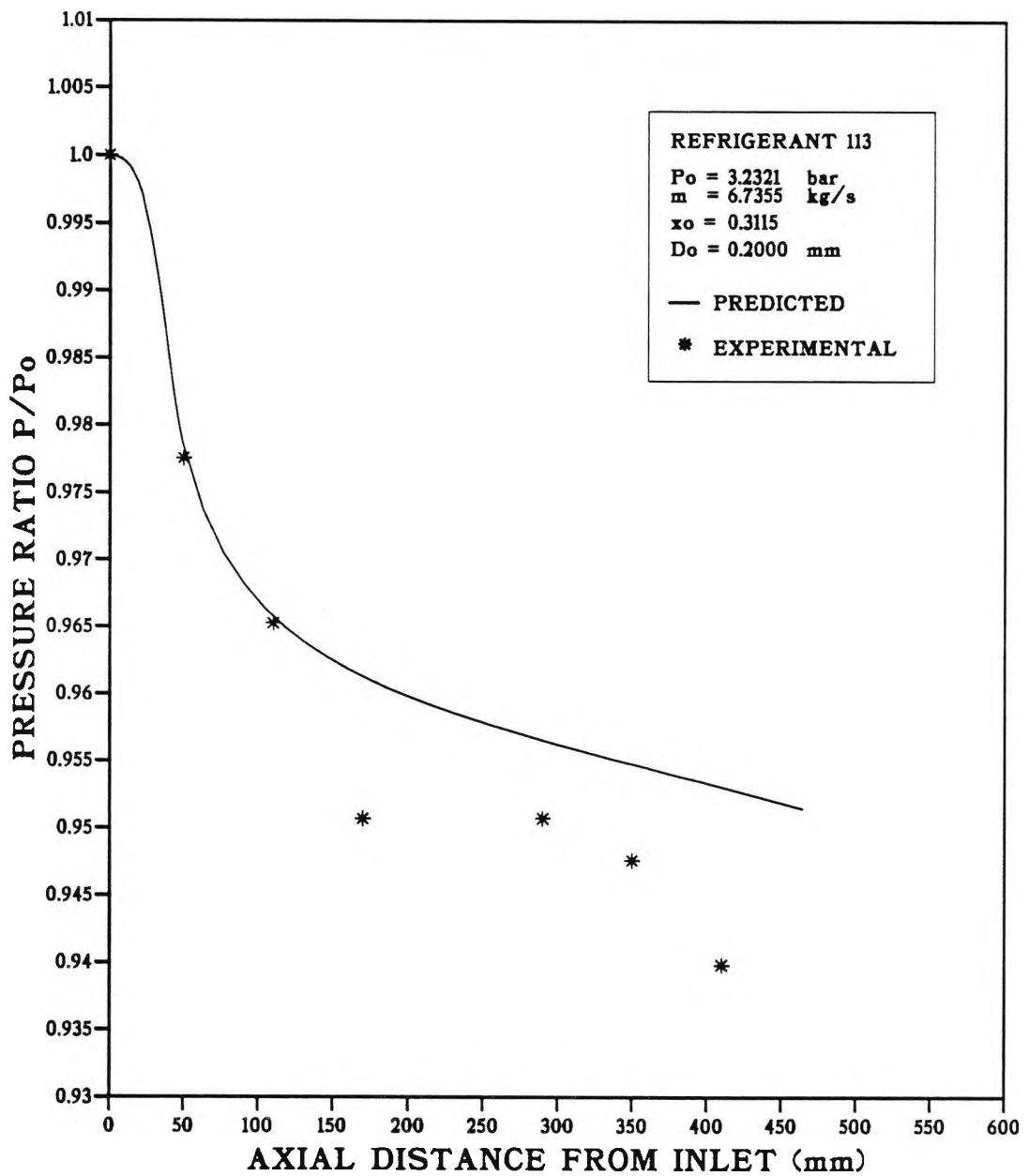


Fig.8.16. Experimental and Computed Pressure Distributions
 (Test Run: R.113-B4)

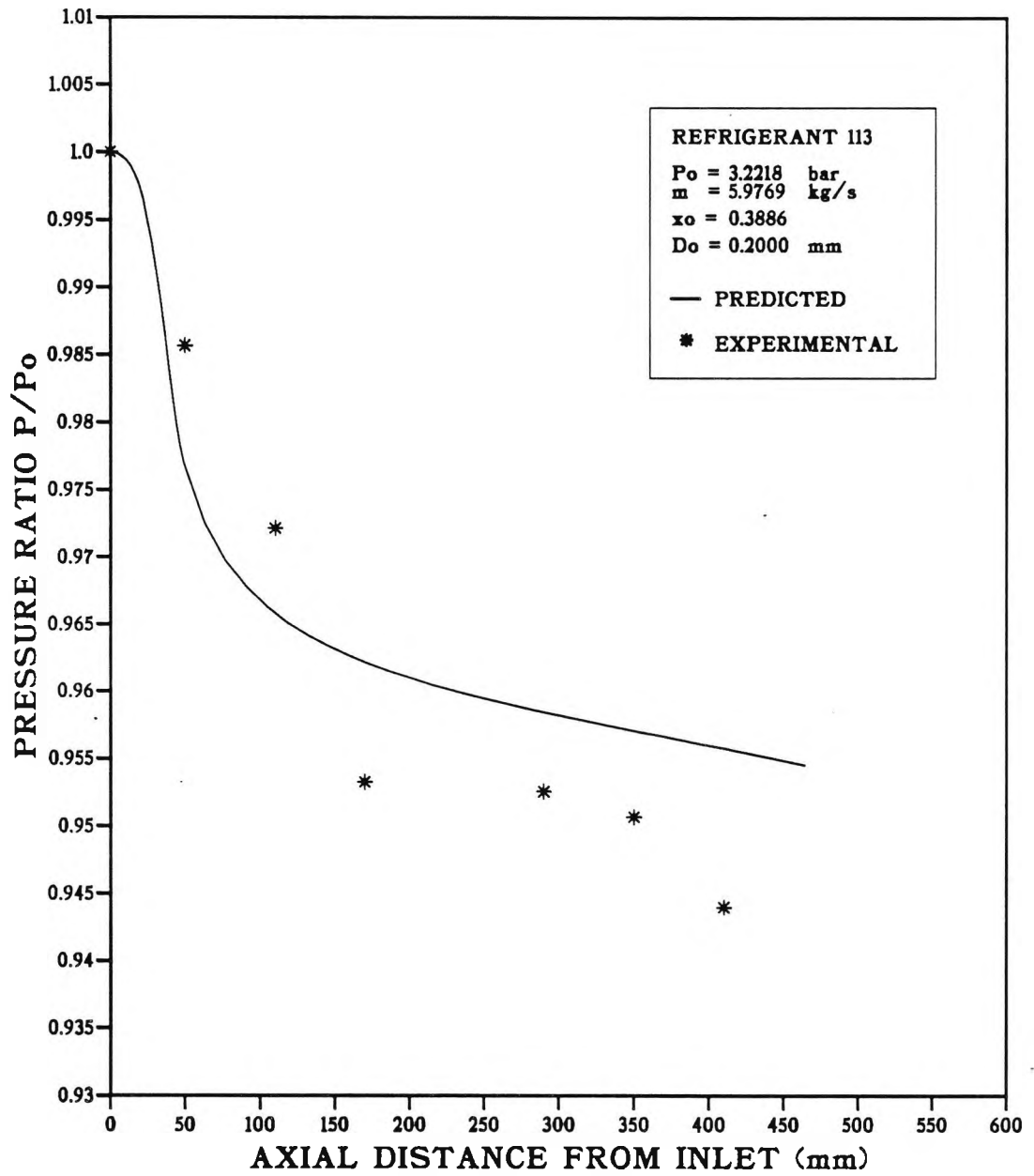


Fig.8.17. Experimental and Computed Pressure Distributions
 (Test Run: R.113-B5)

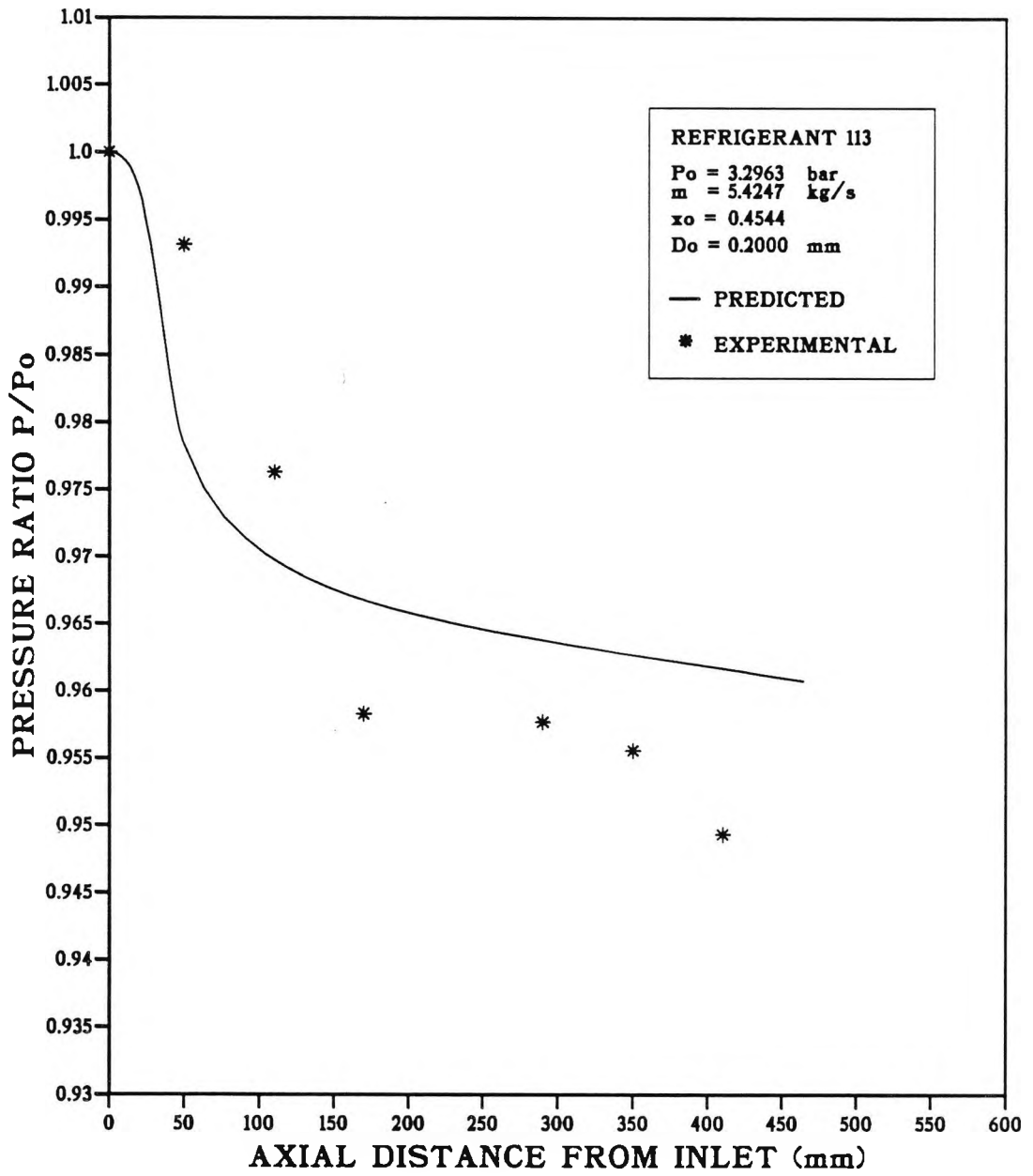


Fig.8.18. Experimental and Computed Pressure Distributions
 (Test Run: R.113-B6)

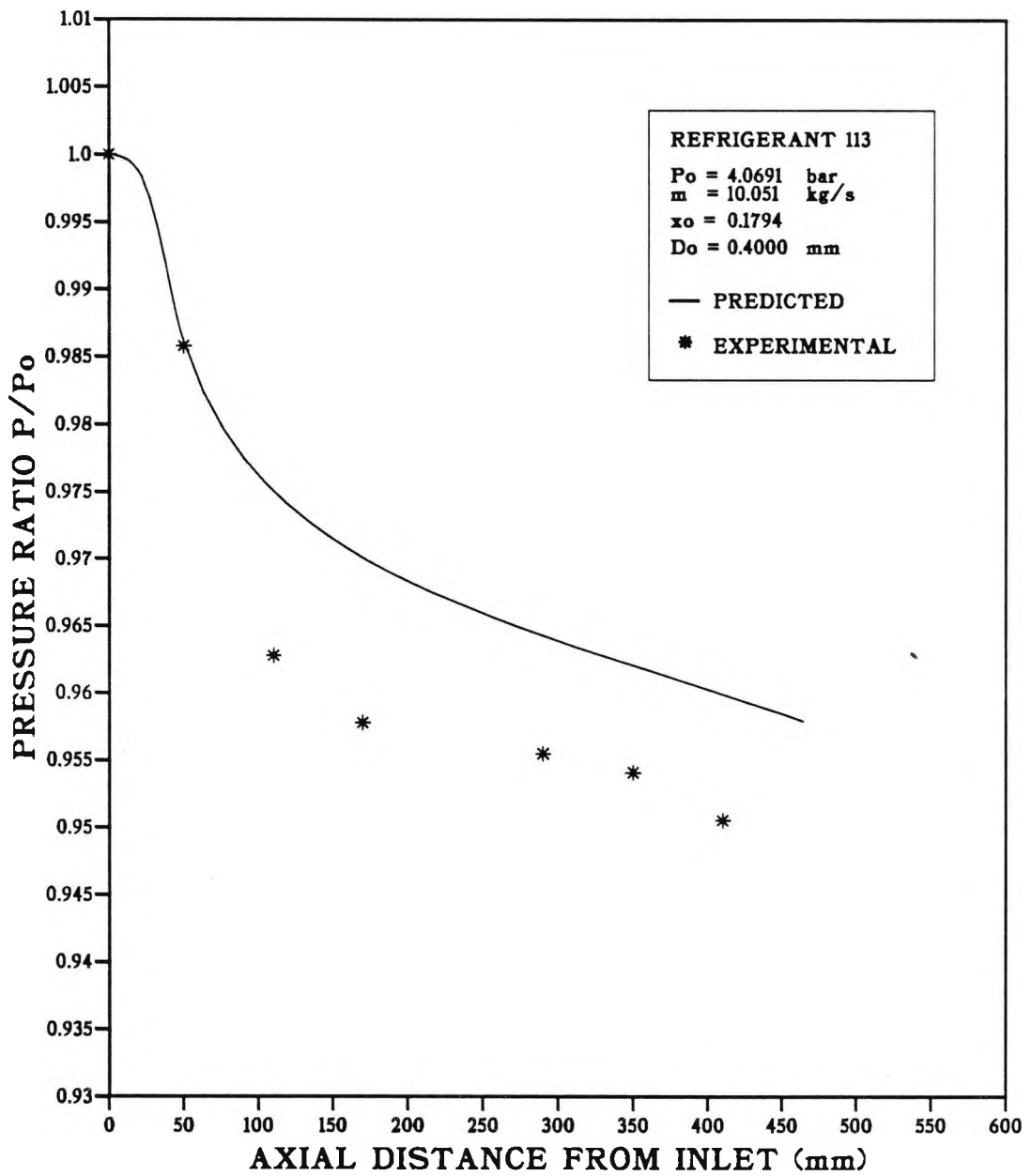


Fig.8.19. Experimental and Computed Pressure Distributions
 (Test Run: R.113-B7)

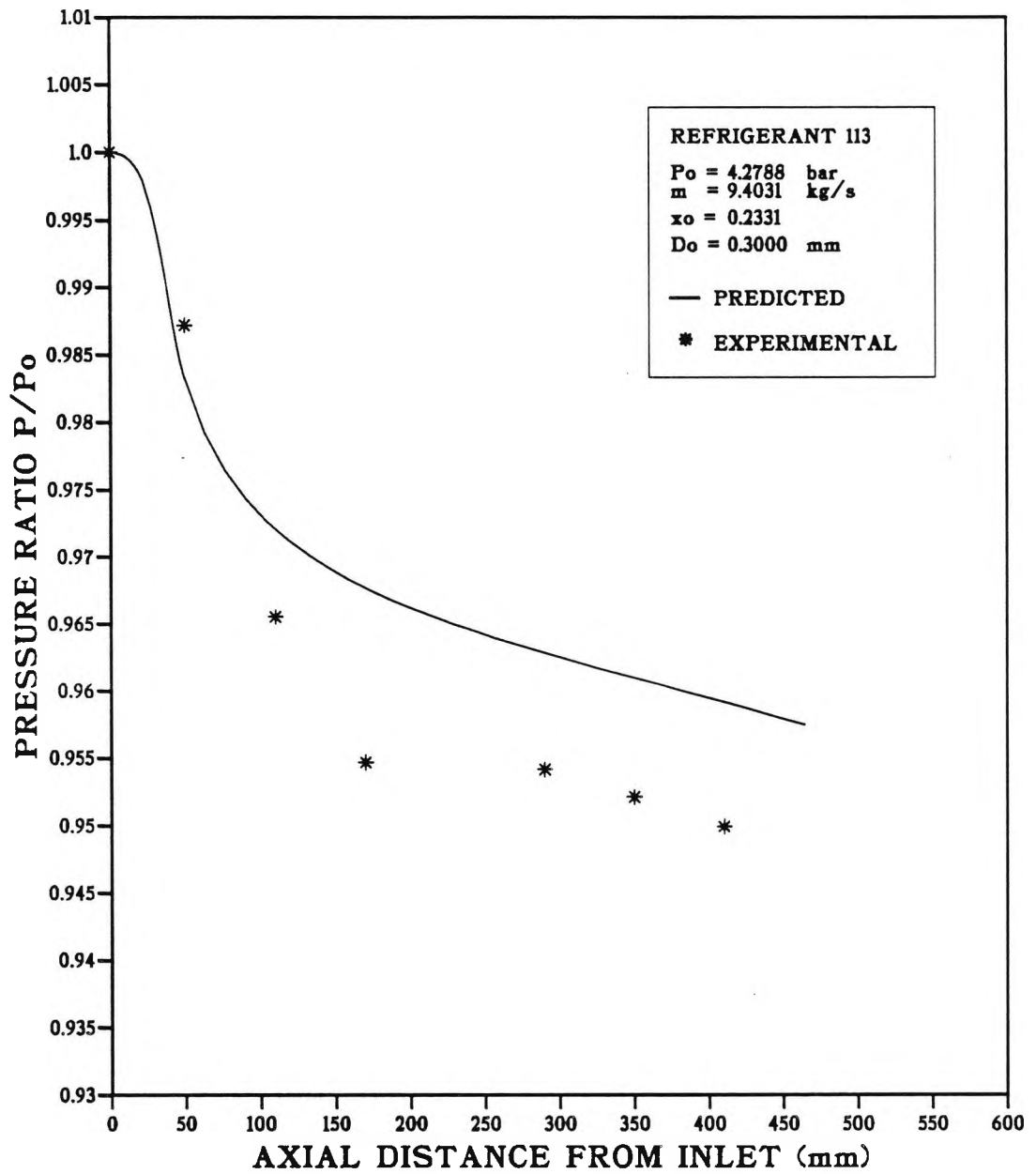


Fig.8.20. Experimental and Computed Pressure Distributions
 (Test Run: R.113-B8)

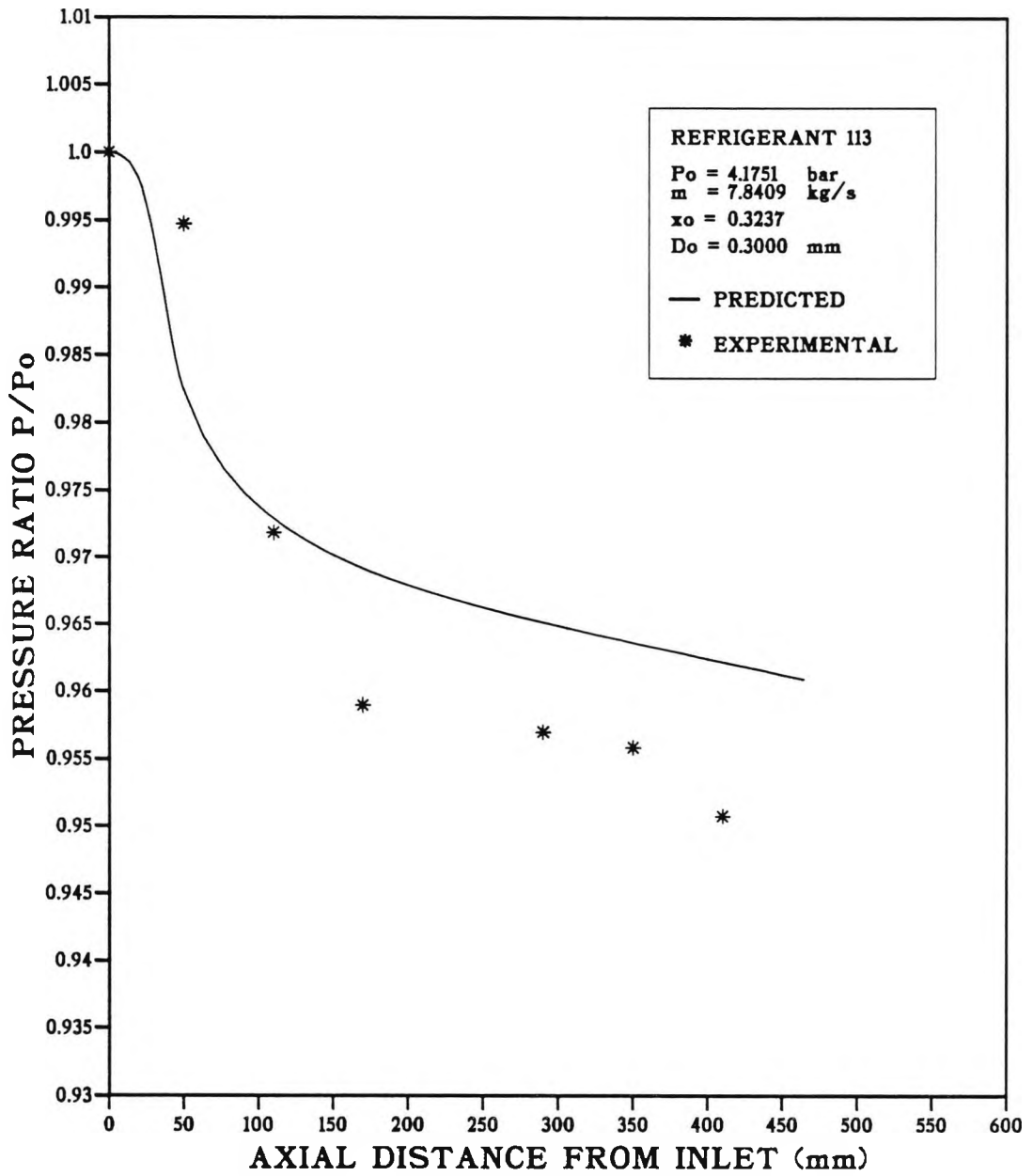


Fig.8.21. Experimental and Computed Pressure Distributions
 (Test Run: R.113-B9)

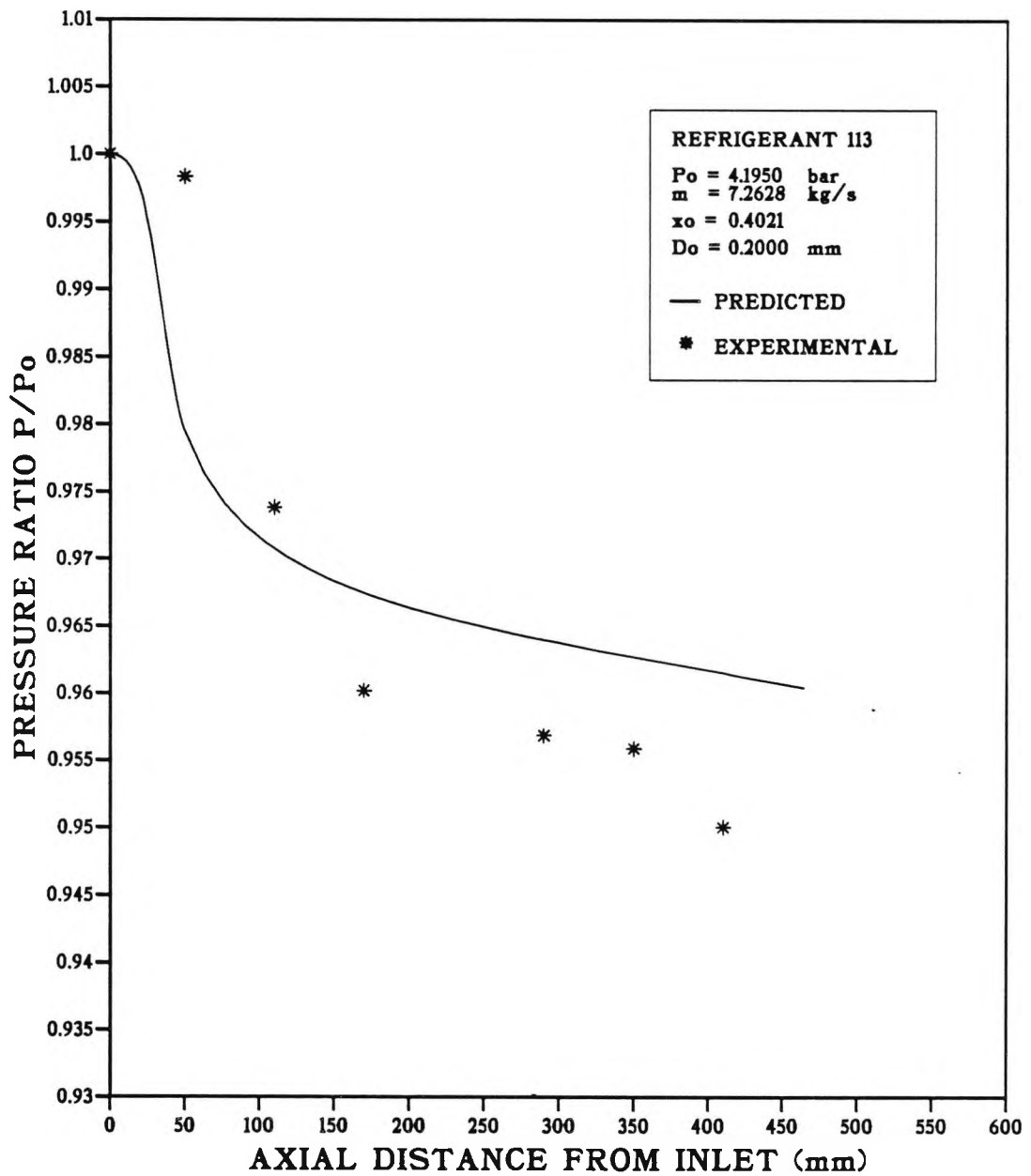


Fig.8.22. Experimental and Computed Pressure Distributions
 (Test Run: R.113-B10)

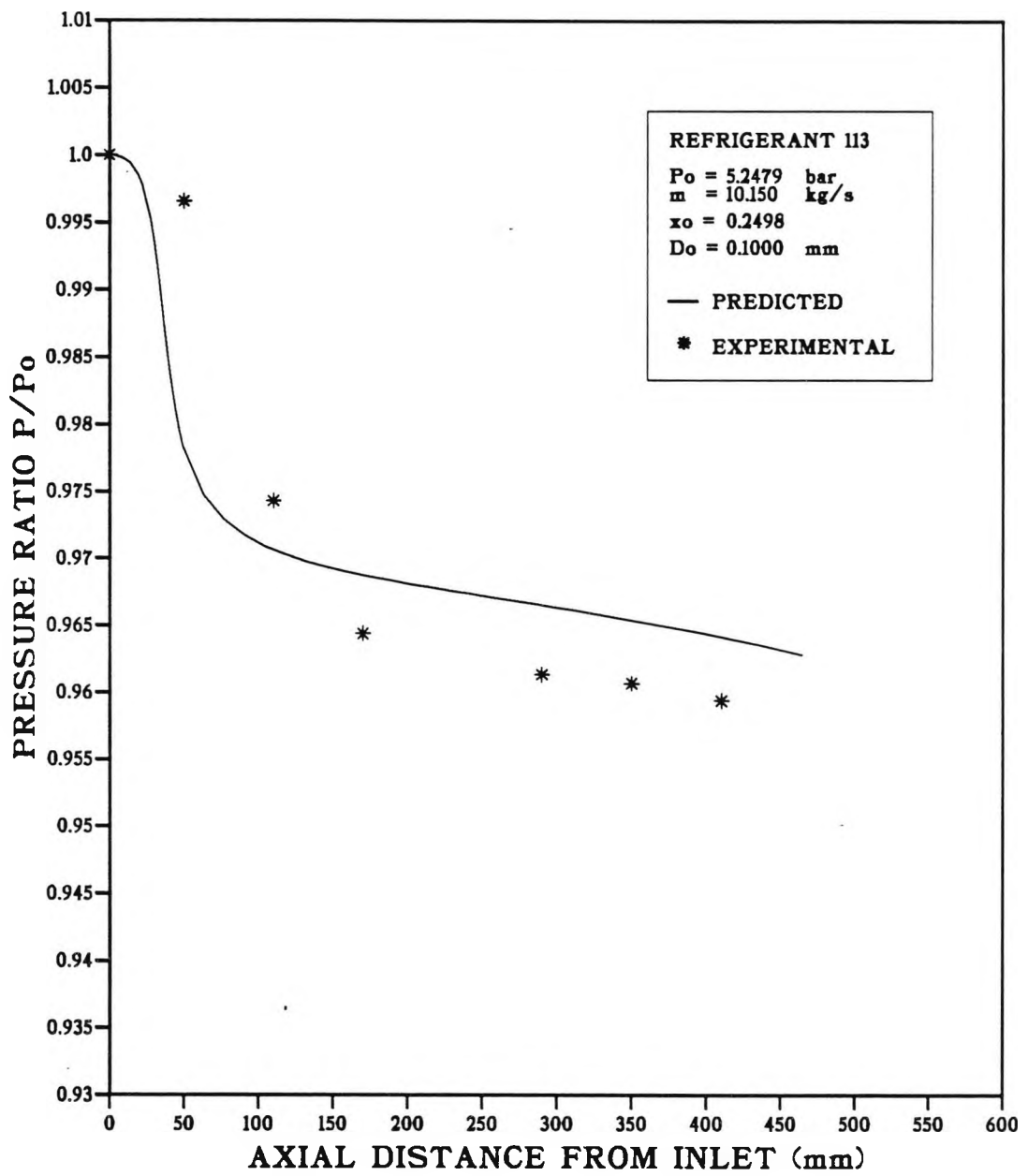


Fig.8.23. Experimental and Computed Pressure Distributions
 (Test Run: R.113-B11)

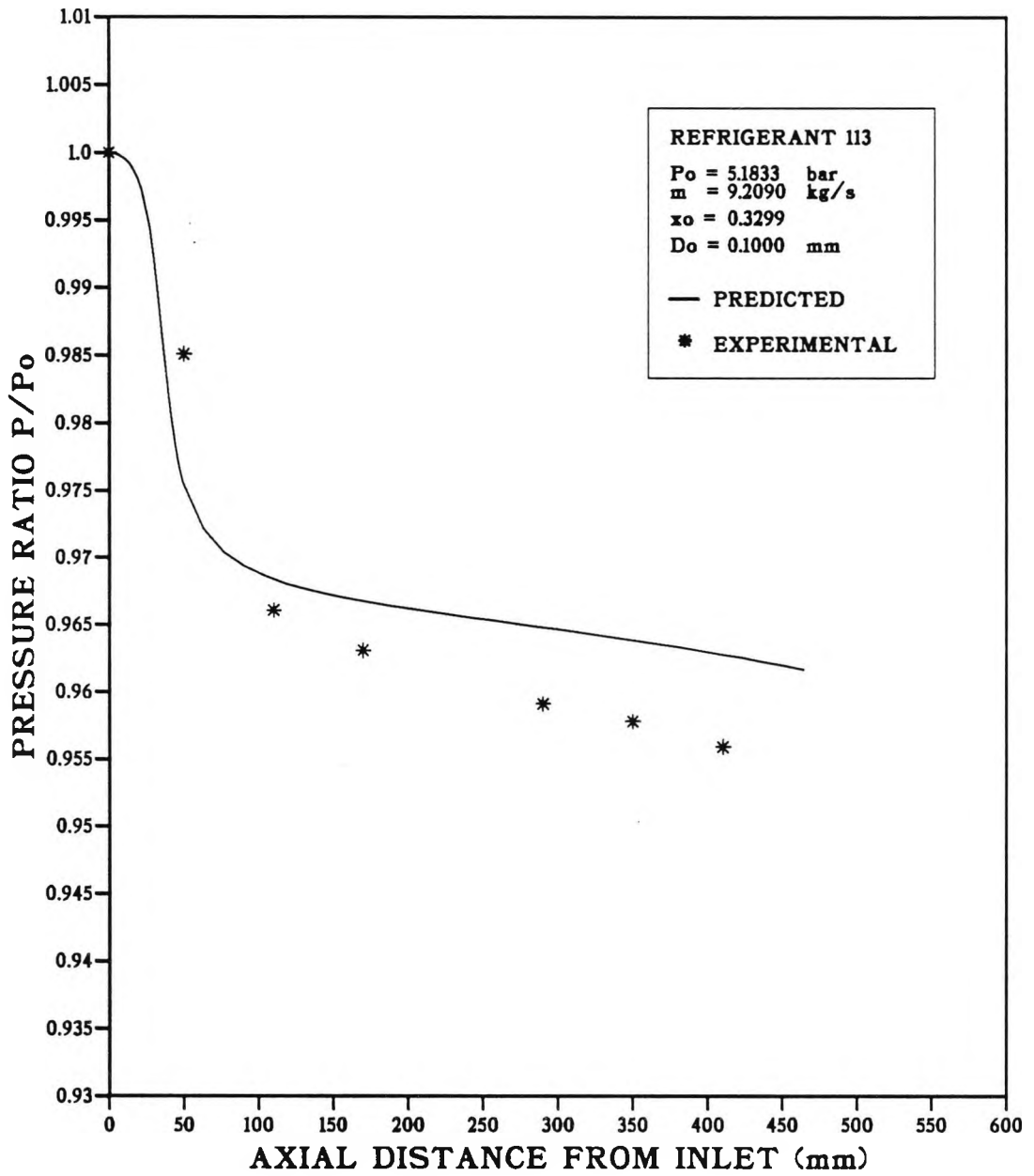


Fig.8.24. Experimental and Computed Pressure Distributions
 (Test Run: R.113-B12)

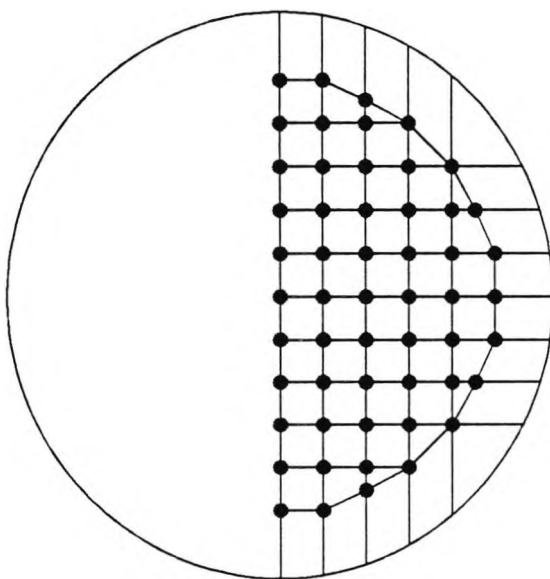


Fig.8.25. Void Fraction Measurement Points
(No.1 Inlet Port Exit)

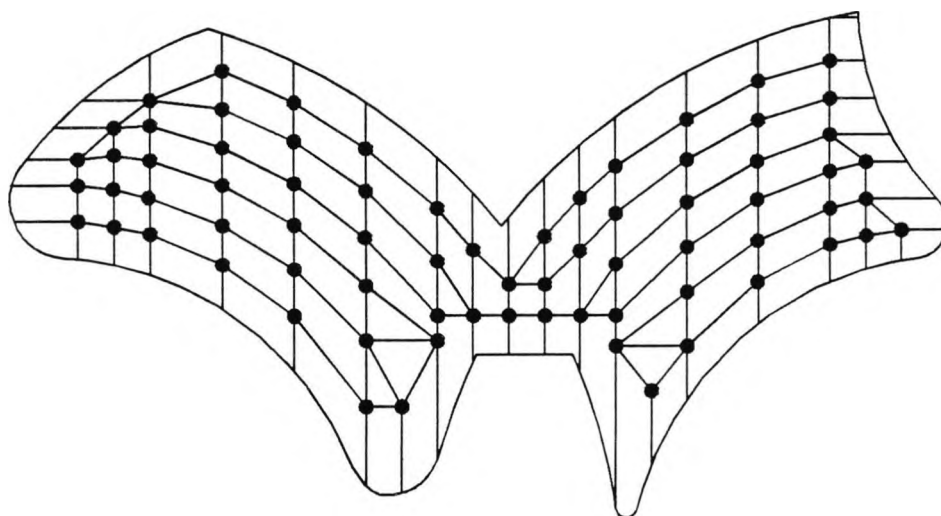


Fig.8.41. Void Fraction Measurement Points
(No.2 Inlet Port Exit)

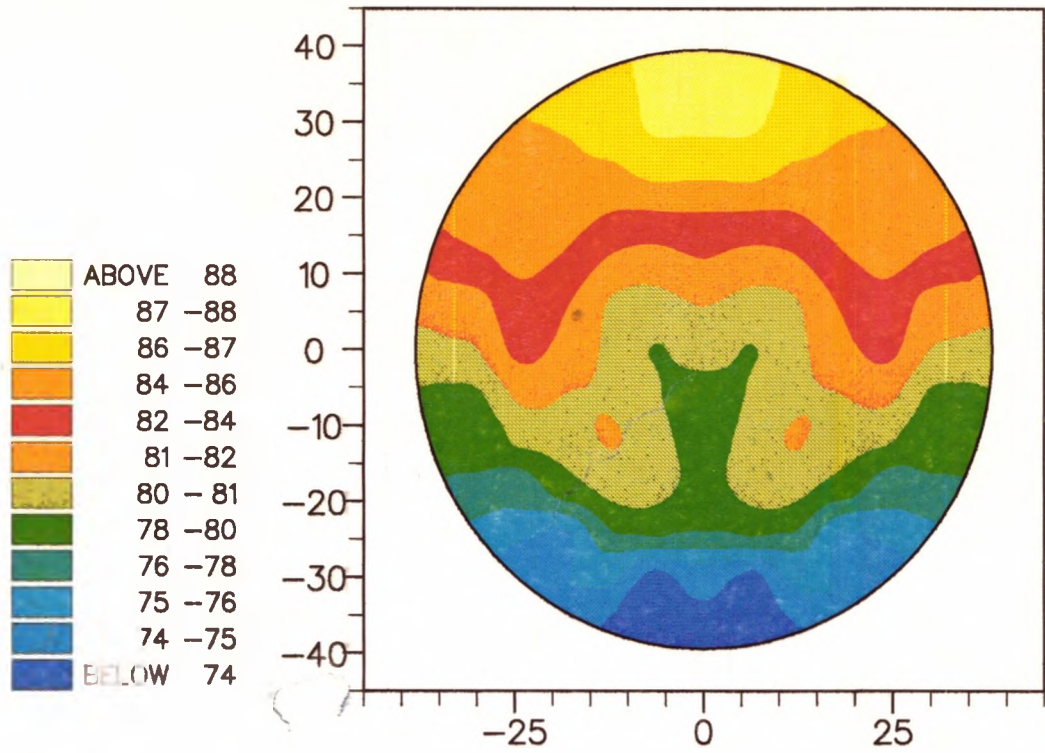


Fig.8.26. Void fraction distribution (R.113-C1)

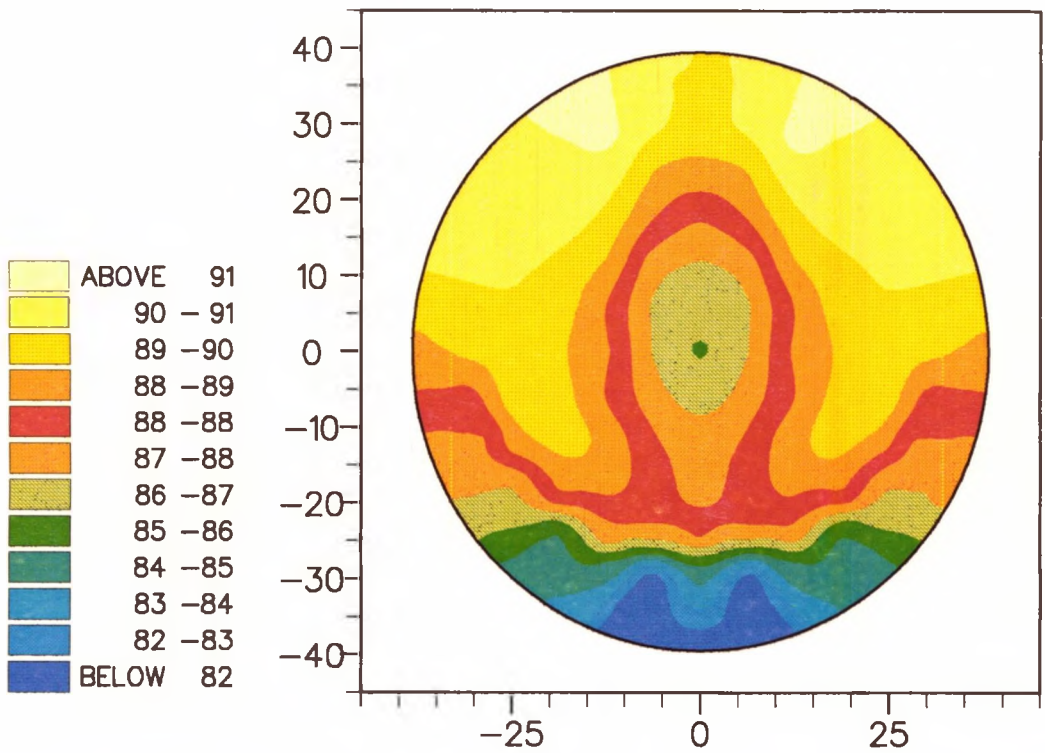


Fig.8.27. Void fraction distribution (R.113-C2)

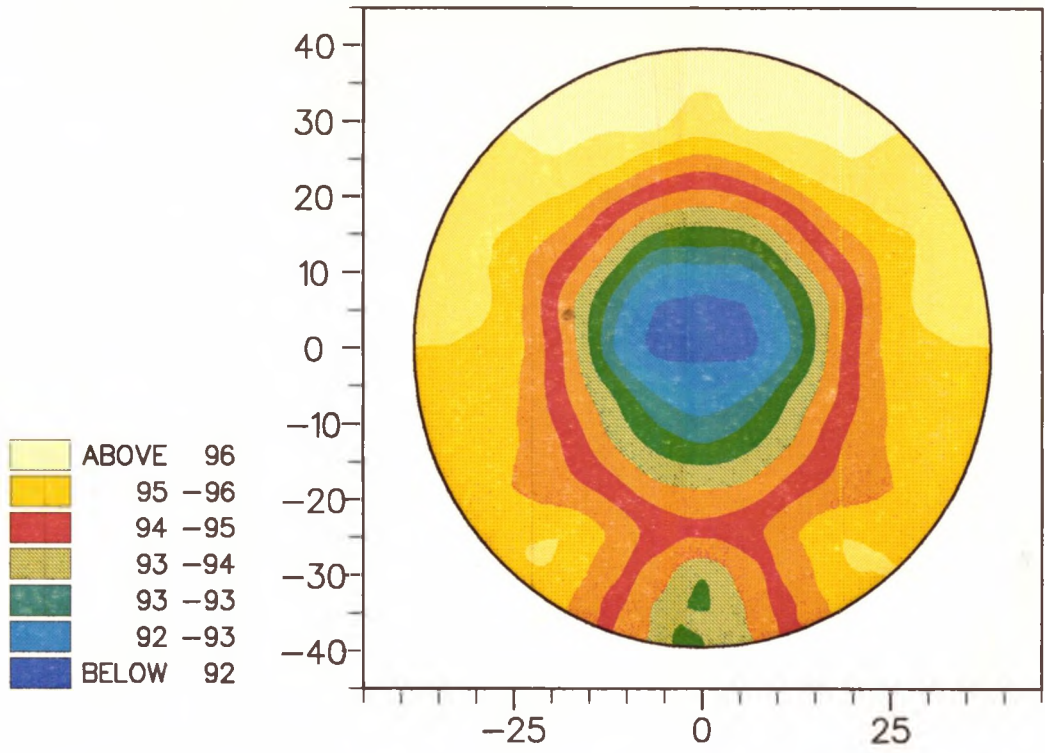


Fig.8.28. Void fraction distribution (R.113-C3)

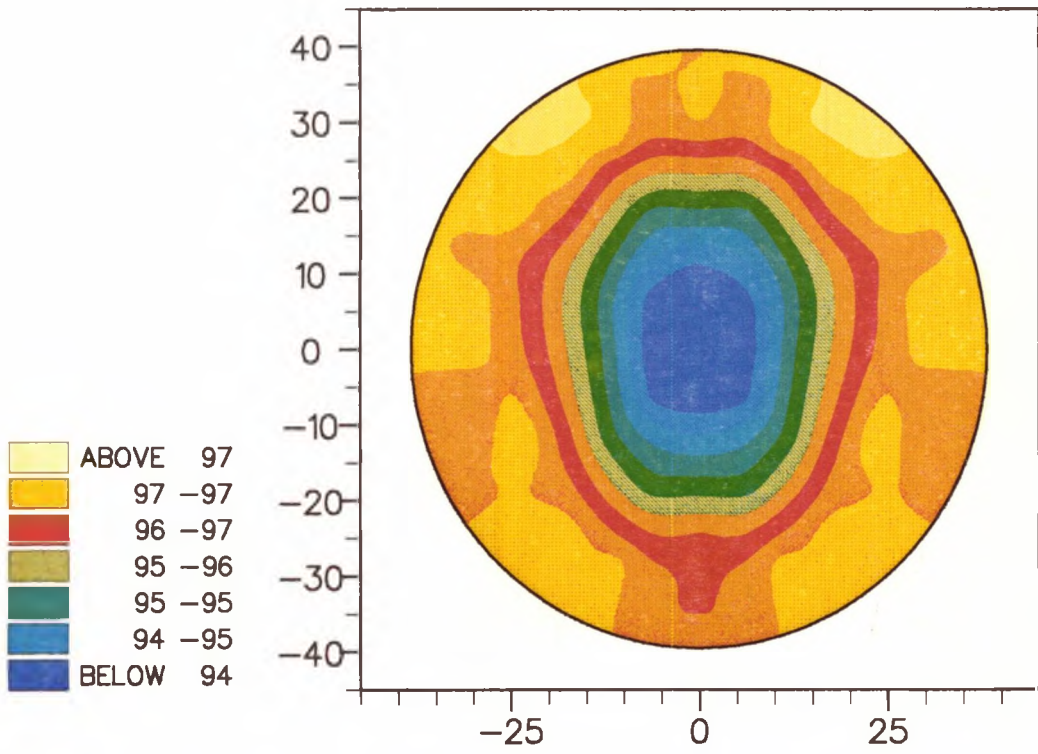


Fig.8.29. Void fraction distribution (R.113-C4)

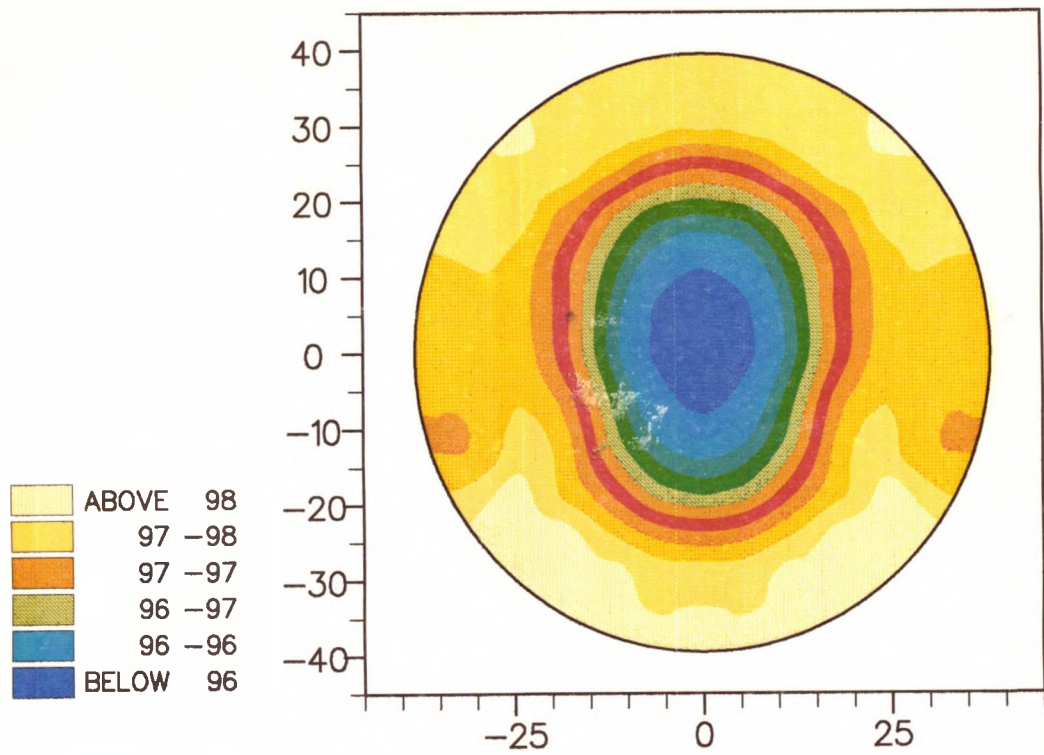


Fig.8.30. Void fraction distribution (R.113-C5)

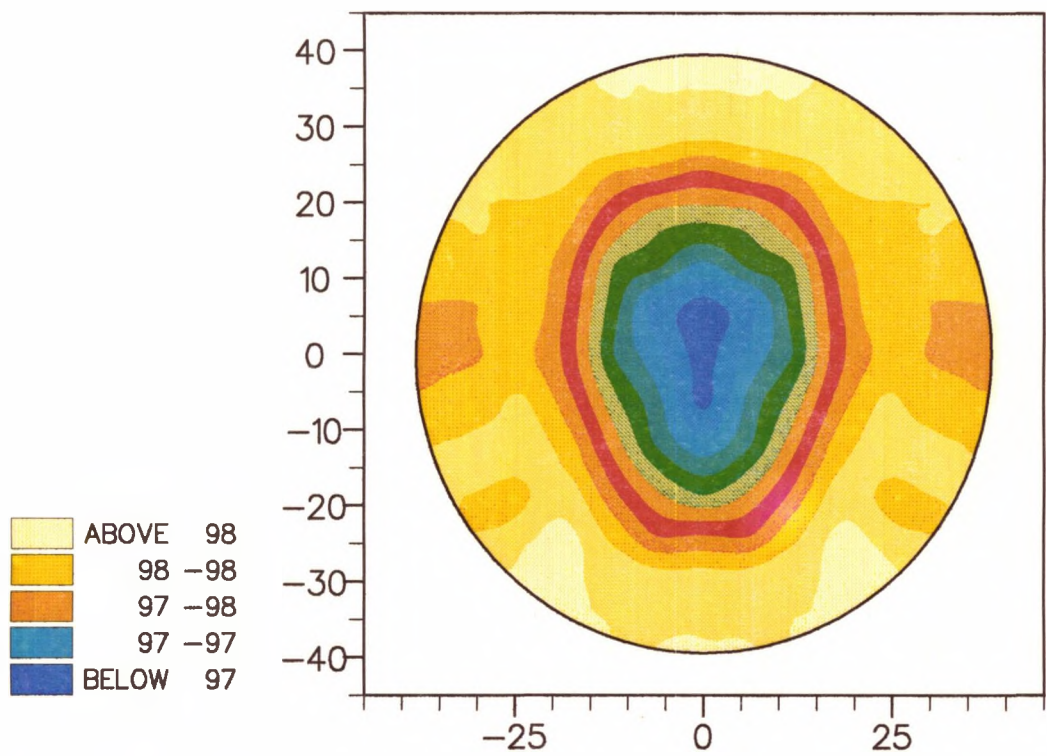


Fig.8.31. Void fraction distribution (R.113-C6)

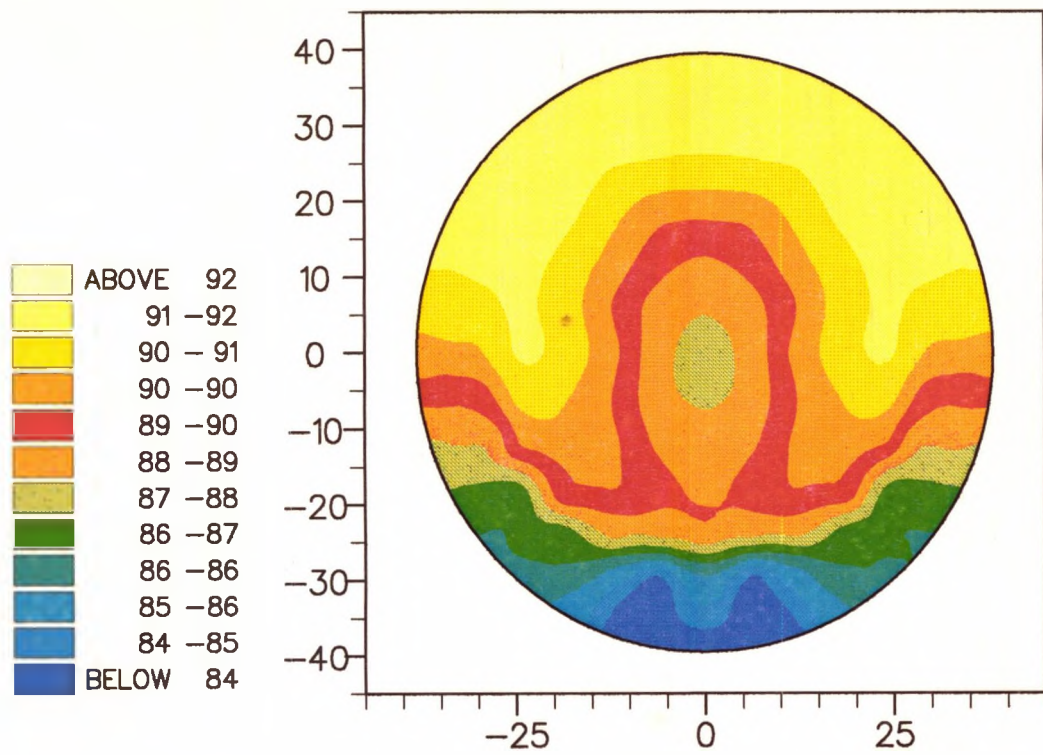


Fig.8.32. Void fraction distribution (R.113-C7)

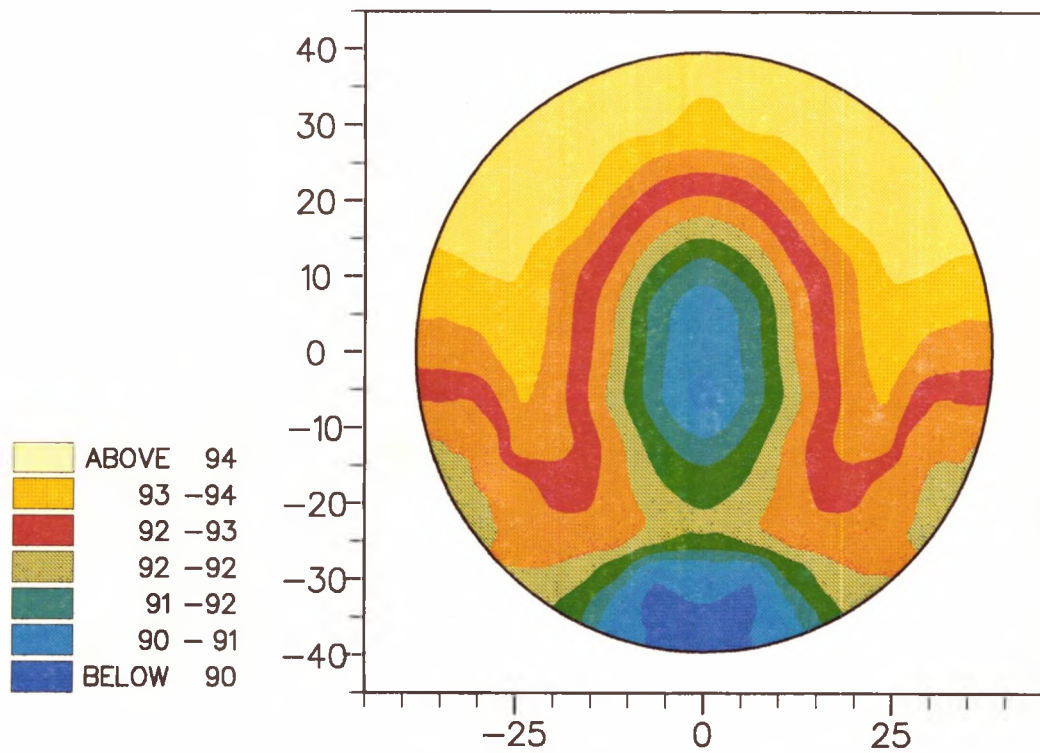


Fig.8.33. Void fraction distribution (R.113-C8)

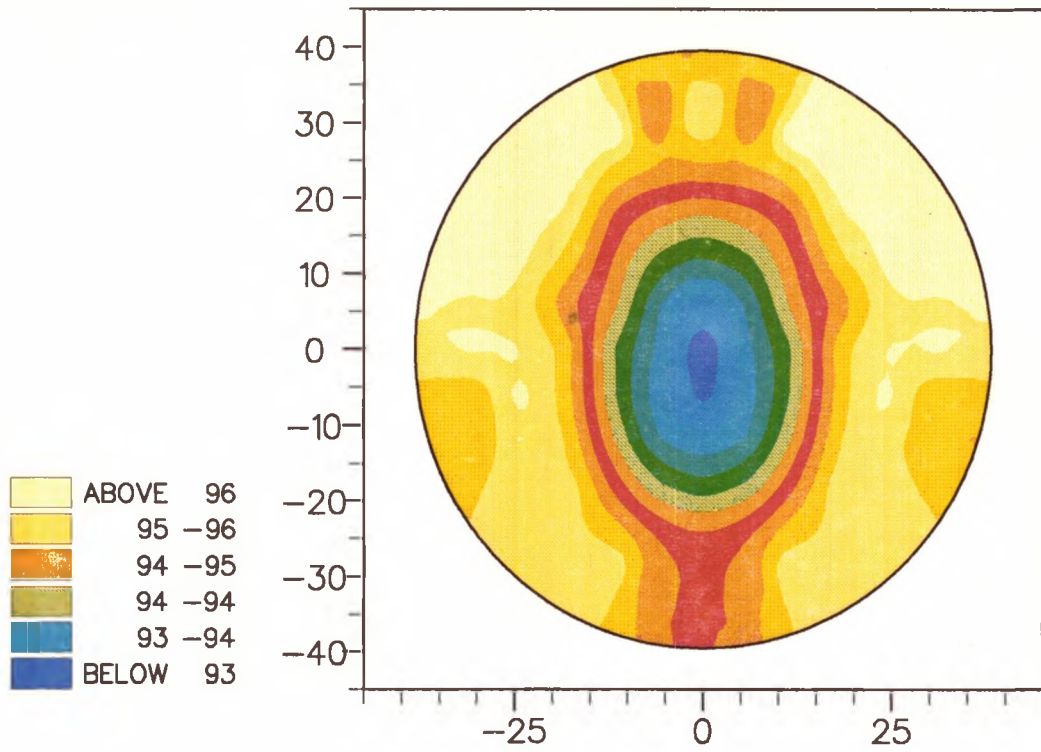


Fig.8.34. Void fraction distribution (R.113-C9)

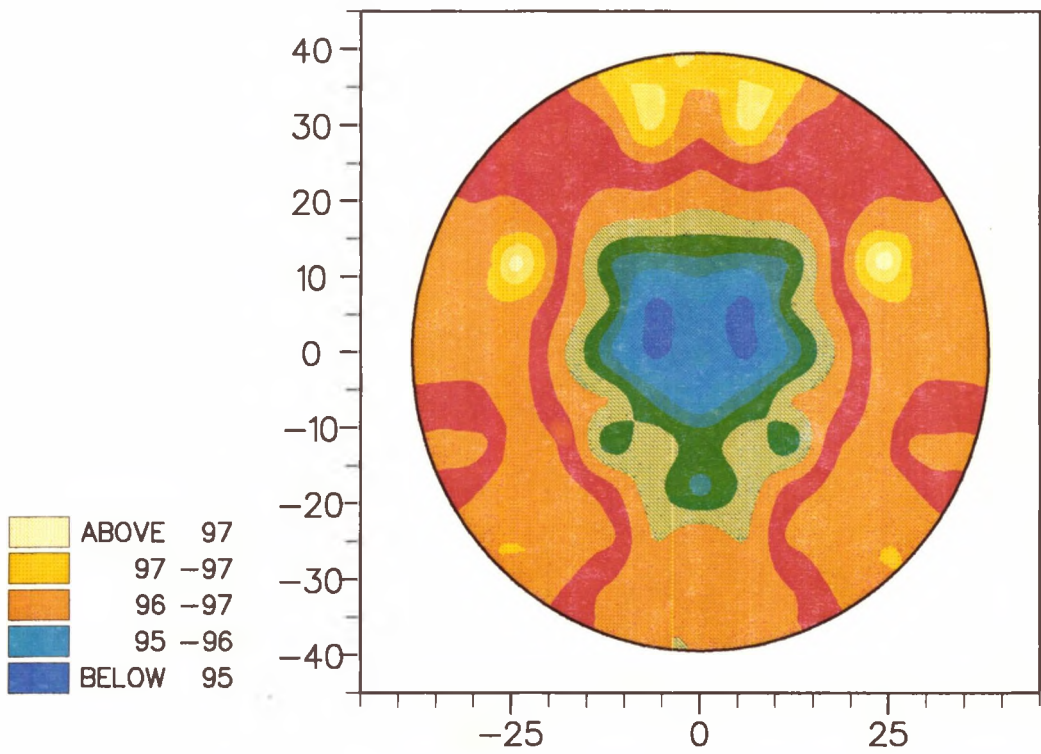


Fig.8.35. Void fraction distribution (R.113-C10)

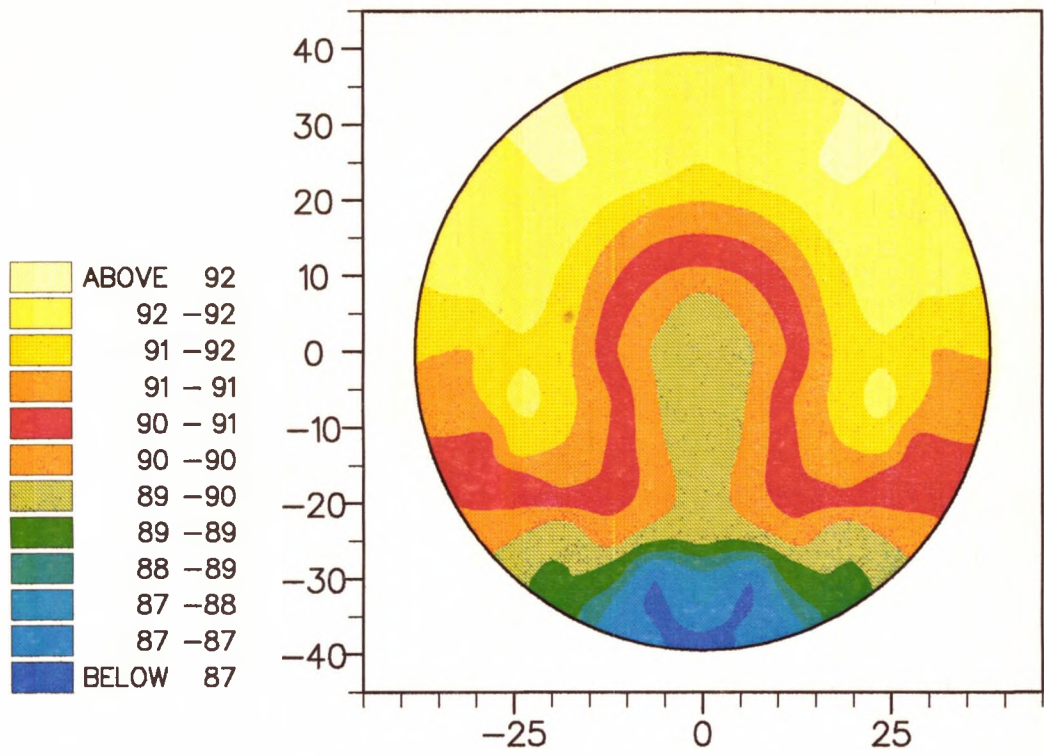


Fig.8.36. Void fraction distribution (R.113-C11)

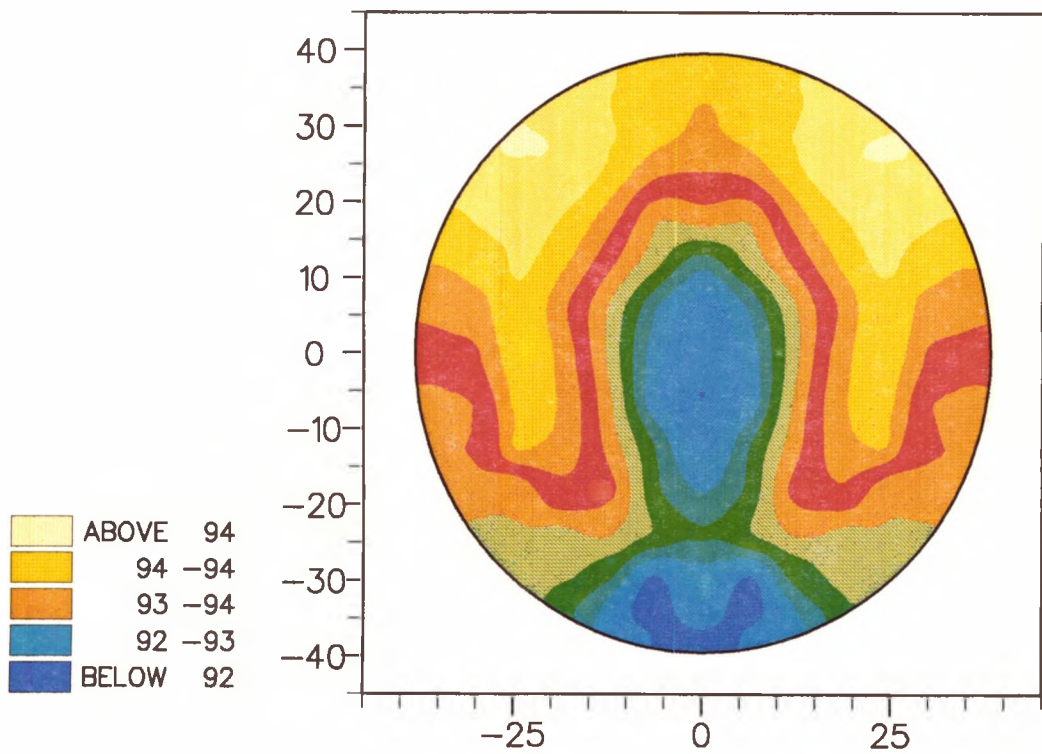


Fig.8.37. Void fraction distribution (R.113-C12)

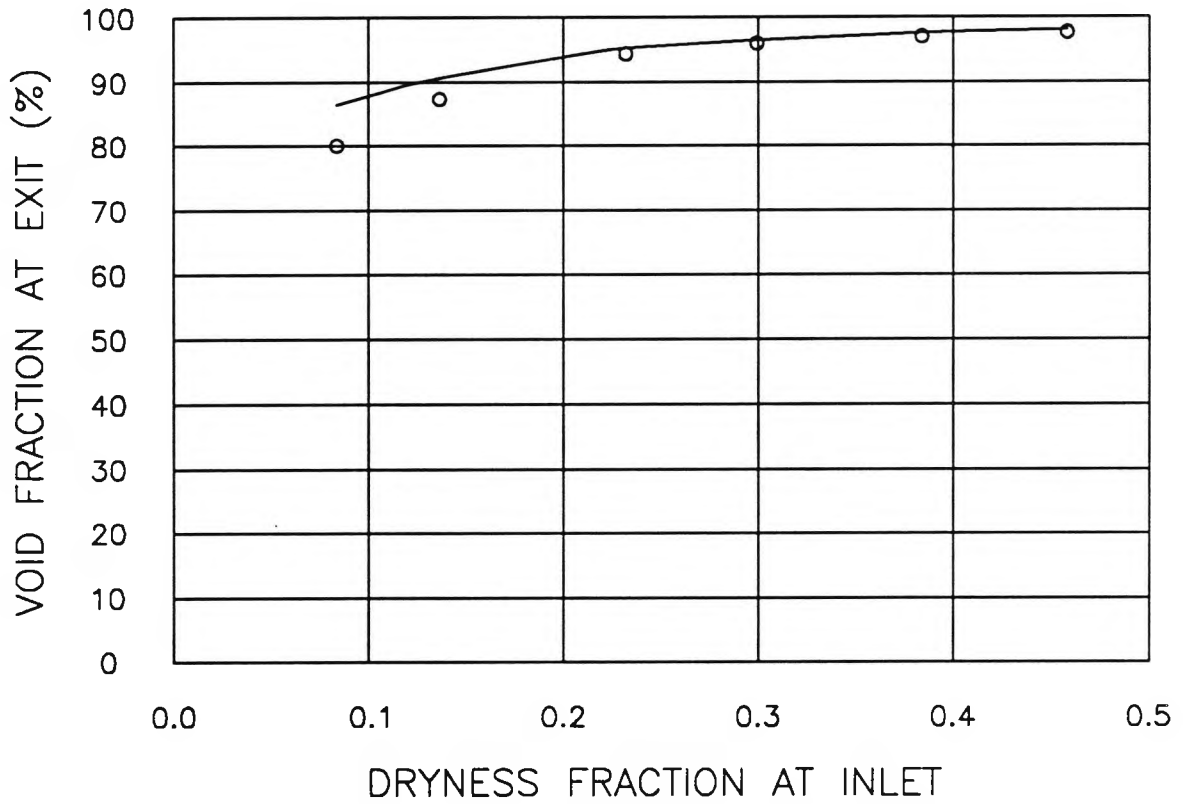


Fig.8.38. Comparison of Experimental and Computed Average Void Fractions at No.1 Inlet Port Exit (90°C)

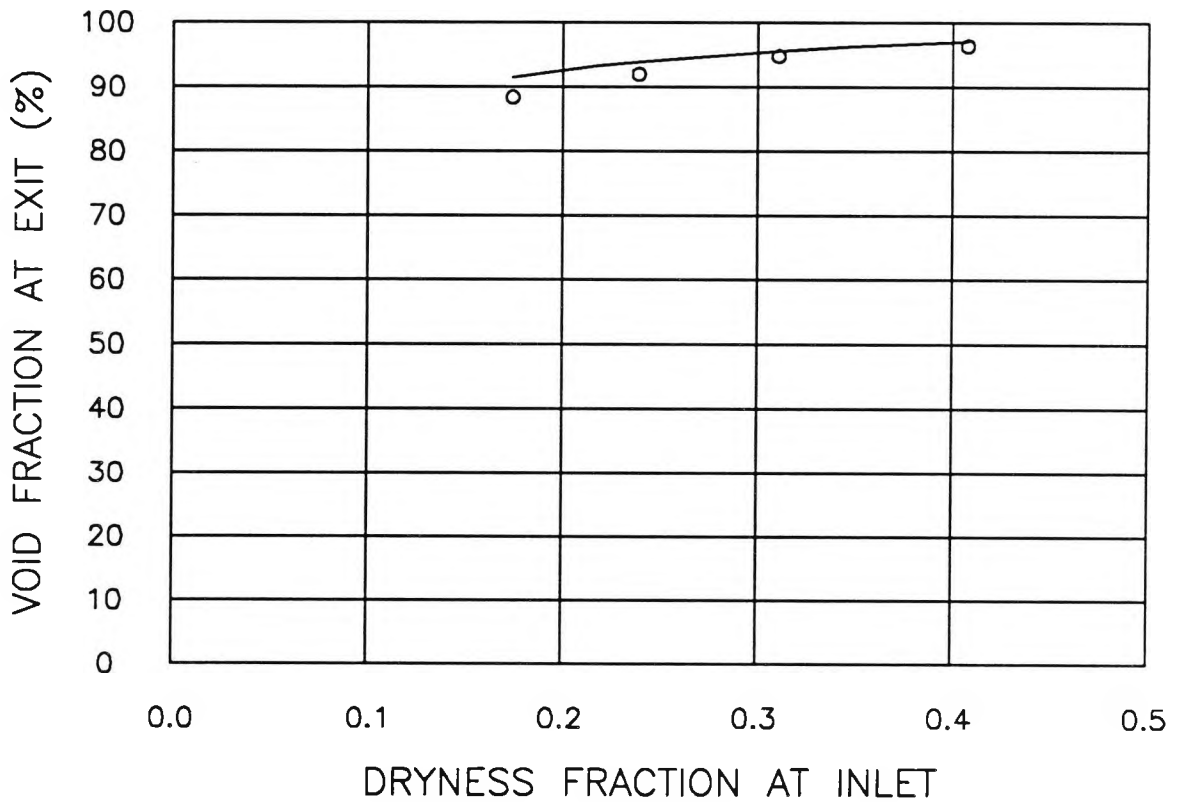


Fig.8.39. Comparison of Experimental and Computed Average Void Fractions at No.1 Inlet Port Exit (100°C)

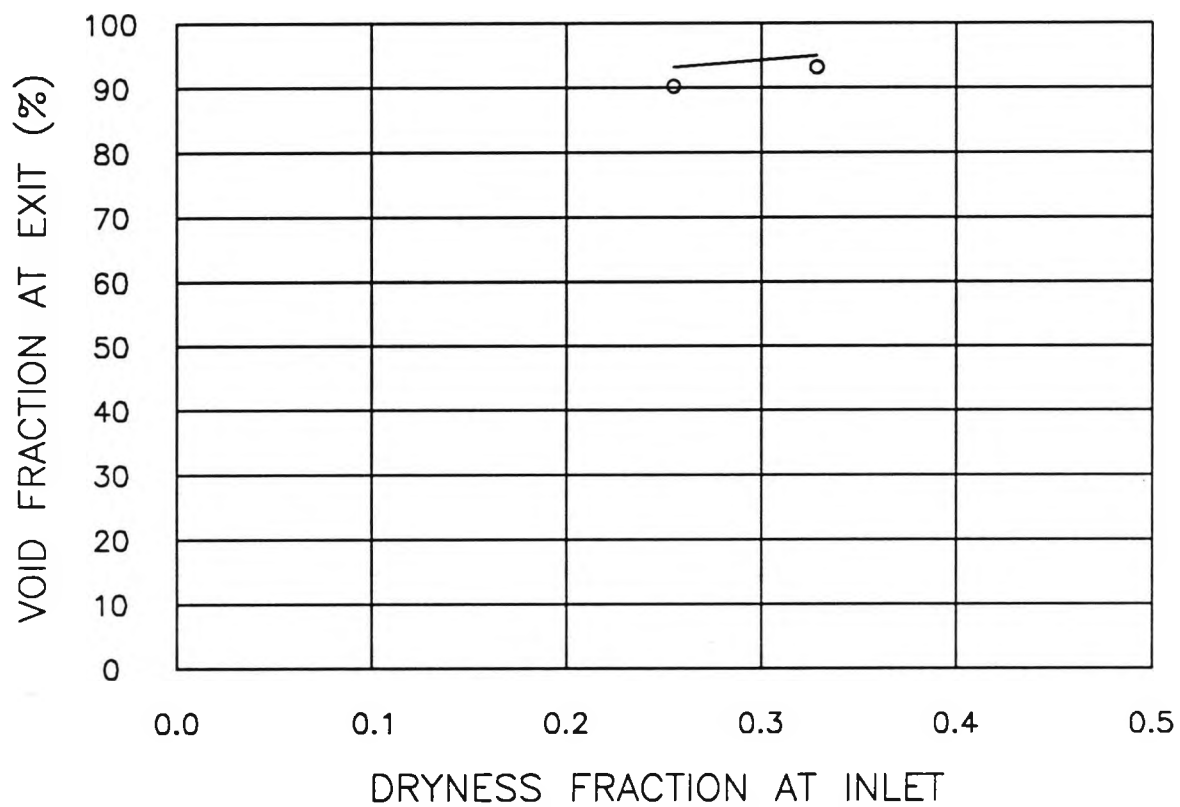


Fig.8.40. Comparison of Experimental and Computed Average Void Fractions at No.1 Inlet Port Exit (110°C)

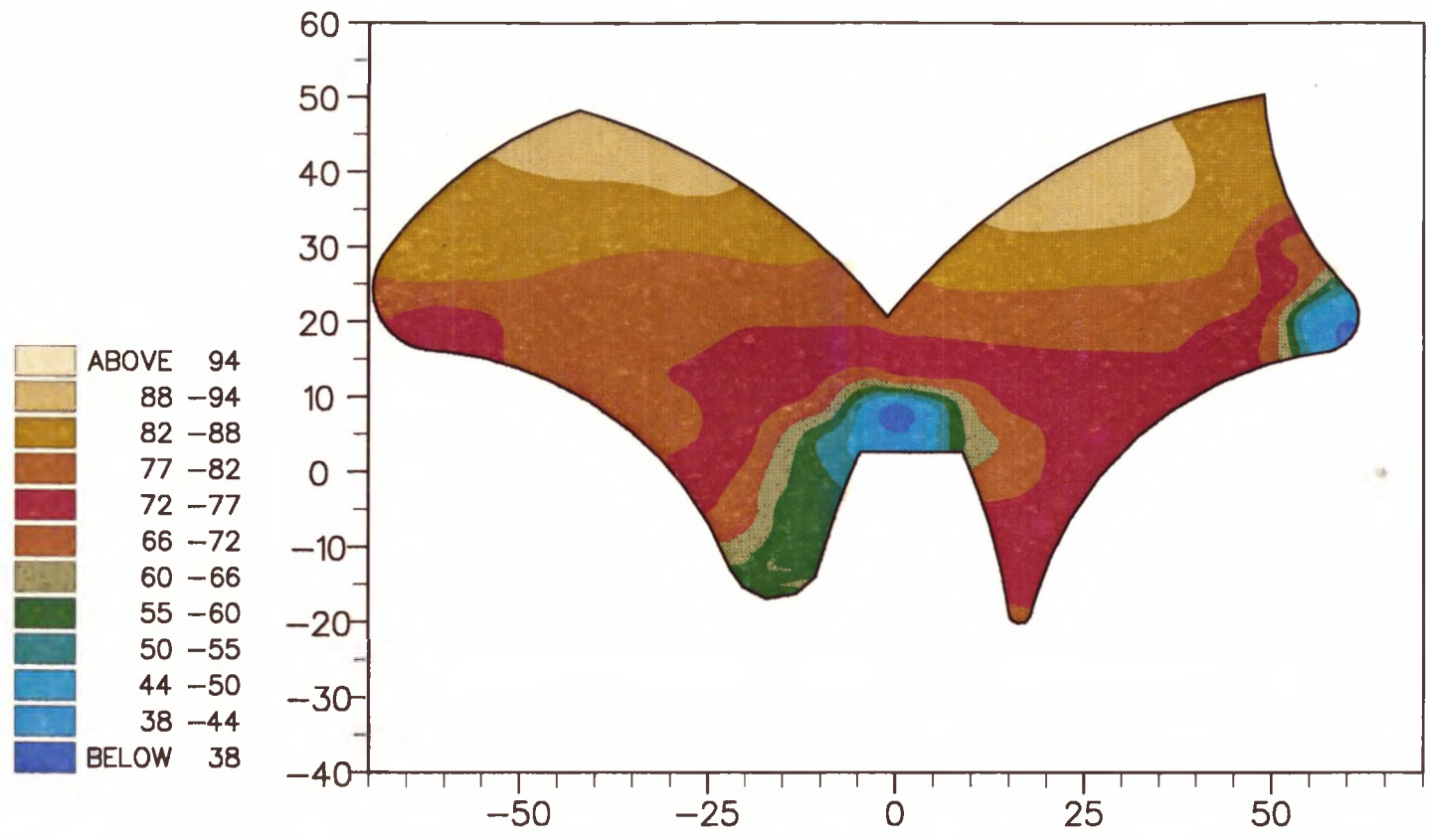


Fig.8.42. Void fraction distribution (R.113-B1)

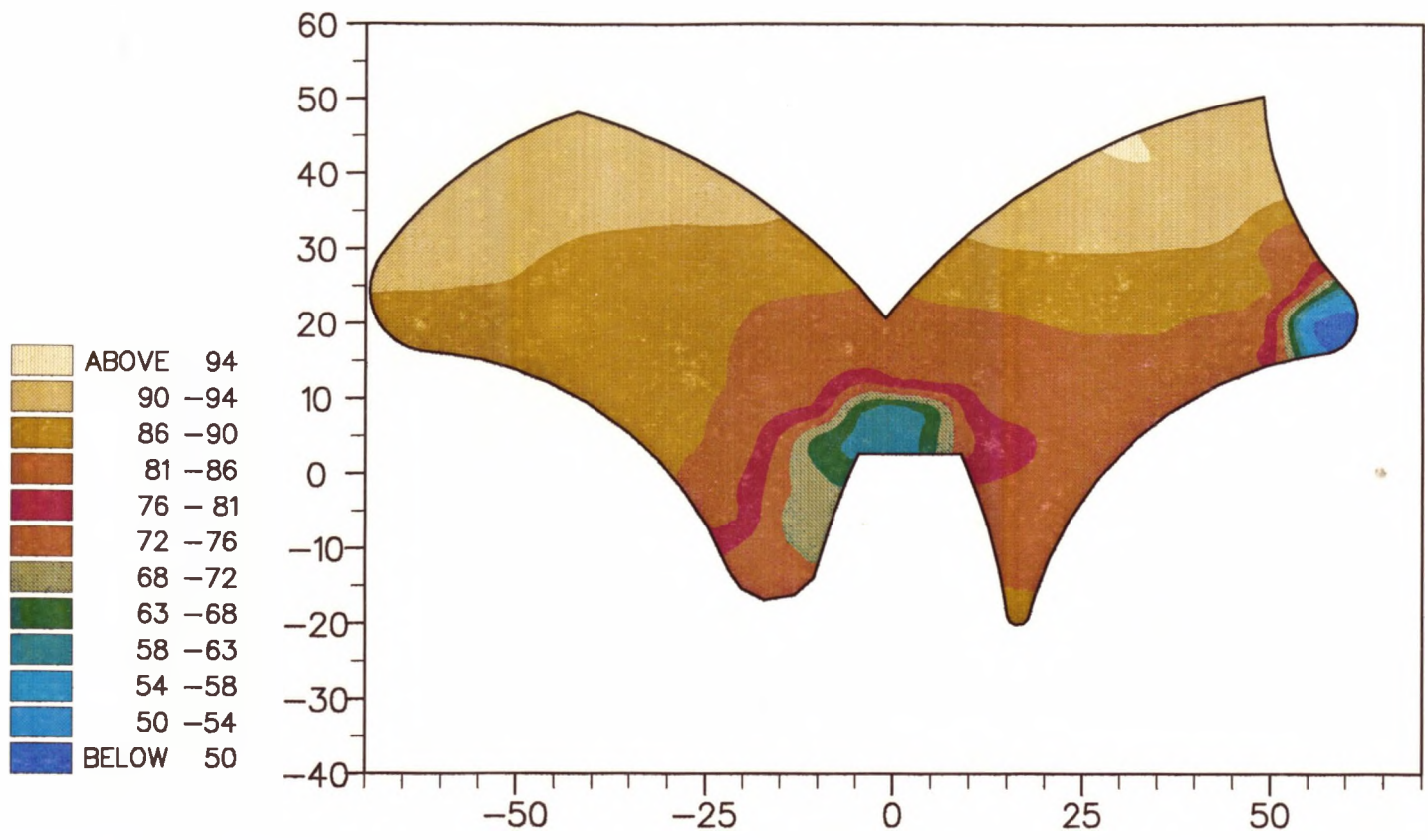


Fig.8.43. Void fraction distribution (R.113-B2)

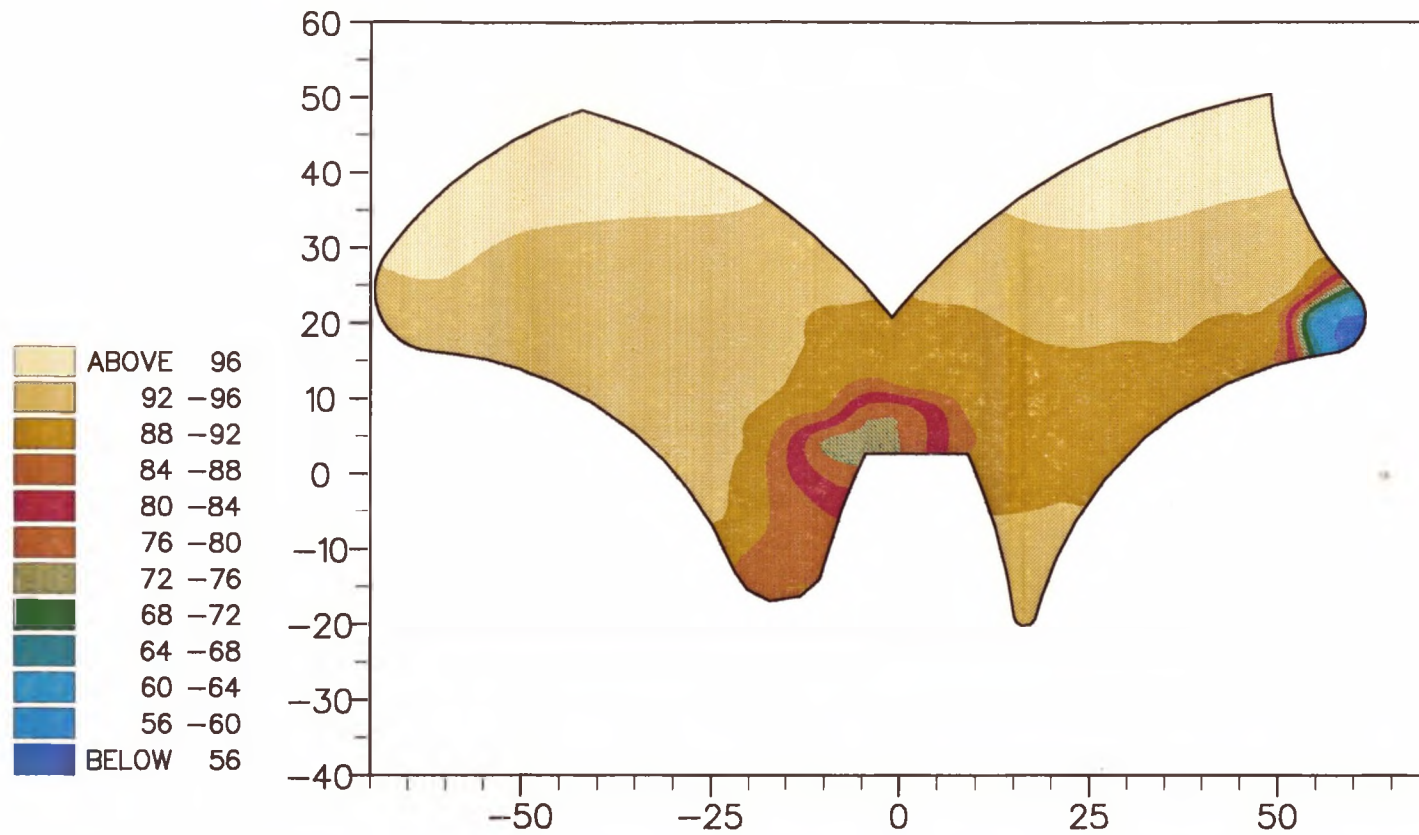


Fig.8.44. Void fraction distribution (R.113-B3)

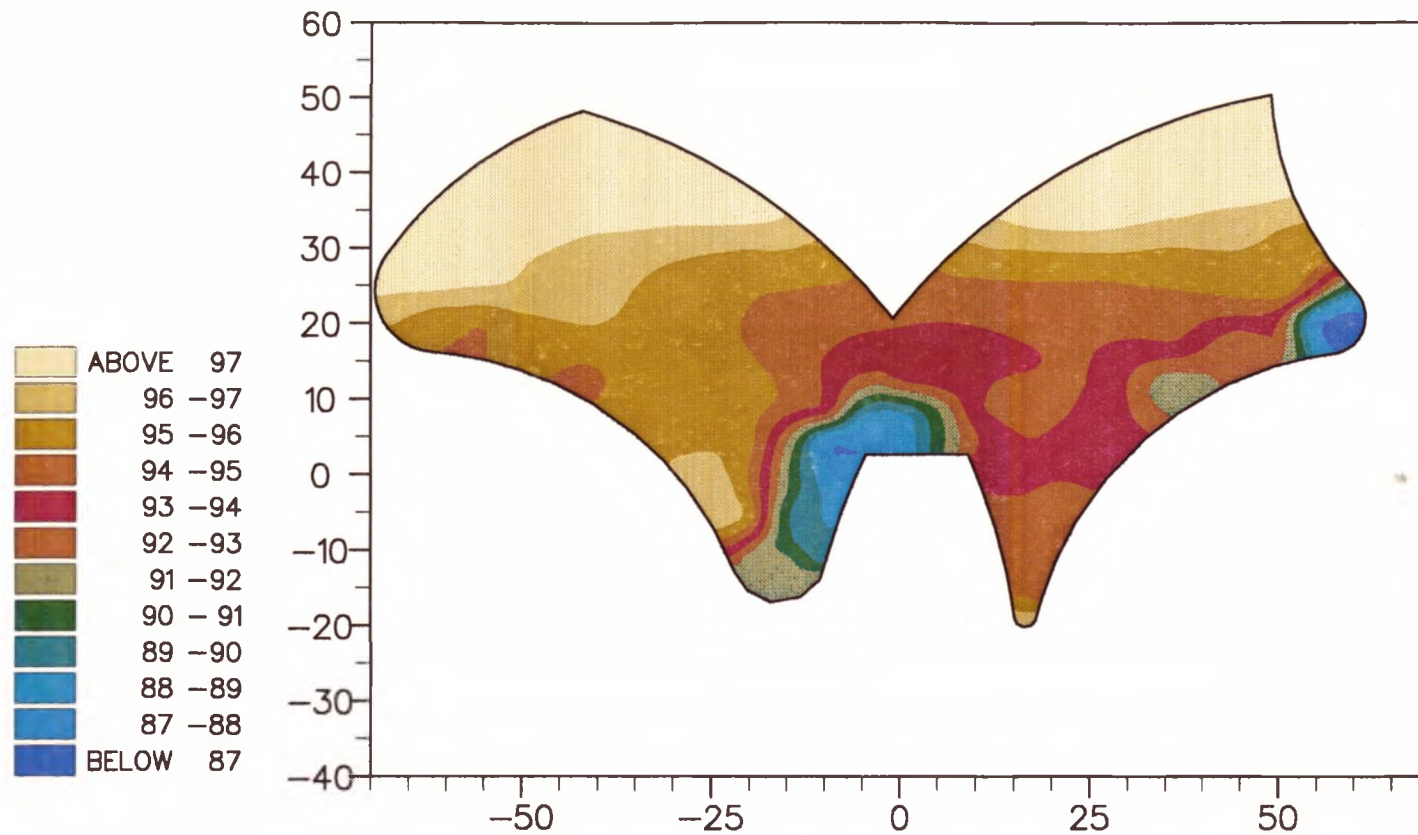


Fig.8.45. Void fraction distribution (R.113-B4)

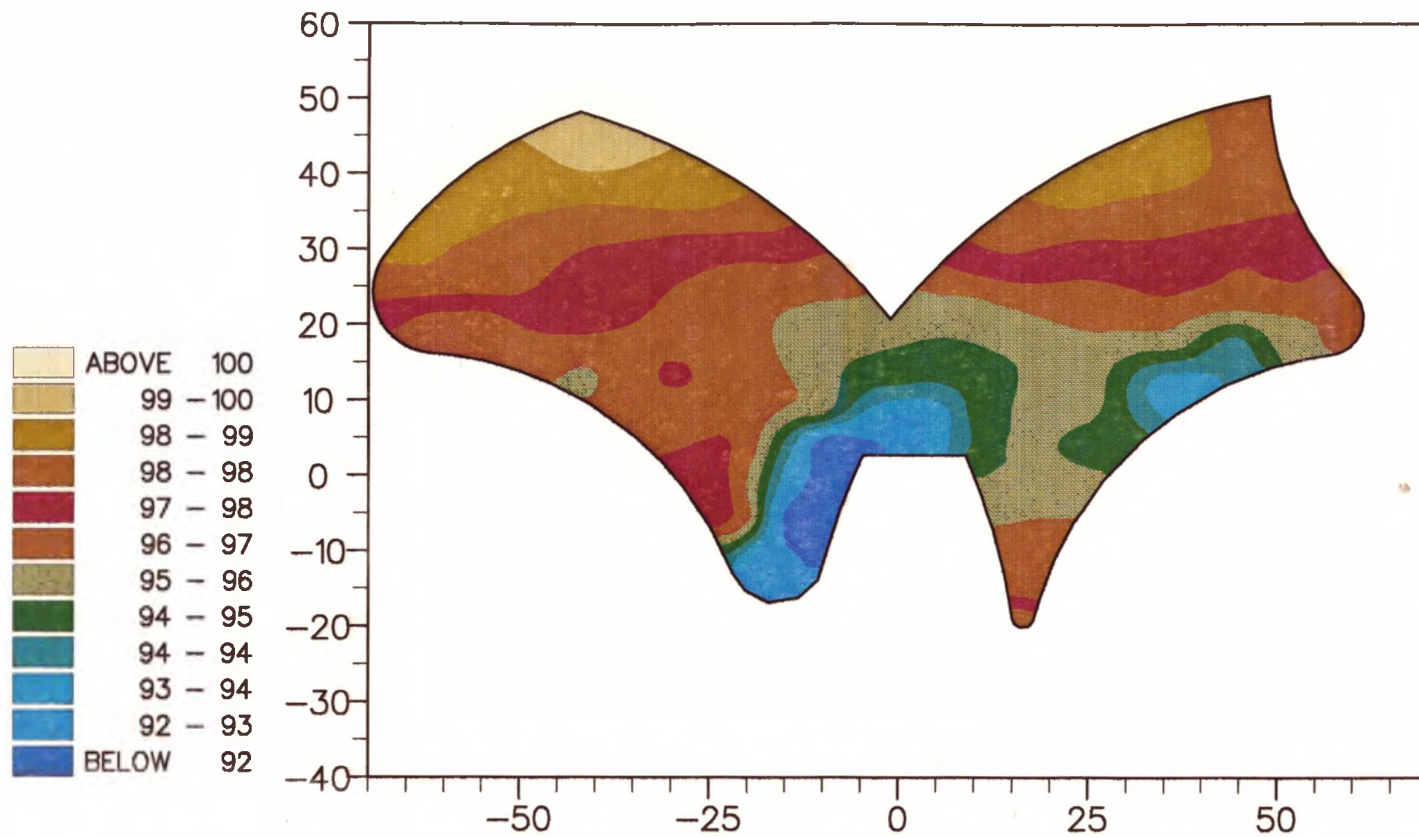


Fig.8.46. Void fraction distribution (R.113-B5)

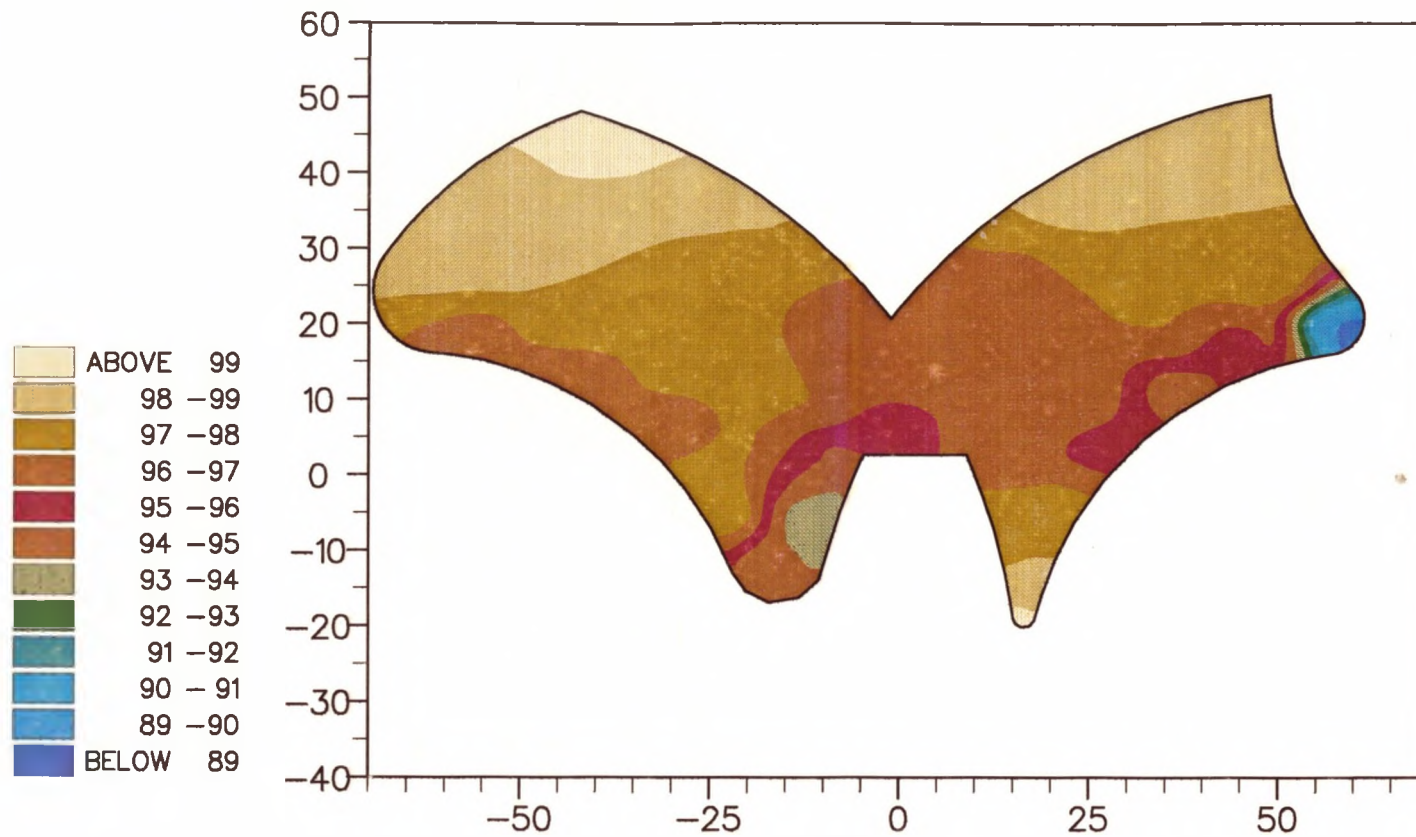


Fig.8.47. Void fraction distribution (R.113-B6)

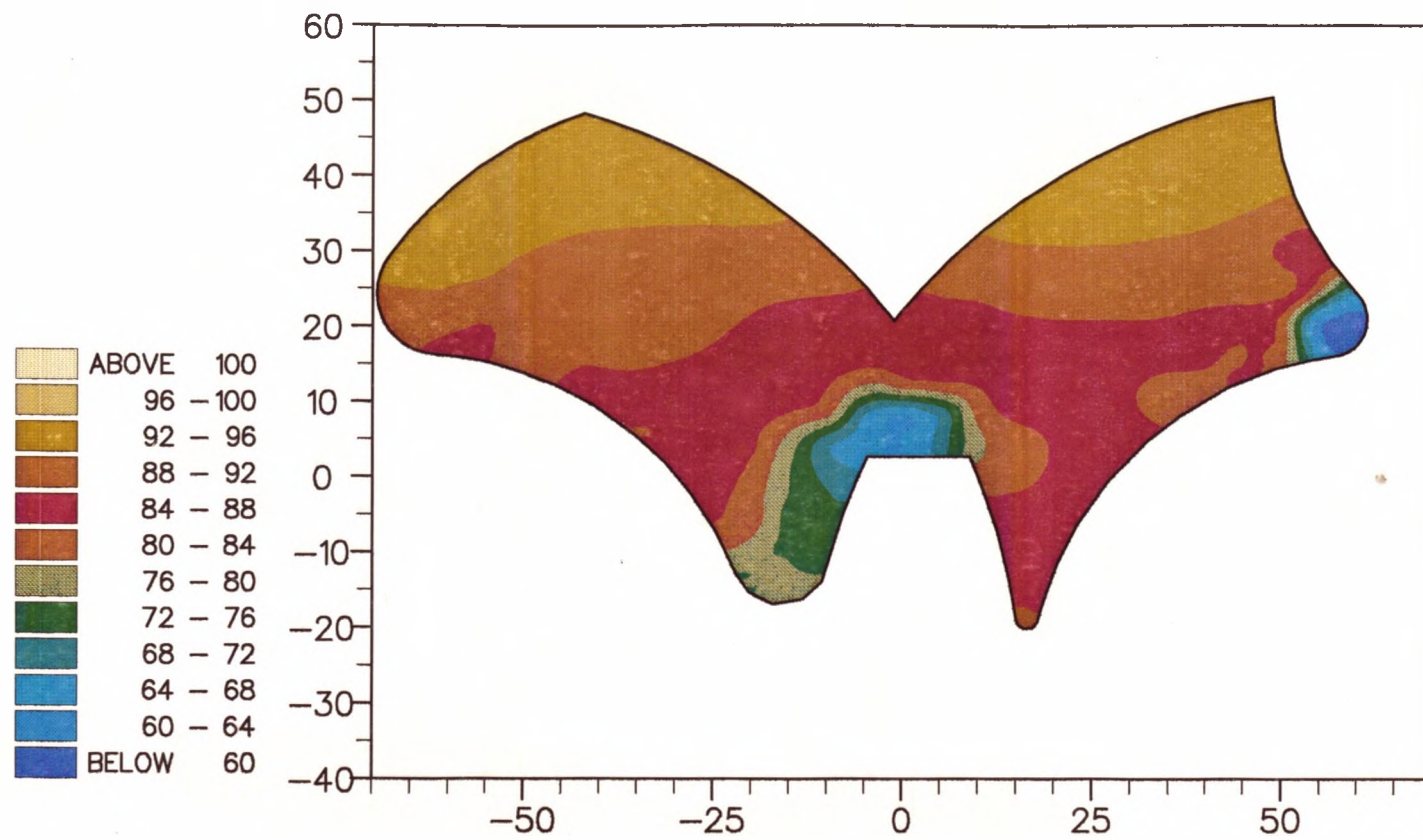


Fig.8.48. Void fraction distribution (R.113-B7)

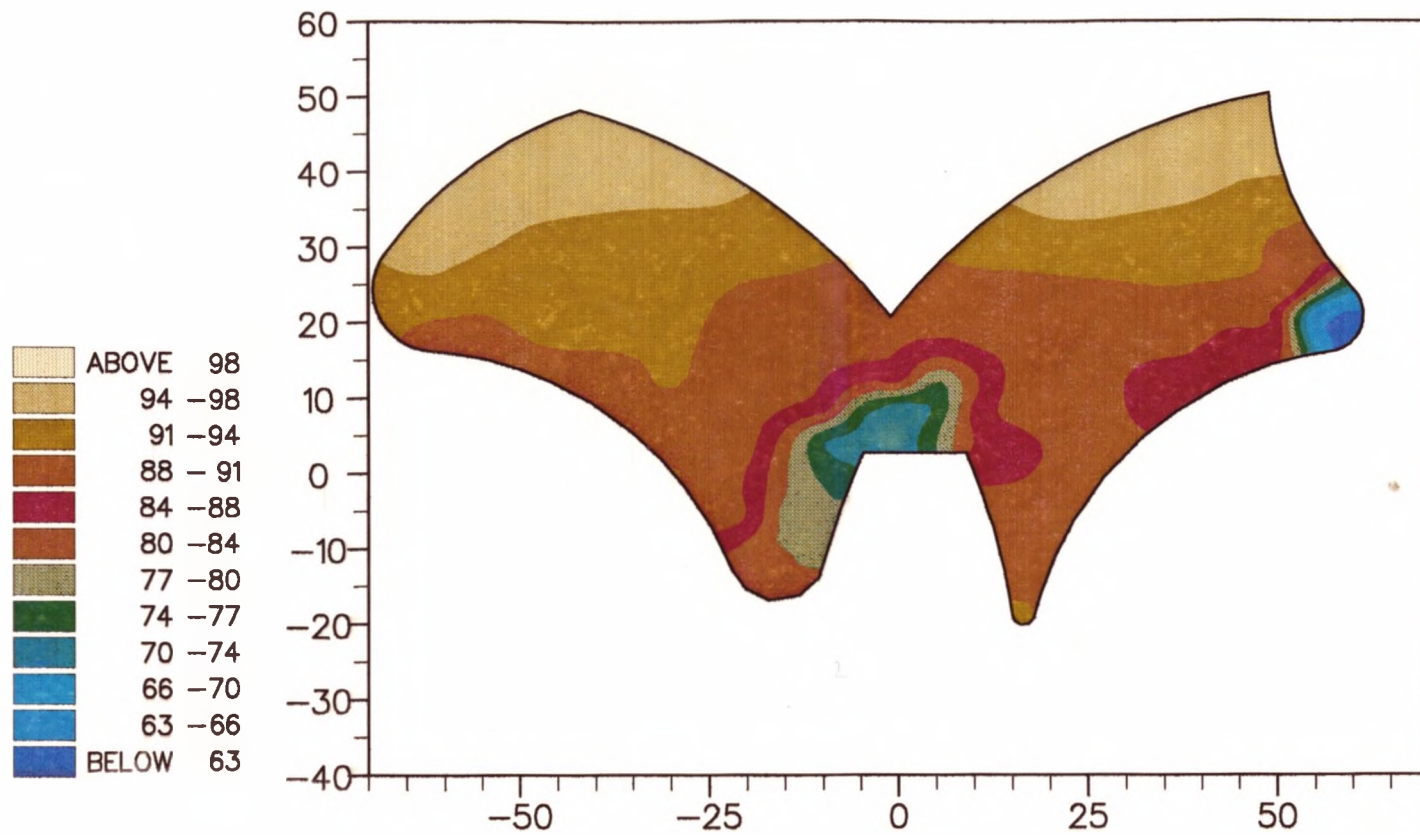


Fig.8.49. Void fraction distribution (R.113-B8)

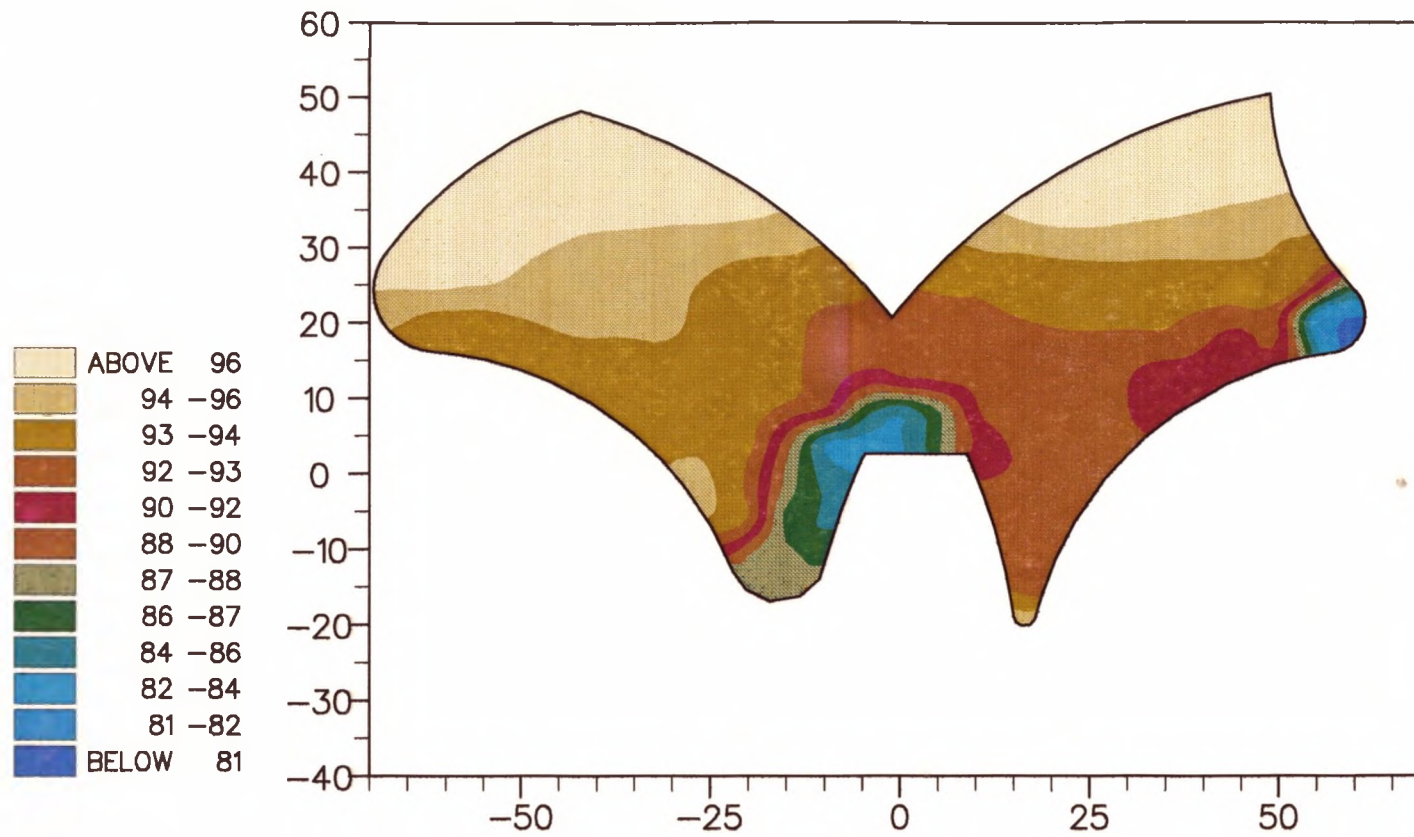


Fig.8.50. Void fraction distribution (R.113-B9)

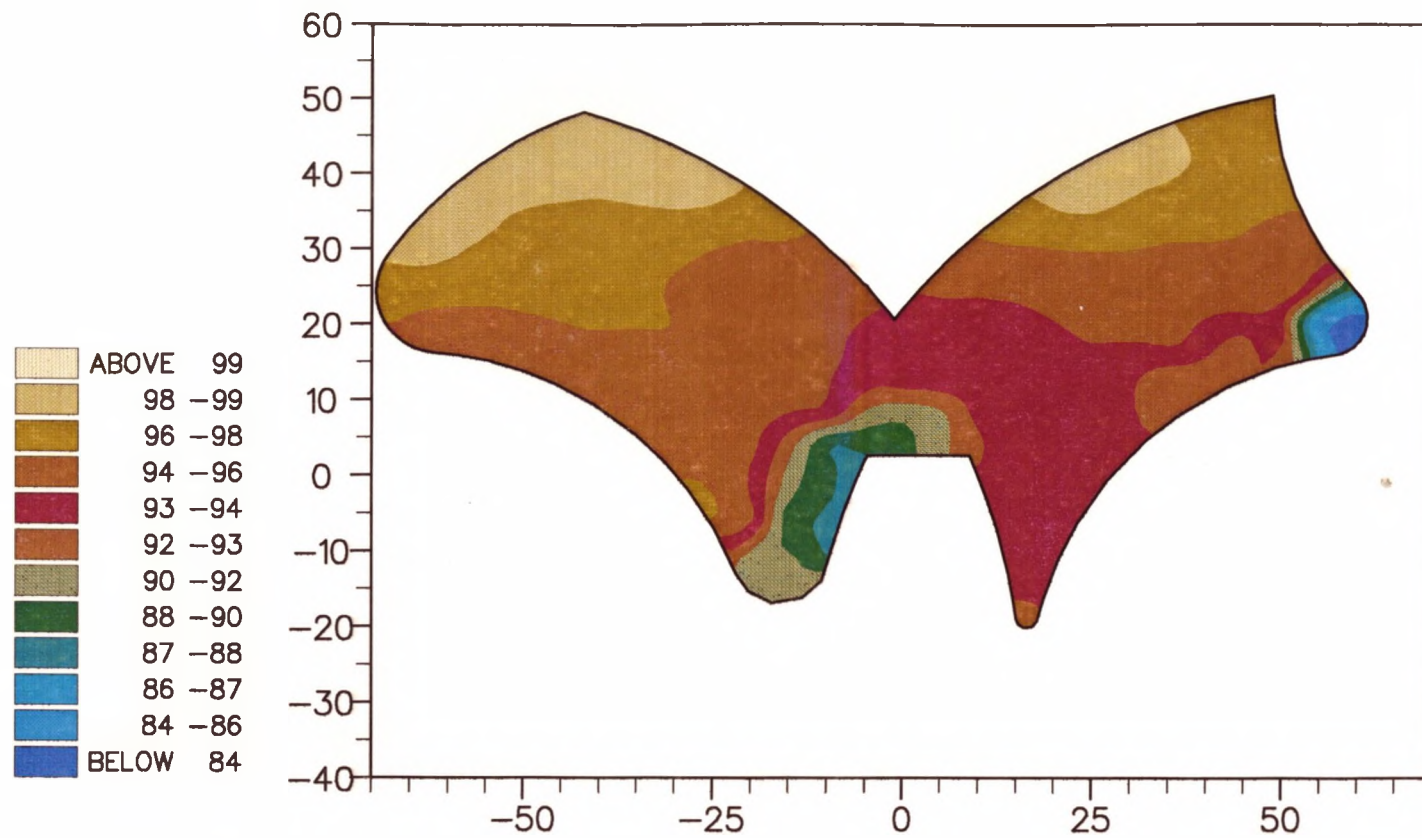


Fig.8.51. Void fraction distribution (R.113-B10)

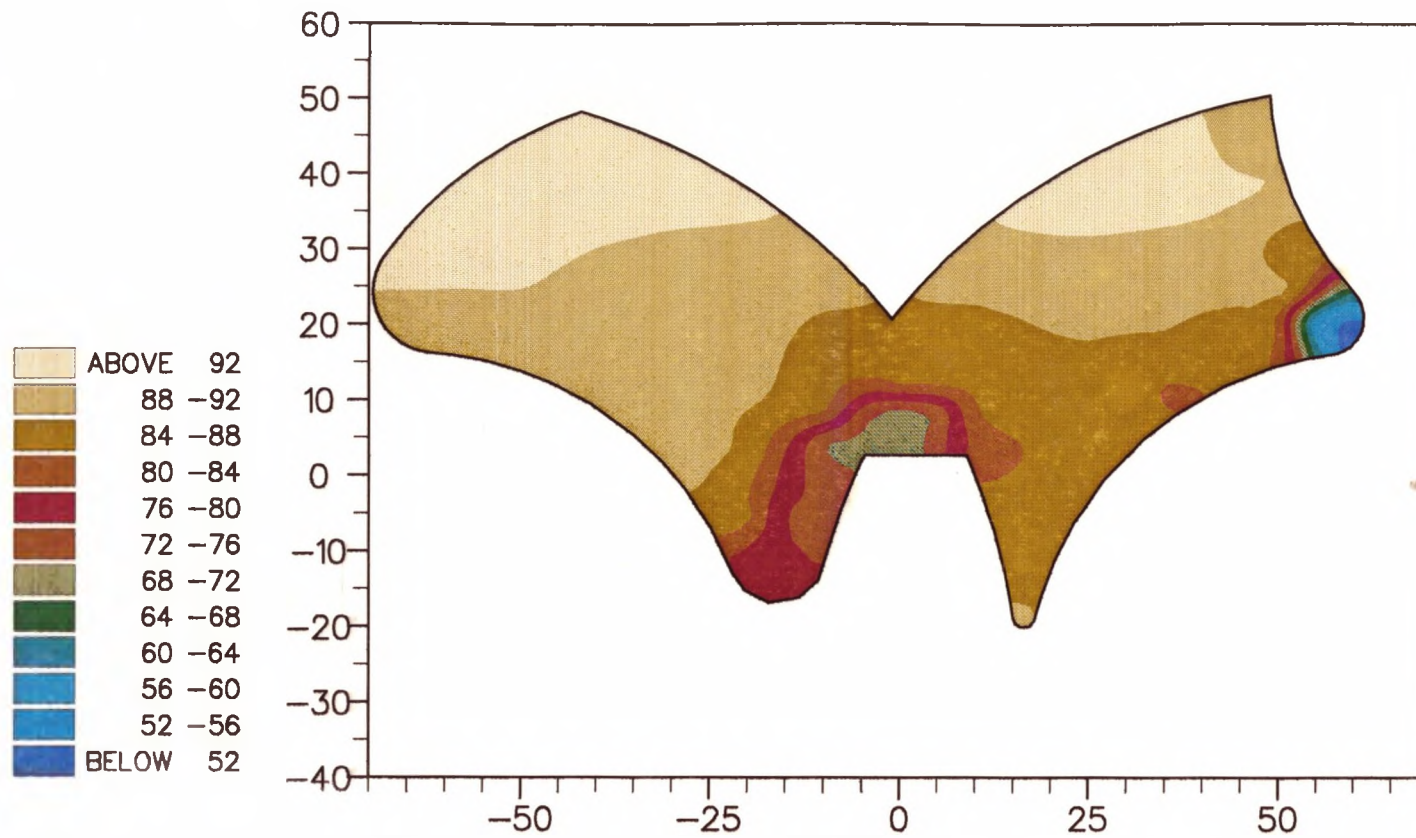


Fig.8.52. Void fraction distribution (R.113-B11)

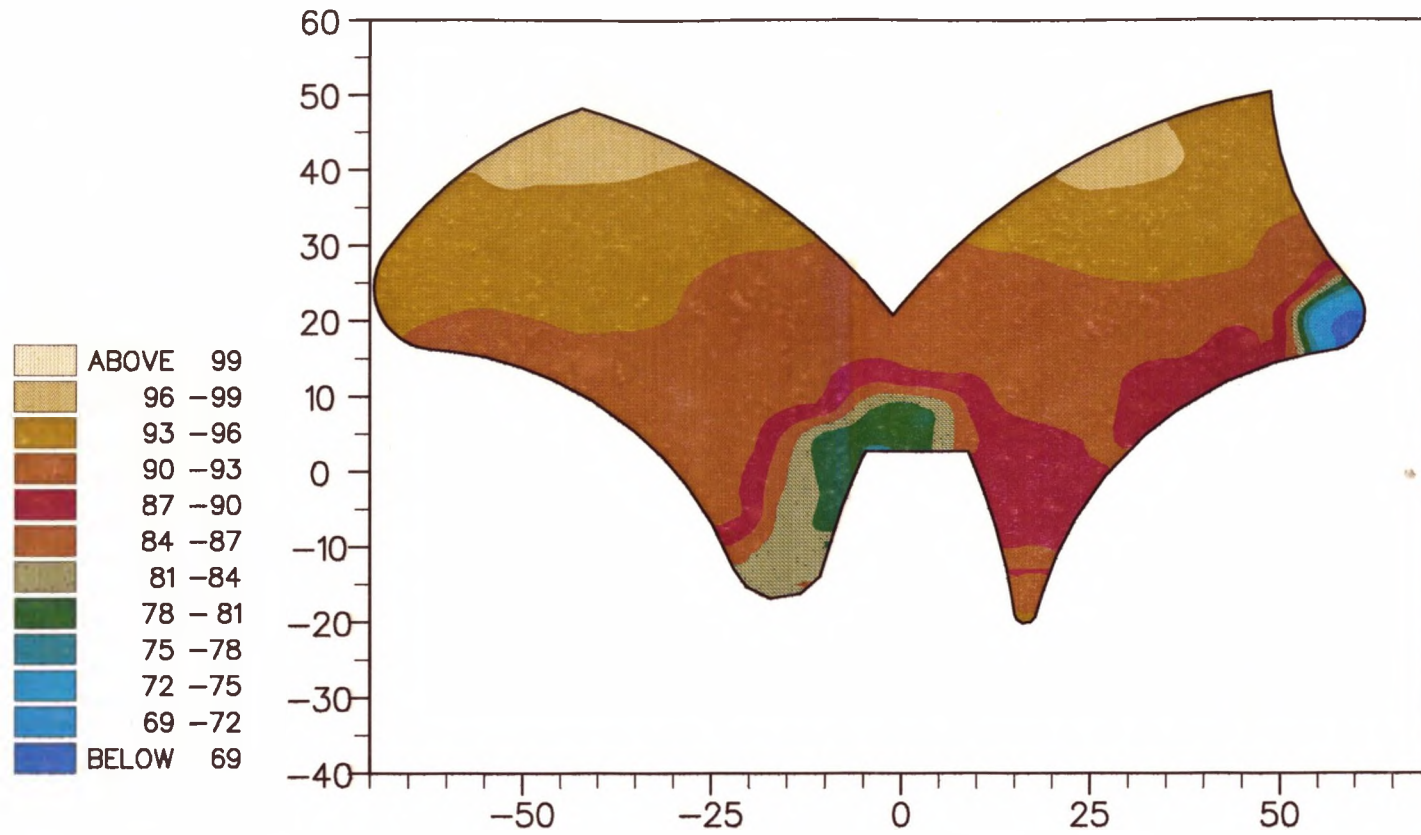


Fig.8.53. Void fraction distribution (R.113-B12)

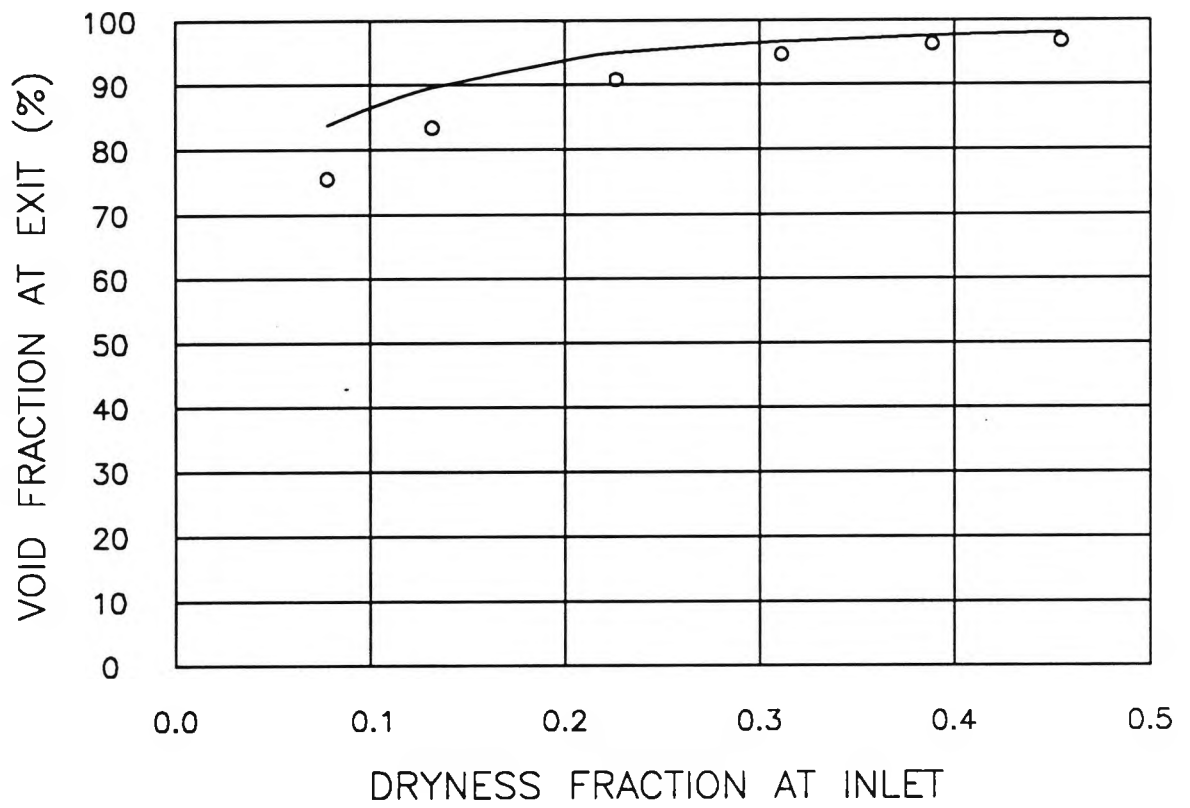


Fig.8.54. Comparison of Experimental and Computed Average Void Fractions at No.2 Inlet Port Exit (90°C)

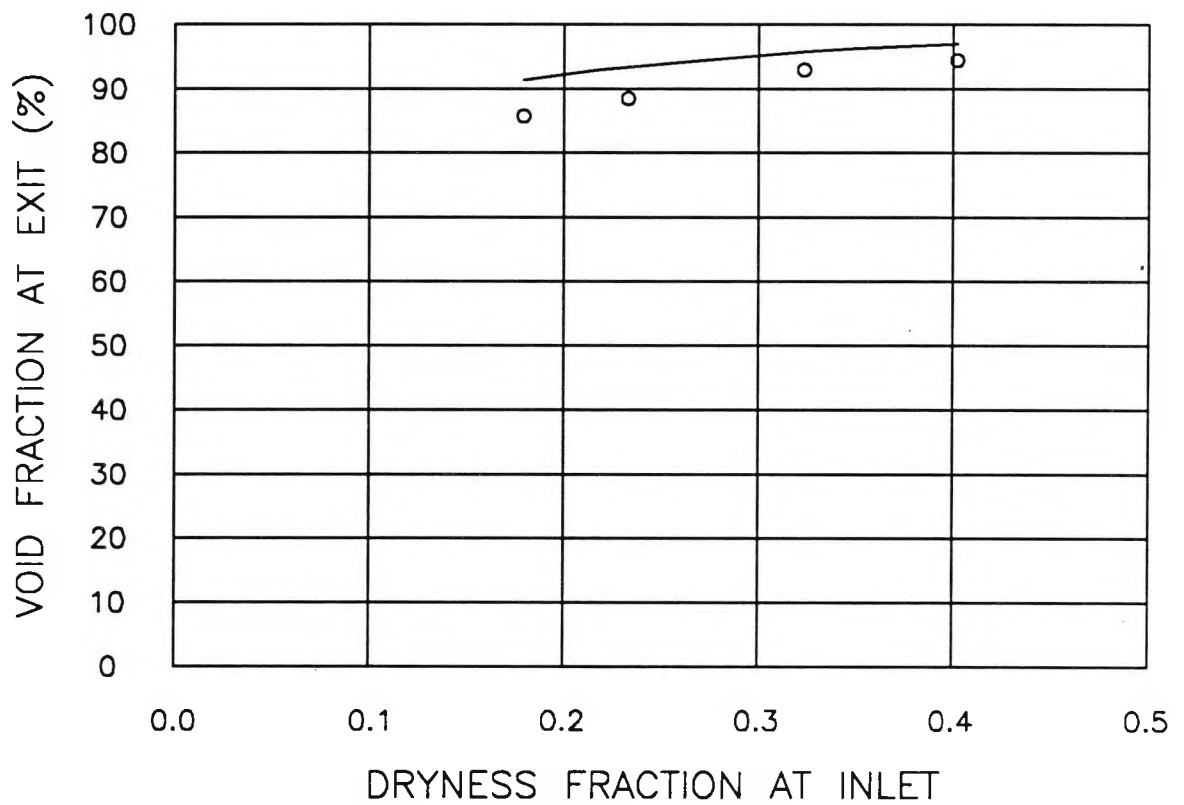


Fig.8.55. Comparison of Experimental and Computed Average Void Fractions at No.2 Inlet Port Exit (100°C)

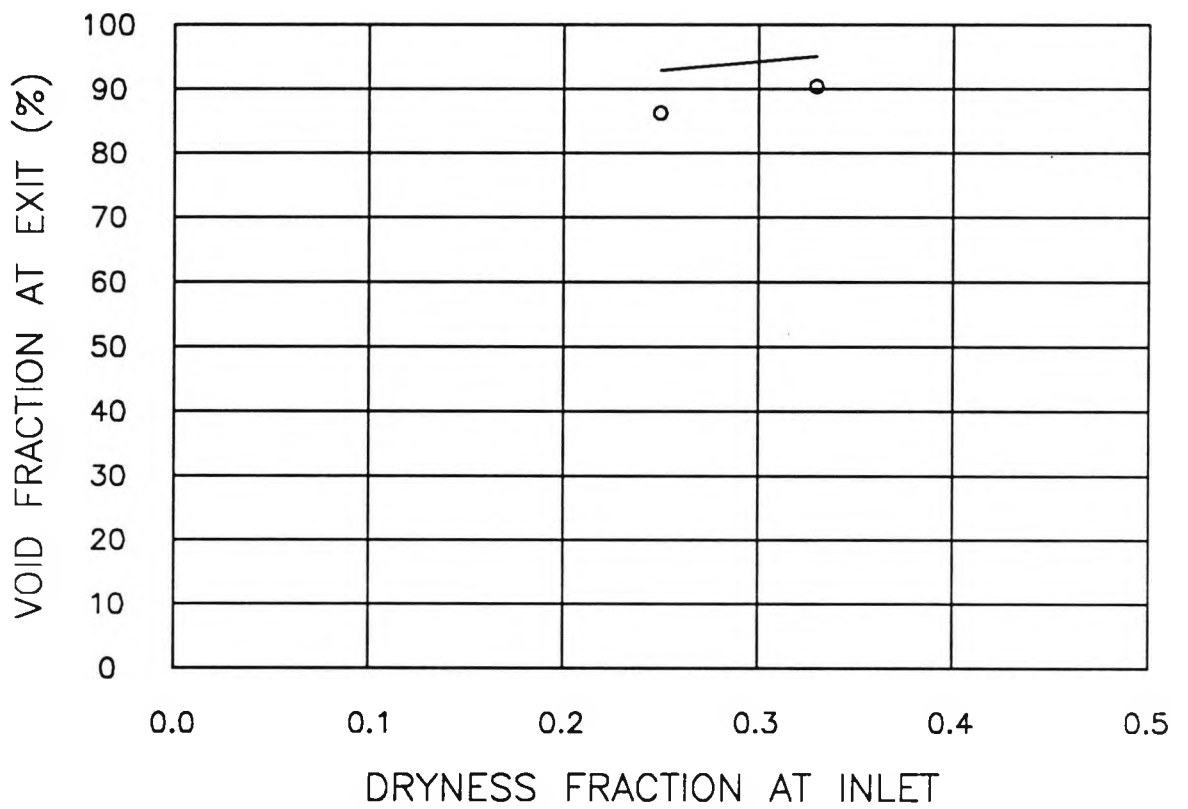


Fig.8.56. Comparison of Experimental and Computed Average Void Fractions at No.2 Inlet Port Exit (110°C)

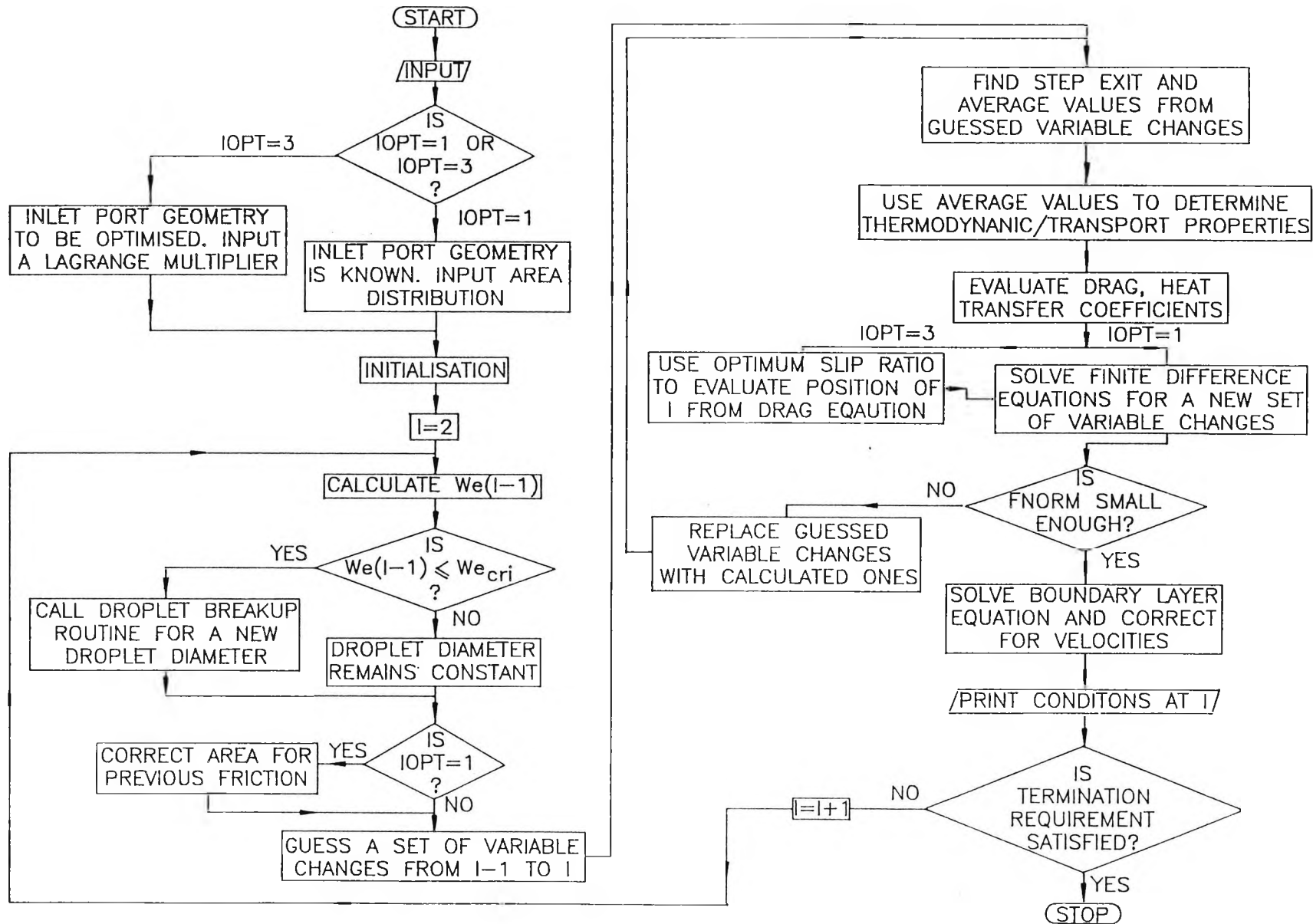


Fig.A.1. Flow Chart of Numerical Solution Procedure